Advances in Atom and Single Molecule Machines
Series Editor: Christian Joachim

Christian Joachim
Gwénaël Rapenne *Editors*

Single Molecular Machines and Motors

Proceedings of the 1st International Symposium on Single Molecular Machines and Motors, Toulouse 19–20 June 2013

Springer

Advances in Atom and Single Molecule Machines

More information about this series at http://www.springer.com/series/10425

Christian Joachim · Gwénaël Rapenne
Editors

Single Molecular Machines and Motors

Proceedings of the 1st International Symposium on Single Molecular Machines and Motors, Toulouse 19–20 June 2013

Springer

Editors
Christian Joachim
CEMES-CNRS and University Paul Sabatier
Toulouse
France

Gwénaël Rapenne
CEMES-CNRS and University Paul Sabatier
Toulouse
France

ISSN 2193-9691 ISSN 2193-9705 (electronic)
Advances in Atom and Single Molecule Machines
ISBN 978-3-319-13871-8 ISBN 978-3-319-13872-5 (eBook)
DOI 10.1007/978-3-319-13872-5

Library of Congress Control Number: 2014957631

Springer Cham Heidelberg New York Dordrecht London

Printed on acid-free paper

Springer International Publishing AG Switzerland is part of Springer Science+Business Media (www.springer.com)

Preface

This book is the fifth volume of the Springer Series "Advances in Atom and Single Molecule Machines". It compiles a selection of contributions presented during the international symposium "Single Molecular Machines and Motors" organized at CEMES-CNRS in Toulouse (France) during 19–20 June 2013. It was the first symposium of the kind, involving a large number of laboratories from academics to high-tech companies from all around the world working on that particularly original aspect of single molecular machines and motors.

The fields of molecular machines are currently very active because of their long-term potential. The expected advantages of these bottom-up approaches are now well known: ultimate size, possibility to design finely-tuned molecular devices and their low energy consumption. In the constant quest for the miniaturization of machines and functional molecular devices, single molecules are expected to play a major role since multistep chemical synthesis allows chemists to prepare tailor-made compounds with predetermined shape, movement or functions. This has stimulated the design and synthesis of a variety of compounds that resemble macroscopic machinery. However, the ultimate miniaturization of mechanical devices is reached only when addressing one single molecule and not a population of molecules in solution or on a surface. Artificial nanomachines have emerged as a new multidisciplinary field combining analytical techniques such as near-field microscopy, which allows to image a single molecule with intramolecular contrast, to study its motions and to manipulate it, but also multistep organic synthesis and theoretical chemistry to name a few. The molecule-surface symbiosis enables us to study how to guide and trigger complex molecular motions.

This symposium brought together researchers working on different strategies to synthesize and study single molecules displaying original mechanical properties at the nanometre and at the atomic scale. The main goal was to gather scientists from different communities (physics, chemistry and theory) in order to steer discussions and gather the main challenges using different techniques and approaches involved in the most recent developments in all aspects of this field but also to foster young Ph.D. and post-docs researchers towards this multidisciplinary approach.

We are happy to thank our sponsors for the first edition of this symposium: CNRS, Omicron, Région Midi-Pyrénées, Labex NEXT, the French embassy in the USA and the Université Paul Sabatier. In addition, Springer Verlag and its staff members are also deeply thanked for the publication of this book. The organizing committee also wishes to thank all the participants for their active participation in the symposium.

For the organizing committee
Christian Joachim
Gwénaël Rapenne

Contents

Single-Molecule Measurements of Synthetic Molecular Machines at Work

Anne-Sophie Duwez

Abstract Molecular motors are ubiquitous in nature and are essential in controlling and performing numerous biological functions. They are able to rectify random motion to generate directional force and carry out macroscopic tasks (Schliwa in Molecular motors. Wiley-VCH, Weinheim, 2003 [1]). This ability has inspired attempts to create synthetic machines exhibiting control over rotary or linear motion (Kinbara and Aida in Chem Rev 105:1377–1400, 2005 [2], Kay et al. in Angew Chem Int Ed 46:72–191, 2007 [3]). Whereas some examples of synthetic systems able to use biased Brownian motion to perform work and collectively induce movement of much larger objects have been reported (Kay et al. in Angew Chem Int Ed 46:72–191, 2007 [3], Browne and Feringa in Nat Nanotech 1:25–35, 2006 [4], Berná et al. in Nat Mater 4:704–710, 2005 [5]), seeing such a single molecule at work remains a major challenge. Some elegant experiments on single-molecule machines adsorbed on a surface, imaged and manipulated with the tip of a scanning tunnelling microscope have been realized (Grill et al. in Nat Nanotech 2:95–98, 2007 [6], Manzano et al. in Nat Mater 8:576–579, 2009 [7]). However, in this case, the molecule is adsorbed on the surface, and the experiments are done in ultra-high vacuum at low temperature, which can be a limitation for systems designed to perform work in solution at room temperature or even in physiological conditions. Here, we discuss how a single synthetic small machine at work can be addressed by AFM-based single-molecule force spectroscopy, a tool able to monitor mechanical forces with sub-nanometer resolution and which has been widely used to investigate molecular-level processes in macromolecules and biological machines (Bustamante et al. in Annu Rev Biochem 73:705–748, 2004 [8], Special Issue in Annu Rev Biochem 77:45–228, 2008 [9], Evans in Annu Rev Biophys Biomol Struct 30:105–128, 2001 [10], Liang and Fernández in ACS Nano 3:1628–1645, 2009 [11], Puchner and Gaub in Curr Opin Struct Biol 19:605–614, 2009 [12]).

A.-S. Duwez (✉)
Department of Chemistry, University of Liege, 4000 Liege, Belgium

C. Joachim and G. Rapenne (eds.), *Single Molecular Machines and Motors*,
Advances in Atom and Single Molecule Machines, DOI 10.1007/978-3-319-13872-5_1

1 Introduction

Molecular biological machines have inspired chemists who have, for some years now, been synthesizing systems capable of mimicking the natural world by producing a mechanical work that can manifest itself at the microscopic or macroscopic scale, such as the transport of a droplet up an inclined surface against gravity [5], the rotation of sub-millimetric objects on a substrate [13], or the deflection of a microcantilever [14]. Rotaxanes are prototypical synthetic molecular machine systems. They are made of a molecular ring threaded onto a molecular axle. The thread bears one or more recognition sites called stations, onto which the ring can bind through intramolecular bonds according to its affinities. The chemical environment also forces the ring to preferentially remain on one of the stations where it can make the strongest bonds. This site is thermodynamically favoured. Rotaxanes can behave as molecular shuttles: The ring can be translocated from one binding site on the thread to the other one through biased Brownian motion in response to an external trigger [3].

The collective dynamics of such systems have been studied with increasing structural sensitivity and temporal precision [15, 16]. In contrast, much of the exquisite and detailed information about how biomolecular machines operate has been gleaned from direct measurements made on single molecules with manipulation techniques such as optical tweezers or force clamp atomic force microscopy (AFM). Such measurements have shown that single biological machines are able to generate force against loads of 5–60 pN and have highlighted many details about their mechanical properties [8, 9]. AFM-based single-molecule force spectroscopy is a tool able to monitor mechanical forces with sub-nanometer resolution and has been widely used to investigate molecular-level processes [8–12]. For more than a decade, it has been used to probe individual (bio)molecules, providing unprecedented insights into their structure and function. For example, proteins, DNA, polysaccharides, supramolecular polymers, and polyelectrolytes have been investigated in their native environment, revealing details about the strength of inter- and intramolecular interactions, folding and unfolding pathways, mechanics, conformational changes, reactivity, and kinetics. However, few SMFS investigations have been successively realized on interlocked molecules [17] such as catenanes and rotaxanes [18, 19], whose large amplitude dynamics and conformational changes make them prototypical structural elements of synthetic molecular machines. The rarity of such studies comes from the difficulty of developing proper tools and preparing appropriate molecules that can be interfaced with single-molecule force spectroscopy techniques, especially when one wants to probe sub-molecular motions. Implementing single-molecule force spectroscopy on smaller molecules remains a major challenge.

In Sect. 2, we shall discuss two examples of synthetic polymers used to convert energy into mechanical work during single-molecule reversible cycles probed by AFM. Due to their size, macromolecules can be easily interfaced with and then probed by AFM-based single-molecule force spectroscopy. On the contrary, small

molecules are much more difficult to interface with the AFM without hindering their function. The very small changes produced (sub-molecular movements and force generated) are also much more difficult to detect. In Sect. 3, we shall discuss two examples of rotaxanes investigated in an irreversible rupture process (de-threading) on one hand and in reversible cycles that allow the direct measurement of the force generated and the work produced on the other hand.

2 Synthetic Polymers

2.1 Polyazobenzene Peptide

The first example of a single-molecule operating cycle in which a polymer was shown to contract against an external force acting along the polymer backbone, thus delivering mechanical work, was reported by Gaub and co-workers [20].

Azobenzene units are well-known chromophores that can be reversibly switched at two different wavelengths between an extended *trans*- and a shorter *cis*-configuration. The authors show that polyazopeptide chains can be reversibly shortened against an external force by photochemical switching between *trans*- and *cis*-azobenzene isomeric configurations. The azobenzene units were introduced into a polypeptide backbone (Fig. 1a). To ensure stable attachment, the polymer end groups were covalently coupled to both the AFM tip and a supporting glass slide by heterobifunctional chemistry.

First, the polymer was measured in its initial configurationally mixed state. The force curve was recorded. Then, five pulses at $\lambda = 420$ nm were applied that drove the polymer into the saturated *trans*-state. The polymer was stretched and the force was measured, revealing a marked lengthening of the polymer. The polymer was relaxed again, and five pulses of $\lambda = 365$ nm were applied to drive the polymer into the saturated *cis*-state. As a result, the polymer exhibited marked shortening. The measurements also show that switching is possible even against an external force. Only at forces above 500 pN, the authors did not observe the optical *trans–cis* isomerization reaction. These experiments show that it is possible to handle and manipulate an individual polyazopeptide, mechanically measure its length and its compliance, optically excite this polymer and pump it into a predominantly *cis*- or predominantly *trans*-state, and finally detect this transition mechanically. As closed cycles can be repeated several times before the polymer or its attachment ruptures, optomechanical cycles, in which the polymer chain converts optical excitation into mechanical work, could be realized (Fig. 1b). An individual polyazobenzene peptide was first lengthened by five pulses with $\lambda = 420$ nm at a force of 80 pN (I) and then expanded mechanically to a restoring force of 200 pN (II). Then, five pulses at $\lambda = 365$ nm were applied, resulting in a contraction of the polymer against the external force (III). Then, the force on the polymer was reduced to 85 pN (IV). Finally, the cycle was completed by applying five pulses at $\lambda = 420$ nm, resulting in an optical expansion of the

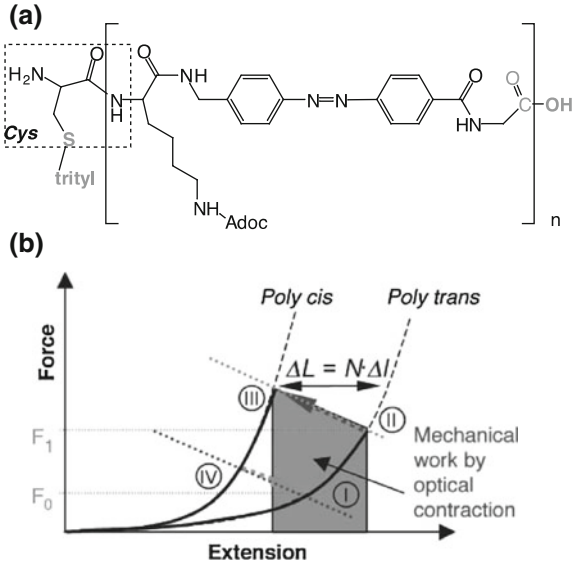

Fig. 1 **a** Chemical structure of the polyazobenzene peptide. **b** Principle of the optomechanical cycle. Force–extension cycle starts at point I on the force–distance curve of the long polymer configuration, at which the polymer is in its extended configuration. When an external load is applied to the polymer, it will follow the force–distance curve of the extended polymer configuration up to point II, where the system is switched back to its short configuration, point III, by an external stimulus (here, light). The removal of the load results in (reversible) relaxation of the polymer, which brings the system to point IV. From there, it is switched back to the starting point of the cycle by another external stimulus. The work output of the system is the mechanical energy related to the contraction $L = N \times \Delta l$ of the polymer against the external load. The external input needed to perform this mechanical work is the energy of the external stimulus (plus the energy needed to apply the load). As for any thermodynamic cycle, the efficiency of energy conversion can then be defined by the ratio W_{out}/W_{in}. Adapted from [20]

molecule to its original length. From the cycle, it is possible to estimate the quantum efficiency of the *trans–cis* switching process. The mechanical work performed by the azobenzene polymer chain upon its transition from II to III is simply given as $W = \Delta L \times F_{II \rightarrow III}$, that is about 4.5×10^{-20} J. If it is assumed that each switching of a single azobenzene unit is initiated by a single photon carrying an energy of 5.5×10^{-19} J ($\lambda = 365$ nm), the efficiency is estimated at 10 %.

2.2 Poly(ferrocenylsilane)

Vancso and co-workers investigated stimulus-responsive poly(ferrocenylsilane) (PFS) polymers as a model system for the realization of single-molecule closed cycles powered by an electrochemical redox process [21].

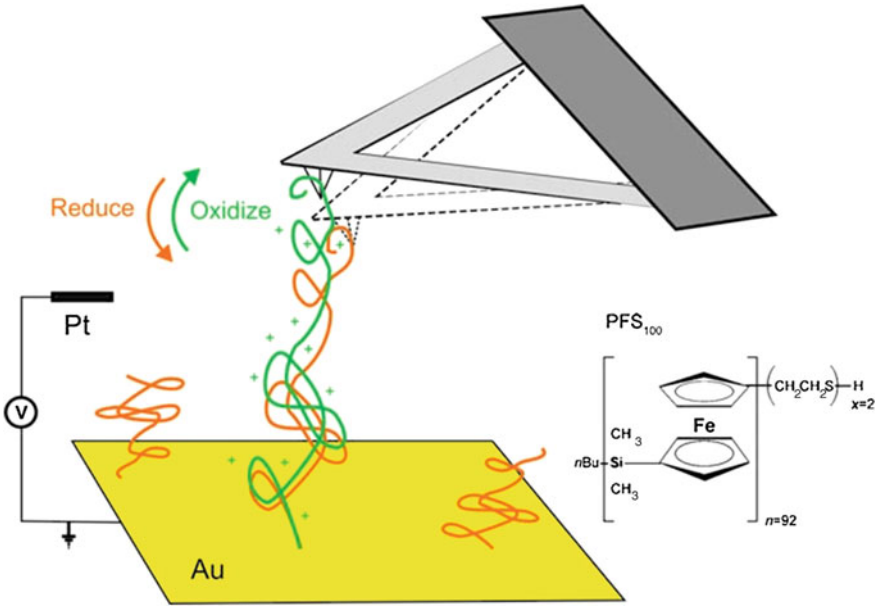

Fig. 2 Stretching of single stimulus-responsive ethylene sulfide end-capped PFS (PFS100) chains by electrochemical AFM-based single-molecule force spectroscopy. Copyright Wiley-VCH Verlag GmbH & Co. KGaA. Reproduced with permission from [21]

They realized closed electromechanical cycles by addressing single polymer chain by an AFM tip and the stretching and relaxing of the molecule in situ under different applied electrochemical potentials (Fig. 2). They made a quantitative analysis of the efficiency of the closed cycles as a function of extension of the molecule. The experiments were conducted such that the AFM tip was repeatedly approached very close to the substrate surface and retracted to a distance of 80 nm from the substrate. If a PFS chain was indeed fished by the tip by simple physisorption, a restoring force was detected upon retraction. The single-chain elasticity of such a bridging chain was subsequently probed, typically up to five times before desorption, in consecutive force–extension curves. Individual PFS chains kept in an extended state between the AFM tip and the surface were electrochemically oxidized at constant z position by applying a potential of +0.5 V followed by deflection–displacement measurements under constant potential. The complete oxidation of the PFS chains was verified by the cyclic voltammetry data captured in situ. Similarly, single chain was stretched in the oxidized state, followed by electrochemical reduction at constant z position and continued force spectroscopy. In the experiments, it was observed that the force at fixed maximum extension decreased upon oxidation and increased upon reduction to the neutral state. This observation is related to the lengthening of the oxidized chain with respect to the neutral chain which can be attributed to the electrostatic repulsion among the oxidized ferrocene units along the chain Thus, the change in the redox states is

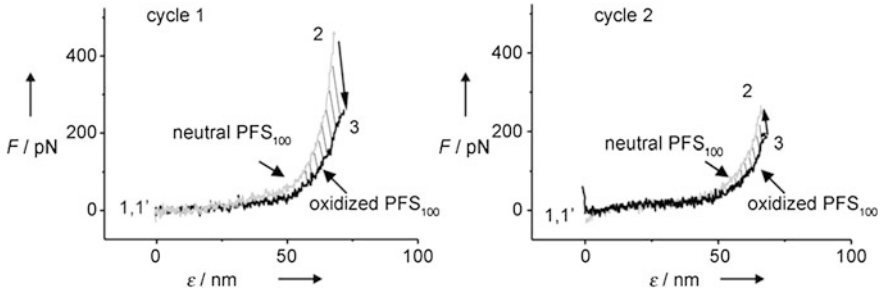

Fig. 3 Force–extension curves of cycle 1 and cycle 2. The enclosed areas of the cycles correspond to the mechanical work input or output of the single-polymer-chain mechanoelectrochemical cycle. Adapted from [21]. Copyright Wiley-VCH Verlag GmbH & Co. KGaA. Reproduced with permission

directly coupled to a mechanical output signal of the force sensor. The two data sets in Fig. 3 display the entire mechanoelectrochemical cycle for two individual molecules in both possible directions (from neutral to oxidized state and from oxidized to neutral state). As the two chains possess, within experimental error, the same length at a force value of 200 pN when they are neutral, the data can be directly compared. The areas enclosed between the corresponding curves for the oxidized and reduced PFS100 macromolecules in cycles 1 and 2 correspond to the work input (W_{in}) and work output (W_{out}) of the electromechanical cycles, respectively. Since all the electrochemical parameters are known, as well as the number of transferred charges during the oxidation/reduction processes, the efficiency of the single-molecule electromechanical cycle could be estimated. For cycle 1, the work was estimated at 2.2×10^{-18} J for an extension from 40 to 68 nm, while for cycle 2, it was 0.7×10^{-18} J for an extension from 40 to 66 nm. The corresponding efficiencies of cycles 1 and 2 can be estimated at 26 and 8 %, respectively. The difference in the values originates from the variable maximum extension of the chain as a consequence of the variable maximum forces applied in the experiments. It is important to note that the efficiency values obtained from cycles 1 and 2 are calculated by assuming ideal conditions of energy input, that is, no dissipative processes take place, which may lead to an overestimation of these values.

3 Rotaxanes

3.1 Estimation of the Energy Produced by a Redox-Controllable Rotaxane

Stoddart and co-workers have pulled the molecular ring over the bulky end groups of a redox-active rotaxane with an AFM tip [18]. They compared the large forces required to de-thread oxidized and unoxidized molecules.

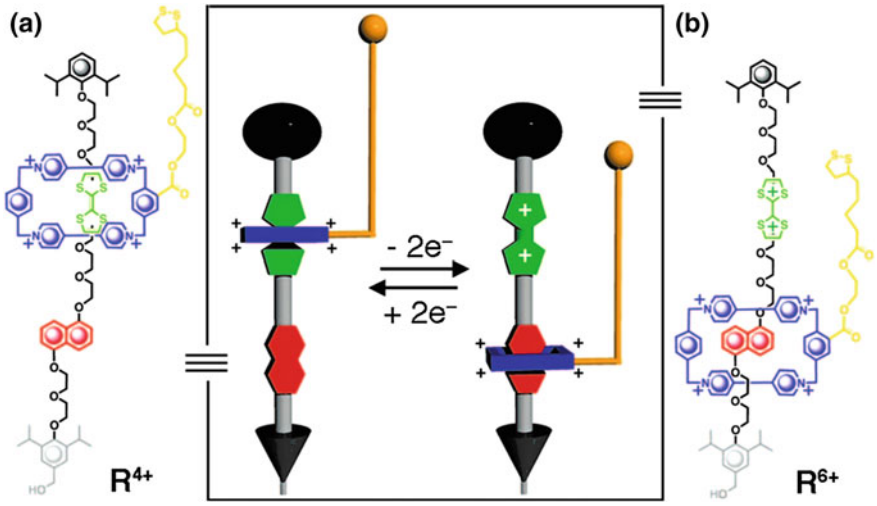

Fig. 4 Chemical structure and schematic representation of bistable [2]ro-taxane R^{4+}, in which an electron-poor cyclobis(paraquat-*p*-phenylene) (CB-$PQT4^{4+}$) ring is confined to an axis containing two electron-rich recognition sites, tetrathiafulvalene (*TTF*) and 1,5-dioxynaphthalene (*DNP*), by the presence of bulky 2,6-diisopropylphenyl ether stoppers at each end. One of these stoppers, the one closer to DNP, carries a hydroxymethyl group on its 4th position for subsequent attachment to silicon wafers. **a** The $CBPQT^{4+}$ ring, which carries a very short tether terminated by a thioctic acid ester for attachment to a gold-coated AFM tip, displays a stronger interaction with TTF than with DNP and thus resides selectively on the former. **b** Chemical oxidation of TTF to TTF^{2+} results in a strong charge–charge repulsion between the $CBPQT^{4+}$ ring and TTF^{2+}, a situation that causes the $CBPQT^{4+}$ ring to shuttle to DNP in the oxidized [2]rotaxane R^{6+}. Copyright 2006 National Academy of Sciences, USA. Reproduced with permission from [18]

They have used the switchable, bistable [2]rotaxane $\mathbf{R}^{4+}$ shown in Fig. 4, which can function by the redox-controlled mechanical shuttling of the ring along its axis. The molecule was specifically designed with a short thioctic acid linker tethered to the ring for tight attachment to a gold AFM tip and with a hydroxymethyl group on one of the stoppers for attachment to SiO_2 via covalently bound monolayers of isocyanatopropyl linkers. They used AFM force spectroscopy to probe the steric and electrostatic interactions present in the ground (Fig. 4a) and oxidized (Fig. 4b) states of $\mathbf{R}^{4+}$. Control AFM measurements consist in probing molecules to measure the repulsive steric interactions (Fig. 5a) between the cyclobis(paraquat-*p*-phenylene) ($CBPQT^{4+}$) ring and the diisopropylphenyl ether stopper. The probing of the $\mathbf{R}^{6+}$ molecules in an oxidizing solution was used to measure the repulsive force (Fig. 5b) between the $CBPQT^{4+}$ ring and an oxidized tetrathiafulvalene (TTF^{2+}), which is responsible for molecular actuation. On the basis of the differences in the force required to pass the ring over the stopper in presence and absence of the Fe $(ClO_4)_3$ oxidizing agent, they made an estimation of the repulsive electrostatic barrier, which is ultimately responsible for the molecule's actuation.

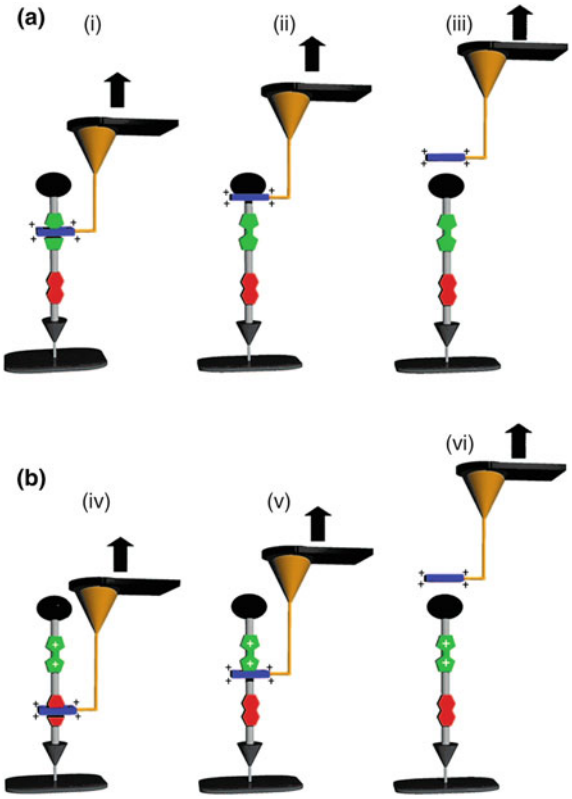

Fig. 5 Schematics of the AFM force spectroscopy experiment on the [2]rotaxane R^{4+}. **a** Ground-state probing in the absence of oxidant. (*i*) [2]Rotaxane R^{4+} confined to a silicon surface and attached to a gold AFM tip via two gold–sulfur bonds. (*ii*) Retraction of the AFM tip from the surface pulls the $CBPQT^{4+}$ ring away from the TTF unit and toward the bulky stopper. (*iii*) Continued retraction causes the $CBPQT^{4+}$ ring to pass over the stopper at which point the rupture force required to overcome this physical barrier is measured. **b** Oxidized-state probing performed in the presence of 10^{-4} M $Fe(ClO_4)_3$ in EtOH. (*iv*) The attachment of a gold AFM tip to [2]rotaxane R^{6+} whose ring is now located on the lower DNP unit as a result of the chemically induced oxidation of the TTF unit to TTF^{2+} and subsequent electrostatic repulsion of $CBPQT^{4+}$. (*v*) Retraction of the AFM tip forces the $CBPQT^{4+}$ ring toward the TTF^{2+} despite the electrostatic repulsion between the two moieties. (*vi*) Continued retraction of the AFM tip enables the $CBPQT^{4+}$ ring to overcome the electrostatic barrier imposed by TTF^{2+}, resulting in rupture of the mechanical bond posed by the stopper. When measuring the higher energy electrostatic repulsion of the oxidized molecule, the subsequent de-threading event is not measured because of the dynamic instability of the AFM probe. Copyright 2006 National Academy of Sciences, U.S.A. Reproduced with permission from [18]

By using the measured force spectroscopy values of 66 pN for the de-threading barrier under non-oxidative conditions and 145 pN for the oxidant-induced electrostatic repulsion barrier, along with the distance of 8.6 Å of the energy barrier produced from molecular simulations for the de-threading of the $CBPQT^{4+}$ ring over the bulky stopper and 13.0 Å as the distance necessary for the $CBPQT^{4+}$ ring

to travel from the DNP recognition site to the TTF^{2+} dication, the difference in interaction energies can be calculated as 19 kcal mol^{-1}. By combining the 19 kcal mol^{-1} difference in oxidative and non-oxidative interaction energies with the theoretically determined value of 46 kcal mol^{-1} for the energy associated with ground-state de-threading, a final value of 65 kcal mol^{-1} was obtained, representing the amount of repulsive actuation energy between $CBPQT^{4+}$ and TTF^{2+} produced by the oxidation of R^{4+}. As estimated by this approach, 65 kcal mol^{-1} represents the upper limit of the total actuation energy.

Unfortunately, the irreversible rupture of molecules due to the de-threading required by this experiment prohibits the realization of a relaxing step to complete the cycle required to directly probe the mechanical forces generated against an external load and to verify the estimation of 65 kcal mol^{-1}.

Furthermore, this experiment did not allow detection of the breaking and making of the intercomponent interactions involved in ring movement along the axle.

3.2 Direct Measurement of the Force Generated by a H-bonded Rotaxane

Recently, in collaboration with David Leigh, University of Manchester, we succeeded in detecting sub-molecular movements in a H-bonded rotaxane and in measuring the force generated by this molecule against a load [19].

We have designed a hydrogen-bonded rotaxane-based molecular shuttle with a tether attached to the ring to track its motion by an AFM cantilever (Fig. 6). The [2] rotaxane consists of a ring mechanically locked onto a thread by two bulky groups situated at either end of the axle (Fig. 7). The thread bears both fumaramide and succinic amide–ester sites, each of which can bind to the macrocycle through up to four intercomponent hydrogen bonds [22]. The ring predominantly resides over one of the two sites, the occupancy ratio being higher than 95:5. A poly(ethylene oxide) (PEO) chain, suitable for binding to an AFM tip, was attached to the macrocycle by a Cu(I)-catalyzed azide–alkyne cycloaddition (CuAAC) 'click' reaction in collaboration with C.-A. Fustin, Université catholique de Louvain. Close to the fumaramide binding site, a disulfide group was introduced to enable the grafting of the rotaxane onto a gold surface. The rotaxane–tether molecules were grafted onto gold/mica substrates in a dilute distribution (isolated molecules).

We used the cantilever of an AFM microscope to catch the tether, then apply a mechanical load to the ring of the rotaxane, and follow its movement. The caught molecules were stretched in a controlled manner by moving the tip away from the substrate at a fixed pulling rate, and the force–extension profiles were measured (Fig. 8). If the force exerted on the tether is higher than the force of the hydrogen bonds that bind the ring to its preferred site, the ring detaches from its station. It is then pulled along the axle, away from its most stable binding site. Figure 8a shows a high-resolution force–extension curve, and Fig. 8b shows our interpretation of

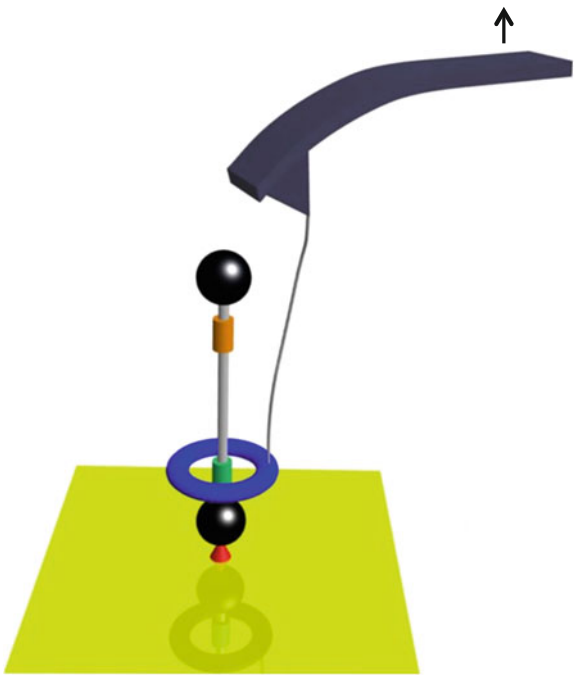

Fig. 6 Single-molecule force spectroscopy of the rotaxane. The rotaxane is grafted onto gold, and the PEO tether is caught by the AFM tip and stretched by moving the tip away from the surface. Adapted from [19]

events taking place when pulling on the rotaxane–PEO molecule that could explain the observed force profile. The progressive stretching of the PEO tether gives the characteristic parabolic profile (I) of a random coil, which loses entropy on stretching, inducing a restoring force. Once the force exerted on the tether exceeds the strength of the hydrogen bonds between the macrocycle and the fumaramide group, the hydrogen bonds break (II). The macrocycle is now free to move along the thread up to the succinic amide–ester site, the tension in the PEO backbone is reduced, and the force decreases (III) until the displacement of the cantilever again increases the tension in the PEO tether. Further cantilever displacement continues the stretching of the PEO until the force exceeds the interaction strength of the chain with the tip, which leads to detachment (IV). The peak characteristic of the rupture of the hydrogen bonds appears at 27 ± 8 pN in dimethylformamide and at 45 ± 10 pN in tetrachloroethane (TCE). This difference is consistent with the relative strengths of solute–solute hydrogen bonding in the two solvents [23], intercomponent hydrogen bonds being stronger in TCE, the less polar solvent. To further support the hypothesis that this peak is the signature of the breaking of the intercomponent hydrogen bonds, we fitted the pulling profiles using entropic elasticity models, such as the worm-like chain model that predicts the relationship between the extension of a linear polymer and the entropic restoring force. The force curves could be fitted using a persistence length of 0.35 ± 0.05 nm, close to

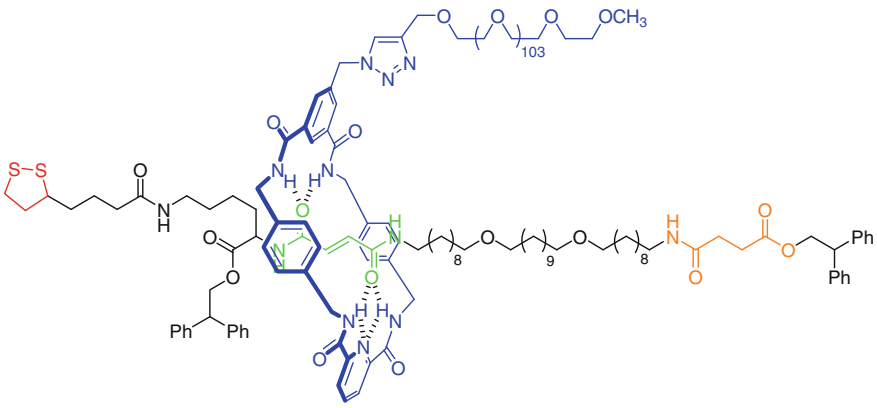

Fig. 7 Chemical structure of the rotaxane molecule, synthesized by the group of D.A. Leigh, University of Manchester. The rotaxane consists of a benzylic amide molecular ring (*in blue*) mechanically locked onto an axle by bulky diphenylethyl ester groups situated at either end. The axle bears a fumaramide group (*in green*) and a succinic amide–ester group (*in orange*), either of which can act as a binding site for the ring through up to four intercomponent hydrogen bonds. The affinity of the ring for the fumaramide site is much higher than for the succinic amide–ester site, so that the fumaramide/succinic amide–ester occupancy ratio is higher than 95:5. Next to the fumaramide binding site, a disulfide group (*in red*) was introduced to enable the grafting of the molecule onto gold substrates. A 4600 M_n PEO tether (*in blue*) is attached to the ring in order to link the molecule to the AFM probe and track the motion of the ring along the axle

the theoretical persistence length of PEO (0.37 nm). The fits of the profile before and after the rupture peak give the increase in length (ΔL_c) of the molecule after rupture of the intercomponent hydrogen bonds. The average ΔL_c obtained, 3.9 ± 0.5 nm, is consistent with the theoretical length of the fully extended thread between the two binding sites, about 4.5 nm, providing further evidence that the small peak is due to the rupture of the interactions between the macrocycle and the fumaramide binding site.

Pulling–relaxing cycles were also recorded (Fig. 9a), and we observed that while relaxing the tension in the PEO tether, the force suddenly increased. An increase of tension while decreasing the tip–surface distance can be explained by the appearance of force acting on the tether at the other end (Fig. 9b). This means that the macrocycle has travelled back from the succinic amide–ester site to the fumaramide site and that it is able to generate force when rebinding against the external load exerted by the cantilever. It means that if we trap the ring and then slightly decrease the force on the tether while maintaining the pulling, the ring is capable of pulling more strongly to recover its preferred position. Figure 9c shows that in TCE, the macrocycle is able to travel back against an external load of 30 pN. The mechanical work produced by this sub-molecular motion is about 6 kcal mol^{-1}.

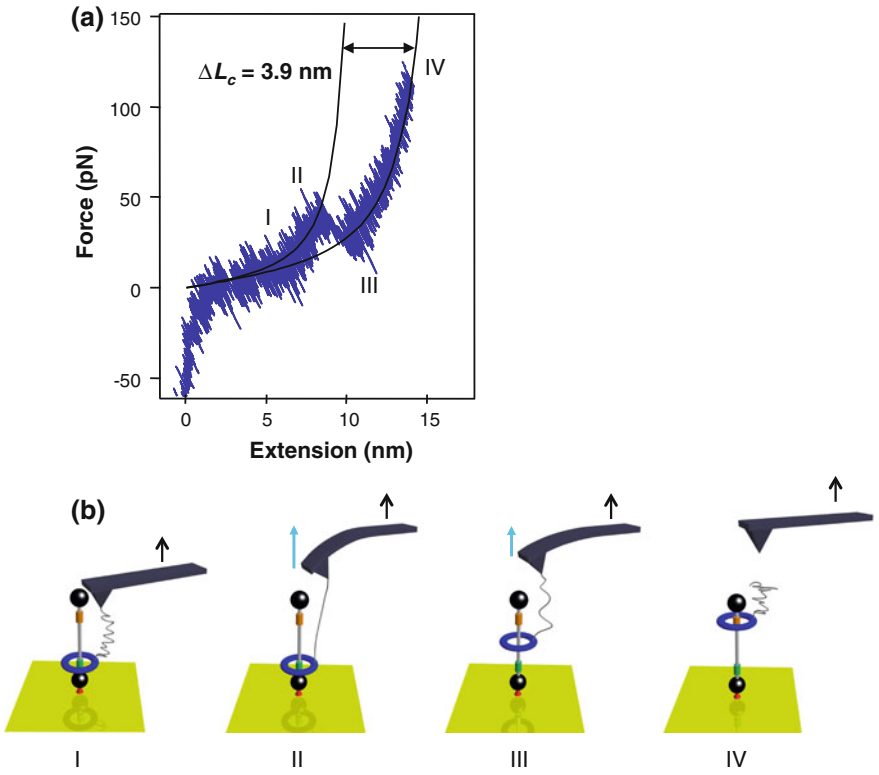

Fig. 8 **a** High-resolution force–extension curve for the rotaxane–PEO molecule in TCE with worm-like chain model fits to the data (*thin solid lines*) with an increase in length (ΔL_c) of the molecule after rupture of the hydrogen bonds of 3.9 nm. **b** Interpretation of the sequence of events taking place when pulling on the rotaxane–PEO. *Black arrows* show the direction of cantilever displacement. Blue arrows show the direction of the force exerted on the molecular ring. (*I*) Progressive stretching of the PEO tether. (*II*) Once the force exerted on the tether exceeds the force of the hydrogen bonds between the ring and the fumaramide site, the hydrogen bonds break. (*III*) After rupture, the ring is free to move along the thread, the tension in the PEO backbone is partly released, and the force decreases until the displacement of the cantilever increases again the tension in the PEO tether. (*IV*) Further cantilever displacement continues the stretching of PEO until the force exceeds the interaction strength of the chain with the tip, which leads to detachment. Adapted from [19]

For the first time, a quantitative measurement of the work done by a single synthetic molecule less than 5 nm long has been achieved. It shows that the biased Brownian motions caused by thermal energy can be harnessed within a single synthetic small molecule, to generate significant directional forces of similar magnitude to those generated by natural molecular machines, which are a lot bigger.

The study of systems at the single molecule level has considerable importance on a fundamental level. Indeed, the laws of physics and chemistry which govern the

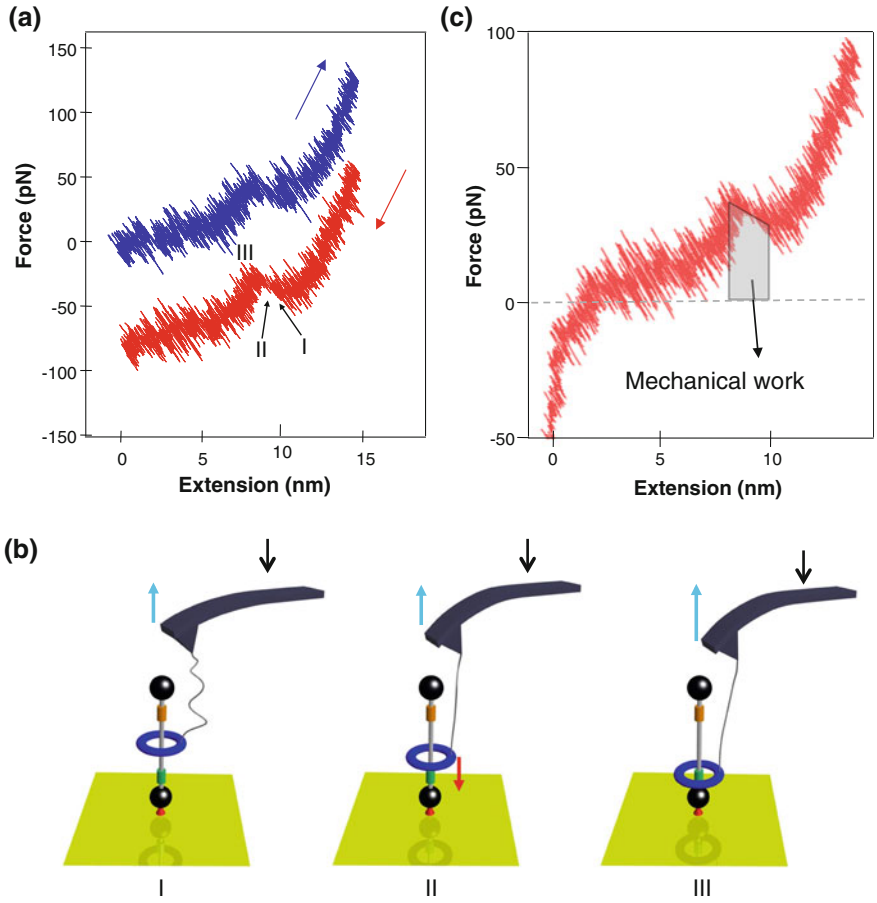

Fig. 9 Pulling–relaxing cycles for the rotaxane–PEO molecule. **a** Pulling (*blue*) and relaxing (*red*) curves for a single rotaxane–PEO molecule in TCE. The relaxing trace is offset vertically for clarity. **b** Schematic of the relaxing experiment showing our interpretation of events. *Black arrows* show the direction of cantilever displacement. *Blue arrows* show the direction of the force exerted on the ring. (*I*) Progressive release of the tension in the PEO tether. (*II*) The force suddenly increases as a result of the ring shuttling in the opposite direction (*red arrow*) to the force exerted on it (*blue arrow*). (*III*) The ring has rebound to the fumaramide site. **c** Relaxing curve (data as in **a**) with the area under the trace representing the work done by the molecule as the ring shuttles back to its preferred binding site. Adapted from [19]

macroscopic world are no longer necessarily valid at the molecular level. The principles of thermodynamics describe processes of energy exchange (work and heat) of macroscopic systems with their environment. In a general way, in macroscopic systems, the average behavior is reproducible and the fluctuations are of little importance. When the dimensions of the system become nanoscopic, the fluctuations can give rise to significant deviations with regard to the average

behavior. An individual molecule can, for example, extract energy (which comes from thermal energy) from its environment to perform a mechanical work higher than the energy available in the molecule. This is inconceivable for a set of billions of molecules because they all have to do it at the same time, which is statistically impossible. Thus, well-known concepts of physics and chemistry must be redefined or improved in order to reconcile the nanoscopic and macroscopic worlds. It is from this perspective that for several years, theoretical physicists have established fluctuation theorems. These theorems reconcile what we observe on a large scale and for a large number of molecules in equilibrium with the data obtained for a single molecule (or a small number of molecules) in non-equilibrium conditions. For the first time, we have shown that it is possible to apply modern theories of non-equilibrium statistical mechanics to AFM force measurements.

For a reversible process, the mechanical work equals the Gibbs free energy change of the process, but the distribution of work trajectories typically results in hysteresis because of the fluctuations.

Recent developments in non-equilibrium statistical mechanics enable recovery of the reversible work, and thus the zero-force free energy, from the distribution of work trajectories in pulling–relaxing cycles.

Fluctuation theorems relate the equilibrium free-energy change ΔG to non-equilibrium measurements of the work done on a single molecule. The Crooks fluctuation theorem [24] relates ΔG to the probability distributions of the non-equilibrium work measured during the forward and reverse changes that occur when a system is driven away from thermal equilibrium by the action of an external perturbation. It enables us to quantify the amount of hysteresis observed in the values of the irreversible work done during a rupture and rebinding process. The CFT predicts that $(P_W/P_{WR}) = \exp((W - \Delta G)/k_BT)$ where ΔG is the free-energy change between the final and the initial states and thus equals to the reversible work associated with this process. P_W is the probability distribution of the values of the work during the rupture process, and P_{WR} corresponds to the reverse process. The CFT states that although the probability distribution of the work performed on the molecule during the rupture process and the work done by the molecule during the rebinding process depend on the pulling protocol, their ratio depends only on the equilibrium free-energy difference, ΔG. Thus, the value of ΔG can be determined once the two distributions are known, regardless of the pulling speed [25].

We used the Crooks fluctuation theorem to estimate the free energy driving the macrocycle to bind to the fumaramide binding site at zero force. The work done on/by the molecules during pulling/relaxing is given by the areas below the corresponding force–extension curves (gray area Fig. 9c). The contribution arising from the entropy loss due to the stretching of the PEO was obtained by integration of the worm-like chains reference curves and subtracted from the total work values. The rupture and rebinding work distributions overlap over a large range of work values (Fig. 10), which means that we are indeed in the near-equilibrium regime. They cross at a value of the work ΔG of $9.3 \pm 2.3\ k_BT = 5.5 \pm 1.3$ kcal mol^{-1}. This value is in good agreement with the difference in energy between the molecular ring binding to the fumaramide and succinic amide–ester binding sites determined by

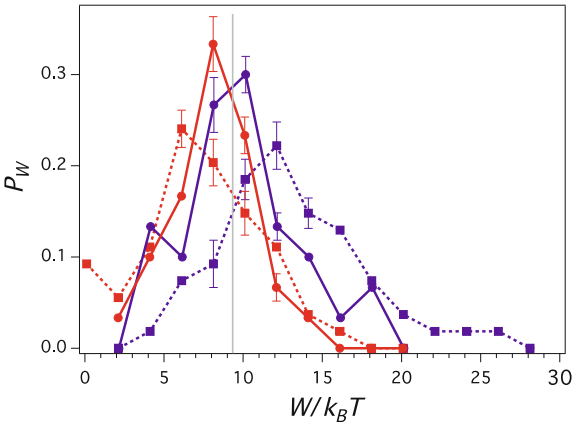

Fig. 10 Work distributions for the rupture peak (*blue*) and rebinding peak (*red*). Loading rate: 500 pN s^{-1} (*line*) and 5,000 pN s^{-1} (*dots*). The distributions show a crossing around $\Delta G = 9.3 \pm 2.3\, k_BT$ (after correction for entropy loss due to the stretching of the PEO). From SI of [19]

1H NMR for bulk solutions of related rotaxane molecules [22, 26, 27]. The work value for a loading rate of 500 pN s^{-1} (Fig. 8c) is close to this binding-energy difference between the two hydrogen-bonding motifs, indicating that under these conditions, the rotaxane is able to make use of almost all the energy available from hydrogen bonding to perform work along the direction of the applied load.

Studying the movements in a single molecule of less than 5 nm long by force spectroscopy and measuring the work it can perform is a breakthrough. If manipulations at the molecular level have been known for 15 years, so far it was a matter of measuring the movements within biological molecules which are a thousand times bigger than a rotaxane molecule.

References

1. Schliwa, M.: Molecular Motors. Wiley-VCH, Weinheim (2003)
2. Kinbara, K., Aida, T.: Toward intelligent molecular machines: directed motions of biological and artificial molecules and assemblies. Chem. Rev. **105**, 1377–1400 (2005)
3. Kay, E.R., Leigh, D.A., Zerbetto, F.: Synthetic molecular motors and mechanical machines. Angew. Chem. Int. Ed. **46**, 72–191 (2007)
4. Browne, W., Feringa, B.L.: Making molecular machines work. Nat. Nanotech. **1**, 25–35 (2006)
5. Berná, J., et al.: Macroscopic transport by synthetic molecular machines. Nat. Mater. **4**, 704–710 (2005)
6. Grill, L., Rieder, K.-H., Moresco, F., Rapenne, G., Stojkovic, S., Bouju, X., Joachim, C.: Rolling a single molecular wheel at the atomic scale. Nat. Nanotech. **2**, 95–98 (2007)
7. Manzano, C., Soe, W.H., Wong, H.S., Ample, F., Gourdon, A., Joachim, C.: Step-by-step rotation of a molecule-gear mounted on an atomic-scale axis. Nat. Mater. **8**, 576–579 (2009)

8. Bustamante, C., Chemla, Y.R., Forde, N.R., Izhaky, D.: Mechanical processes in biochemistry. Annu. Rev. Biochem. **73**, 705–748 (2004)
9. Special Issue. Annu. Rev. Biochem. 77, 45–228 (2008)
10. Evans, E.: Probing the relation between force–lifetime–and chemistry in single molecular bonds. Annu. Rev. Biophys. Biomol. Struct. **30**, 105–128 (2001)
11. Liang, J., Fernández, J.M.: Mechanochemistry: one bond at a time. ACS Nano **3**, 1628–1645 (2009)
12. Puchner, E.M., Gaub, H.E.: Force and function: probing proteins with AFM-based force spectroscopy. Curr. Opin. Struct. Biol. **19**, 605–614 (2009)
13. Eelkema, R., et al.: Molecular machines: nanomotor rotates microscale objects. Nature **440**, 163 (2006)
14. Liu, Y., et al.: Linear artificial molecular muscles. J. Am. Chem. Soc. **127**, 9745–9759 (2005)
15. Panman, M.R., et al.: Operation mechanism of a molecular machine revealed using time-resolved vibrational spectroscopy. Science **328**, 1255–1258 (2010)
16. Rijs, A.M., et al.: Controlled hydrogen-bond breaking in a rotaxane by discrete solvation. Angew. Chem. Int. Ed. **49**, 3896–3900 (2010)
17. Janke, M., et al.: Mechanically interlocked calix[4]arene dimers display reversible bond breakage under force. Nat. Nanotech. **4**, 225–229 (2009)
18. Brough, B., Northrop, B.H., Schmidt, J.J., Tseng, H.R., Houk, K.N., Stoddart, J.F., Ho, C.M.: Evaluation of synthetic linear motor-molecule actuation energetics. Proc. Nat. Acad. Sci. USA **103**, 8583–8588 (2006)
19. Lussis, P., Svaldo-Lanero, T., Bertocco, A., Fustin, C.-A., Leigh, D.A., Duwez, A.-S.: A single synthetic small molecule that generates force against a load. Nat. Nanotech. **6**, 553–557 (2011)
20. Hugel, T., et al.: Single-molecule optomechanical cycle. Science **296**, 1103–1106 (2002)
21. Shi, W., Giannotti, M.I., Zhang, X., Hempenius, M.A., Schönherr, H., Vancso, G.J.: Closed mechanoelectrochemical cycles of individual single-chain macromolecular motors by AFM. Angew. Chem. Int. Ed. **46**, 8400–8404 (2007)
22. Altieri, A., et al.: Remarkable positional discrimination in bistable light- and heat-switchable hydrogen-bonded molecular shuttles. Angew. Chem. Int. Ed. **42**, 2296–2300 (2003)
23. Hunter, C.A.: Quantifying intermolecular interactions: guidelines for the molecular recognition toolbox. Angew. Chem. Int. Ed. **43**, 5310–5324 (2004)
24. Crooks, G.E.: Entropy production fluctuation theorem and the nonequilibrium work relation for free-energy differences. Phys. Rev. E **60**, 2721–2726 (1999)
25. Collin, C., Ritort, F., Jarzynski, C., Smith, S.B., Tinoco Jr, I., Bustamante, C.: Verification of the Crooks fluctuation theorem and recovery of RNA folding free energies. Nature **437**, 231–234 (2005)
26. Leigh, D.A., Wong, J.K.Y., Dehez, F., Zerbetto, F.: Unidirectional rotation in a mechanically interlocked molecular rotor. Nature **424**, 174–179 (2003)
27. Kay, E.R., Leigh, D.A.: Hydrogen bond-assembled synthetic molecular motors and machines. Top. Curr. Chem. **262**, 133–177 (2005)

An Atomistic View of DNA Dynamics and Its Interaction with Small Binders: Insights from Molecular Dynamics and Principal Component Analysis

Barbara Fresch and Francoise Remacle

Abstract DNA oligomers are promising building blocks for the development of bottom-up nano-devices and molecular logic machines. To control and exploit their unique capabilities of self-assembling and molecular recognition, a deep understanding of their dynamical properties is essential. We theoretically investigate the dynamics of a DNA dodecamer and its complexes with two common ligands, Hoechst 33258 and the ethidium cation, by means of classical molecular dynamics (MD) simulations and principal component analysis (PCA). We study the structural relation between the flexibility of the double helix and the binding process. The dynamics of a terminal base pair unbinding is also analysed as an example of process that involves multiple energy minima in the underlying free energy landscape.

1 Introduction

Biomolecules are often taken as prototypes of efficient molecular machines as they are able to perform highly complex and specialized functions. They are flexible structures, and their conformational changes are the basis of molecular recognition, allosteric regulation, self-assembly and other capabilities enabling their biological functions. Synthetic molecular machines are commonly built by assembling different molecular units to mimic simple motions typical of macroscopic objects, i.e. the directional mechanical motion of one component relative to another [1–3]. Well-known examples of this approach are rotaxane-based molecular machines [4, 5] in which a "wheel" is moving along an "axis". Even if this perspective allowed invaluable progresses in the understanding and control of motion at the molecular level, the dynamical properties enabling the functioning of many biological molecular machines are much more complex than a simple directional

B. Fresch (✉) · F. Remacle
Department of Chemistry, B6c, University of Liege, 4000 Liege, Belgium

C. Joachim and G. Rapenne (eds.), *Single Molecular Machines and Motors*,
Advances in Atom and Single Molecule Machines, DOI 10.1007/978-3-319-13872-5_2

motion of a component. Functional internal motions may be subtle and usually involve complex correlations between atomic motions.

DNA oligomers in solution, for example, display a rich dynamical behaviour. Despite timescale limitations, classical molecular dynamics (MD) simulations unveil mechanistic details of this motion with an atomic resolution. MD provides information on oligonucleotide flexibility that are difficult, if not impossible, to observe experimentally. Nonetheless, the information contained in a MD trajectory is encoded in a collection of $3N * n$ coordinates if N is the number of atom in the system under study and n the number of configurations recorded during the simulation time. The understanding and the interpretation of such a huge amount of data call for statistical tools that allow extracting most relevant motions and decrease the dimensionality of the problem. Principal component analysis (PCA) [6], also called "essential dynamics" when applied to a molecular trajectory [7], is a statistical analysis technique that allows handling this issue. PCA is based on the definition of a new set of collective coordinates (the principal components (PCs) or "modes") that allow the identification of large-scale concerted motions. The principal components are obtained as the eigenvectors of the atomic displacement covariance matrix. They define directions in the $3N$-dimensional space of atomic coordinates, and the corresponding eigenvalues indicate the extent of the total motion occurring in each direction. It turns out that for many biomolecules, as proteins and nucleic acids, as few as 10–20 modes are sufficient to account for 90 % of the total motion observed during the dynamics. Therefore, PCA allows the reduction of the dimensionality of the dynamics (in relation to data compression applications) and, more importantly for our purposes, it reveals concerted atomic motions that can be related to molecular functions, thus serving as a bridge to connect structural and functional properties of biomolecules.

In this contribution, we analyse the dynamics of a short DNA oligomer (12 base pairs) by all-atom MD simulations and principal components analysis. DNA is well suited to serve as a model to explore relations between structure, dynamics and functions in biologically relevant molecules. On the one side, nucleic acids show exceptional capabilities in molecular recognition and self-assembly. To carry on its biological functions, DNA is transiently deformed, cut and resealed, damaged and repaired, and the strands pulled apart and then re-annealed. Still, a DNA duplex in the canonical B-helix structure is characterized by an overall simple dynamics [8], which on a coarse-grained scale resembles the dynamics of an elastic rod [9, 10]. Nonetheless, from a closer perspective, sequence specific "dynamical motifs" play a significant role in molecular recognition and add complexity to the overall picture [11, 12]. We present a computational study of two different aspects of the dynamics of the DNA oligonucleotide. Firstly, we consider the dynamics involved in the interaction between the DNA dodecamer and two binders: Hoechst 33258 and the ethidium cation. These ligands are well known, and their complexes with DNA have been studied both experimentally and theoretically (see e.g. Refs. [13–15] and references therein). We chose them as prototypes of two different mechanisms of interaction with the DNA double helix: Hoechst is a minor groove binder that binds selectively to A-rich part of the DNA sequence, while ethidium cation intercalates

between base pairs (bps) without strong sequence specificity. We demonstrate that the binding of Hoechst modifies the dynamics of the helix by "locking" the minor groove in a conformation that maximizes the interaction with the ligand. Therefore, the "groove breathing" motion observed in the free DNA oligonucleotide is suppressed upon the binding of Hoechst. The intercalation of ethidium cations induces stretching and untwisting of the double helix greatly enhancing its flexibility [16].

As a second topic, we consider the dynamics of base pair opening in a terminal position of the DNA duplex. Breaking and re-annealing of terminal base pairs are routinely observed in nanosecond MD simulations of short oligonucleotides at room temperature. The opening of a terminal base pair is a conformational transition that brings the dynamics of the system out of the harmonic regime. We will analyse how the underlying energy landscape is related to the principal components extracted from the trajectory.

We first introduce in Sect. 2 the main concepts of PCA applied to a MD trajectory. We then analyse the structure (Sect. 3) and the dynamics (Sect. 4) of the DNA–ligand complexes. Section 5 is devoted to the study of terminal base pair opening. We give the computational details of the MD simulations and of the post-processing of the obtained trajectories in Sect. 6, and we conclude in Sect. 7 summarizing the main points and giving some perspectives on future works.

2 Principal Component Analysis of an MD Trajectory

PCA is a statistical tool that extracts large-scale motions occurring in the MD trajectory, revealing the structure underlying the atomic fluctuations. It defines a new coordinate system through a linear transformation of the atomic coordinates. Such collective coordinates are then used to define a low-dimensional subspace (often called "essential subspace") in which a significant part of the molecular motion is expected to take place.

A collective coordinate set can be determined as a set of eigenvectors that diagonalizes a second moment matrix. The dynamics of a molecule composed of N atoms is specified by $3N$ Cartesian coordinates $\mathbf{x}(t)$. From a MD trajectory, after the elimination of the overall translational and rotational motion, the variance–covariance matrix of positional fluctuations can be constructed:

$$\mathbf{C} = \left\langle (\mathbf{x}(t) - \langle \mathbf{x} \rangle)(\mathbf{x}(t) - \langle \mathbf{x} \rangle)^T \right\rangle \tag{1}$$

where T indicates the transposed vector and $\langle \ldots \rangle$ denotes the average on the sampled configurations. In practice, an ensemble of $3N$-dimensional coordinate vectors $\mathbf{x}^i$, for $i = 1, \ldots n$, is generated by recording, at a discrete time interval, the configurations generated during the trajectory. Each element $\mathbf{C}_{pq}$ of the covariance matrix is then calculated as the covariance between the pth and the qth entry of the coordinate vector $\mathbf{x}$ on the ensemble of n realizations, namely

$$\mathbf{C}_{pq} = \frac{1}{n}\sum_{i=1}^{n}\left(x_p^i - \langle x_p\rangle\right)\left(x_q^i - \langle x_q\rangle\right) \tag{2}$$

where x_p^i and x_q^i are the elements of $\mathbf{x}^i$, while $\langle x_p\rangle$ and $\langle x_q\rangle$ denote their average over the ensemble of n realizations. The result is a time-independent matrix of dimension $3N \times 3N$.

A set of eigenvalues and eigenvectors is obtained by solving the standard eigenvalue problem

$$\mathbf{CT} = \Lambda\mathbf{T} \tag{3}$$

with Λ being the diagonal matrix of the eigenvalues and T the transformation matrix whose columns are the eigenvectors of $\mathbf{C}$. The ith eigenvector represents the axis of the ith collective coordinate in the conformational space, while the associate eigenvalue λ_i gives the mean square fluctuation along that axis. Six of the $3N$ eigenvalues are practically zero since the overall translational and rotational motion are removed from the trajectory before the analysis. To obtain $3N$-6 physically meaningful eigenvalues, it is formally necessary to include $3N$-6 configurations in the PCA to ensure completeness of the data set. The motions along these new coordinates are often termed "modes", although they are not necessarily vibrational. In normal mode analysis (NMA), the collective coordinates are defined by the transformation that diagonalizes the Hessian matrix and each (harmonic) mode is associated to its frequency. In principle, one can use the mass-weighted displacement of all the atoms to define the covariance matrix of Eq. (1). This form of PCA is often referred as "quasi-harmonic analysis" since it is equivalent to NMA if the analysed motion is due to fluctuations within a truly harmonic conformational energy surface [17]. However, PCA analysis is more general and can be performed by considering only the coordinates of a chosen subset of atoms. In NMA, higher is the displacement represented by a normal mode, lower is its frequency. Since PCA does not require any assumption on the harmonicity of the motion, the principal components are sorted according to variance rather than frequency. Nonetheless, the largest amplitude components of PCA usually represent the slowest concerted motion represented in the analysed trajectory.

If $\boldsymbol{\eta}_i$ represents the ith eigenvector, or PC, of $\mathbf{C}$, we can define the projection of the original MD trajectory onto the new direction defined by this principal component

$$p_i(t) = \boldsymbol{\eta}_i \cdot (\mathbf{x}(t) - \langle\mathbf{x}\rangle) \tag{4}$$

The time evolution of the projections gives indication on the characteristic of the motion along the PC and contributes to the characterization of the underlying energy landscape [18, 19], as we will further illustrate in the following. By binning the values of the time-dependent projection $p_i(t)$, one obtains the corresponding probability distribution $P(p_i)$. Notice that the variance of the distribution of each

Fig. 1 Schematic representation of the free energy surface for **a** harmonic, **b** singly hierarchical and **c** multiple hierarchical modes, respectively

projection is the variance of the atomic fluctuation along the *i*th principal component, i.e. the corresponding eigenvalue, $\lambda_i = \left\langle p_i(t)^2 \right\rangle$. A Gaussian distribution of the projection p_i corresponds to sampling around one single structure and indicates that the explored region of energy landscape is well described by a quadratic potential ("harmonic modes") or it is at least characterized by a harmonic envelope ("quasi-harmonic or singly hierarchical modes") [20], see Fig. 1a, b. On the other hand, in a sufficiently converged trajectory [21], diffusive dynamics of a principal component leading to bi-modal probability distribution along the trajectory indicates a transition between multiple local energy minima ("multiple hierarchical mode"), see Fig. 1c.

As it is often the case in MD, sampling issues have an important impact on the meaning and on the relevance of the results obtained from the PCA. The ability of the analysis to extract meaningful information on important functional motions and features of the energy landscape depends on the statistical relevance of the configurational subspace sampled within the simulation. To evaluate the reliability of the principal components, it is good practice to divide the simulation in two halves and compare the corresponding modes. Two sets of eigenvectors $\boldsymbol{\eta}_i$ and $\boldsymbol{\upsilon}_j$ can be compared with each other by taking their inner product

$$S_{ij} = \boldsymbol{\eta}_i \cdot \boldsymbol{\upsilon}_j \tag{5}$$

Subnanosecond MD simulations of protein dynamics showed that even if the individual principal components extracted from different portions of the dynamics correlate poorly, the subspace spanned by the major principal components converge remarkably rapidly [22]. The degree of overlap between essential subspaces is often measured as the root mean square inner product (RMSIP) of the two sets of eigenvectors

$$\mathrm{RMSIP}_M = \sqrt{\frac{1}{M}\sum_{i=1}^{M}\sum_{j=1}^{M}\left(\boldsymbol{\eta}_i \cdot \boldsymbol{\upsilon}_j\right)^2} \tag{6}$$

where M is the dimension of the subspaces. In order to visualize and interpret the motion defined by a PC, it is useful to project it back to Cartesian coordinates as follows

$$\mathbf{x}_i(t) = p_i(t) \cdot \boldsymbol{\eta}_i + \langle \mathbf{x} \rangle \tag{7}$$

We will use the Cartesian representation of the modes given by Eq. (7) to illustrate the atomic displacement involved in the principal components.

3 Two Case Studies: DNA–Hoechst and DNA–Ethidium Complexes

We perform 15 ns equilibrium simulations of the free DNA dodecamer (5′-GGTA AATTTAGG—3′) in the standard B-helix form and of the complexes DNA–Hoechst 33258 (1:1) and DNA–ethidium cation (1:3), see Fig. 2a. For the details about the simulation protocol, see computational details in Sect. 6.

Hoechst is a fluorescent bis-benzimidazole molecule used in several applications in pharmacology. It interacts with DNA by entering the minor groove with a clear selectivity for A–T-rich tract of the double helix [8, 23]. In Fig. 2b, we show the structure of the complex used in the simulations. An H-bond analysis of the obtained trajectory reveals that the interaction occurs mainly through the formation of hydrogen bonds between the N-donors of the Hoechst and the free oxygen of the thymine bases T19-20-7, and a weaker hydrogen bond is also established with the nitrogen of the adenine base A6, see Fig. 2a for the numbering convention. The ethidium cation is a simple polycyclic aromatic molecule with short side chains only and represents a typical DNA intercalator without strong sequence specificity. An intercalator binds to the DNA double helix via the non-covalent stacking interaction with the DNA base pairs. Here, we study the DNA–ethidium cation (1:3) complex whose structure is shown in Fig. 2b. Deformations of the DNA double-helix structure are usually described in terms of base pair step helicoidal parameters (*roll*, *tilt*, *twist*, *shift*, *slide* and *rise*) [24, 25]. In Fig. 2c, we report the comparison of the more significant parameters between the free DNA duplex (blue bars), the Hoechst complex (red bars) and the ethidium complex (grey bars), characterizing the different base pair steps (the first bp step is defined by the G1-C24 and the G2-C23 base pairs, the second is between G2-C23 and T3-A22 and so on). The height of the bars in Fig. 2c denotes the average value of the roll, rise and twist parameters during the trajectory, while the error bars denote their standard deviation. Notice that the local flexibility of DNA helix is highly sequence dependent; pyrimidine–purine base pair steps, for example exhibit the largest flexibility and extreme local deformations in B-form DNA [26]. Accordingly, we find that bp steps 3 and 9 (TA) are characterized by a significant value of *roll*, a local helix deformation towards the major groove together with a lower value of the helical twist. It is well known that the binding of Hoechst to the DNA double helix

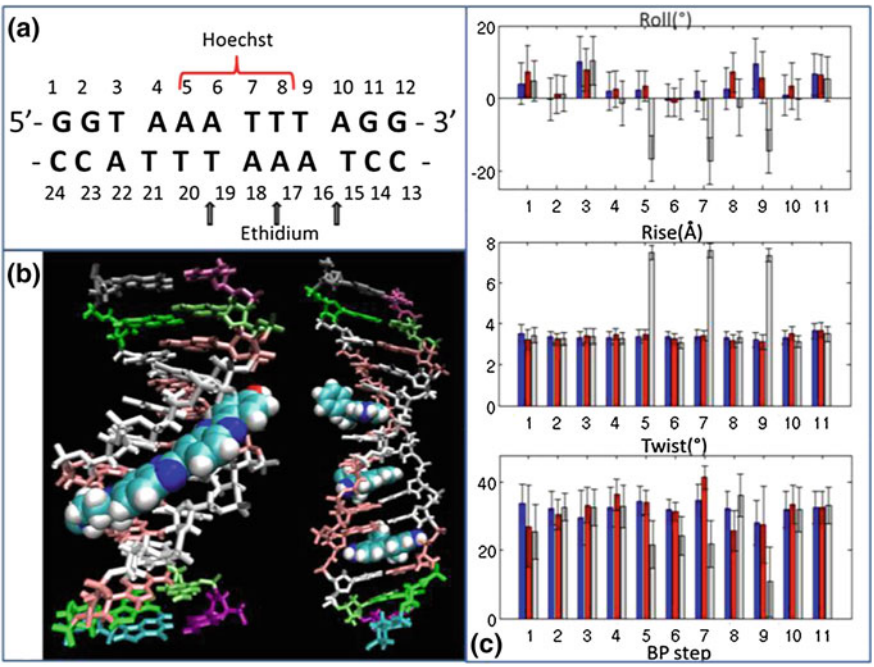

Fig. 2 Structural aspects of the DNA dodecamer and its complexes with Hoechst and ethidium cation. **a** Sequence of 24 bases in the oligomer with relative numbering. The base pairs are identified by the number of the nucleotide in the 5′ → 3′ strand. The base pair steps are numbered as the left base pair, i.e. the bp step between the 1st bp (GC) and the 2nd bp (GC) is number 1 and so on. The *red parenthesis* indicates the bps interacting with Hoechst, while the *arrows* indicate the intercalation sites of ethidium cation. **b** Structures of the two complexes obtained as averages over the MD trajectory. **c** Comparison of structural parameters of the double helix (*Roll*, *Rise and Twist*) between the free DNA (*first bar*, *blue*), Hoechst complex (*second bar*, *red*) and ethidium complex (*third bar*, *grey*). The height of the bars is the average value of the parameter along the trajectory, while error bar represents the standard deviation

does not imply significant structural reorganizations. We observe that the average structural parameters of the double helix in the presence of the minor groove binder remain practically the same as in the free oligomer. Nevertheless, we do find some minor changes in the bp parameters (defining the relative position and orientations of the two bases) within the base pairs directly involved in the binding (5th, 6th, 7th, 8th bps). Specifically, more negative values of *buckle* and *propeller* suggest that the bases are not coplanar within the base pair in order to maximize the favourable interactions with the binder.

Ethidium intercalation strongly distorts the base pair step forming the intercalation site. In our model, the 5th, 7th and 9th bp steps (AA, TT and TA, respectively) are the intercalation sites and they show, as expected, an increased rise (i.e. vertical distance between base pair planes) and lowered twist (expressing the DNA molecule being unwound). Because the distance between the bps in the intercalation sites are

twice the unperturbed distance (about 7.5 against 3.3 Å), the end-to-end distance of the helix of the DNA–ethidium complex amounts to 54.9 Å, which corresponds to an elongation of about 13 Å with respect to the free oligonucleotide.

4 From Structure to Dynamics

In this Section, we will explore the dynamical implications of the interaction between the DNA double helix and the binders. To this aim, we first perform a PCA analysis of the free DNA dodecamer. The visual inspection of the 15 ns trajectory of the free DNA reveals that short after 7 ns of simulation, the 1st base pair G1-C24 unbinds: first, the H-bonds between the two bases are broken because of a fluctuation twisting the aromatic rings of the two bases out of the common plane. Then, the guanine unstacks from the neighbour cytosine base and flips and undergoes free rotation in the solvent before establishing some non-canonical H-bond with the oxygen atoms of the sugar–phosphate backbone. Fraying and re-annealing of terminal base pairs are often observed in MD simulations of duplexes at room temperature, and the mechanism of unbinding has been well characterized as part of the melting process of the double helix [27–29]. It is clear that structures generated by the dynamics after the terminal base pair opening belong to a region of the configurational space different from the initial energy basin. In other words, the opening event corresponds to the crossing of some barrier in the underlying energy landscape and allows the system to explore another region of the accessible configurational space. We will consider such a scenario in the next section. Here, we want to focus on the dynamical consequences of the ligand binding; therefore, we retain for the analysis only the first 6 ns of simulation in which all the bps of the double helix are preserved. Moreover, we calculate the principal components by building the covariance matrix of the coordinates of the subset of atoms in the sugar–phosphate backbone. On the one hand, restricting the number of atoms considered in the PCA has the advantage that the storage and diagonalization of the covariance matrix is less demanding. On the other hand, a backbone-only analysis is helpful to disentangle different components of the molecular recognition process: variation in the sugar–phosphate backbone affects the minor groove width producing specific movements essential to clamp the ligands [8, 30]. We found, however, that the main collective modes resulting from the backbone PCA are very similar to those obtained from all-atom analysis [31]. In Table 1, we report the number of principal components accounting for 90 % of the variance, the absolute value of the restricted and of the total variance during the trajectory, and the contribution of the first 2 eigenvectors resulting from the backbone PCA of the DNA dodecamer and the DNA complexes. For the free DNA, 20 PCs account for 90 % of the total variance accumulated during the trajectory. We show in Fig. 3a the projections (see Eq. (4)) of the first two modes (38.7 % of the total variance) as a function of the simulation time: they describe motions that are oscillatory about the mean structure, with no net drift that could suggest a change in the overall

Table 1 Number of principal components representing 90 % of the dynamics total variance, absolute value of the explained and total variance (in $Å^2$) and fraction of variance accounted by the first two principal components

	Number of vectors (90 %)	Explained variance/ total variance	% Explained by the first two PCs
DNA 12-mer	20	308.2/341.2	38.7
DNA–Hoechst(1:1)	20	284.1/315.0	41.0
DNA–ethidium(1:3)	14	507.4/559.8	63.4

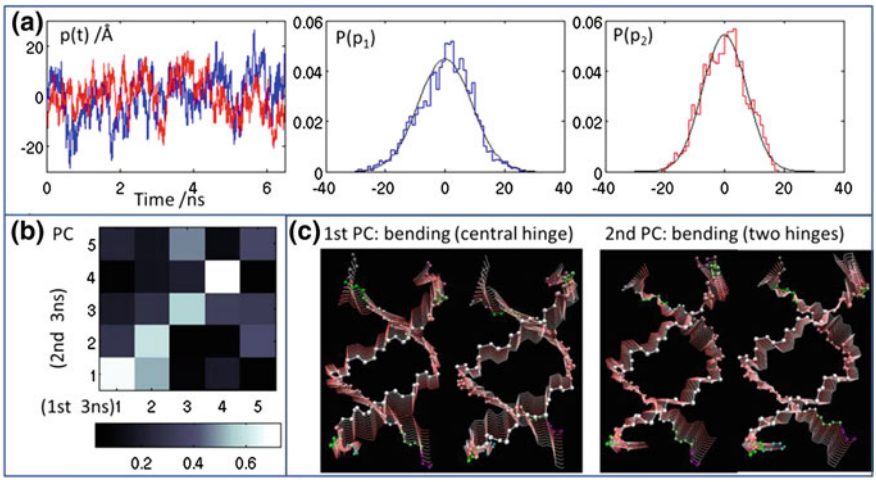

Fig. 3 Principal component analysis of the free DNA dodecamer: **a** projection of the atomic positional fluctuations along the 1st (*blue*) and the 2nd (*red*) principal components as a function of the simulation time and corresponding probability distributions. **b** Matrix of the inner products between the principal components obtained by dividing the trajectory into two halves. **c** Visualization of the atomic motion involved in the 1st and 2nd principal components

conformation of the molecule. The corresponding probability densities, also shown in the figure, are well described by Gaussian distributions expected for motions that explore quasi-harmonic energy basin (see Fig. 1). In Fig. 3b, we report the similarity between the first 5 modes obtained from the first and the second halves of the total trajectory in the form of the matrix of the inner products between them, see Eq. (5). The higher value of the products clustered along the diagonal shows the good convergence of the main principal components. The overlap of the essential subspaces spanned by the first five PCs of the two different portions of the trajectory calculated as the RMSIP defined in Eq. (6) amounts to 0.8. These observations establish the robustness of the PCs resulting from the total trajectory. The first two modes are shown in Fig. 3c: they both correspond to bending modes of the duplex as also results from a normal modes analysis of the DNA double helix [10, 32] and resemble the normal motions of a simple elastic rod. What is more interesting for our purpose is to notice that the first principal component entails a sort of "groove

breathing" motion in the central portion of the double helix, with the backbone of the two strands getting far apart which creates a good condition for the possible approach of a binder molecule.

We then consider the essential dynamics of the two complexes: DNA–Hoechst (1:1) and DNA–ethidium cation (1:3). As for the free DNA, we analyse a portion of the trajectory (of about 6 ns) in which no base pair opening is observed and for which the time evolution of the principal components are compatible with the motion in a quasi-harmonic energy basin. As one can see from Table 1, the interaction with Hoechst does not entail a significant change in the overall observed variance, while the structure of the DNA–ethidium complex is definitely more flexible and floppy than the free oligonucleotide, the total variance being significantly higher. In Fig. 4a, we show the total root mean squared fluctuation amplitude of the backbone, specifying the contribution coming from the different nucleotides; the upper part of the graph shows the displacement of the atoms in the nucleotides 1–12, while the lower part shows the displacement of the complementary bases 13–24 (see numbering in Fig. 2a). As a common feature of the free DNA oligonucleotide and both complexes, the terminal portions of the double helix are characterized by higher mobility, while the central part (bps from 5 to 8) is more rigid. In comparison with the free oligonucleotide, all the base pairs in the DNA–ethidium complex experience larger fluctuations during the trajectory, while the presence of the Hoechst molecule reduces the total displacement of the central base pairs but only slightly. However, the total root mean squared displacement along the trajectory does not contain information about the relative direction of the atomic motion. To analyse the changes on the backbone dynamics induced by the presence of the ligands, we look at the main principal components of the dynamics of the DNA–ligand complexes. The analysis of the matrix of the inner products between the principal components of the free DNA and of the DNA–ligand complexes showed in Fig. 4b shows that the PCs of the complexes preserve an overall correlation with the PCs of the free oligonucleotide, especially in the case of Hoechst binding. Nonetheless, by analysing the modes of the DNA–Hoechst complex (see Fig. 4c), we find that the breathing of the groove which was part of the first PC of the free oligonucleotide (Fig. 3c) is completely absent in the first five PCs of the complex. The first mode of the DNA–Hoechst complex is still a bending motion around a central hinge (which explains the correlation with the 1st PC of DNA in Fig. 4b), but the backbone of the two strands moves concurrently in the same direction (which explains the correlation with the 2st PC of DNA in Fig. 4b). In the second mode, the central part of the helix is practically blocked, and the motion is concentrated on the terminal arms. The change in the groove width is thus suppressed by the presence of the Hoechst molecule. This can be intuitively understood since the groove is "locked" in the conformation that maximizes the favourable interaction between the DNA and the binder. On the contrary, the first two principal modes of the DNA–ethidium complex are qualitatively very similar to the first two modes of the free oligonucleotide (compare Fig. 4c with Fig. 3d). Nonetheless, the correlation between the modes of the complex and the free DNA is lower in this case, due to the structural deformation of the helix upon intercalation described in the previous section.

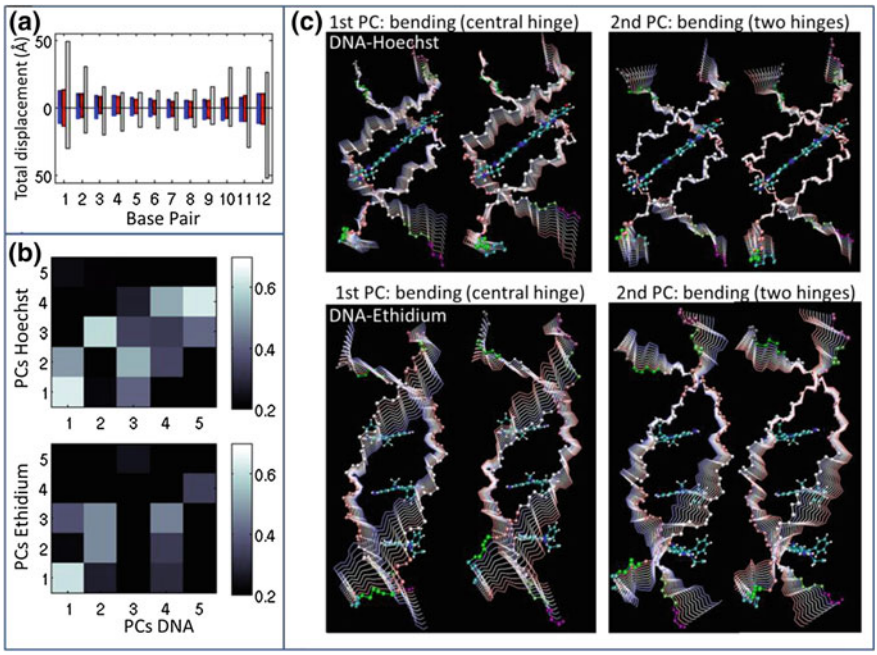

Fig. 4 Principal component analysis of the DNA complexes with Hoechst (1:1) and ethidium cation (1:3): **a** total root mean square displacement of the backbone atoms grouped by nucleotide. The upper part of the graph shows data for nucleotides 1–12 and the lower part for nucleotides 13–24, the numbering convention is given in Fig. 2a. The *bars* refer to free DNA (*blue*), Hoechst complex (*red*) and ethidium complex (*grey*). **b** Matrixes of the inner products between the first five principal components of the free oligonucleotide and of the complexes. **c** Visualization of the atomic motion involved in the 1st and 2nd modes of the DNA–Hoechst and the DNA–ethidium complexes

5 Exploring the Conformational Space: Opening of a Terminal Base Pair

The essential dynamics of the short oligonucleotide presented in the previous section shows that, on relatively short timescales, the dynamics is dominated by fluctuations within a local minimum (that can be approximated well by a system's local normal modes). However, since the energy landscape is characterized by multiple minima, on longer timescales, we can expect that the system crosses some barrier and starts to explore other regions of phase space. When this is the case, the large fluctuations are dominated by a largely anharmonic diffusion between multiple wells. To illustrate this point, we will now consider the whole 15 ns trajectory of the DNA 12-mer. As previously mentioned, an opening of the terminal GC-1 base pair is observed after 7 ns. The fraying of the terminal base pair is energetically costly because it involves the rupture of the H-bonds of the base pair and the

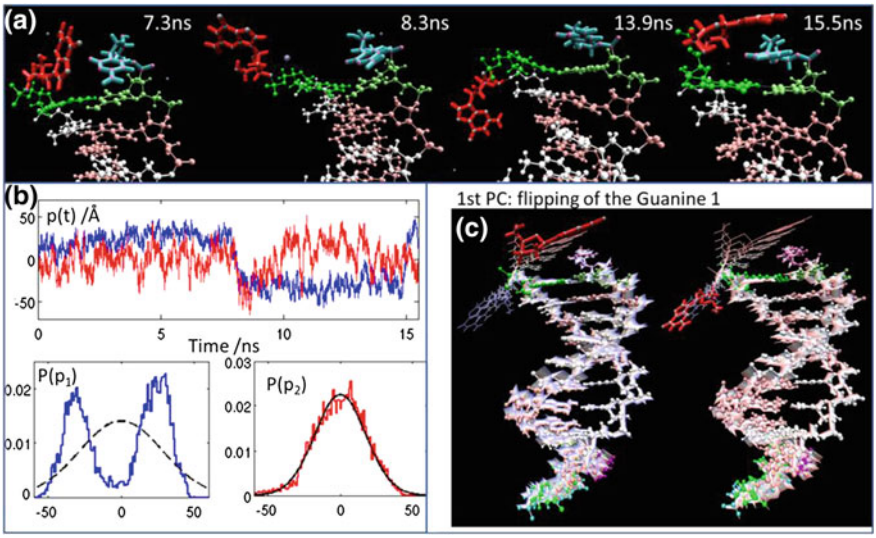

Fig. 5 Principal component analysis of the whole 15 ns trajectory of the free DNA dodecamer showing terminal base pair opening: **a** mechanistic details of the opening of the terminal base pair GC-1. **b** Projection of the atomic positional fluctuations along the 1st (*blue*) and the 2nd (*red*) principal components as a function of the simulation time and corresponding probability distributions. **c** Visualization of the atomic motion involved in the 1st principal component

un-staking of at least one base from the next one. Nonetheless, the increased motional freedom that follows the fraying makes the peeling process entropically driven. The stepwise ("zipper-like") process starting with the fraying/peeling of one of the two double-helix ends and propagating along the dodecamer has been identified as the main unfolding route in the thermal melting of DNA oligonucleotides [29, 33]. In the condition of our simulation (room temperature and absence of external forces), the base pair rupture process is of course reversible and biased towards the re-annealing. The mechanism of the opening we observed is illustrated in Fig. 5a by snapshots of the dynamics taken at different times. After the rupture of the canonical H-bonds, due to a fluctuation which rotates the two bases out-of-plane (snapshot at 7.3 ns in Fig. 5a), the guanine G1 explores different conformations, while the cytosine C24 conserves the inter-strand staking interaction with the next base C23. At 8.3 ns, G1 is completely unfolded before establishing non-canonical H-bonds with the atoms of the backbone and thus residing for about 5 ns in this "peeled conformation" (representative snapshot at 13.9 ns). Short before the end of the simulations, the guanine leaves this kinetic intermediate and goes back on the top of the helix. However, it does not find straightly the optimal Watson–Crick pairing; instead, the structure is again trapped in a local minima characterized by the stacking between G1 and C24 (snapshot at 15.5 ns). It is clear that, because of the opening process described above, the system visits a portion of the energy landscape during the simulation time that is not well approximated by a harmonic potential. Let us see how this is reflected by the essential dynamics resulting from a

PCA analysis of the whole trajectory. To analyse the base opening motion, we do not confine the analysis to the backbone atoms, since it is clear by simple visual inspection that the reaction coordinate is mainly composed of the coordinates of the G1 base atoms. Accordingly, we perform an all-atom PCA. Figure 5b shows the projection along the first two principal components of the dynamics and the corresponding probability distributions. The first PC, which account for the 30 % of the total displacement, shows very clearly the transition between two distinct conformations suggesting the crossing of a barrier in an underlying energy profile characterized by multiple minima (as the one schematically shown in Fig. 1c). The corresponding probability distribution is bi-modal, which is a typical signature of a multiple hierarchical mode. The time dependence of the second mode also shows the signature of the transition around 8 ns, but the overall distribution is well represented by a Gaussian. The Gaussian probability distribution suggests that, along the direction identified by the 2nd PC, the system remains within a single energy basin. Moreover, by plotting the projection of the higher modes as a function of the projection of the first mode, one can verify that the first PC is statistically un-correlated from the others. This means that it represents a good reaction coordinate for the base pair opening process. The motion described by the first PC is shown in Fig. 1c and clearly corresponds to the flipping of the G1 base. Given a longer trajectory which presents multiple binding/unbinding events, thermodynamic properties can be derived as ensemble averages and one can use the principal components to obtain a map of the free energy landscape [19, 34].

6 Computational Details

MD simulations of the DNA, DNA–Hoechst 33258 complex and DNA–ethidium cation (1:3) were performed using AMBER 10.0 with the AMBER ff99bsc0 force field for nucleic acids and the TIP3P water model. The force fields for the ligand have been prepared with ANTECHAMBER and corrected according to the parameterization developed in Ref. [35] for Hoechst and in Ref. [13] for the ethidium cation. The initial structures were solvated in a cubic periodic box, with a minimum buffer of 10 Å between any DNA or solute atom and the closest box edge. Sodium counter-ions were added to establish charge neutrality. The resulting system was energy minimized using steepest decent and conjugate gradient methods to relieve any residual unfavourable steric interactions introduced during the solvation procedure. First, the systems (DNA and DNA complexes) were restrained (500 kcal/mol-Å^2), while the water and counter-ions were subjected to 10,000 cycles of minimization. Then, the full system was allowed to relax during an additional 10,000 cycles of unrestrained minimization. The DNA oligonucleotide and Hoechst 33258/ethidium cations systems were restrained (25 kcal/mol Å^2) during a 20 ps, constant volume MD simulation (NVT), during which water and the Na+ atoms were allowed to move freely and the temperature was raised from 0 to 300 K using a Langevin temperature control. Next, the system was subjected to

150 ps of constant pressure (NPT) MD to achieve proper density and 1 ns of relaxation before production runs. During MD, the long-range electrostatic interactions were treated with the particle mesh Ewald method [36] using a real-space cut-off distance of $r_{\text{cut-off}} = 9$ Å. The SHAKE algorithm [37] was used to constrain bond vibrations involving hydrogen atoms, which allowed a time step of 2 fs. Frames are recorded every 1,000 steps (2 ps).

Analysis of the trajectory to extract the helical parameter of the double helix was performed with the cpptraj module of AmberTools12. PCA analysis was carried on as implemented in the PCA suite software [38].

7 Conclusions

Conformational freedom of molecules is related to the underlying free energy landscape, which for biological molecule is high dimensional and likely characterized by many local minima accessible at room temperature. Some concerted motions are important biologically as they describe the manner in which the biomolecule is particularly flexible. PCA analysis extracts from a MD trajectory a set of collective structural changes of the molecule, i.e. principal components of the dynamics, which contribute significantly to the observed atomic displacement. It is well known that a large part of the overall motion of the system during a simulation can be described in terms of only a few principal components. These large displacement motions dominate the range of molecular configurations explored during thermal agitation, and they are often related to the capability of the molecule to perform biological relevant functions. We have illustrated these concepts by considering the dynamics of a DNA dodecamer in solution. Molecular recognition between the oligonucleotide and binders is related to a groove breathing mode that facilitates the approach of the ligand to the base pairs of the double helix. We observed that the binding of Hoechst in the central part of the dodecamer suppresses this mode by "locking" the minor groove in a configuration that maximises the interaction between the DNA and the drug. The intercalation of three ethidium cations significantly distorts the B-helix structure but does not suppress the breathing mode of the helix backbone. The principal components of the dynamics of a terminal base pair opening are also analysed. We showed that this motion cannot be described within a quasi-harmonic approximation since the system explores multiple minima in the underlying energy landscape. The first principal component, describing the flipping of one terminal base, is a good reaction coordinate for the opening process. The decomposition of MD trajectories in term of principal components is a powerful method to unveil the atomic details of complex dynamical processes involving the DNA double helix. Further work in this direction may improve our understanding of important processes, such as the mechanism of unfolding under the action of external forces as probed my modern single-molecule manipulation experiments, or the effects of specific drugs on the stability and on the elastic properties of DNA.

Acknowledgements This work was supported by the NANOFORCE ULg ARC project. BF thanks ULg for a post-doctoral fellowship. FR is a Director of research from Fonds National de la Recherche Scientifique, Belgium. We thank A.S. Duwez (ULg) for fruitful discussions about related experimental aspects.

References

1. Kay, E.R., Leigh, D.A., Zerbetto, F.: Synthetic molecular motors and mechanical machines. Angew. Chemi. Int. Ed. **46**, 72–191 (2007). doi:10.1002/anie.200504313
2. Joachim, C., Rapenne, G.: Molecule concept nanocars: chassis, wheels, and motors? ACS Nano **7**, 11–14 (2013). doi:10.1021/nn3058246
3. Klok, M., Boyle, N., Pryce, M.T., Meetsma, A., Browne, W.R., Feringa, B.L.: MHz unidirectional rotation of molecular rotary motors. J. Am. Chem. Soc. **130**, 10484–10485 (2008)
4. Berna, J., Leigh, D.A., Lubomska, M., Mendoza, S.M., Perez, E.M., Rudolf, P., Teobaldi, G., Zerbetto, F.: Macroscopic transport by synthetic molecular machines. Nat. Mater. **4**, 704–710 (2005). http://www.nature.com/nmat/journal/v4/n9/suppinfo/nmat1455_S1.html
5. Lewandowski, B., De Bo, G., Ward, J.W., Papmeyer, M., Kuschel, S., Aldegunde, M.J., Gramlich, P.M.E., Heckmann, D., Goldup, S.M., D'Souza, D.M., Fernandes, A.E., Leigh, D. A.: Sequence-specific peptide synthesis by an artificial small-molecule machine. Science **339**, 189–193 (2013)
6. Hayward, S., Groot, B.: In: Kukol, A. (ed.) Molecular Modeling of Proteins. Methods Molecular Biology™, Ch. 5, vol. 443, pp. 89–106 Humana Press (2008)
7. Amadei, A., Linssen, A.B.M., Berendsen, H.J.C.: Essential dynamics of proteins. Proteins: Struct. Funct. Bioinf. **17**, 412–425 (1993). doi:10.1002/prot.340170408
8. Bostock-Smith, C.E., Harris, S.A., Laughton, C.A., Searle, M.S.: Induced fit DNA recognition by a minor groove binding analogue of Hoechst 33258: fluctuations in DNA A tract structure investigated by NMR and molecular dynamics simulations. Nucleic Acids Res. **29**, 693–702 (2001). doi:10.1093/nar/29.3.693
9. Pérez, A., Blas, J.R., Rueda, M., López-Bes, J.M., de la Cruz, X., Orozco, M.: Exploring the essential dynamics of B-DNA. J. Chem. Theory Comput. **1**, 790–800 (2005). doi:10.1021/ct050051s
10. Matsumoto, A., Go, N.: Dynamic properties of double-stranded DNA by normal mode analysis. J. Chem. Phys. **110**, 11070–11075 (1999)
11. Harris, S.A., Gavathiotis, E., Searle, M.S., Orozco, M., Laughton, C.A.: Cooperativity in drug—DNA Recognition: a molecular dynamics study. J. Am. Chem. Soc. **123**, 12658–12663 (2001). doi:10.1021/ja016233n
12. Bothe, J.R., Lowenhaupt, K., Al-Hashimi, H.M.: Sequence-specific B-DNA flexibility modulates Z-DNA formation. J. Am. Chem. Soc. **133**, 2016–2018 (2011). doi:10.1021/ja1073068
13. Kubař, T., Hanus, M., Ryjáček, F., Hobza, P.: Binding of cationic and neutral phenanthridine intercalators to a DNA oligomer is controlled by dispersion energy: quantum chemical calculations and molecular mechanics simulations. Chem. Eur. J. **12**, 280–290 (2006). doi:10.1002/chem.200500725
14. Strekowski, L., Wilson, B.: Noncovalent interactions with DNA: an overview. Mutat. Res. Fundam. Mol. Mech. Mutagen. **623**, 3–13 (2007). 10.1016/j.mrfmmm.2007.03.008
15. Haq, I.: Thermodynamics of drug–DNA interactions. Arch. Biochem. Biophys. **403**, 1–15 (2002). doi:10.1016/S0003-9861(02)00202-3
16. Fresch, B., Remacle, F.: Atomistic account of structural and dynamical changes induced by small binders in the double helix of a short DNA. Phys. Chem. Chem. Phys. **16**, 14070–14082 (2014). doi:10.1039/C4CP01561D

17. Hayward, S., Kitao, A., Gō, N.: Harmonic and anharmonic aspects in the dynamics of BPTI: a normal mode analysis and principal component analysis. Protein Sci. **3**, 936–943 (1994). doi:10.1002/pro.5560030608
18. Tournier, A.L., Smith, J.C.: Principal components of the protein dynamical transition. Phys. Rev. Lett. **91**, 208106 (2003)
19. Maisuradze, G.G., Liwo, A., Scheraga, H.A.: Principal component analysis for protein folding dynamics. J. Mol. Biol. **385**, 312–329 (2009). doi:10.1016/j.jmb.2008.10.018
20. Kitao, A., Hayward, S., Go, N.: Energy landscape of a native protein: Jumping-among-minima model. Proteins Struct. Funct. Bioinf. **33**, 496–517 (1998). doi:10.1002/(SICI)1097-0134(19981201)33:4<496::AID-PROT4>3.0.CO;2-1
21. Hess, B.: Similarities between principal components of protein dynamics and random diffusion. Phys. Rev. E **62**, 8438–8448 (2000)
22. Amadei, A., Ceruso, M.A., Di Nola, A.: On the convergence of the conformational coordinates basis set obtained by the essential dynamics analysis of proteins' molecular dynamics simulations. Proteins Struct. Funct. Bioinf. **36**, 419–424 (1999). doi:10.1002/(SICI)1097-0134(19990901)36:4<419::AID-PROT5>3.0.CO;2-U
23. Haq, I., Ladbury, J.E., Chowdhry, B.Z., Jenkins, T.C., Chaires, J.B.: Specific binding of hoechst 33258 to the d(CGCAAATTTGCG)2 duplex: calorimetric and spectroscopic studies. J. Mol. Biol. **271**, 244–257 (1997). doi:10.1006/jmbi.1997.1170
24. Dickerson, R.E.B.M., Calladine, C.R., Diekmann, S., Hunter, W.N., Kennard, O., von Kitzing, E., Lavery, R., Nelson, H.C.M., Olson, W.K., Saenger, W., Shakked, Z., Sklenar, H., Soumpasis, D.M., Tung, C.S.; Wang, A.H.J., Zhurkin, V.B.: Definitions and nomenclature of nucleic acid structure parameters. EMBO J. **8**, 1–14 (1989)
25. Lu, X.J., Olson, W.K.: 3DNA: a software package for the analysis, rebuilding and visualization of three-dimensional nucleic acid structures. Nucleic Acids Res. **31**, 5108–5121 (2003). doi:10.1093/nar/gkg680
26. Beveridge, D.L., Dixit, S.B., Barreiro, G., Thayer, K.M.: Molecular dynamics simulations of DNA curvature and flexibility: helix phasing and premelting. Biopolymers **73**, 380 (2004)
27. Hagan, M.F., Dinner, A.R., Chandler, D., Chakraborty, A.K.: Atomistic understanding of kinetic pathways for single base-pair binding and unbinding in DNA. Proc. Natl. Acad. Sci. **100**, 13922–13927 (2003). doi:10.1073/pnas.2036378100
28. Kannan, S., Zacharias, M.: Simulation of DNA double-strand dissociation and formation during replica-exchange molecular dynamics simulations. Phys. Chem. Chem. Phys. **11**, 10589–10595 (2009). doi:10.1039/B910792B
29. Perez, A., Orozco, M.: Real-time atomistic description of DNA unfolding. Angew. Chem. Int. Ed. **49**, 4805–4808 (2010). doi:10.1002/anie.201000593
30. Laughton, C., Luisi, B.: The mechanics of minor groove width variation in DNA, and its implications for the accommodation of ligands. J. Mol. Biol. **288**, 953–963 (1999). doi:10.1006/jmbi.1999.2733
31. Harris, S.A., Laughton, C.A.: A simple physical description of DNA dynamics: quasi-harmonic analysis as a route to the configurational entropy. J. Phys.: Condens. Matter **19**, 076103 (2007)
32. Matsumoto, A., Olson, W.K.: Sequence-dependent motions of DNA: a normal mode analysis at the base-pair level. Biophys. J. **83**, 22–41 (2002). doi:10.1016/S0006-3495(02)75147-3
33. Wong, K.-Y., Pettitt, B.M.: The pathway of oligomeric DNA melting investigated by molecular dynamics simulations. Biophys. J. **95**, 5618–5626 (2008). doi:10.1529/biophysj.108.141010
34. Papaleo, E., Mereghetti, P., Fantucci, P., Grandori, R., De Gioia, L.: Free-energy landscape, principal component analysis, and structural clustering to identify representative conformations from molecular dynamics simulations: the myoglobin case. J. Mol. Graph. Model. **27**, 889–899 (2009). doi:10.1016/j.jmgm.2009.01.006
35. Furse, K.E., Lindquist, B.A., Corcelli, S.A.: Solvation dynamics of hoechst 33258 in water: an equilibrium and nonequilibrium molecular dynamics study. J. Phys. Chem. B **112**, 3231–3239 (2008). doi:10.1021/jp711100f

36. Darden, T., York, D., Pedersen, L.: Particle mesh Ewald: An N [center-dot] log(N) method for Ewald sums in large systems. J. Chem. Phys. **98**, 10089–10092 (1993)
37. Miyamoto, S., Kollman, P.A.: An analytical version of the SHAKE and RATTLE algorithm for rigid water models. J. Comput. Chem. **13**, 952–962 (1992). doi:10.1002/jcc.540130805
38. Meyer, T., Ferrer-Costa, C., Pérez, A., Rueda, M., Bidon-Chanal, A., Luque, F.J., Laughton, C.A., Orozco, M.: Essential dynamics: a tool for efficient trajectory compression and management. J. Chem. Theory Comput. **2**, 251–258 (2006). doi:10.1021/ct050285b

Recent Advances in the Chemical Synthesis of Lasso Molecular Switches

Frédéric Coutrot

Abstract Interlocked and interwoven molecules are intriguing structures that can behave as molecular machines. Among them, the [1]rotaxane molecular architecture is unique, since it defines a lasso-type shape, that, if well designed, can be tightened or loosened depending on an external *stimulu*s. This chapter describes an overview of the main strategies used to reach [1]rotaxanes to date and then focuses on the few examples of [1]rotaxanes reported in the literature that behave as mono-lasso or double-lasso molecular machines. Different motions are illustrated like the loosening–tightening of lassos or the controllable molecular "jump rope" movement which is specific to the double-lasso structure.

Keywords Molecular machine · [1]Rotaxane · Lasso · Double-lasso · Jump rope · Lasso peptides

1 Introduction

Interlocked molecular architectures are the class of compounds that have been extensively studied in the past decades. Rotaxanes and catenanes belong to this family of fascinating compounds: They, respectively, consist of a macrocycle surrounding either a molecular axle or another macrocycle. The number [*n*] found in bracket before the chemical terminology "rotaxane" and "catenane" is assigned for the number of elements which are interlocked, without being covalently linked one to each other. It has already been established that the presence of a macrocycle around a thread resulted in tremendous changes of the physical and chemical

F. Coutrot (✉)
Supramolecular Machines and Architectures Team, Institut des Biomolécules Max Mousseron, (IBMM) UMR 5247 CNRS-UM1-UM2, Université Montpellier 2, Place Eugène Bataillon, case courrier 1706, 34095 Montpellier Cedex 5, France
e-mail: frederic.coutrot@univ-montp2.fr
URL: http://www.glycorotaxane.fr

C. Joachim and G. Rapenne (eds.), *Single Molecular Machines and Motors*, Advances in Atom and Single Molecule Machines, DOI 10.1007/978-3-319-13872-5_3

properties of the thread. The same trend has been observed with catenanes, where the properties of a single macrocycle highly differ from the catenated dimer. The fact that the elements of these molecules have the possibility to glide among each other using low interactions gives them very appealing properties. Indeed, not only the new presence of a macrocycle around another element (i.e, a molecular thread in a rotaxane or a macrocycle in the case of a catenane) is responsible for the physical and chemical changes of the element. The different localizations of the macrocycle along the encircled element are also accountable for these changes. As a result, chemists have focused on the design, the synthesis, and the study of numerous molecular machines [1] based on interlocked components which contain several sites of interactions (i.e., molecular stations) for each other. Low interactions between the elements, such as hydrogen bonds, electrostatic, ion–dipole, charge transfer, π–π stacking, and hydrophobic interactions, as well as metal-based coordination, have all been utilized to conceive more or less sophisticated molecular stations. Chemical changes such as protonation, deprotonation, photoisomerization, oxidation, reduction, (…) or variations of the environment of interlocked molecular machines such as variations of the solvent, the temperature (…) can lead to the modification of the affinity between the concerned molecular stations and the surrounding macrocycle in rotaxanes and catenanes. Hence, if the molecule is well designed, these changes can cause the controlled displacement of one macrocycle along other components, resulting in the operation of a molecular switch or machine. Among the numerous interlocked molecular architectures reported to date, the lasso compounds hold a particular place, since their constrained looped shape defines a pseudomacrocyclic cavity. They can be assimilated to [1]rotaxanes, in which a macrocycle is covalently linked to a molecular tail that threads the macrocycle. Many pseudo[1]rotaxanes have been reported in the literature until now [2–9]: In this typical molecular architecture, an equilibrium takes place between the interlocked compound and its uncomplexed analogue, as long as no bulky moiety is present on the threaded axle (particularly at its extremity) to prevent the disassembling process (Fig. 1). Such compounds that contain both a macrocycle and a site of interaction for it are commonly called as “hermaphrodite” molecules.

The synthesis of lasso compounds, in which the interlocked structure is locked at each extremity by two hindering moieties (also commonly called “stoppers”) that prevent the macrocycle to unthread, has been the subject of only a very few report to date. Surprisingly, to the best of our knowledge, only a very small number of lassos have been conceived with the aim of being subjected to molecular machinery. However, the combination of molecular machinery and lariat

Fig. 1 Cartoon representation of the equilibrium between a pseudo[1]rotaxane and its non-interlocked hermaphrodite analogue

architectures can yield to different movements like those of a belt which can tighten or loosen depending on a pH *stimulus*, or a crank in which a rotational and a translational motions are closely related, or a controllable "jump rope movement" depending on both pH and solvents. In this chapter, attention is first focused on the chemical synthesis of [1]rotaxanes, then on the synthesis and studies of mono-lasso molecular machines, and eventually on the more sophisticated double-lasso molecular machines.

2 Main Strategies to Yield Mono-lasso Compounds

Different strategies relative to the synthesis of [1]rotaxanes have been reported in the literature. Whereas most of them involve interactions between sites which are present in both the macrocycle and the axle to be threaded, only one strategy relies on a covalent bond formation of [1]rotaxane devoid from any help of supramolecular interactions. These various main strategies are listed in the following sections.

2.1 Covalent Bond Formation of Lasso Compounds

The first strategy to be discussed is based on covalent bond formation and does not appeal to any low interactions between template moieties (Fig. 2). The synthetic route to [1]rotaxanes relies on a key bicyclic compound, one of the two cycles of which can be selectively opened by the attack of a reactive molecular axle (ended by one bulky stopper) through the inner of the other macrocycle.

By using this strategy, Hiratani et al. reported in 2004 the synthesis of the [1]rotaxane **3** via the intermediate formation of the key bicyclic compound **2**, which can undergo an ester to amide *trans*-acylation (Fig. 3) [10].

More precisely, the naphthyl ester moiety of the key bicyclic macrocycle **2** was submitted to an aminolysis using the 9-(3-(aminopropyl)aminocarbonyl)-anthracene. This reaction led, after purification, to the mono-lasso compound **3** in a satisfactory 45 % yield along with 20 % of its non-interlocked analogue. The formation of these two products is inherent in this strategy and can be ascribed to the attack of the amine either by the inner of the cavity of the crown ether or by the

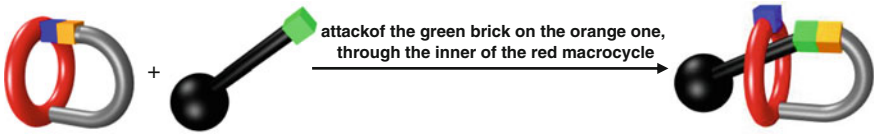

Fig. 2 Cartoon representation of the covalent bond strategy to prepare lasso compounds

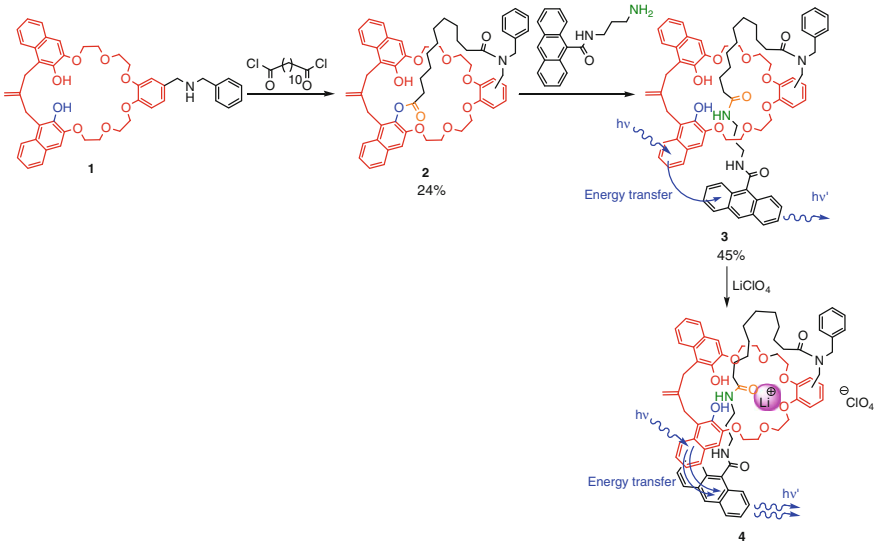

Fig. 3 Covalent bond formation of a lasso compound according to Hiratani et al.

outer of it. Interestingly, and contrary to its non-interlocked analogue, the [1]rotaxane **3** holds specific binding properties related to its interlocked architecture. Indeed, it was found that [1]rotaxane **3** was able to catch the smallest alkali cation lithium with an association constant of 8.4×10^3 L mol^{-1}. Energy transfer from the macrocyclic naphthalene to the tail's anthryl group was then observed and studied in the free lasso **3** and in the lithium-complexed lasso **4**. By comparing with **3**, the fluorescence appeared to be enhanced in the case of the lithium-complexed [1]rotaxane **4**, suggesting that the host–guest interactions restrain the conformation of the lasso and decrease the distance between the naphthalene and the anthryl groups, thus lowering the quenching phenomenon.

The other reported strategies to prepare [1]rotaxanes, which are discussed thereafter, are all based on low interactions as the driving force to assemble the molecular elements into the interlocked structure.

2.2 Template Synthesis of Lasso Compounds

Three main synthetic template strategies have been utilized to generate lasso compounds (Fig. 4).

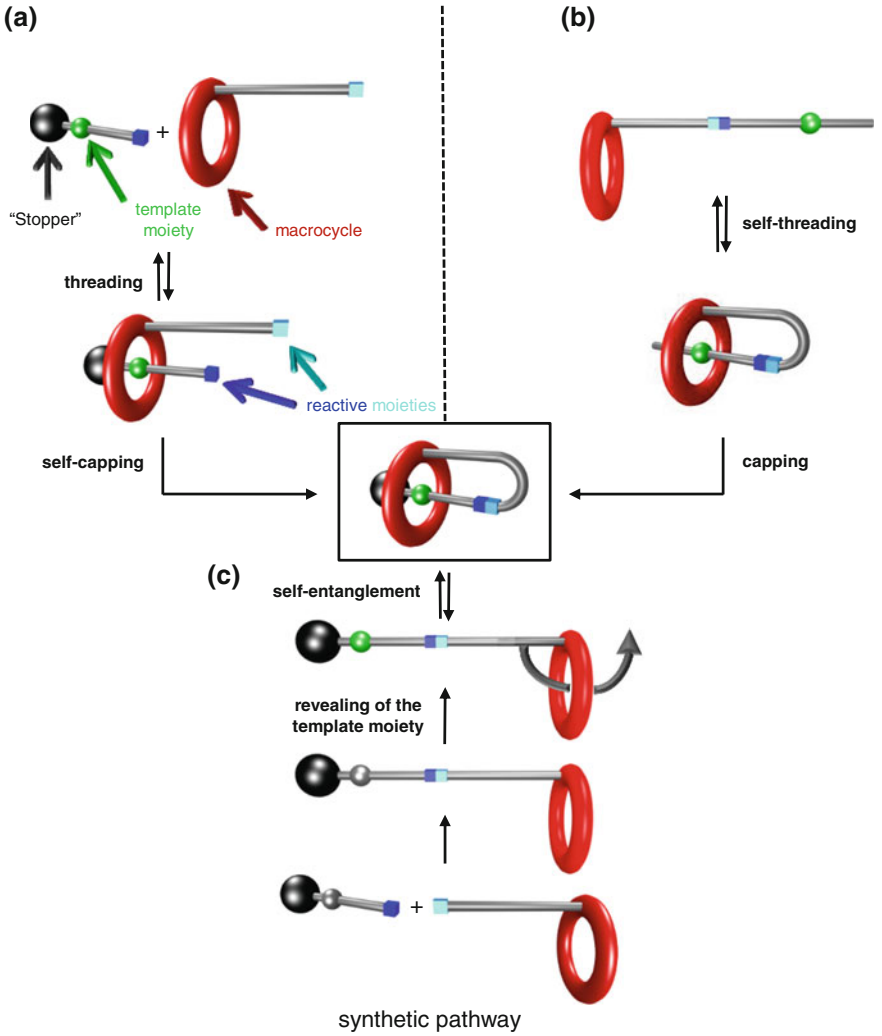

Fig. 4 Cartoon representation of the three main synthetic template strategies to prepare lasso compounds, **a**–**c** synthetic pathway

2.2.1 Synthetic Pathway (a)

The first synthetic strategy (Fig. 4a) can be divided into two key steps: the preliminary templated synthesis of a semi[2]rotaxane (i.e., a threaded molecular axle that possesses only one bulky stopper) and followed by the chemical connection between two reactive functions which belong to the encircled axle and the surrounding macrocycle.

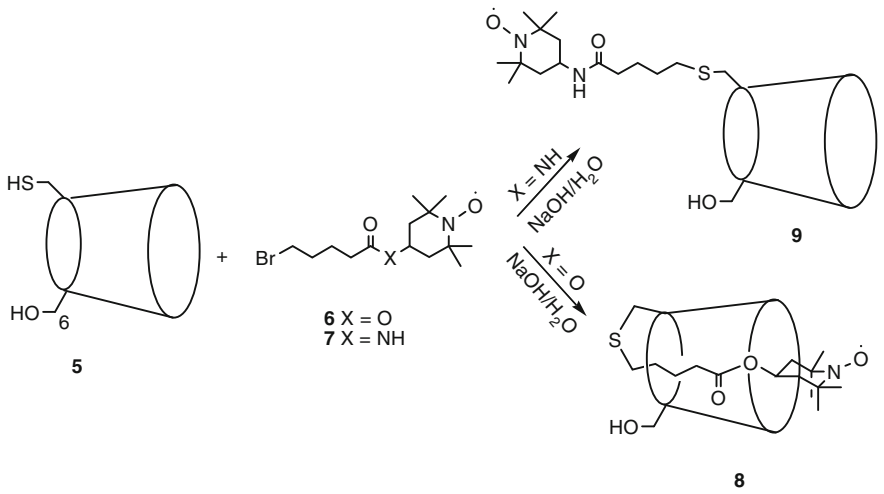

Fig. 5 Synthesis of a [1]rotaxane based on a cyclodextrin by Lucarini et al.

Using this synthetic pathway, Lucarini et al. reported in 2008 the synthesis of a paramagnetic [1]rotaxane based on a β-cyclodextrin and a nitroxide stopper (Fig. 5) [11]. In water, the 6-mercapto-β-cyclodextrin complexes first the bromide guest compound **6**. This encapsulation is due to hydrophobic interactions between **6** and the lipophilic cavity of the cyclodextrin. In the presence of sodium hydroxide, the β-cyclodextrin thiolate moiety of the semirotaxane reacts with the encircled bromide compound via nucleophilic substitution to give the [1]rotaxane **8** in 7.6 % yield. In the case of the bromide compound **7**, which contains an amide group, the fortuitous formation of the non-interlocked compound **9** was observed, without any formation of [1]rotaxane. In **8**, the 2,2,6,6-tetramethylpiperidine-*N*-oxyl (TEMPO) moiety being larger than the smaller rim of the β-cyclodextrin, it acts as an efficient stopper that locks the structure in a [1]rotaxane molecular architecture.

Due to the stabilization of the nitroxides by the β-cyclodextrin and to the lower reactivity of the nitroxyl group in the [1]rotaxane structure, rotaxane **8** was expected to be more resistant toward the nitroxide reduction carried out by enzymes in vivo. Assuming the better in vivo stability of nitroxide [1]rotaxane architecture, with respect to non-interlocked nitroxides, such an interlocked structure brings a particular interest for its use as a protected exogenous radical for spin labels, contrast agents for magnetic resonance imaging, the measure of the spectra of a living body, or oximetry, with a stronger and better resolved electron paramagnetic resonance signals.

2.2.2 Synthetic Pathway (b)

The second strategy (Fig. 4b) is very similar to the first one, but differs by the fact that the initial threading takes place within a single molecule and firstly affords a

pseudo[1]rotaxane, before that this latter is capped, in a second time, at its threaded extremity. In fact, this strategy can only be envisaged if the starting molecule possesses both a macrocycle and a site of interaction for it. A few number of articles report the synthesis of [1]rotaxanes using this synthetic pathway.

In 2007, Tian et al. reported the synthesis of two β-cyclodextrins-based [1]rotaxanes, in which the cyclodextrins are substituted to a diazo-containing tail at different C6 and C2 positions of the glucidic skeleton (Fig. 6) [12].

In water, the molecules **10** and **13** self-assemble in pseudorotaxanes, through the threading of the diazo moiety in the hydrophobic cavity of the cyclodextrin. Depending on the position of the substitution of the tail on the macrocycle, this threading appeared possible either by the smaller or by the bigger rim of the cyclodextrin. The subsequent end-capping reaction of the pseudorotaxanes was carried out in water using a Suzuki coupling with the boronic acid derivative **11** and afforded the [1]molecular rotaxane architectures.

A very similar [1]rotaxane system has been recently used in the domain of nanomaterials [13]. It involves a β-cyclodextrins-based pseudo[1]rotaxane containing in its molecular tail a diazo moiety for the self-inclusion and a terminal 1,2-dithiolane moiety aimed to be grafted on the surface of gold nanoparticles, these latters acting as the stopper.

The formation of a stable [1]rotaxane without the help of any bulky stopper was reported by Kambe et al. The authors proposed the synthesis of a π-conjugated [1]rotaxane **17** containing a permethylated α-cyclodextrin which bears a diphenylacetylene derivative (Fig. 7) [14]. Here again, the employed strategy relies on the initial formation of the pseudorotaxane **16** via self-inclusion within a single molecule in a polar medium to enhance the lipophilic interactions, then by the capping reaction of the threaded tail extremity, this time using a Suzuki–Miyaura coupling. In this example, the main novelty lies in the fact that this latter step was achieved using a non-bulky but conjugated stopper. Although the decomplexation through

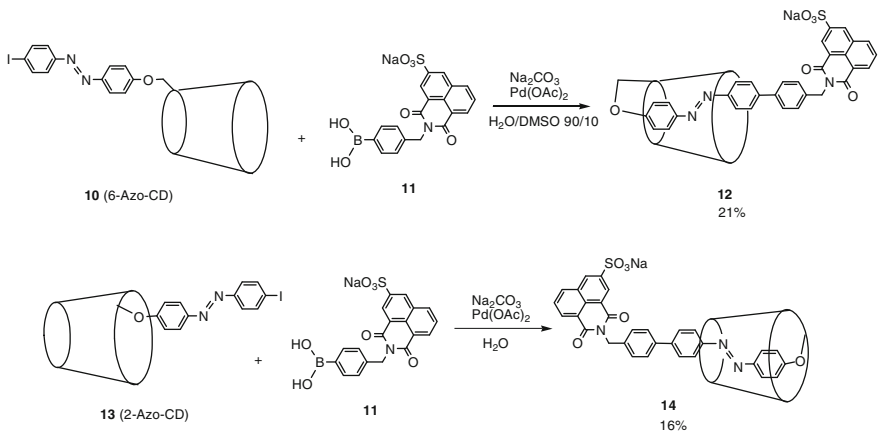

Fig. 6 Synthesis of a [1]rotaxane based on a β-cyclodextrin by Tian et al.

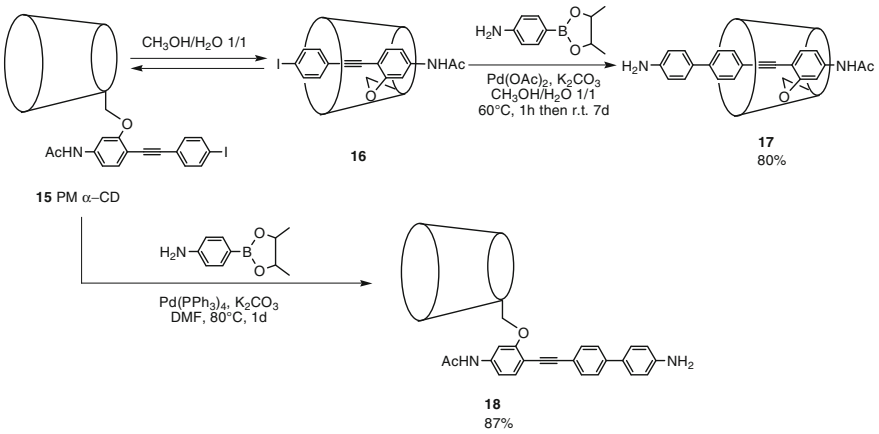

Fig. 7 Synthesis of a [1]rotaxane based on a permethylated α-cyclodextrin and using a non-bulky stopper by Kambe et al.

"flipping" of such a flexible permethylated cyclodextrin-based system was already known, here, the [1]rotaxane product appeared very stable in chloroform even after more than seven days. This stability of the interlocked structure **18** can be explained by the rigid π-conjugated aniline moiety which does not allow any "flipping" mechanism.

2.2.3 Synthetic Pathway (c)

The third strategy (Fig. 4c) relies first on the synthesis of a macrocycle which is linked to a molecular tail containing already a bulky stopper at its extremity. Contrary to the two first strategies (a) and (b), the absence in the molecular axle of any site of interactions for the macrocycle leads exclusively to the non-interlocked product. However, the revealing of a template moiety for the macrocycle leads to a hermaphrodite molecule, in which the revealed moiety can interact with the macrocycle. In this singular case, the classical threading of the molecular tail extremity is not allowed by the presence of the bulky stopper. Nevertheless, if the aromatic-containing macrocycle is well chosen, in terms of size and substitution [15], a movement of rotation of one of its part authorizes the lasso formation via a reversible self-entanglement process. Due to the reversible process, the obtained lasso belongs to the class of pseudo[1]rotaxanes, as long as the flipping mechanism of the macrocycle is possible. One way to stop this mechanism can be the introduction of a side hindering stopper, located in the tail between the site of interaction and the macrocycle. Another way consists of trapping the interlocked structure using strong interactions like a metal–coordination with ligands located on both the macrocycle and the tail.

In 2010, the synthetic routes (a) and (c) were utilized and compared by Mayer et al. [16] for the preparation of a [1]rotaxane, using a metal-directed complexation as the driving force for the interlocking (Fig. 8).

They proposed the synthesis of a model compound **21**, which contains at one extremity a 31-membered ring holding a 1,10-phenanthroline and a covalently linked molecular axle comprising another phenanthroline moiety. At the other extremity lies a tris(*p-tert*-butylphenyl)methyl group [17], which was already known to be unable to pass through the macrocycle [18, 19]. Compound **21** was synthesized from the two alkene-containing compounds **19** and **20** using the Grubb's metathesis. No interlocked product was generated during the metathesis, which is coherent with the absence of any interactions between the macrocycle and the molecular axle. However, as anteriorly mentioned by Sauvage et al. [20], the addition of copper (I) induces a tetrahedral complex, due to the coordination of the metal with the nitrogen atoms of the two phenanthroline moieties. This complexation forces the structure to adopt the [1]rotaxane molecular architecture **22** by tumbling of the macrocycle. Indeed, since the bulky tris(*p-tert*-butylphenyl)methyl extremity of the molecular axle was chosen so that it cannot thread through the macrocycle, the only way to reach the interlocked structure was demonstrated to be a self-entanglement. This interlocking process was found to be also dependent on concentration. At a high dilution (0.1 mM) that minimizes competitive bimolecular chain–chain complexation, the yield of the rotaxane formation was up to 94 %. The entanglement process can be reversed by removing the copper (I) via its complexation with cyanide ions, resulting in the disappearance of the phenanthroline–copper tetrahedral complex, hence to the disentanglement of the structure.

The other already discussed sequential synthetic route (a) toward the lasso molecule **22** was also investigated. It first consists in preassembling the compounds **19** and **20** in the presence of the copper (I), using its ability to coordinate the phenanthroline units of each component. The semirotaxane complex **23** was found to be very stable and was isolated in 98 % yield before being submitted to the Grubb's metathesis. This afforded the lasso compound **22** in a 77 % yield.

Peculiarly, the various possibilities of internal motion that are inherent to the [1]rotaxane molecular architecture have only been the subject of a very few number of articles that are discussed below.

2.3 Examples of Non-controlled Motions in [1]Rotaxanes

An example published by Easton et al. in 2003 [21] must be mentioned as the first synthesized cyclodextrin-based [1]rotaxane. It is based on a cyclodextrin macrocycle and a stilbene-containing thread. The synthetic strategy to reach this [1]rotaxane architecture, which consists of linking the macrocycle of a [2]rotaxane with its encircled axle, has not been discussed before because of its obviousness: Nevertheless, it remains very similar to the presented strategy (a), except that the semi[2]rotaxane is now replaced by a [2]rotaxane. More interesting than the

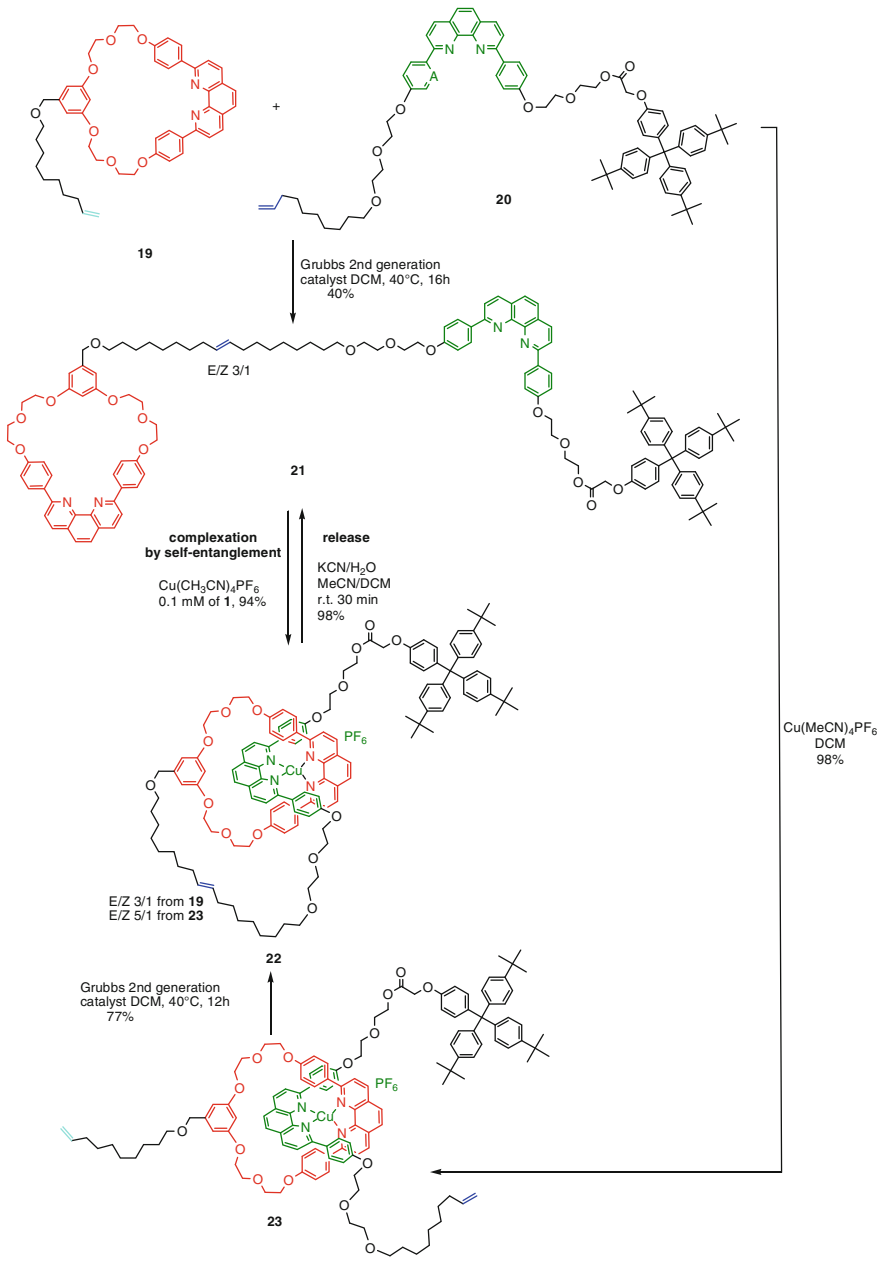

Fig. 8 Synthesis, capture, and release of a self-entangled [1]rotaxane

synthesis is the study of the rotational motion in a mechanical ratchet of a side part of the encircled thread (i.e., acting as a "tooth") restricted by the succinamide spacer joining the cyclodextrin and the threaded axle (i.e., acting as a pawl) (Fig. 9). Experiences on a [2]rotaxane analogue, on one hand, and on a similar [1]rotaxane which does not include the methoxy group, on the other hand, proved that this ratchet mechanism is specific to both the [1]rotaxane architecture and the methoxy group.

Another uncontrolled molecular machine was proposed by Shionoya et al. in 2010 [22]. It concerns the design and the synthesis of a molecular "crank" in which an intramolecular motion transformation between rotation and translation can be observed (Fig. 10). The interlocked molecule **26** contains two disk-shaped rotors, each of them linked either to a dibenzo-24-crown-8 (DB24C8) macrocycle or a carbamoylated amine including molecular tail. The whole structure can be assimilated to a [1]rotaxane because the two disk-shaped rotors are linked together via the coordination of three Ag(I) ions, thus joining the DB24C8 macrocycle to the threaded axle. One disk-shaped rotor possesses six monodentate thiazole moieties (in blue), whereas the other contains only three monodentate oxazoline ligands (purple). Both rotors can complex three Ag(I) ions (in green) via the nitrogen atoms of their ligands, and the possibility of exchange between the six thiazole ligands triggers the free rotational movement of one disk shape (the blue one for example)

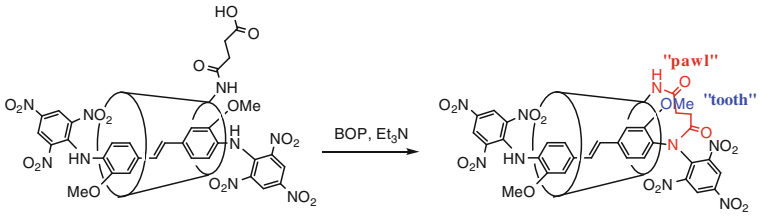

Fig. 9 A ratchet tooth and pawl to restrict a rotational motion in a cyclodextrin [1]rotaxane by Easter et al.

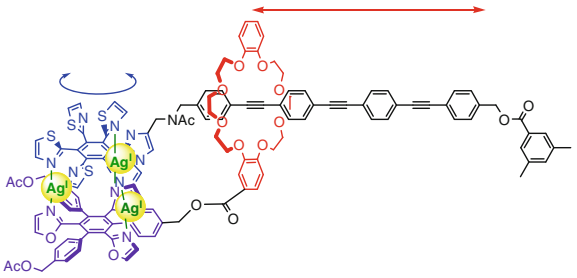

Fig. 10 A molecular "crank" by Shionoya et al.

with respect to the other (the purple one). This motion was correlated with the free translational movement of the DB24C8 (in red) along the threaded tail. It is noteworthy that this latter does not contain any molecular station for the DB24C8 in the targeted molecule **26**. Indeed, the initial ammonium moiety, which acts as a necessary template for the interlocking of the molecule during the synthesis, has been carbamoylated so that a free shuttling displacement of the DB24C8 could take place.

These last examples of rotational and rotational related to translational motions naturally lead us to discuss now about the notion of the accurate control of various movements of the elements in a [1]rotaxane. As one of the most interesting internal motion, the molecular machinery of controlling the shuttling of the macrocycle along the thread in a [1]rotaxane architectures has been the object of only a very few examples, which are given below.

3 Mono-lasso Molecular Machines

3.1 Synthesis of Light-Driven [1]Rotaxanes

In 2007, Tian et al. described the synthesis of a light-driven [1]rotaxane based on a β-cyclodextrin as the host and a diazo-containing tail as the guest (Fig. 11) [23]. They used the above-discussed strategy (b) consisting of a self-inclusion of an azobenzene-modified β-cyclodextrin and the subsequent tail capping of the pseudorotaxane intermediate by Suzuki coupling. The self-inclusion being mainly based on hydrophobic interactions, the pseudorotaxane **12** was only produced in a

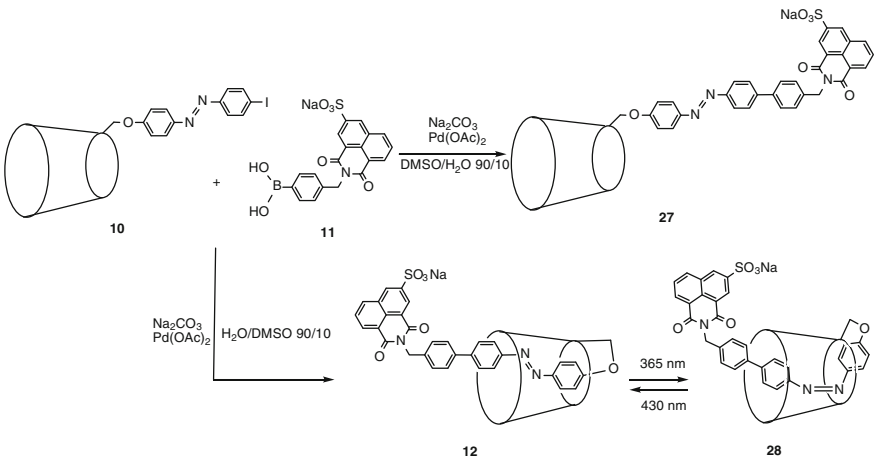

Fig. 11 Synthesis of a light-driven [1]rotaxane molecular machine based on a cyclodextrin by Tian et al.

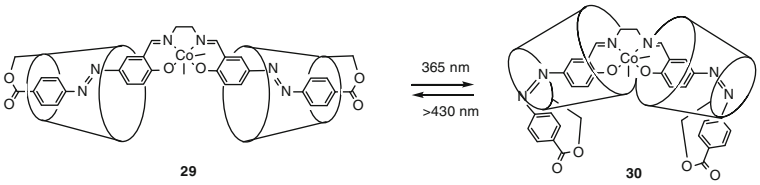

Fig. 12 Synthesis of a light-driven [1]rotaxane molecular machine by Tian et al.

mixture water/dimethylsulfoxide (90/10), whereas the use of an increased amount of dimethylsulfoxide resulted in the exclusion of the azobenzene arm from the β-cyclodextrin cavity, thus allowing the preparation of the non-interlocked analogue **27**. Interestingly, the *E*/*Z* photoisomerization of the azobenzene moiety of [1]rotaxanes **12** and **28** triggered a very slight reversible shuttling movement of the β-cyclodextrin along the thread.

Tian et al. reported a little bit later another light-driven [1]rotaxane, this time based on a Cobalt coordinated [1]rotaxane molecular machine which can adopt contracted or stretched states upon light irradiation (Fig. 12) [24]. The Co (III) has been used to coordinate the oxygen atoms of the phenolates and the nitrogen atoms of the Schiff bases, thus allowing a higher rigidity and linearity of the molecule. In **29** and **30**, the photoisomerization of the two azobenzene moieties allows to amplify the stretching and contraction movement that was observed before with the [1]rotaxanes **12** and **28** containing only one azobenzene and one cyclodextrin (Fig. 11).

A few number of other [1]rotaxane molecular machines, this time containing several molecular stations for the macrocycle, have also been recently synthesized and studied. Contrary to the examples described above, they display a much larger amplitude of movement of the macrocycle along the threaded axle, so that the lasso can adopt two very different conformations. They are not based anymore on cyclodextrins but on crown ether macrocycles and have the feature to be pH-responsive. They are inventoried below.

3.2 Synthesis of pH-Sensitive [1]Rotaxanes Based on Two Molecular Stations

3.2.1 Via the Self-threading and the Subsequent Tail Capping (Synthetic Pathway (b))

All the following examples of lasso molecular machines rely on the utilization of crown ethers as macrocycles and threads containing ammonium and triazolium moieties as molecular stations. Coutrot et al. have been the first to report the use of a *N*-alkyl triazolium as molecular stations [25] for crown ethers such as DB24C8 or

benzo*meta*phenylene-25-crown-8 (BMP25C8). The *N*-methyl triazolium station can be very straightforwardly introduced, from an alkyne and an azide compounds, using a two-step sequence: (1) copper (I)-catalyzed Huisgen alkyne-azide 1,3-dipolar cycloaddition (CuAAC click chemistry) and (2) *N*-methylation of the triazole. The *N*-methyl triazolium moiety proves to be a poorer molecular station for crown ethers than ammonium stations. Indeed, it is quite impossible to use triazoliums as templates for rotaxane formations [26]. However, in interlocked rotaxane architectures, after deprotonation of the ammonium moiety, the *N*-methyltriazolium group turns out to be a molecular station of sufficient affinity for crown ether macrocycles and interacts both by hydrogen bonding or charge transfer.

The bistable ferrocene-based [1]rotaxane **33** was synthesized in 2012 by Qu et al. [27] according to the strategy (b) and using Coutrot's system [25] of molecular stations for the DB24C8 (Fig. 13). The hermaphrodite molecule **31**, which contains an ammonium template linked to a DB24C8 macrocycle via a ferrocene linker, was first synthesized. In the nonpolar solvent dichloromethane, the extremity of the tail is threaded through the macrocycle so that the oxygen atoms of the DB24C8 interact with the ammonium station by hydrogen bonds and ion–dipole interactions. At this stage, the hermaphrodite compound **31** and the pseudorotaxane **32** are in equilibrium. The introduction of a dimethoxybenzene stopper at the alkyne extremity was achieved via the "click chemistry" in a solvent that does

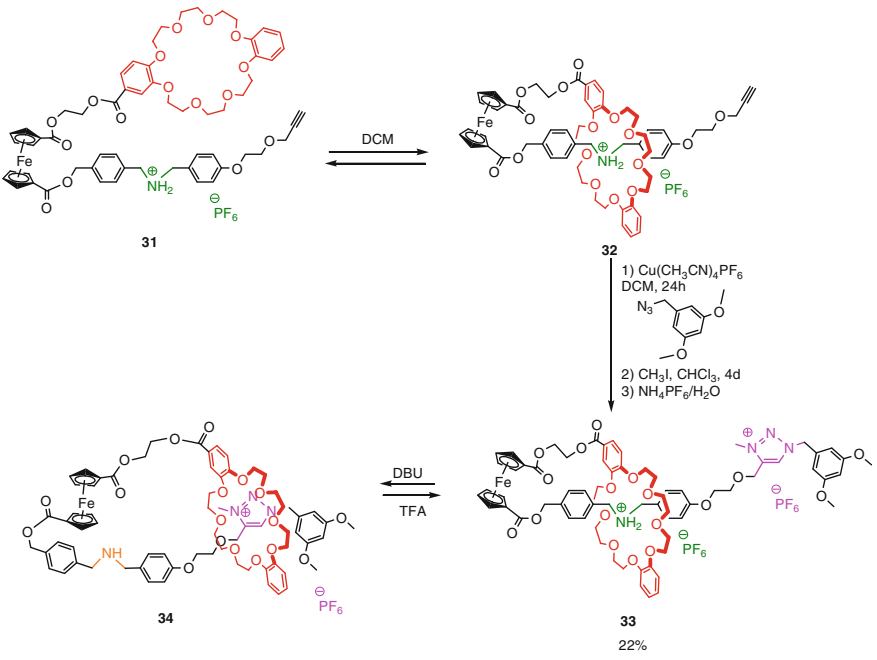

Fig. 13 Synthesis of a pH-sensitive [1]rotaxane molecular switch with an electrochemical signal output by Qu et al.

not disrupt the interactions that are responsible for the interlocked architecture. Then, the triazole moiety underwent a methylation using methyl iodide and an anion exchange with ammonium hexafluorophosphate. Using Coutrot's synthetic pathway [25], the two-station [1]rotaxane **33** was obtained from the hermaphrodite molecule **31** with an overall yield of 22 %. Molecular machinery was then envisaged on **33** using a variation of pH as the external *stimulus*. Upon deprotonation, the DB24C8 shuttles toward the triazolium station, thus loosening the lasso molecule. The process can be reversed in trifluoroacetic acid, resulting in the tightening of the lasso. Interestingly, cyclic voltammetry experiments showed very different electrochemical properties of the free ferrocene unit for the lasso compounds in the two very different conformational states. Indeed, the electrochemical state of the protonated lasso **33**, in which the ammonium is included in the inner of the macrocycle, appeared reversible. On the contrary, an electrochemically irreversible state is observed at the deprotonated state when the amine group is excluded from the macrocycle. Such a system holds potential for designing smart materials with switchable properties.

Starting from the pseudorotaxane **32** and using the same strategy to yield lasso architecture, Qu et al. described in 2013 an analogous redox-active ferrocene-based system, although slightly more sophisticated insofar as the movement of its DB24C8 displays a larger amplitude and the threaded axle holds a 4-morpholin-naphthalimide as a stopper whose fluorescence can be adjusted by a distance-dependent photoinduced electron transfer process (Fig. 14) [28].

The system works here as an INHIBIT logic gate (Fig. 15) that can be observed by the naked eye. The intensity of the fluorescence of the [1]rotaxanes appeared to be very different depending on the pH. Indeed, by comparing with the protonated [1]rotaxane **35**, the emission intensity at 521 nm of the deprotonated [1]rotaxane **36** dramatically decreases. This observation can be ascribed to the spatial proximity between the electron-rich ferrocene unit and the electron-deficient 4-morpholin-naphthalimide fluorescent moiety. This proximity allows the photoinduced electron transfer process between the two complementary units, thus resulting in the quenching of the fluorescence. Fluorescence can be restored to its original level, either by decreasing the pH (addition of trifluoroacetic acid) or by oxidizing the ferrocene unit by the help of $Fe(ClO_4)_3$. When oxidized, ferrocene is no more an electron-donating group (compounds **37** and **38**). As a result, no photoinduced electron transfer is possible whatever the distance between the ferrocene and the 4-morpholin-naphthalimide units, this distance being related to the two conformations of the [1]rotaxane which can be obtained upon variation of pH. The authors claimed important potential for the development of complicated logic circuits with memories or sequential functions.

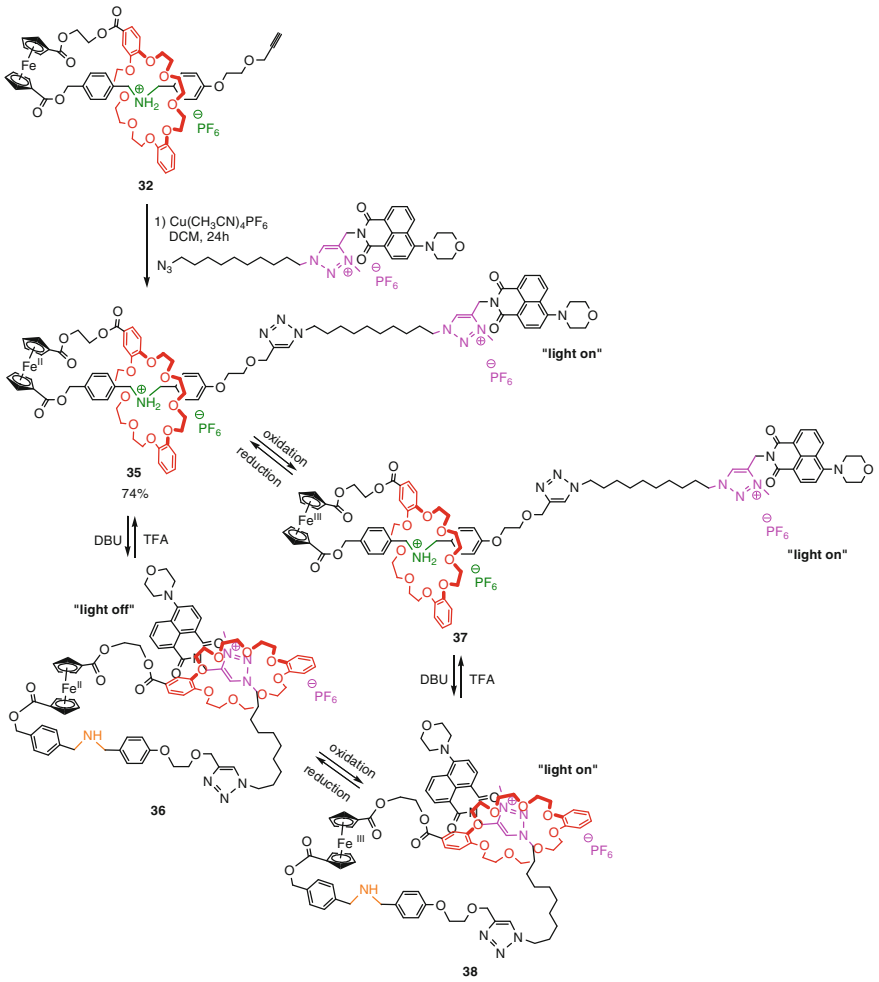

Fig. 14 Synthesis of a pH-sensitive [1]rotaxane molecular switch holding a fluorescence signal by Qu et al.

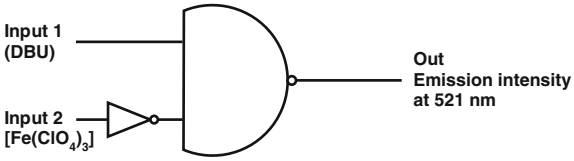

Fig. 15 Representation of the INHIBIT gate that characterizes the intensity of fluorescence of the [1]rotaxane molecular switches **35–38** upon pH and redox *stimuli*

3.2.2 Via the Self-Entanglement Strategy (Synthetic Pathway (c)) and the Subsequent Introduction of a Kinetic Molecular Barrier

The self-entanglement of a hermaphrodite molecule was recently employed by Coutrot et al. to synthesize two novel [1]rotaxane lasso compounds, which were also able to behave as pH-sensitive molecular switches. The synthetic route to the mono-lasso molecular switches relies here on a two-step sequence: (1) self-entanglement of a hermaphrodite molecule to afford a pseudo[1]rotaxane and (2) trapping of the macrocycle via the incorporation of a kinetic molecular barrier (Fig. 16).

The concept of introducing a molecular barrier to make the molecular machines compartmentalized was developed anteriorly by Leigh et al. [29–33]. Coutrot et al. extended this concept to the *N*-substituted triazolium series, with the aim to use the molecular barrier as a molecular station too [34]. The self-entanglement of the initial hermaphrodite molecule containing a template moiety (green ball) for a macrocyclic host (in red) leads to the pseudo[1]rotaxane, via the rotation of a part of the macrocycle (step 1, Fig. 16). At this stage, the pseudo[1]rotaxane remains in equilibrium with its non-interlocked precursor analogue and can be trapped via the incorporation of a kinetic molecular barrier (pink ball), as a bulky side chain, at a reactive site of the axle located between the template moiety and the macrocycle (step 2, Fig. 16). Bistable molecular machinery on the lasso is then possible only if the threaded axle owns two molecular stations for the macrocycle. In this example, the molecular barrier has been chosen and utilized so that it can also act as a molecular station for the macrocycle, but with a much poorer affinity than the initial template moiety. In the protonated state, the green molecular station has a better affinity for the macrocycle than the pink molecular station, hence resulting in a

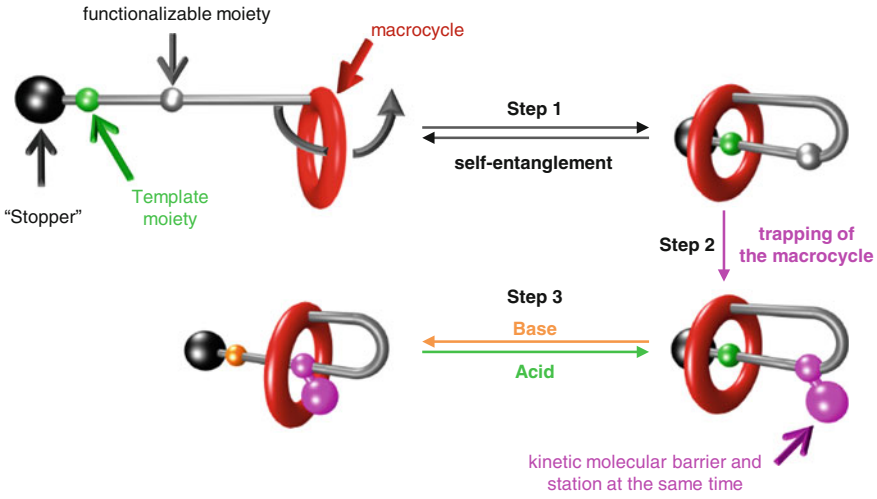

Fig. 16 Cartoon representation of the self-entanglement and trapping strategy proposed by Coutrot et al.

loosened conformation of the lasso compound. However, deprotonation of the green molecular station triggers the shuttling of the macrocycle toward the pink molecular station, thus causing the tightening of the lasso.

The first targeted mono-lasso has been designed so that the interlocking could be achieved using a template strategy involving hydrogen bonds and ion–dipole interactions between an ammonium moiety and a crown ether macrocycle [35]. The previously prepared hermaphrodite precursor **39u** consists of a benzo*meta*phenylene-25-crown-8 (BMP25C8) macrocycle linked to a molecular axle which contains both an anilinium and a triazole moiety. The anilinium was chosen as the templating site for the crown ether, whether the triazole, which is located between the macrocycle and the anilinium station, has been chosen as the precursor of the triazolium-based molecular barrier and second station.

Since the di-*tert*-butyl anilinium extremity of the molecular axle is too bulky to thread through the macrocycle (i.e., it plays the role of a molecular "stopper"), the only way to yield the lasso architecture relies on the self-entanglement. Thus, the size of the crown ether appears crucial for the efficiency of the pseudo[1]rotaxane formation. Even though a smaller macrocycle such as the dibenzo-24-crown-8 was known to be a better host for the anilinium moiety [36] than the bigger BMP25C8, it could not be utilized in this strategy, due to its smaller cavity (caused by its *ortho*-substitution) that would not allow any self-entanglement. On the contrary, the *meta* substitution of the BMP25C8 enlarges the inner of the macrocycle and allows for the free rotation around the two phenoxy substituting σ bonds of the aromatic ring. This internal movement of the BMP25C8 results in the threading of the anilinium-containing molecular axle by self-entanglement (Fig. 17).

The equilibrium between the uncomplexed hermaphrodite molecule **39u** and the pseudolasso **39** was studied. The pseudolasso was preferentially obtained in hydrogen-bond-promoting solvents and at the lowest concentration. The best self-entanglement (45 % of lasso **39**) was obtained in dichloromethane at a concentration of 5×10^{-4} M, whereas the *ratio* of lasso **39/39u** highly decreased in favor of **39u,** respectively, in acetonitrile (14 % of lasso **39**), methanol (4 % of lasso **39**), and dimethylsulfoxide (0 % of lasso **39**) and upon increasing the concentration in dichloromethane (23 % of lasso **39** at 5×10^{-2} M).

The subsequent trapping of the pseudolasso **39** toward the stable "locked" lasso molecular architecture was realized by benzylation of the triazole moiety (Fig. 18).

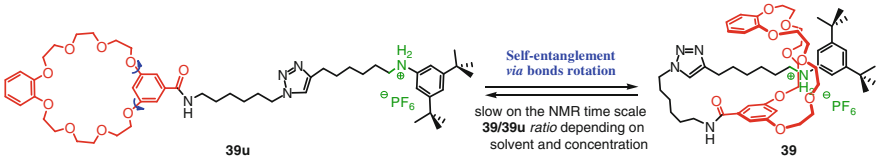

Fig. 17 Self-entanglement of the hermaphrodite molecule **39u** enclosing a BMP25C8 macrocycle and an anilinium-containing molecular axle by Coutrot et al.

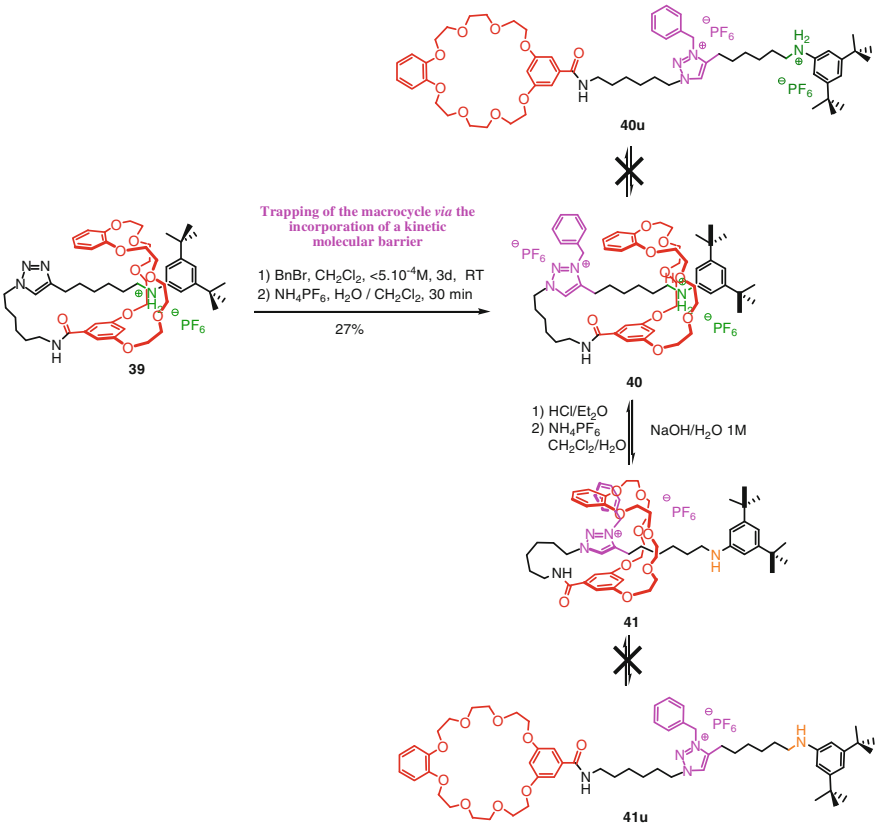

Fig. 18 Trapping the lasso structure via the *N*-benzylation of the triazole moiety and pH-responsive molecular machinery by Coutrot et al.

The locked [1]rotaxane **40** was isolated in 27 % yield. At this point, the efficacy of the barrier was demonstrated by the absence of any equilibrium between **40** and its uncomplexed hermaphrodite analogue **40u**.

The molecular machinery was then studied, and the evidences were obtained by accurate 1D, 2D, or ROESY ^{1}H NMR experiments of the protonated and deprotonated lasso molecular switches and of their respective non-interlocked analogues. Deprotonation of the loosened lasso **40** led to the deprotonated tightened lasso **41**, via the shuttling of the BMP25C8 from the anilinium to the triazolium molecular station. Here again, at basic pH, in the absence of the best anilinium station, the benzylic side chain was found to be an effective molecular barrier for the BMP25C8: Indeed, no more equilibrium was observed between the lasso compounds **41** with their respective non-interlocked analogues **41u**.

Inspired by the fact that lasso molecules can also be identified in nature, the same authors pursued their research by trying to give a biological application to synthetic lasso molecular machines. Of particular interest is the case of the different families

of natural lasso peptides, which, for most of them, are resistant against the proteolytic degradation and the chemical and thermal degradation and, for some of them, proved to inhibit the HIV replication or the gram-negative RNA polymerase. Their very interesting biological activities essentially lie on their specific constrained conformation. Their chemical synthesis remains a tough challenge so far, which explains why no lasso peptide has been synthesized using chemical protocols to date. Furthermore, natural lasso peptides are not subjected to molecular machinery, although applying molecular machinery to a lasso peptide could be of very high interest. For example, one may envisage that bending more or less the tridimensional structure of a peptide using *stimuli*-responsive molecular machinery in a lasso structure could result in the tailoring of the activity or affinity of the peptide for, respectively, its enzyme or receptor.

Considering these words, Coutrot et al. reported a variation in the structure of the lasso, by incorporating a tripeptide sequence between the macrocycle and the triazolium molecular station [37]. They opted for the simplest model tripeptide GlyGlyGly and considered if the tightening or the loosening of the lasso could trigger a more or less bent conformation of the peptide sequence (Fig. 19).

It is noteworthy that the peptide moiety did not perturb the self-entanglement strategy or the operation of the molecular machinery which was observed anteriorly on the non-peptide lasso compounds **40/41**. Hence, in the peptide-containing lasso compounds **42** and **43**, the authors proposed that the variation of the pH causes the reversible protonation–deprotonation of the anilinium molecular station, therefore the variation of the shape of the lasso which results in the modification of the peptide shape. Beyond this preliminary and essentially chemical objective, the extension to other peptide sequences of interest is suggested by the authors and could open new avenues to peptide-containing molecular switches with controllable potential medicinal applications.

Few other more sophisticated and unique lasso structures have also been recently reported: They essentially differ from the number of threaded macrocycles. The following section relates the synthesis and the *stimuli*-responsive behavior of double-lasso molecular machines.

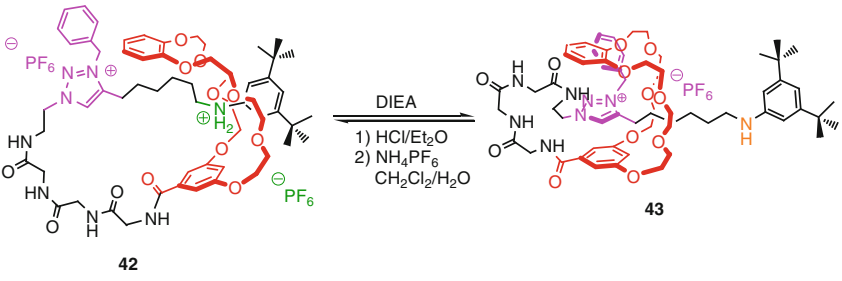

Fig. 19 Molecular machinery on the pH-sensitive peptide-containing lasso molecular switch **42/43** by Coutrot et al.

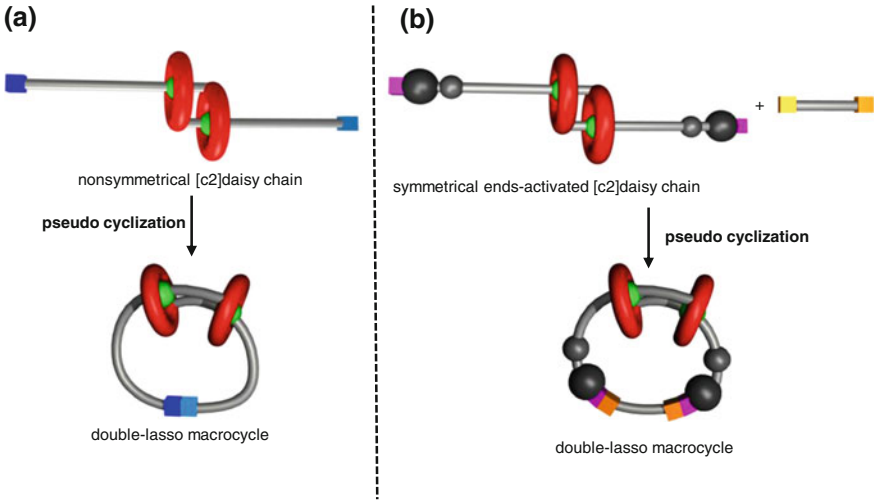

Fig. 20 Cartoon representation of the two strategies used to prepare double-lasso molecules by the cyclization of [c2]daisy chain precursors by Coutrot et al. **a**, **b** Synthetic pathway

4 Double-lasso Molecular Machines

Two unique double-lasso molecular architectures (Fig. 20) have been recently reported by Coutrot et al. [38, 39]. Their preparation relies on the pseudocyclization of a pseudo[2]rotaxane dimer (i.e., a [c2]daisy chain, for a recent review, see [40]) containing two distinct or identical reactive extremities (Fig. 20). The synthetic pathway (a) involves a self-assembled pseudorotaxane dimer as a key starting material, whereas the other synthetic pathway (b) implies a stable and isolable rotaxane dimer containing two stoppers at each extremity of the interwoven structure.

4.1 Synthesis of Double-lasso Macrocycles from Non-symmetrical [c2]Daisy Chain

The first strategy to reach double-lasso macrocycle is essentially based on the preparation of the non-symmetrical [c2]daisy chain enantiomers **49/49′** from two different symmetrical [c2]daisy chains **46** and **48** (Fig. 21) [38].

Analogous but shorter symmetrical dialkyne [c2]daisy chains, based on DB24C8 macrocycles and ammonium station, have been reported by Coutrot et al. anteriorly for the conception of pH-sensitive molecular muscles [41, 42]. In the pseudo[2] rotaxane dimers **49/49′**, the alkyne and azide moieties, which are located at the extremity of the threaded axles, were chosen in order to undergo a copper

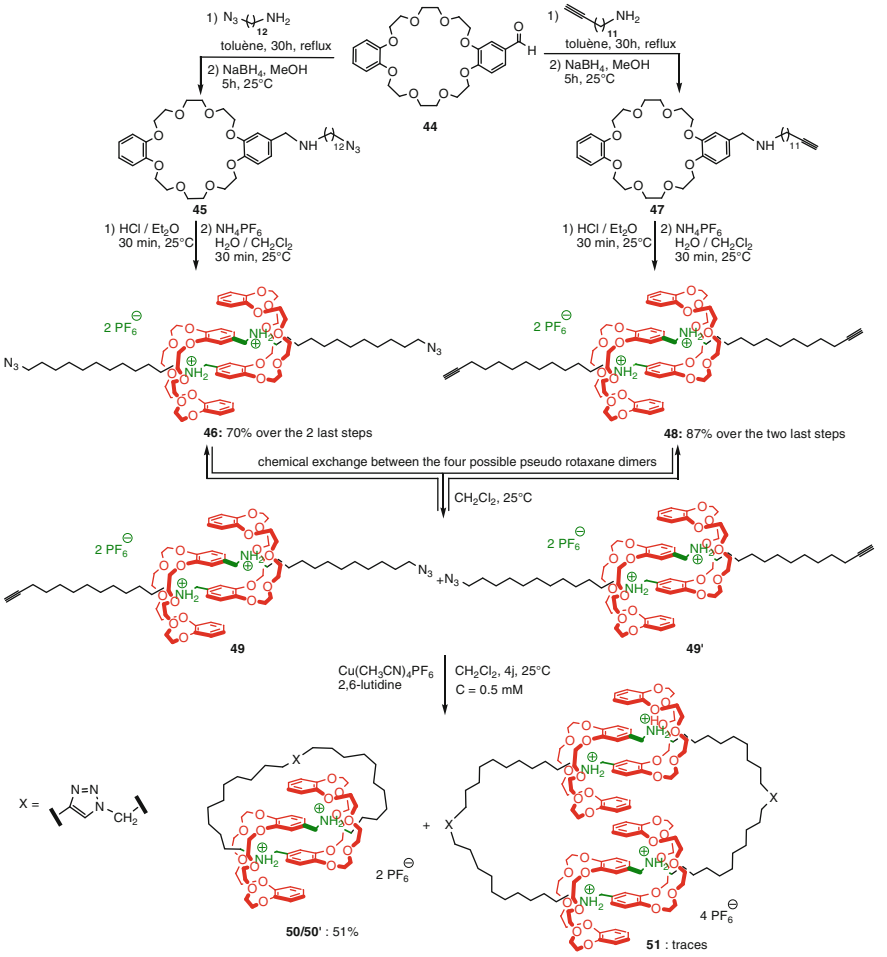

Fig. 21 Synthesis of the double-lasso macrocycle **50** by Coutrot et al.

(I)-catalyzed Huisgen alkyne-azide 1,3-dipolar cycloaddition (CuAAC click chemistry), thus to create afterward a second molecular station by alkylation of the triazole. They were obtained via the chemical exchange between two different symmetrical diazide and dialkyne [c2]daisy chain precursors **46** and **48**. These latter were produced using a reductive amination reaction from the aldehyde derived from the dibenzo-24-crown-8 **44**.

The necessary exchange between the pseudorotaxane dimers **46** and **48** occurs quickly and leads to the non-symmetrical pseudorotaxane dimer isomers **49/49′**. Contrary to compounds **46** and **48**, and due to the different alkyne and azide extremities, the rotaxane dimer **49** is now devoid of any S_2 symmetry: Therefore, it consists of a stoichiometric mixture of enantiomers. After about 60 min in

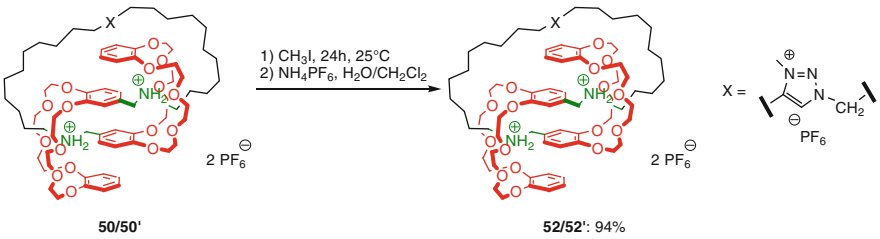

Fig. 22 Attempt to prepare a double-lasso molecular machine by Coutrot et al.

dichloromethane, the equilibrium was reached and a statistical distribution between **46**, **48,** and **49** was observed by MALDI-TOF mass spectrometry (i.e., **46**:**48**:**49/49′** 25:25:50). This observed statistical distribution suggests that the azide or alkyne extremities of each hermaphrodite molecule have no influence on the [c2]daisy self-assembling. The further in situ cyclization of the non-symmetrical pseudorotaxane dimers **49/49′** was carried out and afforded the double-lasso macrocycle **50/50′** in a 51 % yield, which is in concordance with the *ratio* observed for precursors **49/49′**. Only traces of the tetra-lasso macrocycle **51** were detected by MALDI-TOF MS.

The authors then explored the possibility to control the change of the shape of the novel double-lasso structure using molecular machinery. For that, the two triazole moieties were efficiently methylated to create a second molecular station for the DB24C8 macrocycles [43] (Fig. 22).

Unfortunately, neither the deprotonation nor the "one pot" carbamoylation of the ammonium molecular stations led to any reaction that could cause the shuttling of the macrocycles. One may suggest that one triazolium molecular station is not sufficient to bind the two DB24C8 macrocycles.

Another strategy to yield a workable two-station double-lasso molecular machine was envisaged by the authors, this time from a symmetrical ends-activated [c2]daisy chain building block.

4.2 Synthesis and Operation of Double-lasso Molecular Machines from a Symmetrical Ends-Activated [c2]Daisy Chain Building Block

4.2.1 Synthesis of the Double-lasso Molecular Machines

In this unique example (Fig. 23), the strategy is based on the efficient preliminary synthesis of the [c2]daisy chain building block **54**, which contains at each extremity a bulky protected glucidic stopper [39]. It can be synthesized via the CuAAC click chemistry between the dialkyne [c2]daisy chain **48** and the azido glucuronate active ester **53**. The rotaxane dimer **54** consists of a stable and isolable building block that can react at its extremities via its pentafluorophenyl active ester with amine moieties.

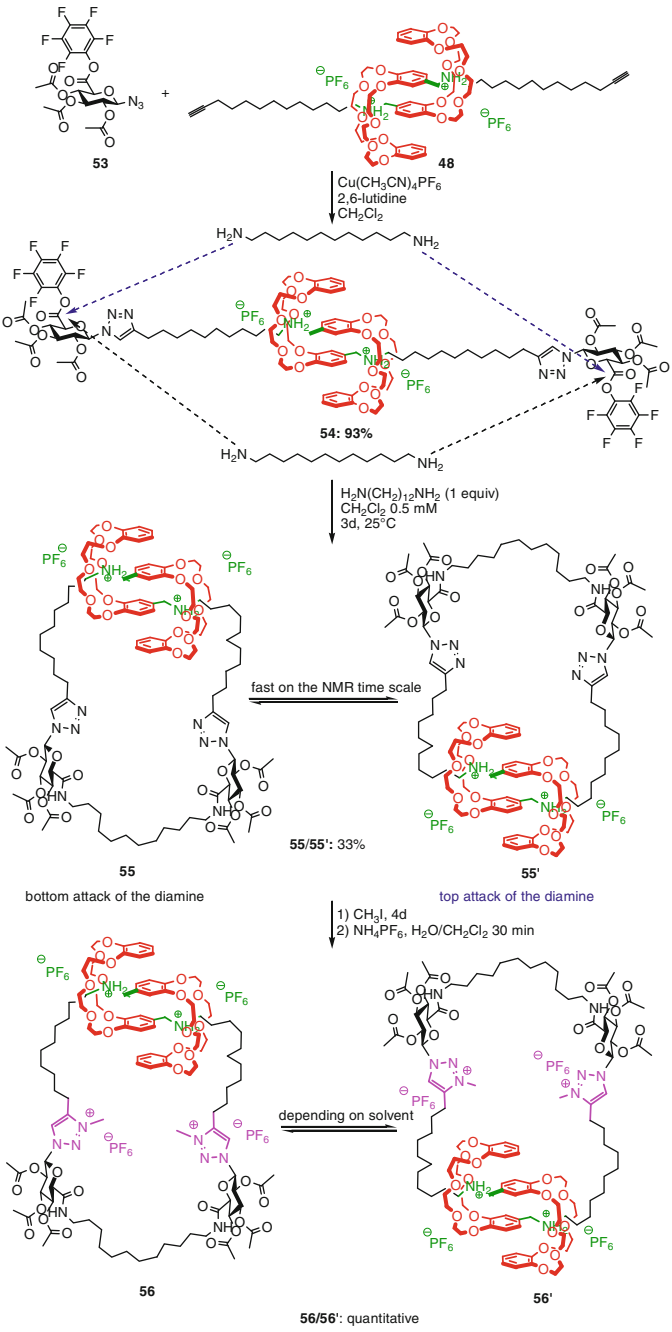

Fig. 23 Synthesis of a double-lasso molecular machine from an ends-activated [c2]daisy chain building block by Coutrot et al.

Beyond its obvious interest as an elaborated [c2]daisy chain building block for the synthesis of sophisticated pH-responsive polymers, the authors envisaged the formation of double-lasso molecular machines. The pseudocyclization was achieved in dichloromethane at high dilution using the dodecanediamine.

Two possibilities of cyclization are possible here: They are due to the attack of the diamine either by the top of the rotaxane dimer **54**, or by the bottom of it, leading to two double-lasso rotamers **55** and **55′**, that can exchange with each other through the rotation of the pseudomacrocycle around the [c2]daisy arrangement. Since the size of the cavity of the pseudomacrocycle is large enough, the exchange between the two left- and right-handed helix-type rotamers appears fast at the NMR timescale and only one set of ^{1}H NMR signal was observed for the two isomers. The *N*-methylation of the triazole moieties was then carried out in order to create the second molecular stations (i.e., the two triazoliums) for the DB24C8 macrocycles.

4.2.2 Tightening and Loosening of the Double-lasso Molecular Machine Triggered by a pH Variation

Contrary to the other previously discussed example of double-lasso molecule **52** which contains only one triazolium site for two macrocycles, the molecular machine appears effective, in the present case, this being ascribed to an equal number of triazolium stations and macrocycles. Indeed, the deprotonation by the sodium hydroxide of the loosened double-lasso **56** triggered the shuttling of the two DB24C8 around the triazolium stations, which led successfully to the tightened double-lasso **57** (Fig. 24) [39].

Lasso **57** proves to be a mixture of isomers, whose exchange is impossible due to the tightened conformation of the lasso (see section below relative to a molecular "jump rope" movement).

Such a molecular machine, which has a cavity of a controllable shape and size, could be of high interest for the future conception of pH-sensitive carriers. If the lasso is well designed in terms of size and nature, one may imagine a guest component confined in the inner cavity of the deprotonated tightened lasso, whereas it is released upon protonation due to the loosening of the lasso that decreases the interactions with the guest molecule.

4.2.3 "Molecular Jump Rope" Motions Dependent on Solvent Polarity and pH

Another distinct movement in the double-lasso molecular machine **56** has also been highlighted. It consists in a controllable rotation (otherwise named a molecular "jump rope" movement) of the loop of the pseudomacrocycle (i.e. the rope) around the [c2]daisy arrangement (i.e., the arms of the girl whose name is Daisy in the cartoon representation illustrated in Fig. 25) [39]. Interestingly, this molecular jump

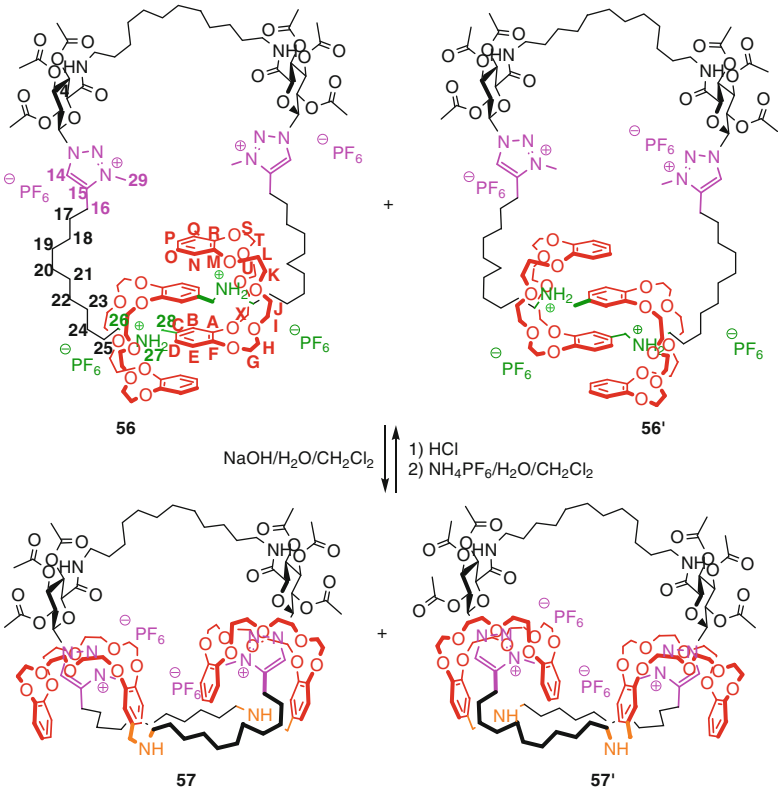

Fig. 24 Tightening and loosening the double-lasso molecular machine 56/57 upon variation of pH by Coutrot et al.

rope movement could be demonstrated thanks to the ^{1}H NMR spectroscopy, especially in the case of a slow rotation of the rope, on the NMR timescale, around the daisy arrangement. Indeed, if the rate of the rotation is slow on the NMR timescale, the two rotamers become two atropoisomers (related to D-sugar and left- or right-handed pseudohelixes) that are distinguishable by the NMR spectroscopy, like diastereomers. For the triazole-based double-lasso **55**, the exchange between each diastereomer appears to be fast at the NMR timescale, and only one set of signals for **55** is observed. It is not always the case for triazolium-based double-lasso macrocycle **56**. Indeed, the molecular jump rope movement appears here to be solvent-dependent, due to the presence of the triazolium moieties which can be closer or further away from each other, thus lowering or increasing the size of the pseudomacrocycle cavity. In dissociating solvents such as dimethylsulfoxide or acetonitrile, the higher repulsion between the triazolium moieties tends to enlarge the size of the cavity of the rope, allowing a fast movement around the [c2]daisy chain moiety. On the contrary, in the non-dissociating solvent dichloromethane, the repulsion between the triazolium moieties is much smaller, triggering the collapse

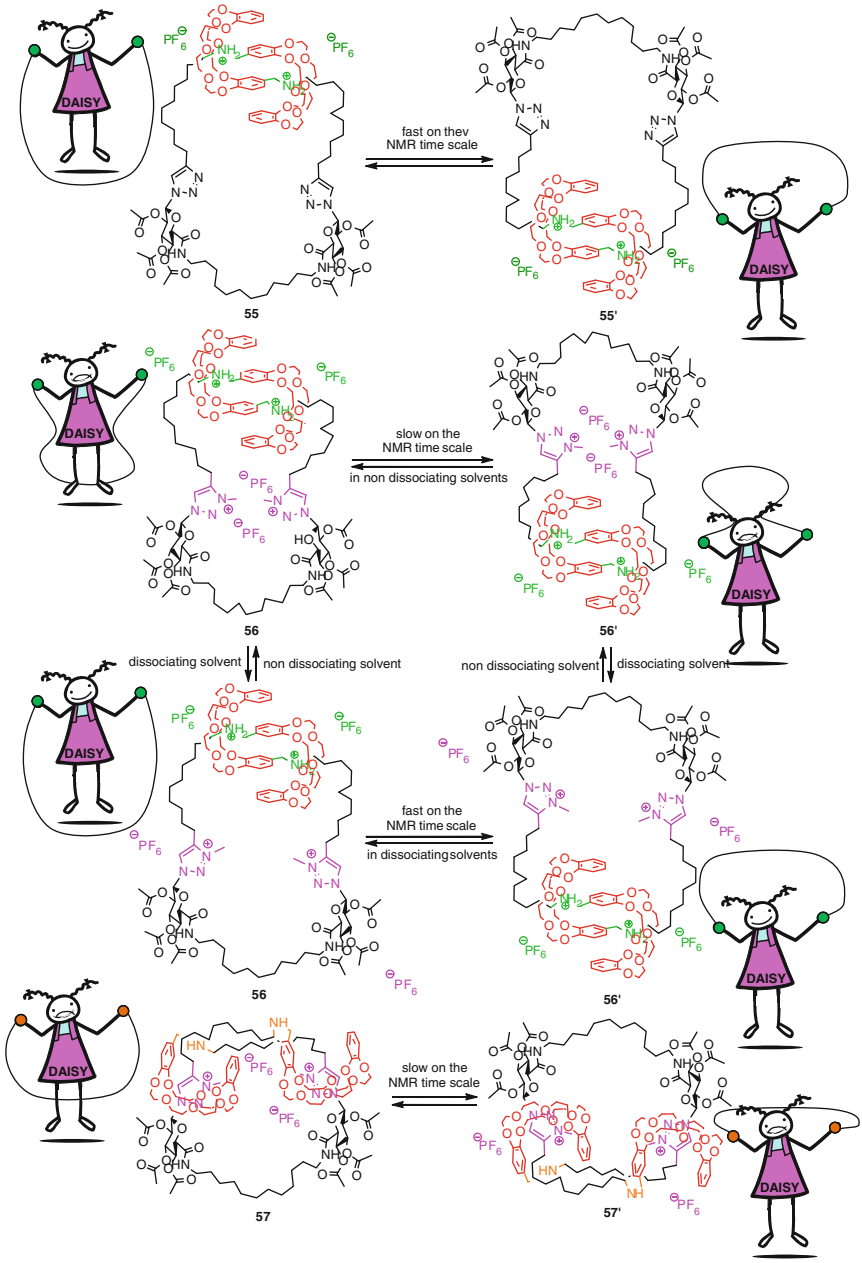

Fig. 25 Molecular "jump rope" movement in double-lasso molecular architectures by Coutrot et al.

of the macrocyclic cavity probably also because of the presence of bifurcated interactions between triazolium cations and hexafluorophosphate counter anions. Hence, the inversion of the helix is hindered in the less polar solvent, and the two rotamers **56** and **56′** are distinguishable by NMR because of the much slower exchange on the NMR timescale. After deprotonation, compounds **57** and **57′** become atropoisomers because the tightening of the double-lasso macrocycle does not permit anymore a free movement of the loop of the lasso around the [c2]daisy chain, then preventing the exchange between the two right- and left-handed helix-type structures.

5 Perspectives

Despite the few number of reported papers on [1]rotaxanes, these compounds proved to be very appealing candidates for molecular machinery. Whereas molecular machines based on [2]rotaxane architecture have been studied more extensively, the [1]rotaxanes hold the same opportunity to act as molecular machines and, in addition, they present several advantages that could give rise to many other applications. Indeed, the difference between the two structures relies on the presence of a linker between the macrocycle and the threaded axle, which defines a pseudomacrocycle. The large-amplitude motion of the macrocycle along the threaded pseudomacrocycle can lead to the tightening or the loosening of the lasso. In these two conformational states, the linker, which can be chosen of very different nature (peptide, saccharide, polyether, and polyaromatic), undergoes different conformational changes: If well designed, the incorporation of a bioactive compound (like a peptide), as the linker, could give rise to very different biological responses (in terms of affinity, and activity) depending on the molecular machinery. This could constitute a new field of investigation for lasso compounds. Another interesting purpose of the next few years could be the utilization of the lasso cavity to host a guest molecule in only one of the two tightened or loosened states. As an example, a drug could be encapsulated by an oligosaccharide-containing lasso only at the loosened state, whereas the *stimulus*-dependent tightened conformation would trigger the releasing of the drug as one could squeeze a sponge to extract a substance. By comparison with cyclodextrins, which are very often used to deliver drugs, they usually release continuously their guest components: The lasso molecular machinery could significantly increase the qualities of a molecules carrier by programming a wisely release. And last, but not limited to, the cavity of the lasso compounds could be utilized as nanoreactors in order to catalyze various reactions in only one of the different conformations of the cavity. For sure, the lasso compounds have not yet given all their promises.

References

1. Kay, E.R., Leigh, D.A., Zerbetto, F.: Synthetic molecular motors and mechanical machines. Angew. Chem. Int. Ed. **46**, 72–191 (2007)
2. Balzani, V., Ceroni, P., Credi, A., Gomez-Lopez, M., Hamers, C., Stoddart, J.F., Wolf, R.: Controlled dethreading/rethreading of a scorpion-like pseudorotaxane and a related macrobicyclic self-complexing system. New J. Chem. **25**, 25–31 (2001)
3. Yamauchi, K., Miyawaki, A., Takashima, Y., Yamaguchi, H., Harada, A.: Switching from altro-α-cyclodextrin dimer to pseudo [1]rotaxane dimer through tumbling. Org. Lett. **12**, 1284–1286 (2010)
4. Yamauchi, K., Miyawaki, A., Takashima, Y., Yamaguchi, H., Harada, A.: A molecular reel: shuttling of a rotor by tumbling of a macrocycle. J. Org. Chem. **75**, 1040–1046 (2010)
5. Ashton, P.R., Ballardini, R., Balzani, V., Boyd, S.E., Credi, A., Gandolfi, M.T., Gomez-Lopez, M., Iqbal, S., Philp, D., Preece, J.A., Prodi, L., Ricketts, H.G., Stoddart, J.F., Tolley, M.S., Venturi, M., White, A.J.P., Williams, D.J.: Simple mechanical molecular and supramolecular machines: photochemical and electrochemical control of switching processes. Chem. Eur. J. **3**, 152–170 (1997)
6. Strutt, N.L., Zhang, H., Giesener, M.A., Lei, J., Stoddart, J.F.: A self-complexing and self-assembling pillar[5]arene. Chem. Commun. **48**, 1647–1649 (2012)
7. Legros V., Vanhaverbeke C., Souard F., Len C., Désiré J.: β-cyclodextrin-glycerol dimers: synthesis and NMR conformational analysis. Eur. J. Org. Chem. **2013**, 2583–2590 (2013)
8. Liu, Y., Yang, Z.-X., Chen, Y.: Synthesis and self-assembly behaviors of the azobenzenyl modified β-cyclodextrins isomers. J. Org. Chem. **73**, 5298–5304 (2008)
9. Miyawaki, A., Kuad, P., Takashima, Y., Yamaguchi, H., Harada, A.: Molecular puzzle ring: pseudo[1]rotaxane from a flexible cyclodextrin derivative. J. Am. Chem. Soc. **130**, 17062–17069 (2008)
10. Hiratani, K., Kaneyama, M., Nagawa, Y., Koyama, E., Kanesato, M.: Synthesis of [1]rotaxane via covalent bond formation and its unique fluorescent response by energy transfer in the presence of lithium ion. J. Am. Chem. Soc. **126**, 13568–13569 (2004)
11. Franchi, P., Fani, M., Mezzina, E., Lucarini, M.: Increasing the persistency of stable free-radicals: synthesis and characterization of a nitroxide based [1]rotaxane. Org. Lett. **10**, 1901–1904 (2008)
12. Ma, X., Wang, Q., Tian, H.: Disparate orientation of [1]rotaxanes. Tetrahedron Lett. **48**, 7112–7116 (2007)
13. Zhu, L., Yan, H., Zhao, Y.: Cyclodextrin-based [1]rotaxanes on gold nanoparticles. Int. J. Mol. Sci. **13**, 10132–10142 (2012)
14. Tsuda, S., Terao, J., Kambe, N.: Synthesis of an organic-soluble π-conjugated [1]rotaxane. Chem. Lett. **38**, 76–77 (2009)
15. Rowan, S.J., Cantrill, S.J., Stoddart, J.F., White, A.J.P., Williams, D.J.: Toward daisy chain polymers: "Wittig exchange" of stoppers in [2]rotaxane monomers. Org. Lett. **2**, 759–762 (2000)
16. Xue, Z., Mayer, M.F.: Actuator prototype: capture and release of a self-entangled [1]rotaxane. J. Am. Chem. Soc. **132**, 3274–3276 (2010)
17. Gibson, H.W., Lee, S.-H., Engen, P.T., Lecavalier, P., Sze, J., Shen, Y.X., Bheda, M.: New triarylmethyl derivatives: "blocking groups" for rotaxanes and polyrotaxanes. J. Org. Chem. **58**, 3748–3756 (1993)
18. Jiménez, M.C., Dietrich-Buchecker, C., Sauvage, J.-P.: Towards synthetic molecular muscles: contraction and stretching of a linear rotaxane dimer. Angew. Chem. Int. Ed. **39**, 3284–3287 (2000)
19. Jimenez-Molero, M.C., Dietrich-Buchecker, C., Sauvage, J.-P.: Chemically induced contraction and stretching of a linear rotaxane dimer. Chem. Eur. J. **8**, 1456–1466 (2002)
20. Dietrich-Buchecker, C., Sauvage, J.-P., Kern, J.-M.: Templated synthesis of interlocked macrocyclic ligands: the catenands. J. Am. Chem. Soc. **106**, 3043–3045 (1984)

21. Onagi, H., Blake, C.J., Easton, C.J., Lincoln, S.F.: Installation of a ratchet tooth and pawl to restrict rotation in a cyclodextrin rotaxane. Chem. Eur. J. **9**, 5978–5988 (2003)
22. Okuno, E., Hiraoka, S., Shionoya, M.: A synthetic approach to a molecular crank mechanism: toward intramolecular motion transformation between rotation and translation. Dalton Trans. **39**, 4107–4116 (2010)
23. Ma, X., Qu, D., Ji, F., Wang, Q., Zhu, L., Xu, Y., Tian, H.: A light-driven [1]rotaxane via self-complementary and Suzuki-coupling capping. Chem. Commun. 1409–1411 (2007)
24. Gao, C., Ma, X., Zhang, Q., Wang, Q., Qu, D., Tian, H.: A light-powered stretch-contraction supramolecular system based on cobalt coordinated [1]rotaxane. Org. Biomol. Chem. **9**, 1126–1132 (2011)
25. Coutrot, F., Busseron, E.: A new glycorotaxane molecular machine based on an anilinium and a triazolium station. Chem. Eur. J. **14**, 4784–4787 (2008)
26. Chao, S., Romuald, C., Fournel-Marotte, K., Clavel, C., Coutrot, F.: A strategy utilizing a recyclable macrocycle transporter for the efficient synthesis of a triazolium-based [2]rotaxane. Angew. Chem. Int. Ed. **53**, 6914–6919 (2014)
27. Li, H., Zhang, H., Zhang, Q., Zhang, Q.-W., Qu, D.: A switchable ferrocene-based [1]rotaxane with an electrochemical signal output. Org. Lett. **14**, 5900–5903 (2012)
28. Li, H., Zhang, J.-N., Zhou, W., Zhang, H., Zhang, Q., Qu, D., Tian, H.: Dual-mode operation of a bistable [1]rotaxane with a fluorescent signal. Org. Lett. **15**, 3070–3073 (2013)
29. Chatterjee, M.N., Kay, E.R., Leigh, D.A.: Beyond switches: ratcheting a particle energetically uphill with a compartmentalized molecular machine. J. Am. Chem. Soc. **128**, 4058–4073 (2006)
30. Alvarez-Pérez, M., Goldup, S.M., Leigh, D.A., Slawin, M.Z.: A chemically-driven molecular information ratchet. J. Am. Chem. Soc. **130**, 1836–1838 (2008)
31. Carlone, A., Goldup, S.M., Lebrasseur, N., Leigh, D.A., Wilson, A.: A three-compartment chemically-driven molecular information ratchet. J. Am. Chem. Soc. **134**, 8321–8323 (2012)
32. Kay, E.R., Leigh, D.A.: Beyond switches: rotaxane- and catenane-based synthetic molecular motors. Pure Appl. Chem. **80**, 17–29 (2012)
33. Leigh, D.A., Zerbetto, F., Kay, E.R.: Synthetic molecular motors and mechanical machines. Angew. Chem. Int. Ed. **46**, 72–191 (2007)
34. Busseron, E., Coutrot, F.: *N*-benzyltriazolium as both molecular station and barrier in [2] rotaxane molecular machines. J. Org. Chem. **78**, 4099–4106 (2013)
35. Clavel, C., Romuald, C., Brabet, E., Coutrot, F.: A pH-sensitive lasso-based rotaxane molecular switch. Chem. Eur. J. **19**, 2982–2989 (2013)
36. Coutrot, F., Busseron, E., Montero, J.-L.: A very efficient synthesis of a mannosyl orthoester [2]rotaxane and mannosidic [2]rotaxanes. Org. Lett. **10**, 753–757 (2008)
37. Clavel, C., Fournel-Marotte, K., Coutrot, F.: A pH sensitive peptide-containing lasso molecular switch. Molecules **18**, 11553–11575 (2013)
38. Romuald, C., Cazals, G., Enjalbal, C., Coutrot, F.: Straightforward synthesis of a double-lasso macrocycle from a nonsymmetrical [c2]daisy chain. Org. Lett. **15**, 184–187 (2013)
39. Romuald, C., Arda, A., Clavel, C., Jiménez-Barbero, J., Coutrot, F.: Tightening or loosening a pH-sensitive double-lasso molecular machine readily synthesized from an ends-activated [c2] daisy chain. Chem. Sci. **3**, 1851–1857 (2012)
40. Rotzler J., Mayor M. (2013) Molecular daisy chains. Chem. Soc. Rev. **42**, 44–62
41. Coutrot, F., Romuald, C., Busseron, E.: A new dimannosyl[c2]daisy chain molecular machine. Org. Lett. **10**, 3741–3744 (2008)
42. Romuald, C., Busseron, E., Coutrot, F.: Very contracted to extended co-conformations with or without oscillations in two- and three-station [c2]daisy chains. J. Org. Chem. **75**, 6516–6531 (2010)
43. Romuald, C.: Des muscles moléculaires dans tous leurs états aux noeuds moléculaires à cavité modulable inédite. Thesis, University of Montpellier 2, Montpellier (2011)

Triptycene or Subphthalocyanine Wheels and Polyaromatic Hydrocarbon Nanovehicles

Henri-Pierre Jacquot de Rouville, Romain Garbage, Agnès M. Sirven, Claire Kammerer and Gwénaël Rapenne

Abstract Technomimetic molecules are molecules designed to imitate macroscopic objects at the molecular level, also transposing the motions that these objects are able to undergo. This chapter focuses on the synthesis and study of molecular wheels, triptycenes and subphthalocyanines, and their introduction into nanovehicles, nanowheelbarrow with two wheels and nanocars equipped with four wheels. The architecture is based on polyaromatic hydrocarbons which provide us with an interesting cargo zone.

Keywords Single molecule · STM · Wheelbarrow · Nanocars · Nanowheels · Polyaromatic hydrocarbons · Triptycene · Subphthalocyanine

1 Introduction

The extension of the concept of a machine to the molecular level is important not only for basic research but also for the growth of nanoscience and nanotechnology. In the last decade, chemists have demonstrated imagination and skill in the design and synthesis of synthetic molecular systems acting as machines at the molecular level [1]. A molecular machine can be defined as a molecule for which a certain part can be set into a controlled motion as a consequence of an appropriate external stimulus [2].

Nanovehicles are molecular machines basically composed of a chassis and wheels [3], typically one or two for a barrow [4], four for a nanocar [5], or more for nanotrucks and nanotrains [6]. Another aspect is the options you can also add to these simple units, the more important being an internal source of energy such as a

H.-P. Jacquot de Rouville · R. Garbage · A.M. Sirven · C. Kammerer · G. Rapenne (✉)
CEMES-CNRS, NanoSciences Group and MANA Satellite, 29 rue Jeanne Marvig, BP 94347, 31055 Toulouse Cedex 4, France

H.-P. Jacquot de Rouville · R. Garbage · C. Kammerer · G. Rapenne
Université de Toulouse, UPS, 118 route de Narbonne, 31062 Toulouse Cedex 9, France

C. Joachim and G. Rapenne (eds.), *Single Molecular Machines and Motors*,
Advances in Atom and Single Molecule Machines, DOI 10.1007/978-3-319-13872-5_4

motor to gain autonomy or a cargo zone to be able to transport nanoloads such as atoms or small molecules on surfaces on a long scale.

In order to build such nanovehicle, the choice of the wheel is a very important parameter. It must allow the entire functionalized molecule to move easily on the surface by its rolling motion. As pioneers in the field, we proposed triptycene [7] to act as rolling elements (wheels) [8] and synthesized the first nanovehicle [9], while two years later, Tour's group joined the field and prepared a family of nanovehicles [10] consisting of a molecular-scale chassis, axles, and wheels ([60]-fullerenes at that time) that can roll across solid surfaces. This chapter presents the main results we obtained from the first direct proof of the rolling motion of a wheel, their introduction in two- or four-wheel nanovehicles, to the synthesis of second generation of wheels which are bowl-shaped to minimize their interaction with the surface.

2 Rotation of a Triptycene Wheel by STM Tip Pushing

On a surface, the mechanical motion of a single molecule is essentially classical due to the reservoir role of the surface. Any collective motions of certain atoms subsets in a single molecule require a specific preparation of the molecule. Pushing on a molecule with a tip apex is a convenient way adapted to the classical motion we are looking for. To prove the ability of the triptycene fragment to act as a wheel at the nanoscale, we designed an axle to be able to link two wheels. The butadiyne linker being a good candidate [11] since it allows almost a free rotation of the fragments attached combined with a linear geometry.

2.1 A Bis(ethynyltriptycene) as Prototype of a Wheel Dimer

Triptycene [7] is a very interesting building block since its symmetry and rigidity could be exploited on surfaces. Several examples of molecular devices not developed in this article have been reported where the key fragment is one or more triptycenes, such as molecular gears [12, 13], motors [14], gyroscopes [15, 16], and brakes [17, 18]. Synthesis of the 9-ethynyltriptycene wheel **1** can be performed in three steps from commercial 9-bromoanthracene by a modified published procedure [4] as shown in Scheme 1. The procedure involves the coupling of 9-bromoanthracene with a monoprotected alkyne followed by a [4 + 2] addition of benzyne (prepared in situ by reaction of anthranilic acid with isopentylnitrite) and deprotection of the silyl group. The use of a (3-cyanopropyl)dimethylsilyl protecting group, a polar analog of trimethylsilyl [19], allowed the easy separation of triptycene **1** obtained after reaction with benzyne, from the starting unreacted anthracene.

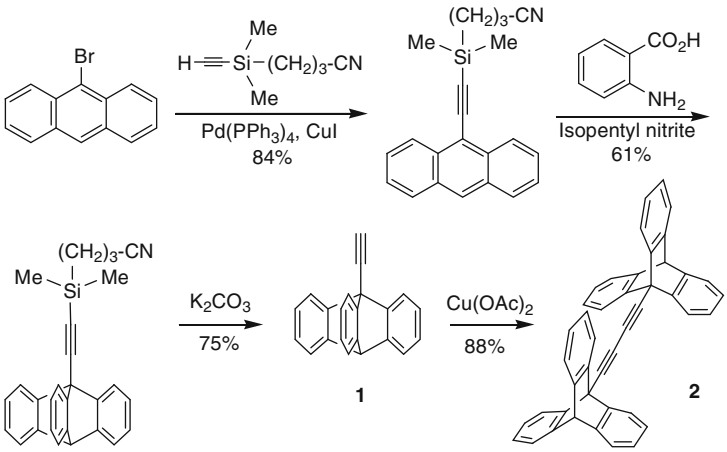

Scheme 1 Synthesis of the bis(ethynyltriptycene) wheel dimer

The Glaser homocoupling of the 9-ethynyltriptycene wheel **1** using copper(II) acetate gave the dimer of wheel with a butadiyne spacer (**2**). This model compound has been studied as prototype of a wheel dimer.

2.2 Clean Deposition on a Cu(110) Surface

Deposition of the wheel dimer **2** on a Cu(110) surface has been achieved very cleanly by sublimation under high vacuum [20]. Figure 1 shows the image obtained; each bright lobe corresponds to one triptycene, and therefore, a pair of lobe constitutes the image of a dimer as confirmed by calculations. No fragmentation nor decomposition has been observed. Molecules were deposited at room temperature. First, they saturated the step-edges and then were adsorb isolated on terraces.

2.3 Unidirectional Rotation of the Wheel

By working at low temperature under ultra-high vacuum, it was possible to prove the rotation of a wheel, for the first time, on a surface by inducing the translation of the molecule with a step-by-step rotation of the wheels upon pushing with the STM tip [20]. In order to understand the motion of this molecule in detail, it has been important to study the manipulation signal, i.e., tunneling current at constant tip height during the motion, because the STM images before and after manipulation do not give information about the type of movement in between.

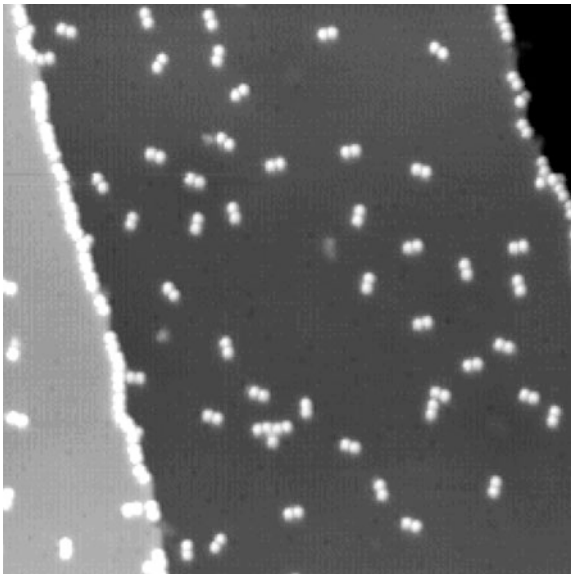

Fig. 1 Image of the dimer of wheels (**1**) on a Cu(110) surface (50 × 50 $nm^{2,}$ U = 1 V, I = 0.2 nA)

The tip was moved across the molecular axle at constant height, while the tunneling current was recorded at the same time. A "hat-shaped" signal appears which has been assigned to a rolling motion of the molecular wheels. Typically, the wheel-dimer molecules are not moved far on the surface if a rolling signal is recorded and one wheel is left in its initial position while the other one moves. In few cases, it has been observed the rolling of both wheels. This behavior seems to depend on the precise shape of the tip apex, allowing access to both wheels during manipulation (Fig. 2).

This dimer of triptycene linked to an axle was the first designed wheel to yield rotation upon pushing of the wheels using the STM tip. It must be noted that pushing a molecule on a surface with an STM tip necessarily induces a form of unidirectional rotation controlled by the tip apex motion. This directionality can be

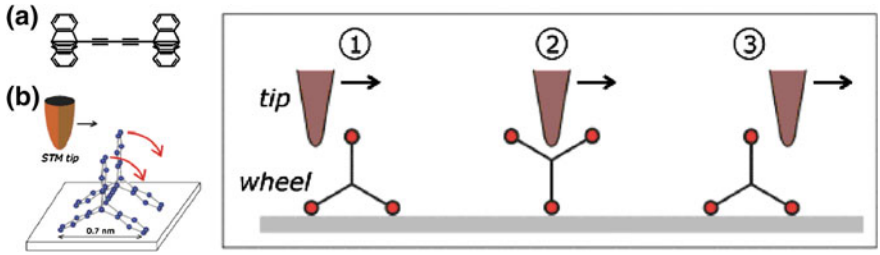

Fig. 2 **a** Molecular axle equipped with two triptycene wheels and **b** rotational motion: step 1: the STM tip approaches the molecule; step 2: the rotation of the wheel starts; step 3: the STM tip lies on the other side of the wheel after a 120° rotation

perturbed by the surface corrugation which imposes its own directionality controlled by the various stable adsorption energy locations of the molecule on the surface.

3 Two-wheel Nanovehicles: Molecular Wheelbarrows

This result opens the way to more complex molecules designed to be capable to undergo simultaneously translation and rotation motions. With this aim in view, we designed a molecular wheelbarrow as a further step toward the development of nanomachines displaying complex functionalities at the atomic scale. We synthesized two prototypes of molecular wheelbarrows, undertaken following a modular strategy which allows to vary the key parts of the molecule, in particular the region which will be in contact with the tip of the STM during the manipulation of the molecule.

3.1 Design

The first example ever of synthesized nanovehicle was the molecular wheelbarrow composed of a platform, two wheels and two legs [9]. In the case of a macroscopic wheelbarrow, pushing the wheelbarrow results in the rotation of the wheel. In Fig. 3, a molecular analog of a wheelbarrow is shown. Its skeleton is made of polycyclic aromatic hydrocarbons (PAHs) that, due to their rigidity, are easily manipulated by the STM tip. The wheelbarrow is constituted of two legs (3,5-di-*tert*-butylphenyl groups, in green) and two wheels (ethynyltriptycene groups, in red) connected to a polycyclic aromatic hydrocarbon platform.

The two 3,5-di-*tert*-butylphenyl legs (in green) which equip the left side of the molecule were shown to be held in a conformation in which the phenyl groups are

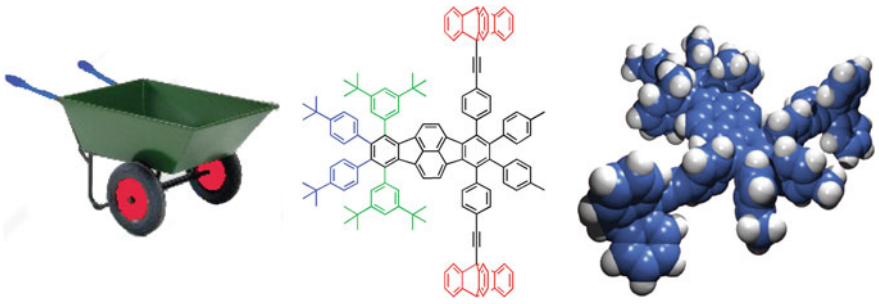

Fig. 3 Chemical structure of a molecular wheelbarrow (*center*), space-filling model showing the minimum energy conformation of the molecular analog (*right*), and its macroscopic analog (*left*)

nearly perpendicular to the main aromatic board. Moreover, *tert*-butyl groups connected to PAHs are also used to increase organic solubility and are easily observed by STM techniques, inducing a good contrast in the image. The two 4-*tert*-butylphenyl groups (in blue) play the role of handles for subsequent manipulation with the tip of the microscope. The right side corresponds to the axle with two 9-triptycenyl groups of C_3 symmetry acting as wheels (in red). Figure 5 (*right*) shows one of the possible conformations of this molecule obtained by semiempirical calculation with the two three-cogged wheels which can freely rotate around the axle due to the acetylenic spacers.

3.2 Synthesis

The synthesis of the molecular wheelbarrow has been achieved in 12 steps and an overall yield of 2 % [9]. As shown on Scheme 2, our strategy used the repetition of a double Knœvenagel–Diels–Alder reaction sequence on an α-diketo fragment. The first sequence allows the connection of the two 3,5-di-*tert*-butylphenyl legs, while the second sequence provides the precursor for wheels connection. For that purpose, we selected 1,3-di(4-iodophenyl)propan-2-one to introduce iodine centers via a double Knœvenagel condensation. Finally, a double Sonogashira coupling yields the molecular wheelbarrow.

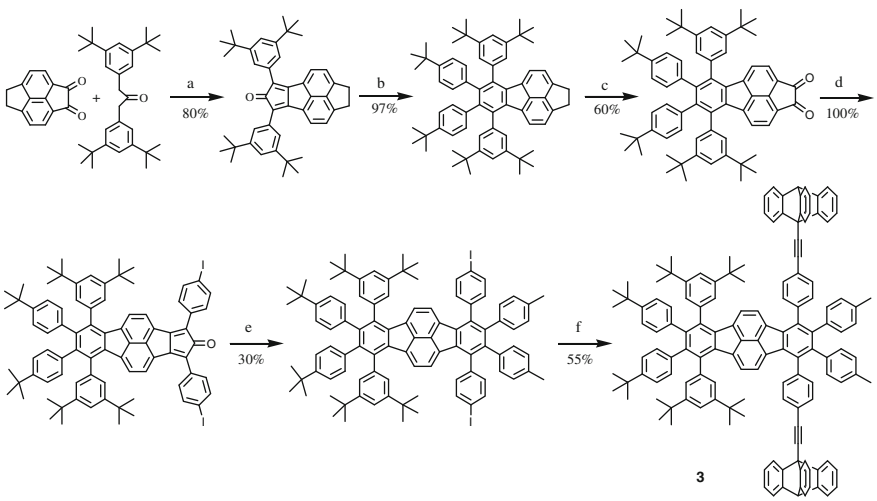

Scheme 2 Synthesis of a molecular wheelbarrow: *reagents and conditions*: **a** EtOH, 20 h, Ar, 20 °C; **b** di(4-*tert*-butylphenyl)acetylene, diphenylether, 16 h, Ar, reflux; **c** $(C_6H_5SeO)_2O$, chlorobenzene, 62 h, Ar, reflux; **d** 1,3-di(4-iodophenyl)propan-2-one, KOH, EtOH, Ar, reflux; **e** di(4-tolyl)acetylene, diphenylether, 16 h, Ar, reflux; **f** 9-ethynyltriptycene, $Pd(PPh_3)_4$ 10 mol%, CuI 20 mol%, Piperidine-THF (1:1), 24 h, Ar, 20 °C, 46 %

The starting cyclopentadienone was obtained via a first double Knœvenagel reaction of 1,3-bis(3,5-di-*tert*-butylphenyl)propan-2-one with diketopyracene (step a). The Diels–Alder reaction of the cyclopentadienone with di(4-*tert*-butylphenyl) acetylene (step b) provided an ethane-bridged precursor with a 97 % yield. The ^{1}H-NMR spectrum clearly showed the 2:1 ratio between the different types of *tert*-butyl groups. Oxidation of the ethane bridge of the pyracene fragment with benzeneseleninic anhydride (step c) yielded the diketo fragment necessary for the connection of the second axle. This is the key step of our strategy. Halogens are introduced at this stage for subsequent coupling in order to connect the triptycene wheels. The following double Knœvenagel condensation with 1,3-di(4-iodophenyl)propan-2-one (step d) followed by another Diels–Alder reaction with di(4-tolyl)acetylene provided the diiodo precursor with 30 % yield (step e). The two wheels were then simultaneously covalently attached to the axle by a double coupling of 9-ethynyltriptycene under classical Sonogashira conditions (step f). The double coupling afforded the molecular wheelbarrow **3** in 46 % yield.

Interaction between the STM tip and the molecule is a key issue that is why it is interesting to prepare wheelbarrows with different handles. With our modular strategy, this is possible to vary the handles by using different dienophile derivatives in step b. For instance, the use of acenaphthylene instead of di(4-*tert*-butylphenyl)acetylene gave access to an alternative wheelbarrow (**4**) with a more rigid and aromatic handle fragment (Fig. 4).

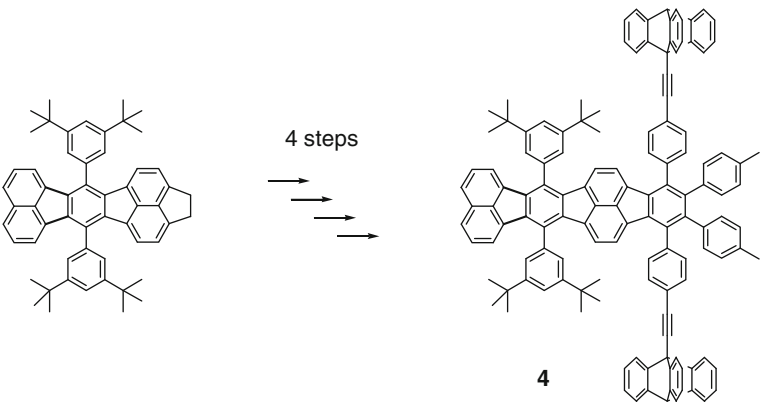

Fig. 4 Alternative wheelbarrow with different handles

3.3 Deposition and STM Study as a Single Molecule

Such a molecular-scale machine inevitably displays a high level of complexity due to the integration of several functionalities on the same molecule. This complexity is reflected in the relatively large molecular weight of the wheelbarrow

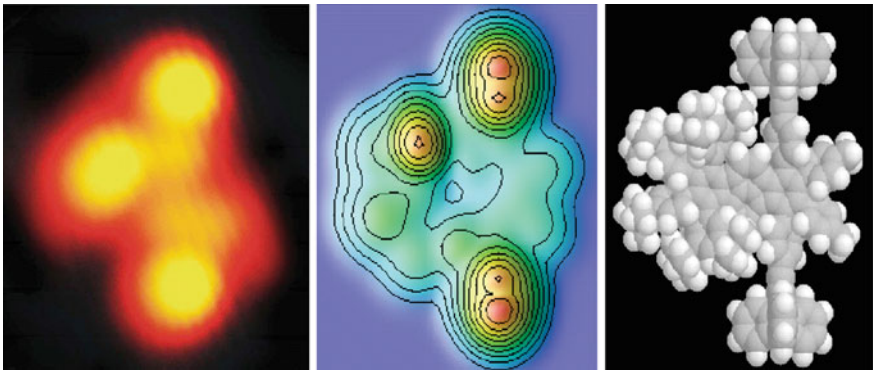

Fig. 5 Experimental STM image of the molecular wheelbarrow on Cu(100) (*left*) and the molecular conformation (*right*) corresponding to the ESQC calculated image (*center*)

(1,802 g·mol^{-1}), which is a general problem for the deposition of large molecules due to the possibility of thermal fragmentation. In the present case, the required linear wheel axle includes two thermally sensitive triple bonds. However, we successfully imaged a few intact molecular wheelbarrows on a Cu(100) surface as shown in Fig. 5 and identified by comparison with calculated images [21]. As expected for such a complex chemical structure, it leads to a rather complicated STM image, dominated by three intense maxima separated by various weaker structures. Because of the characteristic dimensions and the equivalency of different molecules in the STM images, it is very likely that intact molecular wheelbarrows have been imaged.

Manipulation resulted in a change of conformation of the molecule which confirmed us the molecularity of the object observed, the spots observed are not an assembly of fragments. Unfortunately, lateral motion of the wheelbarrow was not possible. This was explained by a very strong interaction between the molecule and the metallic surface of copper used in our experiments especially due to the deformation of the triptycene wheels which tend to strongly physisorb by parallelization of the two phenyl rings close to the surface. The initial angle of 120° between two phenyl rings of the triptycene in the gas phase approached 140° on a copper surface.

4 Alternative Wheels: The Subphthalocyanines

4.1 How to Decrease the Molecule-surface Interaction

To obtain movable molecules, we designed, synthesized, and imaged a new family of nanowheels, the subphthalocyanines which combine the strong rigidity of their backbone with a low interaction with the surface. Molecule-surface interaction is

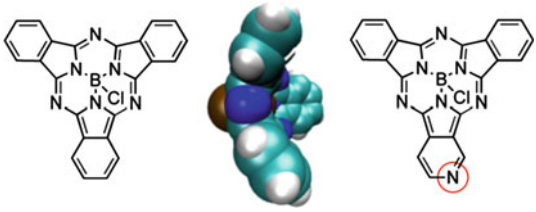

Fig. 6 Chemical structure of a subphthalocyanine (*left*), side view of the CPK model showing its bowl-shaped structure (*center*), and the tagged subphthalocyanine (*right*)

particularly important when the aromatic fragments can be parallel to the metallic surface by deformation of the molecule but thanks to a bowl-shaped structure and their orthogonal connection which bring impossible to have them parallel with the surface [22]. Therefore, combining a strong rigidity and a low affinity for the surface should facilitate a rolling motion of the wheel.

In our design, we also added a tag to be able to directly follow the rolling motion of the wheel just by imaging the molecule [23], while it was only previously possible by a fine study of the variation of the time dependant variations of tunneling electric current intensity passing from the tip to the surface through the pushed molecule during its manipulation.

As shown in Fig. 6, the first nanowheel is symmetric while the second one integrates a tag on one of the three subunits (an additional nitrogen atom on the periphery of the molecule). The molecular modeling also presents the curvature of this building block.

4.2 Synthesis of Symmetric and Dissymmetric Subphthalocyanines

Reaction of 1,2-dicyanobenzene with boron trichloride in a two-phase system composed of a 1:1 mixture of *o*-xylene and hexane gave the boron subphthalocyanine chloride symmetric wheel (Scheme 3, X=CH) [22]. The dissymmetrized wheel (Scheme 3, X=N) was synthesized following a statistical reaction. Two equivalents of 1,2-dicyanobenzene were reacted in the presence of boron trichloride with one equivalent of 3,4-dicyanopyridine.

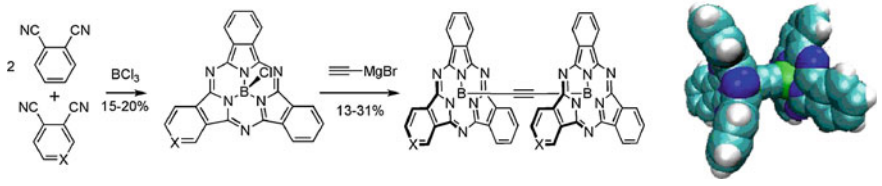

Scheme 3 Synthesis of the symmetric (X=CH) or tagged subphthalocyanine (X=N) and formation of the axle equipped with two tagged wheels; the CPK model illustrates the curvature of the wheels

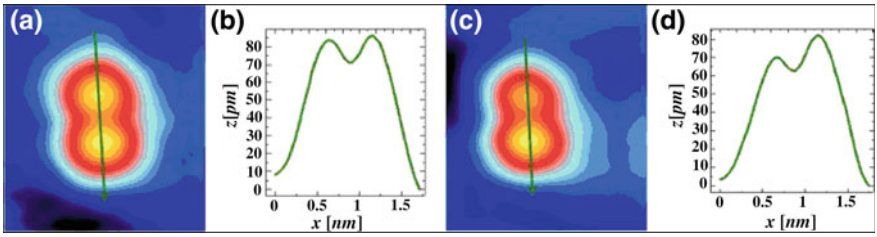

Fig. 7 STM images of the dimer of tagged nanowheels on Au(111) with both tags up (**a**) and only one tag up (**c**) (2.25 × 2.5 nm^2, $V = 0.12$ V, $I = 20$ pA). When the tag is down, the wheel appears as a smaller lobe. The *vertical line* indicates the direction of the linescans in (**b**) and (**d**)

Synthesis of the dissymmetrized wheel dimers bridged by an acetylene spacer was achieved in a single step by reaction of the wheel with ethynylmagnesium bromide. After chromatography, the 2-wheel equipped axle was obtained as a dark purple solid. Surprisingly, both carbon atoms of ethynylmagnesium bromide reacted in a one-pot fashion, allowing the formation of the dimers in a single step, while a two-step process was initially envisaged.

4.3 Deposition and STM Study as a Single Molecule

STM images of the molecule recorded at low temperature in ultra-high vacuum displayed two types of conformation of the wheels (Fig. 7). There is a large difference between a wheel with the tag up and a wheel with the tag down. The former one appears with a larger lobe compared to the latter. This asymmetry, as anticipated by our ESQC STM image calculations [13], corresponds to different positions of the nitrogen tags. In Fig. 7a, both tags are pointing up, whereas in Fig. 7c, one of the tags is pointing down.

Due to the efficiency of the tag, LT-UHV STM imaging has proven sufficient to identify the conformation of the wheels on the surface and is thus expected to be sufficient to prove the rotation in future nanovehicles equipped with such subphthalocyanine wheels.

5 Four-wheel Nanovehicles: Molecular Nanocars

5.1 Design

The next step has been to synthesize nanovehicles with four wheels, i.e., the nanocars [5]. For this purpose, we have developed the synthesis of a larger chassis, compared to the wheelbarrow, to be able to sterically accommodate the four wheels

on the same molecular structure. For this purpose, our nanocars have been built around a perylene chassis.

5.2 Synthesis of a Nanovehicle

As shown on Scheme 4, our strategy starts from the synthesis of di(4-iodophenyl) cyclopentadienone which has been obtained from a double Knœvenagel reaction between acenaphthenequinone and 1,3-di(4-iodophenyl)propan-2-one under basic conditions (step a). Then, a Diels–Alder reaction with 1,2-di(3,5-di-*tert*-butylphenyl)ethyne gave, after aromatization by evolution of carbon monoxide, the half-chassis (step b) which was dimerized following a Scholl-type oxidative coupling using $FeCl_3$ as oxidant (step c).

Unfortunately, our methodology did not allow us to connect the subphthalocyanine wheels. In a last step, the chassis was equipped with four ethynyltriptycenyl wheels to yield our first prototype of nanocar. Again, the triptycenyl wheels were covalently attached on this platform through ethynyl spacers to ensure a very low rotation barrier [11]. As a consequence, like in the case of molecular wheelbarrows, nanocars equipped with triptycene wheels will be unable to move because of the strong physisorption of the triptycene groups on metallic surfaces. But to overcome

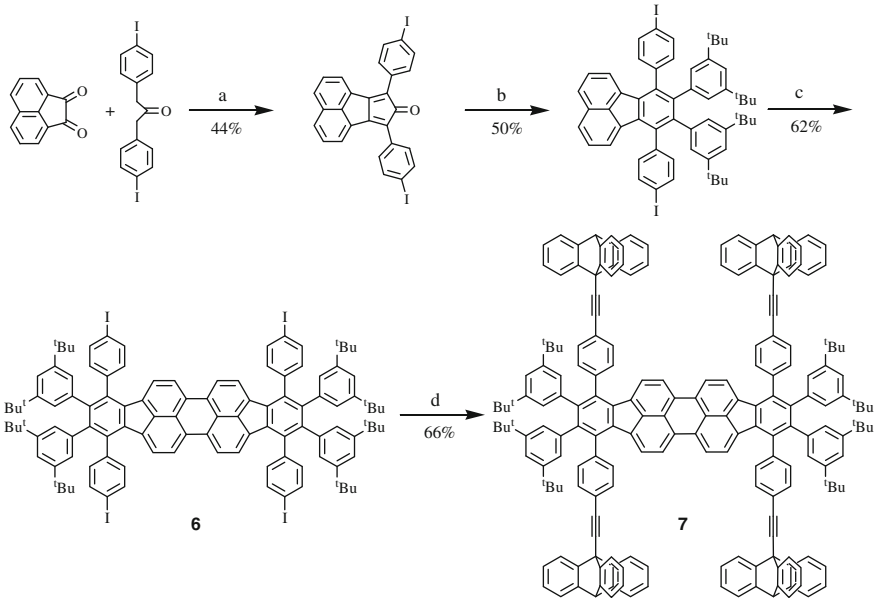

Scheme 4 Synthesis of a nanocar. **a** KOH, RT, 2 h, Ar; **b** 1,2-di(3,5-di-*tert*-butylphenyl)ethyne, Ph_2O, 250 °C, MW (300 W), 45 min; **c** $FeCl_3$ 25 eq, CH_2Cl_2: CH_3NO_2 (9:1), Ar; **d** 9-ethynyltriptycene 10 eq, $Pd(PPh_3)_4$ 10 %, CuI 20 %, piperidine: THF (1:1), 80 °C, 6 h, Ar

this problem, we are currently exploring the potentiality of semi-conducting surfaces such as SmSi or SiB, where the triptycene fragments have shown to be easily movable in a controlled way [24, 25]. These semi-conducting surfaces are potentially very interesting, since the study can be performed at room temperature. This is very important to start to develop practical applications.

5.3 Synthesis of Different Polyaromatic Chassis

To improve the cargo zone of our chassis, we also explored the formation of curved chassis. Using the same synthetic scheme as before which allowed us to obtain planar chassis (Scheme 4), we replaced 3,5-di-*tert*-butylphenyl fragments by 4-*tert*-butylphenyl building blocks. In this case, dimerization of the half-chassis following the same Scholl-type oxidative coupling gave an overcyclized perylene platform bearing six additional C–C bonds (**8**) shown in bold on Scheme 5.

A geometry optimization showed that this overcyclized chassis has a curved shape at both extremities (Fig. 8). This specificity is of interest, since it provides an

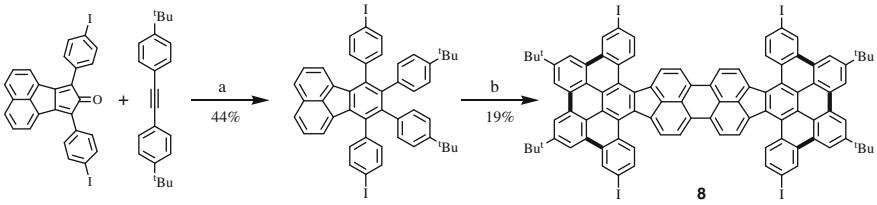

Scheme 5 Synthesis of a new curved polyaromatic platform. **a** Ph_2O, 260 °C, microwaves (300 W), 45 min; **b** $FeCl_3$ 25 eq, CH_2Cl_2: CH_3NO_2 (9:1), RT, 15 min Ar. The additional unexpected carbon–carbon bonds obtained are highlighted in *bold*

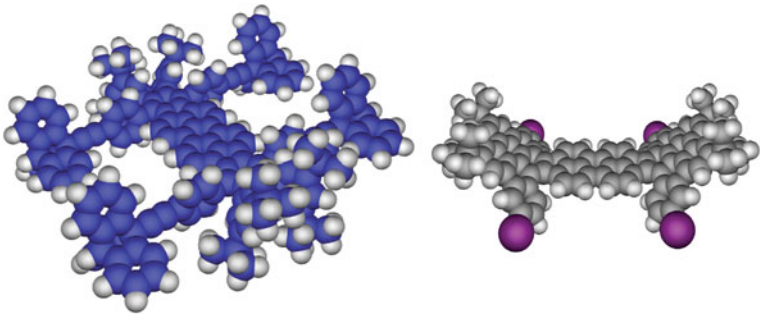

Fig. 8 Chemical structure of nanocar **7** with a planar chassis (*left*) and side view of the optimized geometry of the overcyclized tetraiodinated precursor **8** showing the curvature of the polyaromatic fragment (*right*)

appropriate shape to act as cargo zone. As in fullerenes, this geometry can be simply explained by the presence of alternating five- and six-membered rings in the polycyclic aromatic hydrocarbon platform. The last step consisted to connect the four triptycene wheels via a quadruple Sonogashira coupling and successfully formed the corresponding nanovehicle in 34 % yield.

6 Conclusion and Perspectives

In summary, we have presented the design and the synthesis of polyaromatic hydrocarbons designed by analogy with macroscopic wheels, wheelbarrows, and nanocars. In terms of synthesis, the next step is now to build more complex architectures such as a nanocar with four wheels or a family of nanotrucks with six to twelve wheels. Since polyaromatic hydrocarbon molecules allow us to transport atoms on a small distance of a few nanometers, we hope that a molecule equipped with wheels will be capable to move atoms or small molecules around over large distances across surfaces, with potentials applications in molecular electronics.

As source of propulsion we are using the tunneling electrons from the STM tip like it has been done very recently to rotate clockwise or anticlockwise a molecular motor [26]. Chemical propulsion from a chemical reaction, the Ring Opening Metathesis Polymerization, has been explored by Tour [27], but the major drawback of this strategy is the generation of waste on the surface. Of course light, without waste and need of nanoconnection (necessary in the case of electrons as energy source), is very attractive and an example has been described recently by Feringa [28]. However, this is very difficult to transform the isomerisation of some enlightened fragment to a controlled motion on a surface.

As perspective, one can imagine to obtain in the future, functional nanovehicles for the world's technological needs. Anyway, there is also a lot to learn on the behavior of single molecules at the nanoscale for the progress of all the fields connecting to nanosciences.

Acknowledgments This work was supported by the CNRS, the Université Paul Sabatier (Toulouse), the Institut Universitaire de France, the European Union and the ANR P3N (AUTOMOL project n°ANR 09-NANO-040). We are also grateful to the researchers who participated in all the work discussed here and whose names appear in the references.

References

1. Balzani, V., Credi, A., Venturi, M.: Molecular Devices and Machines. Concepts and Perspectives for the Nanoworld, 2nd edn. Wiley-VCH, Weinheim (2008)
2. Rapenne, G.: Synthesis of technomimetic molecules: towards rotation control in single molecular machines and motors. Org. Biomol. Chem. **3**, 1165 (2005)

3. Joachim, C., Moresco, F., Rapenne, G.: Molecule concept-nanocars: chassis, wheels and motors? ACS Nano **7**, 11 (2013)
4. Rapenne, G., Jimenez-Bueno, G.: Molecular machines: synthesis and characterization of two prototypes of molecular wheelbarrows. Tetrahedron **63**, 7018 (2007)
5. Jacquot de Rouville, H.-P., Garbage, R., Cook, R.E., Pujol, A.R., Sirven, A.M., Rapenne, G.: Synthesis of polycyclic aromatic hydrocarbon-based nanovehicles equipped with triptycene wheels. Chem. Eur. J. **18**, 3023 (2012)
6. Vives, G., Tour, J.M.: Synthesis of single-molecule nanocars. Acc. Chem. Res. **42**, 473 (2009)
7. Chen, C.-F., Ma, Y.-X.: Iptycenes Chemistry: From Synthesis to Applications. Springer, Berlin (2013)
8. Joachim, C., Moresco, F., Rapenne, G., Meyer, G.: The design of a nanoscale molecular barrow. Nanotechnology **13**, 330 (2002)
9. Jimenez-Bueno, G., Rapenne, G.: Technomimetic molecules: synthesis of a molecular wheelbarrow. Tetrahedron Lett. **44**, 6261 (2003)
10. Shirai, Y., Osgood, A.J., Zhao, Y., Kelly, K.F., Tour, J.M.: Directional control in thermally driven single-molecule nanocars. Nano Lett. **5**, 2330 (2005)
11. Toyota, S.: Rotational isomerism involving acetylene carbon. Chem. Rev. **110**, 5398 (2010)
12. Chance, J.M., Geiger, J.H., Mislow, K.: A parity restriction on dynamic gearing immobilizes the rotors in tris(9-triptycyl)germanium chloride and tris(9-triptycyl)cyclopropenium perchlorate. J. Am. Chem. Soc. **111**, 2326 (1989)
13. Frantz, D.K., Linden, A., Baldridge, K.K., Siegel, J.S.: Molecular spur comprising triptycene rotators and bibenzimidazole-based stators. J. Am. Chem. Soc. **134**, 1528 (2012)
14. Kelly, T.R., Silva, H.D., Silva, R.A.: Unidirectional rotary motion in a molecular system. Nature **401**, 150 (1999)
15. Godinez, C.E., Zepeda, G., Garcia-Garibay, M.A.: Molecular compasses and gyroscopes. Synthesis and characterization of molecular rotors with axially substituted bis[2-(9-triptycyl) ethynyl]arenes. J. Am. Chem. Soc. **124**, 4701 (2002)
16. Lemouchi, C., Vogelsberg, C.S., Zorina, L., Simonov, S., Batail, P., Brown, S., Garcia-Garibay, M.A.: Ultra-fast rotors for molecular machines and functional materials via halogen bonding: crystals of 1,4-bis(iodoethynyl)bicyclo[2.2.2]octane with distinct gigahertz rotation at two sites. J. Am. Chem. Soc. **133**, 6371 (2011)
17. Kelly, T.R., Sestelo, J.P., Tellitu, I.: New molecular devices: in search of a molecular ratchet. J. Org. Chem. **63**, 3655 (1998)
18. Nikitin, K., Bothe, C., Muller-Bunz, H., Ortin, Y., McGlinchey, M.J.: Rational design of molecular brakes. Organometallics **31**, 6183 (2012)
19. Höger, S., Bonrad, K.: 3-Cyanopropyldimethylsilylacetylene, a polar analogue of trimethylsilylacetylene: synthesis and applications in the preparation of monoprotected bisacetylenes. J. Org. Chem. **65**, 2243 (2000)
20. Grill, L., Rieder, K.H., Moresco, F., Rapenne, G., Stojkovic, S., Bouju, X., Joachim, C.: Rolling a single molecular wheel at the atomic scale. Nat. Nanotechnol. **2**, 95 (2007)
21. Grill, L., Rieder, K.H., Moresco, F., Jimenez-Bueno, G., Wang, C., Rapenne, G., Joachim, C.: Imaging of a molecular wheelbarrow by scanning tunneling microscopy. Surf. Sci. **584**, 153 (2005)
22. Jacquot de Rouville, H.-P., Garbage, R., Ample, F., Nickel, A., Meyer, J., Moresco, F., Joachim, C., Rapenne, G.: Synthesis and STM imaging of symmetric and dissymmetric ethynyl-bridged dimers of boron-subphthalocyanine bowl-shaped nano-wheels. Chem. Eur. J. **18**, 8925 (2012)
23. Nickel, A., Meyer, J., Ohmann, R., Jacquot de Rouville, H.-P., Rapenne, G., Joachim, C., Cuniberti, G., Moresco, F.: STM manipulation of boron-subphthalocyanine nano-wheel dimers on Au(111). J. Phys. Condens. Matter **24**, 404001 (2012)
24. Palmino, F., Makoudi, Y., Duverger, E., Arab, M., Chérioux, F., Rapenne, G., Ample, F., Bouju, X.: Self-alignment of organic molecular lines at room temperature by template effect of pre-structured Sm/Si(111)-8x2 interface. Chem. Phys. Chem. **9**, 1437 (2008)

25. Bouju, X., Chérioux, F., Coget, S., Rapenne, G., Palmino, F.: Directional molecular sliding at room temperature on a silicon runway. Nanoscale **5**, 7005 (2013)
26. Perera, U.G.E., Ample, F., Echeverria, J., Kersell, H., Zhang, Y., Vives, G., Rapenne, G., Joachim, C., Hla, S.-W.: Clockwise or counterclockwise unidirectional step-by-step rotation of a single molecular motor. Nat. Nanotechnol. **8**, 46 (2013)
27. Godoy, J., Vives, G., Tour, J.M.: Toward chemical propulsion: synthesis of ROMP propelled nanocars. ACS Nano **5**, 85 (2011)
28. Kudernac, T., Ruangsupapichat, N., Parschau, M., Maci, B., Katsonis, N., Harutyunyan, S.R., Ernst, K.-H., Feringa, B.L.: Electrically driven directional motion of a four-wheeled molecule on a metal surface. Nature **479**, 208 (2011)

The Design of a Single-Molecule Motor

Jorge Echeverria and Christian Joachim

Abstract Several methods have been developed in the last decades to manipulate molecules on surfaces using the tip of a scanning tunneling microscope. Some of those molecules have been designed with the aim of achieving controllable unidirectional motion and, eventually, to generate a motive power and perform work. Single-molecule motors have been mainly inspired by their macroscopic analogous, and their capacity to act as real motors is fairly limited to date. Here, we present some advances in the understanding of molecule motors based on their chemical composition and on their intramolecular electronic characteristics. Thinking of a single-molecule motor as a molecule with specific electronic states and thousands of mechanical degrees of freedom will open the path for the design of new improved and more efficient prototypes.

1 Introduction

A molecular motor is a single molecule able to transform external energy to motive power. On a surface, movement can be linear or rotatory and able to move atomic-scale objects or small molecules at a predetermined location. Up to now, mainly, molecule rotors have been explored expecting that some will eventually demonstrate a motor functioning. It is also a general belief that if a single and small molecule can be put in a random rotation state and stopped at will on a surface, it may be too small in size (or in number of internal degrees of freedom) to drive an external load as compared to a macromolecular motor.

J. Echeverria · C. Joachim (✉)
Groupe Nanoscience, Centre d'Elaboration es Materiaux et D'études Structurales, CNRS, 29 Rue J. Marvig, BP 94347, 31055 Toulouse Cedex, France
e-mail: joachim@cemes.fr

C. Joachim and G. Rapenne (eds.), *Single Molecular Machines and Motors*,
Advances in Atom and Single Molecule Machines, DOI 10.1007/978-3-319-13872-5_5

For a rotating molecule motor to deliver some work alone, a first condition is that it can be driven unidirectionally in a controlled way. One-way rotations have been recently demonstrated with simple molecular structures [1] and with more elaborated molecules where the rotation potential energy profile is independent of the supporting surface and governed mainly by intramolecular interactions. It remains to be determined how adding an atomic-scale load to such a molecular motor will stop its one-way rotation. In this chapter, we gradually discuss how to design a molecular motor. In a first section, we use macroscopic intuition for the design, deviating from it when necessary. In the second section, the different types of molecular dynamics for the rotator are discussed from an ideal coherent quantum behavior to the more useful semi-classical rotational motion. In the third section, the conditions on the rotation potential energy hypersurface of its electronic states are given for a one-way rotation. It is also explained how to maintain the rotation when increasing the motor load. Finally, possible measurements of the motive power of a single-molecule motor will be presented including the use of solid-state nanomechanical devices.

2 The Intuitive Design of a Molecular motor

A rotating molecular motor is made of a rotator, an atomic-scale axle and a stator to be adsorbed on a surface. The surface itself can also play the role of a stator, but it is more interesting that the stator is a rigid chemical group part of the molecular motor and holding the atomic-scale axle as in the example presented in Fig. 1 [2, 3]. In this case, the energetics of the rotation will be controlled intrinsically by the intramolecular

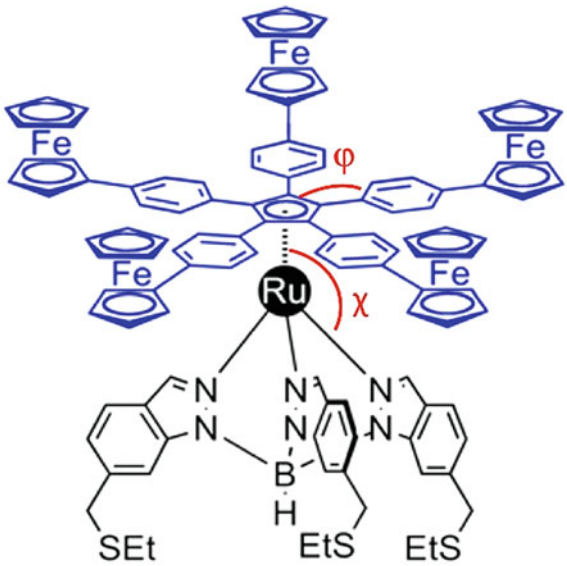

Fig. 1 The detailed chemical structure of a molecular motor. The rotation angle θ is defined along the axis passing through the Ru atom and the centroid of the central phenyl ring. φ is the flipping dihedral angle in one arm of the rotator, and χ is a leg deformation angle

mechanics of the molecular motor itself. This is clearly an advantage to fine-tune the rotator properties independently from the atomic-scale properties of the supporting surface. However, this can also be inconvenient when the atomic-scale object driven by the molecular motor is too small to interact with the top rotator.

Molecular structures like the one presented in Fig. 1 are directly inspired by the known structures of macroscopic motors. However, in terms of structure and static properties, there are notable differences between the two. First, a molecular structure is not a rigid body. Consequently, the relationship between the expected one-way rotation of the top rotator around its atomic-scale axle and the detailed motion of each atom composing the rotator is not quite direct as for example in a macroscopic rigid body benefiting from material cohesion. Second, like any molecules, a molecular motor is characterized by its electronic ground and excited states. This means that the rotator rotation can be controlled, for example, by delivering energy to the ground-state ro-vibrational states, to the excited states, or to a mixing of both playing with the lifetime of the excited states. This spectral characteristic is certainly absent in a macroscopic-scale motor and in a micromotor, and difficult to master in a protein macromolecular motor.

In the Born–Oppenheimer approximation, each molecular motor $E_p(R_1, \ldots, R_n)$ electronic state depends on the detailed vector coordinates $(R_1, \ldots, R_n)$ of all atoms constituting the molecular motor. To track the rotation of the rotator and the eventual deformations of the molecular structure while rotating or loading, one has to perform a coordinate transformation passing from the Cartesian to the so-called internal coordinates of the molecular structure. In that case and, for example, for the Fig. 1 molecular motor, the important coordinate is the θ rotation angle of the rotator. But aside from the θ angle, there are in general 3 sets of internal coordinates to describe the mechanics of a molecular motor: the main intramolecular deformation angles (like the φ and the χ in Fig. 1), the intermediate conformation angles of the rotator, and the stator chemical structure plus also all the interatomic vibration modes of the molecule motor chemical structure. The θ angle plus the main intramolecular conformation angles are in general small in number in comparison with all other intramolecular degrees of freedom.

Generally, there is a tendency in the literature to consider only θ and the ones corresponding to φ and the χ when going from the $E_p(R_1, \ldots, R_n)$ to the internal coordinates Born–Oppenheimer potential energy surfaces. For the Fig. 1 molecular motor, this leads to a $E_p(\theta, \varphi_1, \ldots \varphi_5, \chi_1, \ldots \chi_3)$ potential energy surface depending on nine angles: the top rotor rotation angle θ around the central Ru axis, five flipping angles φ_1 to φ_5 of the five rotor phenyl arms, and three stator legs' deformation angles χ_1 to χ_3. Even with those nine coordinates, the corresponding $E_0(\theta, \varphi_1, \ldots \varphi_5, \chi_1, \ldots \chi_3)$ ground-state potential energy surface is considerably difficult to design and then to master since all the intramolecular mechanisms of the motor will be described by plotting a path on the surface to take into account the change of the selected internal coordinate as a function of θ. When passing from Cartesian to internal coordinates, the coordinate reduction is valid only if during a free rotation of the rotator, there is not so much deformations of its background chemical structure. This approximation will be much more critical for a molecular

motor loaded with a nanoscale load, where the motive power of the motor (if any) will necessarily induce a deformation of its molecular structure when transferring a part of its motion to the load.

Having separated the important and not important internal degrees of freedom to describe the functioning of a molecular motor, the intuitive awaited characteristic of its ground-state potential energy surface is the presence of a ratchet effect when developing the θ rotation trajectory on the surface. For the Fig. 1 molecular motor and starting from one of the possible $E_0(\theta, \varphi_1, \ldots \varphi_5, \chi_1, \ldots \chi_3)$ energy minima, a simple way to characterize this θ rotating trajectory is to increase θ step by step, exclusively clockwise or anticlockwise, while minimizing the molecule motor potential energy for each θ on $E_0(\theta, \varphi_1, \ldots \varphi_5, \chi_1, \ldots \chi_3)$. This delivers a θ parametric rotation trajectory on the $E_0(\theta, \varphi_1, \ldots \varphi_5, \chi_1, \ldots \chi_3)$ manifold. For the Fig. 1 motor, this θ parametric trajectory was calculated using the ASED+ semi-empirical technique [4]. Along this rotation trajectory, the resulting $E_0(\theta)$ potential energy curve for the Fig. 1 motor is highly asymmetric, with a potential barrier height of $\Delta V = 0.25$ eV as presented in Fig. 2. In this case, the combination of the rotor upper C_5 and the stator lower C_3 concurrent symmetries [5] leads to fifteen potential wells per turn. This periodic series of barriers along the θ trajectory is due to the interaction between the 5 phenyl rings of the rotator arms and the three motor legs attached to the metal surface. During the clockwise (or anticlockwise) rotation and every time one arm interacts with one leg, the corresponding phenyl ring flips in order to avoid the leg and the latter is consequently deformed. On the Fig. 2 curve, this results in a ratchet-like potential energy variation.

However, the asymmetry calculated along the rotation trajectory on the ground-state $E_0(\theta, \varphi_1, \ldots \varphi_5, \chi_1, \ldots \chi_3)$ potential energy surface is artificial because it is created by forcing the rotation in a given direction during the step-by-step θ increase. There is no asymmetry when passing from one minimum to the next on $E_0(\theta, \varphi_1, \ldots \varphi_5, \chi_1, \ldots \chi_3)$ and, thus, no breaking of the microreversibility principle. Therefore, by forcing a θ rotation, we are anticipating the good functioning of the molecule motor but not demonstrating it. Therefore, an ideal one-way rotation trajectory was created on $E_0(\theta, \varphi_1, \ldots \varphi_5, \chi_1, \ldots \chi_3)$ by such forced rotation as if the rotor was already rotating one way instead of finding the optimized excitation process to approach such possible "ideal" ratchet-like rotation trajectory.

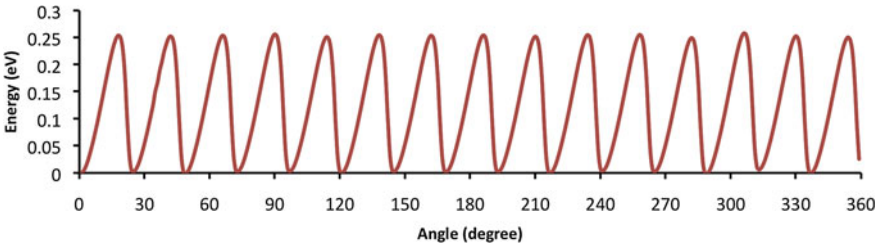

Fig. 2 The asymmetric potential energy profile for a forced rotation of the top rotator of the Fig. 1 molecular motor during a complete 360° turn of the rotator

Since the number of degrees of freedom is generally quite large, the ones to consider, the ones to minimize, and the ones to freeze must be carefully chosen to model the intramolecular mechanics of a molecular motor. To describe the functioning of many molecular motors like the one presented in Fig. 1, at least two degrees of freedom, the θ rotation angle, and a generic torsion angle φ must be considered and not only θ as used to plot the Fig. 2. For example, with the Fig. 1 molecular motor, this torsion angle φ can be defined by the dihedral angle between a given phenyl ring of the rotor and the central cyclopentadienyl ring. In this case, a model $E_0(\theta, \varphi)$ ground-state potential energy surface is constructed to maintain the essential of the mechanical behavior of the motor:

$$E_0(\theta, \varphi) = V_0 \sin^2(\theta/L + \varphi) \cos^2(\theta/L + \varphi) e^{-\varphi^2} + k\varphi^6 \quad (1)$$

where L is the period along the rotation angle. Instead of the fifteen minima of the Fig. 1 molecule motor, the number of minima was limited here to four per turn ($L = 1$) to simplify the analysis. However, the potential (1) can be easily adapted to molecule motors with a different number of arms by simply modifying the value of the period L. During the rotor rotation, the steric repulsion between a rotor phenyl and one of the three stator legs is taken into account in (1) by a φ [6] term (with $k = 5 \times 10^{-3}$ J for the Fig. 1 molecule). V_0 models the energy barrier height and k the strength of the deformation. This $E_0(\theta, \varphi)$ periodic potential energy surface is presented in Fig. 3.

On the $E_0(\theta, \varphi)$ surface and going from one minimum A to one minimum B, there is no symmetry breaking and therefore no native way to favor more the up trajectory in pink that the down one in yellow. A ratchet effect will appear here only when a θ rotation is forced on the potential surface. In this case and following a given rotation direction, the energy variation on the minimized $E_0(\theta, \varphi)$; for example, using the standard nudged elastic band (NEB) method [6] will lead to a θ parametric potential energy curve similar to the one presented in Fig. 2.

In order to provide a net electronic energy to a molecular motor, its $E_p(R_1, \ldots, R_n)$ electronic excited states for $p > 0$ must be involved in the mechanism of

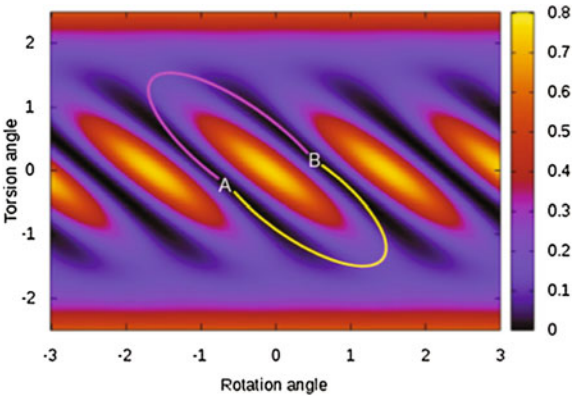

Fig. 3 Potential energy surface given by (1), used to simulate the ground-state $E_0(\theta, \varphi)$ of a molecule motor. The *lateral bar* represents the scale of $E_0(\theta, \varphi)$ in eV for $V_0 = 1$ eV

rotation. Nowadays, their detailed description is still very delicate, especially for molecular structure like the Fig. 1 molecule. In this particular case, we have considered that the first excited states are described by single Slater determinants using several unoccupied monoelectronic molecular electronic states. This leads to a first approximation of the first $E_p(\theta, \varphi_1, \ldots \varphi_5, \chi_1, \ldots \chi_3)$ excited states of the motor. We have also assumed that the coordinate changes from $E_p(R_1, \ldots, R_n)$ to $E_p(\theta, \varphi_1, \ldots \varphi_5, \chi_1, \ldots \chi_3)$ are valid, i.e., that the same internal coordinates can be used for both the ground and these first excited states. Since our goal here is to demonstrate how the excited states can be used to reach unidirectional rotation, the excited states' potential energy surface can be described using the same genuine (θ, φ) internal coordinates as the ground state, using now the corresponding $E_p(\theta, \varphi)$ potential energy surfaces associated with the rotation [7]. For simplicity, we can select (1) for the analytic expression of the first excited-state $E_1(\theta, \varphi)$ and include, for example, a shifting term in the first excited-state $E_1(\theta, \varphi)$ to change the angular position of its minima relative to $E_0(\theta, \varphi)$.

3 Toward a Semi-classical Rotation Dynamics on a Surface

After building a general model for representing the potential energy surfaces of a molecule motor, the next step is to construct its general equations of motion. A preparation of the molecule motor in a coherent non-stationary quantum superposition of states by mixing its ground and some molecule electronic excited states will provide the energy required to drive the rotation [8]. But only one initial preparation in time will not be enough to ensure a regular motion, and not at all enough to bring some motive power. In both cases, the molecular motor will loose very fast its coherence, that is, the coherence of its initial quantum preparation, whatever the precise preparation of the initial ro-vibrational wave packet. The reason is that a preparation of a coherent state of rotation is so delicate that the large number of degrees of freedom of a molecule motor are going to introduce very rapid decoherence processes. Therefore, this preparation has to be cyclic in time and the result of this quantum control will be only measurable by following the quantum-averaged rotation angle $<\theta>$ and the quantum-averaged deformation angle $<\varphi>$. For those two angles used in our molecular motor model, the well-known modulus–argument Madelung decomposition can be used to construct the system of semi-classical dynamic equations of motion:

$$I\frac{\mathrm{d}^2\langle\theta\rangle}{\mathrm{d}t^2} = -\nabla_\theta\left(\sum |c_n(t)|^2 E_n(\theta,\varphi)\right) - \gamma\frac{\mathrm{d}\langle\theta\rangle}{\mathrm{d}t} + F(t)a \tag{2}$$

$$I\frac{\mathrm{d}^2\langle\varphi\rangle}{\mathrm{d}t^2} = -\nabla_\varphi\left(\sum |c_n(t)|^2 E_n(\theta,\varphi)\right) - \gamma\frac{\mathrm{d}\langle\varphi\rangle}{\mathrm{d}t} + F(t)a \tag{3}$$

.

Figure 1 molecular rotor is a good example to provide some order of magnitude for all the parameters appearing in (2) and (3). The rotator can be considered as a disk of mass $m = 600$ amu and of radius $a = 1$ nm leading to an extremely small $I = 10^{-42}$ kg m^2 momentum of inertia with respect to θ. Of course, the Fig. 1 rotor is not a homogeneous disk of matter. However, in this case, considering only the θ rotation angle is a good enough approximation. A friction coefficient $\gamma = 5 \times 10^{-31}$ kg m^2 s^{-1} can be also chosen to run (2) and (3) in an overdamped regime after analyzing the damping behavior of the system. This friction is smaller than the value calculated for a Xe atom sliding on a silver surface [9]. Critically damped and slightly underdamped scenarios have been also tested with similar results. In (3), the momentum of inertia of the rotation along φ is certainly smaller (around 10^{-44} kg m^2) than in (2). However, we have observed by performing a few test calculations that this difference has very little effect on the dynamic behavior of the (2) and (3) equation system, with a small decrease in the final speed of about 2 % by taking a different value. Accordingly, the same value of $I = 10^{-42}$ kg m^2 was used both in (2) and (3). Notice also that we have not taken into account the presence of thermal noise in our model since most of the experiments exploring single-molecule motors on a surface are up to now performed at very low temperature [10].

The coherent non-stationary preparation is described in (2) and (3) by the $c_n(t)$ summation over the $E_n(\theta, \varphi)$ electronic ground and excited states' potential energy surfaces. If the superposition coherence is preserved step by step along the rotation time, a semi-classical motion will result. The motion is based on the multiple potential energy surfaces $E_n(\theta, \varphi)$ employed for the dynamics and according to the $c_n(t)$ amplitudes of the superposition. However, such coherence is very difficult to preserve on the long run even by a very regular repreparation of the superposition. All the $c_n(t)$ for $n > 0$ will progressively decay in time toward the ground state with an average decay rate β. In (2) and (3), the external driving force $F(t)$ is there to sustain a rotation and compensate for decoherence and relaxation.

Considering the $E_0(\theta, \varphi)$ ground state, one $E_1(\theta, \varphi)$ excited state only, and the decay rate β between this first excited and the ground state, a new system of equations can be derived from (2) and (3) to describe the molecule motor dynamics. The new system takes into account the total decoherence of the superposition included in (2) and (3). To construct (4) and (5) below, we have supposed that the $c_n(t)$ quantum amplitude can be substituted by non-quantum beat-like coefficients just preserving their exponential decay time-dependent envelop and renormalizing the relaxation process toward the ground state as compared to the population of the preserved first excited state in the model.

$$I\frac{\mathrm{d}^2\theta}{\mathrm{d}t^2} = \sum_i -(1-\mathrm{e}^{-\beta t})\Gamma(t-t_i)\nabla_\theta E_0(\theta,\varphi) + \sum_i -\mathrm{e}^{-\beta t}\Gamma(t-t_i)\nabla_\theta E_1(\theta,\varphi) - \gamma\frac{\mathrm{d}\theta}{\mathrm{d}t} + \sum_i Fa\Gamma(t-t_i) \tag{4}$$

$$I\frac{d^2\varphi}{dt^2} = \sum_i -(1-e^{-\beta t})\Gamma(t-t_i)\nabla_\varphi E_0(\theta,\varphi) + \sum_i -e^{-\beta t}\Gamma(t-t_i)\nabla_\varphi E_1(\theta,\varphi) - \gamma\frac{d\varphi}{dt} + \sum_i Fa\Gamma(t-t_i) \quad (5)$$

where $\Gamma(t - t_i)$ is a time-shifted step function that permits the force F to act at a given time series t_i and to reset the excited-state preparation with a total depopulation of the ground state. Therefore, there is no more coherence in (4) and (5) between the ground and the excited states than it was in (2) and (3). Notice also that the quantum-averaged rotation angle $<\theta>$ and the quantum-averaged deformation angle $<\varphi>$ are now classical mechanical variables.

4 Conditions for a One-Way Rotation and Motive Power

Before discussing the optimization of the $F(t)$ excitation to drive a rotor, clockwise or anticlockwise, with Eqs. (4) and (5), let us first comment on what happens when the rotor is driven only in its $E_0(\theta, \varphi)$ ground state by a simple external random force $F(t)$. In this case, the systems (4) and (5) simply reduce to the system:

$$I\frac{d^2\theta}{dt^2} = -\nabla_\theta E_0(\theta,\varphi) - \gamma\frac{d\theta}{dt} + F(t)a \quad (6)$$

$$I\frac{d^2\varphi}{dt^2} = -\nabla_\varphi E_0(\theta,\varphi) - \gamma\frac{d\varphi}{dt} + F(t)a. \quad (7)$$

A Gaussian distributed $F(t)$ driving force was applied randomly half of the times on (6) and half of the times on (7). The system (6) and (7) is solved using a Verlet-like algorithm based on the finite differences method. Due to the extremely small I value, much care has been taken to ensure the stability of the numerical solutions. After exploring different friction parameters relative to the average $F(t)$ strength, for finite V_0 value and on the ground-state potential energy surface $E_0(\theta, \varphi)$ given by (1), it was not possible to construct a θ trajectory on the Fig. 3 surface corresponding to a one-way rotation of the rotor even if $F(t)$ is time correlated. In that case, the motion of the system remains chaotic and no net one-way rotation is achieved, as shown in Fig. 4. This fact is in good agreement with the general behavior of Brownian motors, which cannot undergo directed motion even in an anisotropic medium [11]. Notice that if a forced one-way rotation on the Fig. 3 surface would exist, it would produce a parametric $E(\theta)$ potential energy curve as presented in Fig. 2 having a ratchet-like aspect ratio. Such a dimension reduction of the potential energy surface will artificially introduce a ratchet effect, and the 1D dynamical equation driven by the Gaussian $F(t)$ used in this section will lead to an

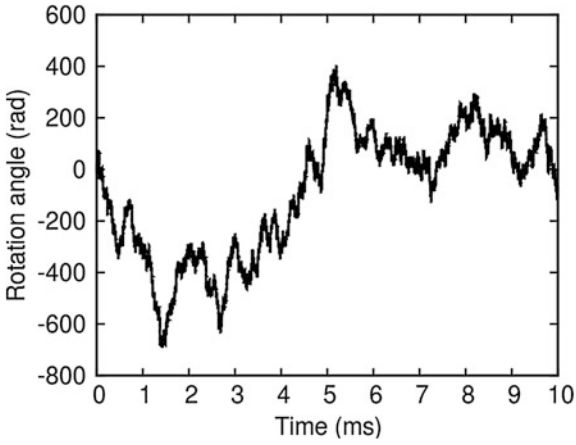

Fig. 4 Chaotic behavior of the single-molecule motor driven by a Gaussian distributed driving force on its ground state and represented by the variation of its rotation angle in time

apparent one-way rotation. However, that is a wrong approximation since what can be called the ratchet angle φ would not be taken into account.

4.1 Driving a One-Way Rotation with a Shot Noise

To drive the rotation of a molecule motor, we consider below the power delivered to the molecular motor by a tunneling current passing through the molecular motor. This requires first to bias the tunneling junction with a voltage in the order of a few volts to reach the excited-state electronic tunneling resonances of the so constituted molecular junction. To target very specific molecular electronic states of the molecule motor, nanoelectrodes ending with an atomic tip apex must be used to be sure that the atoms at the end of those apex are electronically overlapping with specific molecular orbitals of the molecular motor rotor. In such a molecular tunneling junction, the tunneling current intensity through the molecule is the result of billions of electron transfers per second happening at random time. The temperature-independent statistical time distribution of the random process is a Poisson distribution [12]. Its first momentum gives the average tunneling current intensity through the molecule depending on the bias voltage used, whereas its second momentum measures the time fluctuations of this intensity and is characteristic of the shot noise.

The force F during each excitation in (4) and (5) can be constant for all random distributed t_i or also be random in strength, following, for example, a Gaussian distribution. For a tunneling current, the first case is equivalent to consider that each electron transfer event through the molecule is inelastically active. This is certainly not the case in a molecular tunnel junction [12]. Therefore, a Gaussian distribution for F along the random t_i represents better the low efficiency of an inelastic tunneling excitation. By selecting a Poisson time-dependent excitation distribution at t_i,

the energy is provided to the molecular motor by the shot noise. The $E_1(\theta, \varphi)$ excited state is driven here at each time t_i, when a zero-mean Gaussian distributed F is applied to the molecule. Moreover, F must act on θ or φ with an equal probability over time.

Unlike in (6) and (7), where the process is based only on ground-state excitations, a one-way rotation trajectory is now obtained with (4) and (5) using the above-described Poisson noise and with both $E_0(\theta, \varphi)$ and $E_1(\theta, \varphi)$ being fully symmetric in θ and φ. As presented in Fig. 5, the necessary condition for such a rotation is a shift of the $E_1(\theta, \varphi)$ minima relative to the $E_0(\theta, \varphi)$ ones. The rotation stops when there is a coincidence between a $E_1(\theta, \varphi)$ minimum and a $E_0(\theta, \varphi)$ maximum or between the $E_1(\theta, \varphi)$ and $E_0(\theta, \varphi)$ minima. Notice that such behavior was previously reported in another context for the directed transport of Brownian particles in a double symmetric potential [13].

According to Fig. 5, a change in the rotation direction is obtained by changing the min–max relative shift between $E_0(\theta, \varphi)$ and $E_1(\theta, \varphi)$. This fact was observed experimentally with the Fig. 1a molecular motor by locating the tip apex of the STM on different rotor arms to be coupled to different excited states of the molecule at the same positive bias voltage range [7]. This gives a design rule for new molecular motors with a possible reversible choice of the rotation direction since excited states with different min–max relative shifts with respect to the ground state can be reached depending on the location of the excitation. Knowing the detailed topology of the excited electronic states' potential energy surface of a molecular motor becomes now an important part of its design. For instance, an elegant example of a molecule able to shift its min–max using hydrogen bonds was recently reported by Frutos et al. [14].

With the same barrier height (0.25 eV) in $E_0(\theta, \varphi)$ and $E_1(\theta, \varphi)$, a molecular motor of the type presented in Fig. 1 is able to rotate one way in a controllable manner for an average Gaussian F larger than 0.2 pN. The necessary condition is

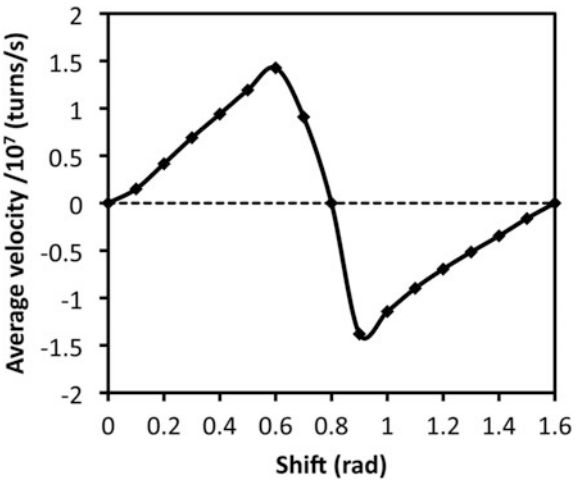

Fig. 5 Effect of the electronic state shift on the rotation efficiency and direction for a model with a symmetric ground state and a symmetric excited state. The average time between hits is 3.5 ns for a 10 ms simulation

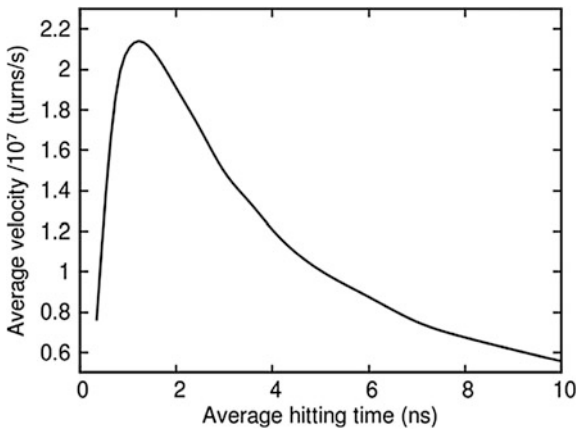

Fig. 6 Average velocity as a function of the average time between two hits, for a model with a shift of 0.6 rad between electronic states

that the $E_0(\theta, \varphi)$ and $E_1(\theta, \varphi)$ min–max are shifted as discussed above and presented in Fig. 4. The average time interval between two t_i that forges the Poisson distribution in (4) and (5) must also be tuned in order to get a stable unidirectional rotation. For example, according to the solution of (4) and (5) and for an excited-state decay time β^{-1} of 1 ns, the rotor of the molecular motor rotates one way for an average time separation between two t_i larger than 0.35 ns, reaching a maximum rotation speed at a 1.25 ns t_i interval. After this threshold, the average speed decays exponentially due to the decrease in the energy supplied to the molecule per unit of time as presented in Fig. 6. Therefore, when β decreases, that is for very long $E_1(\theta, \varphi)$ lifetimes, it is necessary to increase the average excitation time further in order to keep control of the rotation.

The control of the rotation is better when the average time interval between two t_i is long enough as compared to the lifetime of the excited state (here longer than 2 ns). For example, the same rotation velocity is reached ($\sim 7.5 \times 10^6$ turns/s) when the system is driven with an average interval of 0.35 ns or of 7 ns between two consecutive t_i leads. This corresponds to a tunneling current intensity below 1 nA. However, notice that the energy provided in the first case to the molecular motor is twenty times larger than in the second and, thus, the rotation efficiency will be significantly different for both cases. A representation of the two rotation behaviors is presented in Fig. 7.

4.2 The Motive Power

To evaluate how a molecular motor following (4) and (5) can move a load, this system of equations was solved again while applying a constant antagonist force to the rotation direction in (4). As shown in Fig. 8 and at its maximum speed, the motor is able to work against forces up to 0.65 pN. This value is in good agreement

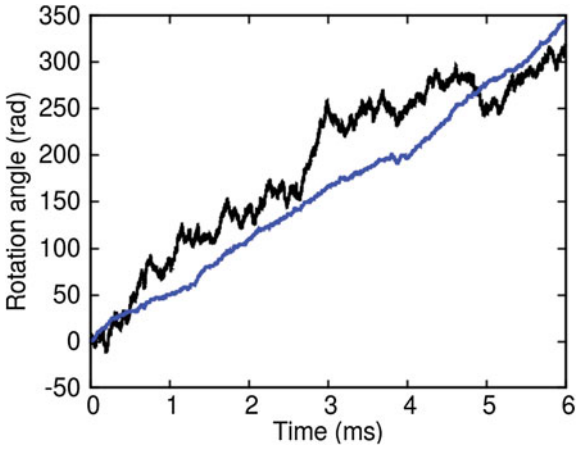

Fig. 7 Angle of rotation as a function of the time. The *red line* is for an average hitting time of 0.35 ns, whereas the *black line* is for an average hitting time of 7 ns

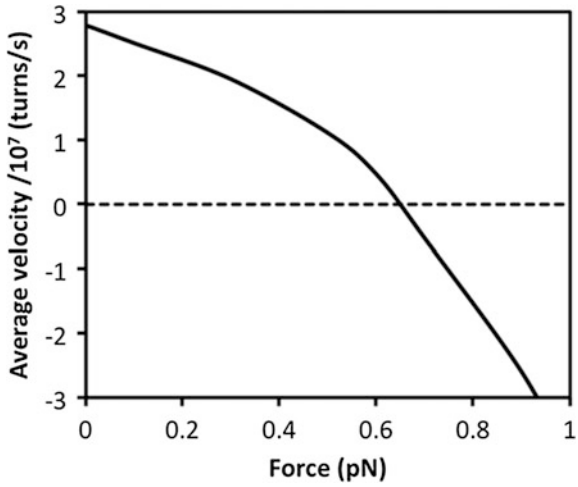

Fig. 8 Average rotation velocity of the molecular motor as a function of the load. The load is modeled as an external applied force against the rotor rotation

with the universal performance road map of motors proposed by Marden et al. [15] as a function of the motor intrinsic mass. According to this road map, our 10^{-24} kg mass molecular motor must bring a maximum output force of about 0.1 pN.

The motor efficiency is $\eta = W/E_{in}$ where E_{in} is the energy delivered to the motor and W the maximum work produced by it. When driving the motor with a tunneling current, it is not the bias voltage V applied to the molecular tunnel junction which must be considered as the energy provided to the motor for its functioning. It is the inelastic tunneling effect that populates the excited states and the spectral power of the corresponding shot noise. The shot noise applied is not a constant excitation, neither in amplitude nor in time. Therefore, the provided energy can only be estimated here considering the maximum of the random force in (4) and (5) with a Gaussian distribution ranging between −300 and 300 pN. For the optimized

one-way rotation conditions discussed above, this leads to $E_{in} = 3 \times 10^{-19}$ J. According to Fig. 8 and in those conditions, the motor is able to develop a maximum work of 6.5×10^{-22} J before stopping and going backward constrained by the external force applied. This gives $\eta = 0.002$ for our shot noise-driven motor. This value is very close to $\eta = 0.001$ for a Brownian motor driven by correlated Gaussian white noises [16] but less than for a motor driven by a temporally asymmetric unbiased external force [17] ($\eta = 0.01$) or for a flashing ratchet [18] ($\eta = 0.05$).

On the other hand, the barrier height along their respective potential energy surfaces of the states controls the rotor average velocity. We have employed for the simulations the value previously calculated with the ASED+ semi-empirical method, which is 0.25 eV for the ground state, leading to a calculated average velocity of 3.43×10^7 turns/s. Increasing the energy barrier of both states up to 0.44 eV leads to a slightly slower rotation (3.28×10^7 turns/s). However, when decreasing the barrier in $E_0(\theta, \varphi)$ to 0.25 eV while keeping $E_1(\theta, \varphi)$ at 0.44 eV, a smaller average velocity is calculated (2.25×10^7 turns/s). In contrast, a barrier of 0.44 eV in $E_0(\theta, \varphi)$ and of 0.25 eV in $E_1(\theta, \varphi)$ leads to a large average velocity of 4.11×10^7 turns/s. Further modifications of the energy barriers must be accompanied by a new optimization of the average time interval between two t_i and of the average Gaussian force in order to keep the one-way rotation.

5 Conclusions and Outlook

In conclusion, with a simple model that takes into account realistic characteristics of a molecular motor, we have demonstrated how the rotor of such molecular motor can rotate one way. We have also estimated the motive power when driven by the shot noise of a tunneling current. Two important facts were discussed: (1) There is no need for a static ratchet effect, and (2) when a molecular motor is driven by a tunneling current, it is not the bias voltage which provides the energy for the rotation. It is the power of the shot noise, characteristic of the tunneling current, which is delivered to the motor. There are a few possibilities to measure the motive power of a single-molecule motor as, for example, loading a certain number of atoms to the rotor, bringing in contact a solid-state nanogear with the molecule motor or placing a NC-AFM tip nearby the rotor, driving the rotor with another tip. All those possibilities require new instrumentation like the development of UHV-compatible nanolithography processes or the construction of ultrastable 4 probes UHV-STM and NC-AFM in the years to come.

Acknowledgments J.E. thanks the *Generalitat de Catalunya* and the European Union for a *Beatriu de Pinós* scholarship.

References

1. Tierney, H.L., Murphy, C.J., Jewell, A.D., Baber, A.E., Iski, E.V., Khodaverdian, H.Y., McGuire, A.F., Klebanov, N., Sykes, E.C.H.: Experimental demonstration of a single-molecule electric motor. Nat. Nanotechnol. **6**, 625–629 (2011)
2. Vives, G., de Rouville, H.-P.J., Carella, A., Launay, J.-P., Rapenne, G.: Prototypes of molecular motors based on star-shaped organometallic ruthenium complexes. Chem. Soc. Rev. **38**, 1551–1561 (2009)
3. Vives, G., Rapenne, G.: Directed synthesis of symmetric and dissymmetric molecular motors built around a ruthenium cyclopentadienyl tris(indazolyl)borate complex. Tetrahedron **64**, 11462–11468 (2008)
4. Ample, F., Joachim, C.: A semi-empirical study of polyacene molecules adsorbed on a Cu (110) surface. Surf. Sci. **600**, 3243–3251 (2006)
5. Echeverría, J., Carreras, A., Casanova, D., Alemany, P., Alvarez, S.: Concurrent symmetries: the interplay between local and global molecular symmetries. Chem. Eur. J. **17**, 359–367 (2011)
6. Sheppard, D., Terrell, R., Henkelman, G.: Optimization methods for finding minimum energy paths. J. Chem. Phys. **128**, 134106–134110 (2008)
7. Perera, U.G.E., Ample, F., Kersell, H., Zhang, Y., Vives, G., Echeverria, J., Grisolia, M., Rapenne, G., Joachim, C., Hla, S.-W.: Controlled clockwise and anticlockwise rotational switching of a molecular motor. Nat. Nanotechnol. **8**, 46–51 (2013)
8. Joachim, C.: The driving power of the quantum superposition principle for molecule-machines. J. Phys. Condens. Matter **18**, S1935–S1942 (2006)
9. Persson, B.N.J., Nitzan, A.: Linear sliding friction: on the origin of the microscopic friction for Xe on silver. Surf. Sci. **367**, 261–275 (1996)
10. Lensen, D., Elemans, J.A.A.W.: Artificial molecular rotors and motors on surfaces: STM reveals and triggers. Soft Matter **8**, 9053–9063 (2012)
11. Astumian, R.: Thermodynamics and kinetics of a Brownian motor. Science **276**, 917–922 (1997)
12. Joachim, C., Ratner, M.A.: Molecular electronics: some views on transport junctions and beyond. Proc. Natl. Acad. Sci. U.S.A. **102**, 8801–8808 (2005)
13. Sanchez-Palencia, L.: Directed transport of Brownian particles in a double symmetric potential. Phys. Rev. E **70**, 011102 (2004)
14. García-Iriepa, C., Marazzi, M., Zapata, F., Valentini, A., Sampedro, D., Frutos, L.M.: Chiral hydrogen bond environment providing unidirectional rotation in photoactive molecular motors. J. Phys. Chem. Lett. **4**, 1389–1396 (2013)
15. Marden, J.H., Allen, L.R.: Molecules, muscles, and machines: universal performance characteristics of motors. Proc. Natl. Acad. Sci. U.S.A. **99**, 4161–4166 (2002)
16. Nie, L.-R., Mei, D.-C.: Effect of correlated noises on Brownian motor. Phys. Lett. A **373**, 3816–3821 (2009)
17. Ai, B., Xie, H., Liao, H., Liu, L.: Efficiency in a temporally asymmetric Brownian motor with stochastic potentials. J. Stat. Mech. Theory Exp. **2006**, P09016–P09016 (2006)
18. Parrondo, J.M.R., de Cisneros, B.J.: Energetics of Brownian motors: a review. Appl. Phys. Mater. Sci. Process. **75**, 179–191 (2002)

The Einstein–de Haas Effect and Its Application to Spin-Driven Molecular Motors

Takashi Uchihashi and Teruo Ono

Abstract When the angular momentum of spin is converted into that of lattice, it gives a mechanical torque for rotation to the system, which is known as the Einstein–de Haas effect. Here, we propose to utilize this principle to create spin-driven molecular motors. Despite the fundamental challenge due to a small driving torque, the mechanism is potentially important in terms of nanotechnology and spintronics. We consider the required conditions for the rotational motion using a classical resonator model as the first step toward its future realization.

1 Introduction

The study on molecular motors is a new interdisciplinary field of research where chemistry, physics, biology, and nanotechnology are involved and intimately related with each other [1–7]. Because the concept of molecular motor has been inspired by protein molecules such as ATPase and kinesin, its main motivation has been to mimic the widely accepted mechanism of biological molecular motors: Feynman's Brownian ratchet [8–10]. Thanks to the ingenious structures of the protein molecules, these nanomachines can produce work from its Brownian motion without violating the second law of thermodynamics. There, crucial ingredients for determining the directional motion are the structural asymmetry of the active component and the time-reversal symmetry breaking due to energy dissipation. Here arises a question: "Is it possible to employ other mechanisms to drive molecular motors?"

T. Uchihashi (✉)
International Center for Materials Nanoarchitectonics, National Institute for Materials Science, 1-1, Namiki, Tsukuba, Ibaraki 305-0044, Japan
e-mail: uchihashi.takashi@nims.go.jp

T. Ono
Institute for Chemical Research, Kyoto University, Gokasho Uji-City, Kyoto 611-0011, Japan

C. Joachim and G. Rapenne (eds.), *Single Molecular Machines and Motors*, Advances in Atom and Single Molecule Machines, DOI 10.1007/978-3-319-13872-5_6

In this chapter, we explore the possibility of using the spin degree of freedom of electrons, which has been disregarded for "conventional" molecular motors, and of resorting to the principle of the Einstein–de Haas effect, a century-old but still intriguing magnetic phenomenon [11, 12]. With a spin injection into a molecule and a subsequent relaxation, the angular momentum of spin $\hbar/2$ is transferred to its mechanical freedom and could rotate the molecule [13–16]. In other words, to dictate the rotational direction of the molecule, we rely on the time-reversal symmetry breaking due to spins, in contrast to the Brownian ratchet motors. This would not only allow us to change the driving direction at will, but also to potentially integrate molecular motors into state-of-the-art spintronics devices.

In the following sections, we explain the principle of the Einstein–de Haas effect and its application to molecular motors using a spin-polarized current. After reviewing its experimental demonstration in a microelectro mechanical systems (MEMS) device, we extend a classical resonator model to the case of a single molecule on a substrate to consider the required condition for the rotational motion. Because of the extremely small angular momentum transfer $\hbar/2$ involved in this process [13–16], detection of the Einstein–de Haas effect in the molecular system is not easy. However, it will be feasible if we can take advantage of resonant behavior of the torsional oscillation. Harnessing this effect to rotate the molecule in a preferential direction and produce a torque for a useful work is more challenging. Keys for the success will include usage of extremely fast current pulse for driving molecular and design of robust molecules. The discussions in this chapter will hopefully stimulate researchers in this field and contribute to the developments of experiments and theories of new molecular motors.

2 The Principle of the Einstein–de Haas Effect

In this section, we review the principle of the Einstein–de Haas effect and its experimental demonstrations. Suppose we have an electron orbiting around the nucleus of an atom (see Fig. 1a). According to the classical electromagnetism, the magnetic moment M emerging from this motion is given by the equation:

$$M = \frac{1}{2} e\omega r^2, \tag{1}$$

where e is the charge of the electron, ω is the angular velocity of the electron motion, and r is the radius of the orbit. This magnetic moment M accompanies an angular momentum P:

$$P = m\omega r^2, \tag{2}$$

where m is the mass of the electron. These two equations lead to the following relation:

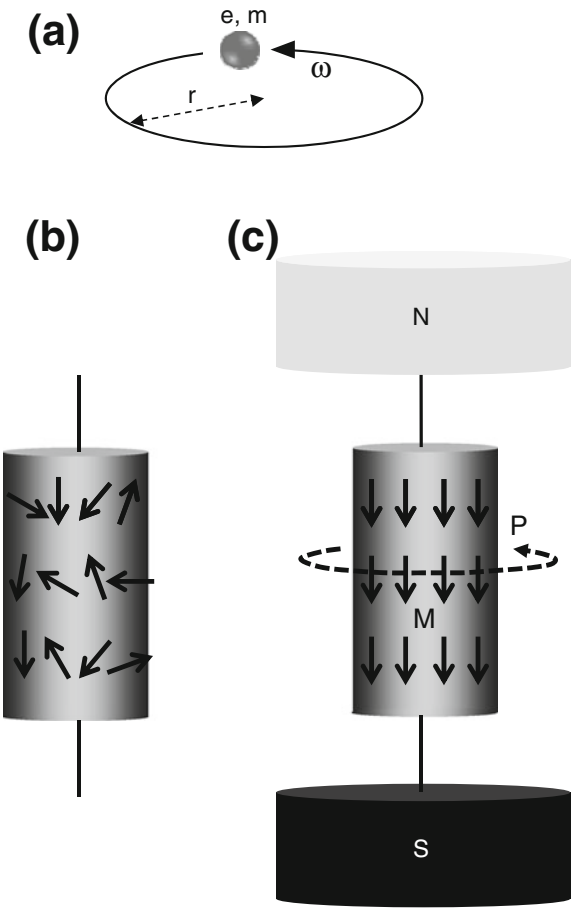

Fig. 1 **a** Schematic drawing of an electron orbiting around the nucleus of an atom. **b**, **c** Schematic illustration of the Einstein–de Haas effect induced by magnetic field. In the beginning, there is no magnetic field and the iron rod is demagnetized and set still (**b**). Sudden application of magnetic field in the direction of the rotational axis magnetizes the iron, resulting in emergence of a magnetic moment M and an angular momentum P (**c**). The *arrows* indicate the magnetic moments and angular momentums due to "molecular currents" (which should be now replaced by spins)

$$M = g\frac{e}{2m}P, \tag{3}$$

where $g = 1$ is the g factor for the orbital angular momentum of electron. In reality, the magnetism of transition metals such as iron and cobalt is mostly attributed to spin, not to orbital angular momentum. But the intimate relation between the magnetic moment M and the angular momentum P still holds for spin, for which $g = 2$ is true in Eq. (3). Although the existence of spin seems unequivocal from the firmly established theory of quantum mechanics, its real identity is puzzling because the spin degree of freedom has nothing to do with the electron motion in real space [17]. The verification of spin as a form of *angular momentum* can be obtained through so-called gyromagnetic effects, one of which is the Einstein–de Haas effect [11, 12].

In 1915, Einstein and de Haas experimentally demonstrated the relation of Eq. (3) [11]. They devised an apparatus where a cylindrically shaped iron rod,

suspended by thin threads, could freely rotate along its rotational axis. (It is worth mentioning that Einstein was a smart experimentalist against the prevailing image [18].) Now, suppose that there is no magnetic field in the beginning and the iron rod is demagnetized and set still (Fig. 1b). Sudden application of magnetic field in the direction of the rotational axis magnetizes the iron, resulting in emergence of a magnetic moment and an angular momentum according to Eqs. (2) and (3) (Fig. 1c). But where has this angular momentum come from? Assuming that we have kept the rotational symmetry of the whole system, the total angular momentum must be conserved to be zero. This means that a change in the angular momentum of the electron system should be compensated by a counter change in that of the lattice system, which is equivalent to a rotation of the cylinder. Thus, mechanical rotation can be induced by magnetization. At the time of the experiment by Einstein and de Haas, the presence of spin was not recognized, so they postulated a permanent "molecular current" (i.e., orbital angular momentum) as the origin of the magnetic moment. They found $g \approx 1$ in accordance with the assumption of molecular current, but subsequent refined experiments showed $g \approx 2$, proving the existence of spin.

In the original experiment by Einstein and de Haas, the rotational motion was induced by applying magnetic field. But there is another situation where the same principle can be applied. Suppose we have a rotatable non-magnetic material (N) with a large spin–orbit interaction, into which we inject a spin-polarized current from a ferromagnet (F) (see Fig. 2a). Because of the spin–orbit interaction, injected spins are frequently flipped during the scattering process and finally randomized

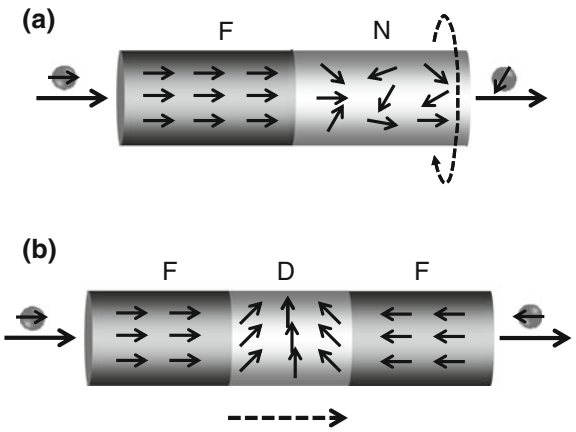

Fig. 2 a Schematic illustration of the Einstein and de Haas effect induced by current. Spin-polarized electrons are injected from the ferromagnetic (*F*) into the nonmagnetic (*N*) side. The loss in averaged spin angular momentum in *N* side is compensated by an increase in lattice angular momentum, resulting in a mechanical rotation. **b** Schematic illustration of current-induced motion of magnetic domain walls. When conduction electrons flow between ferromagnetic regions (*F*) through a domain wall (*D*), they change their spin polarization. They can donate their angular momentums to the local spins and effectively move the domain wall

(spin relaxation). The loss in averaged spin angular momentum should be compensated by an increase in orbital angular momentum of electrons due to the conservation of total angular momentum. This change is then transferred to the one in lattice angular momentum by the electron–lattice interaction. Thus, a rotational motion can be induced by injection of a spin-polarized current [13, 14, 16]. The angular momentum transfer associated with a single spin relaxation is $\hbar/2$. Therefore, the torque T_{spin} produced by this mechanism is

$$T_{\text{spin}} = P\frac{\hbar I}{2e}, \tag{4}$$

where P is the spin polarization of the injected current, $\hbar$ is the reduced Plank constant, and I is the current. For example, assuming $P = 1$ and $I = 10$ μA, one obtains $T_{\text{spin}} = 3.3 \times 10^{-21}$ Nm. This is a very small torque due to the inclusion of $\hbar$ ($= 1.05 \times 10^{-34}$ J s) in Eq. (4), but it is indeed detectable. Zolfagharkhani et al. [15] used a MEMS device that can be twisted around the rotational axis, along which a hybrid ferromagnetic (F)/nonmagnetic (N) metal nanowire was placed. A current was run in such a way that electrons flow from F to N side. Since the initially spin-polarized electrons become depolarized by relaxation, a torque is generated according to Eq. (4). They successfully detected it by utilizing the resonance of the torsional motion of the device. Here, we consider the dynamics of the mechanical resonator twisted by a torsional angle θ. The equation of motion for θ is given by [16]

$$J\frac{\mathrm{d}^2\theta}{\mathrm{d}t^2} + \gamma\frac{\mathrm{d}\theta}{\mathrm{d}t} + K\theta = T_{\text{spin}}(t), \tag{5}$$

where J is the moment of inertia about the rotational axis, $\gamma(\mathrm{d}\theta/\mathrm{d}t)$ describes a frictional damping, and K is the spring constant for elastic torsion. $T_{\text{spin}}(t)$ is the torque given in Eq. (4) where an ac current $I(t) = I_0\cos(\omega t)$ is used. The resonance frequency ω_0 and the quality factor Q of the system are given by $\omega_0 = (K/J)^{1/2}$ and $Q = 2J\omega_0/\gamma$, respectively. On resonance $\omega = \omega_0$, the amplitude of the oscillation is maximized at

$$\theta_{\text{res}} = P\frac{Q\hbar}{4K}\frac{I_0}{e}. \tag{6}$$

Compared with the solution of Eq. (5) for a dc current $I(t) = I_0$:

$$\theta_{\text{dc}} = P\frac{\hbar}{2K}\frac{I_0}{e}, \tag{7}$$

the amplitude of θ is enhanced by a factor of $Q/2$. In the experiment, $\theta_{\text{res}} = 2.6 \times 10^{-5}$ was detected using the ac lock-in technique, with parameters $J = 1 \times 10^{-27}$ kg m^2, $\omega_0 = 4.21 \times 10^7$ s^{-1}, $Q = 2.8 \times 10^4$, and $P = 0.85$.

This phenomenon may as well be called the *current-induced* Einstein–de Haas effect, which is to be distinguished from the original one induced by *magnetic field*. Although the produced torque is minute, the torque required for rotation can also be extremely small in the nanoscale limit of the system. This can be seen from Eqs. (6) and (7) with $K = J\omega_0^2$, which show θ_{res} and θ_{dc} are inversely proportional to the inertia of moment J. Thus, the mechanism is potentially important for molecular motors and for nanotechnology in general.

Interestingly, current-induced motion of magnetic domain walls [19, 20], which is being intensively studied for magnetic random access memories (MRAM) [21], is closely related to the Einstein–de Haas effect described here. The magnetic domain wall is the place where spin polarization is inverted. When conduction electrons flow through it, they change their spin direction adiabatically by following the local magnetization direction (Fig. 2b). Thus, they can donate their angular momentums to the local spins and effectively move the domain wall. In this case, the spin-driven torque is used for the linear motion of the magnetic structure. Below a certain threshold current, however, the domain wall does not move due to the intrinsic pinning effect [22, 23], and the loss of spin angular momentum seems to go nowhere. Actually, this loss is used to mechanically rotate the lattice system of the whole world that sustains the magnetic structure (including the globe!). The above current-induced Einstein–de Haas effect and the magnetic domain wall motion are both based on the angular momentum transfer from a spin-polarized current. It is therefore conceivable to combine them to fabricate novel nanomechanical/spintronics devices in the future.

3 Application of the Einstein–de Haas Effect to Molecular Motors

Although the principle of the Einstein–de Haas effect is well established, its application to molecular systems has not been explored experimentally. In the meanwhile, its theoretical treatment should involve a fully quantum-mechanical analysis, which is presently unknown. In this section, we restrict ourselves to a semi-classical treatment of the dynamics of a molecular system. This, however, should give us an order of magnitude estimation of required driving current and insights into the phenomena.

Let us consider a simple molecule adsorbed on a metal surface, into which a tunneling current is injected from a scanning tunneling microscope (STM) tip (Fig. 3a). Experiments have already shown that molecular rotation is induced by tunneling current of order of nA [24–28], indicating that this will be a good playground for testing the idea. In general, the potential profile of the molecule as a function of the rotational angle θ is complicated, and the asymmetry in the profile is essential for an unidirectional motion caused by the Brownian ratchet [8–10].

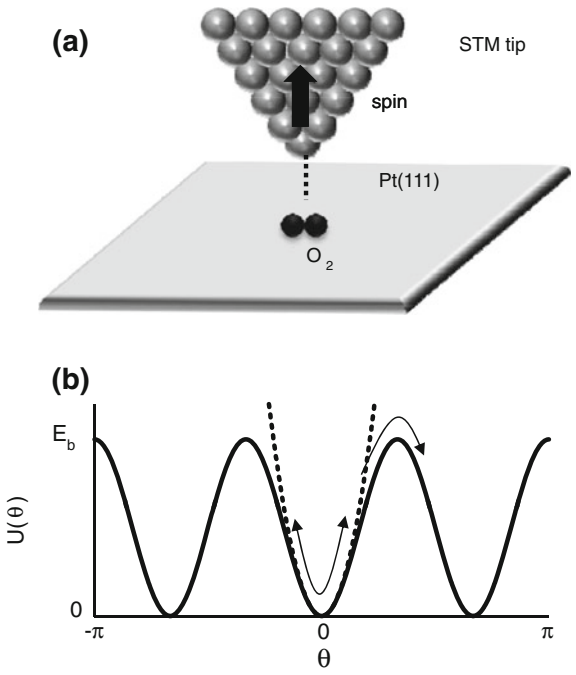

Fig. 3 **a** Schematic illustration of an O_2 molecule adsorbed on a Pt(111) surface. A spin-polarized current is injected into the O_2 molecule to induce rotation based on the Einstein–de Haas effect. **b** Potential profile modeling a single molecule adsorbed on a metal surface. The *solid line* indicates a sinusoidal potential profile of Eq. (8), while the *dashed line* an approximated harmonic potential of Eq. (9)

Here, we assume a symmetric potential profile to exclude such a mechanism and approximate it with a sinusoidal function of form (Fig. 3b, solid line):

$$U(\theta) = \frac{E_\mathrm{b}}{2}[1 - \cos(N_\mathrm{w}\theta)], \tag{8}$$

where E_b is the potential barrier height, and N_w is the number of potential minima within $-\pi < \theta < \pi$. $\theta = 0$ is set at one of the minima of $U(\theta)$. For a torsional (hindered) rotation around $\theta = 0$, Eq. (8) can be approximated by a harmonic oscillator of the form (Fig. 3b, dashed line):

$$U(\theta) \approx \frac{K}{2}\theta^2, \tag{9}$$

where $K = E_\mathrm{b}N_\mathrm{w}^2/2$ is the spring constant for the elastic torsion. Then, the equation of motion for θ at the bottom of the potential well is described by Eq. (5) with the same resonance frequency $\omega_0 = (K/J)^{1/2}$. If we now consider a single-electron injection, the time integral of spin-induced torque $T_\mathrm{spin}(t)$ is equal to the transferred angular momentum $\Delta L = \hbar/2$. We note that the efficiency of angular momentum transfer from spin to lattice can be small due to an imperfect spin polarization and/or relaxation of the injected current. Nevertheless, ΔL is kept constant due to the quantum nature of angular momentum. If the duration of $T_\mathrm{spin}(t)$ is small compared

to the oscillation periodicity $\tau_0 = 2\pi\omega_0^{-1}$, the solution of Eq. (5) is given by Mohanty et al. [16]

$$\theta(t) = \frac{\hbar}{2J\omega_0\sqrt{1-1/Q^2}}\exp\left(-\frac{\omega_0 t}{Q}\right)\sin\left(\omega_0\sqrt{1-1/Q^2}t\right). \tag{10}$$

Namely, after the torque impulse at $t = 0$, the molecule exhibits an exponentially decaying oscillation, and its maximum amplitude $\theta_{\max}$ is

$$\theta_{\max} = \frac{\hbar}{2J\omega_0} \tag{11}$$

for $Q \gg 1$. For a sequence of electron tunneling that cause torque pluses, a multiple-electron effect can be important. This requires that the decay time $\tau_{\text{decay}} = Q/\omega_0$ should be longer than the averaged tunneling interval $\tau_t \equiv e/I$. Within our treatment, this is described by a random-phase superposition of Eq. (10) [16]:

$$\theta(t) = \frac{\hbar}{2J\omega_0\sqrt{1-1/Q^2}}\sum_{l,t_l<t}\exp\left[-\frac{\omega_0}{Q}(t-t_l)\right]\sin\left[\omega_0\sqrt{1-1/Q^2}(t-t_l)\right] \tag{12}$$

where t_l denotes the onset of each oscillation and its averaged time interval is equal to τ_t. Statistically, N oscillations occurring within a decay time τ_{decay} are superposed to enhance the amplitude by a factor of $N^{1/2}$, where $N = \tau_{\text{decay}}/\tau_t$. Figure 4a shows a simulation of the multiple-electron process described by Eq. (12). $Q = 50$ is chosen as a parameter, and $\theta(t)$ and t are normalized by $\theta_{\max}$ and τ_0, respectively. For $\tau_t = 20\tau_0 (> \tau_{\text{decay}} = 7.96\tau_0)$, each oscillation is nearly independent and its maximum amplitude is close to $\theta_{\max}$ (thick solid line). In contrast, for $\tau_t = \tau_0 (< \tau_{\text{decay}} = 7.96\tau_0)$, the oscillation amplitude is enhanced by a factor of $N^{1/2} (=2.82)$ due to the random-phase superposition (thin solid line).

In the sinusoidal potential profile of Eq. (8), a molecular rotation occurs when the "particle" trapped in a potential well escapes to a neighboring one. Approximately, this will occur when the maximum of $\theta(t)$ approaches π/N_w in the harmonic potential of Eq. (9). Here, we take an O_2 molecule adsorbed on a Pt(111) surface for example, which was found to rotate among three equivalent crystallographic orientation ($N_w = 3$) [24]. The small size and mass of the O_2 molecule is advantageous for detecting the effect of the minute spin-induced torque, while the efficiency of angular momentum transfer may be small. For simplicity, we assume that the angular momenta of injected spins are all transferred to the lattice system. The moment of inertia J of an O_2 molecule around its center is given by $J = 2M\,r^2 = 2.0 \times 10^{-46}$ kg m^2, where $M = 2.7 \times 10^{-26}$ kg is the mass of an oxygen atom and $r = 6.0 \times 10^{-2}$ nm is half the bond length of the oxygen molecule. Using the experimentally estimated potential barrier $E_b \approx 0.16$ eV, one obtains $K = E_b N_w^2/2 = 1.15 \times 10^{-19}$ J and $\omega_0 = (K/J)^{1/2} = 2.4 \times 10^{13}$ s^{-1}. These considerations lead to $\theta_{\max} \approx 0.01$ from Eq. (11). Although this value of $\theta_{\max}$

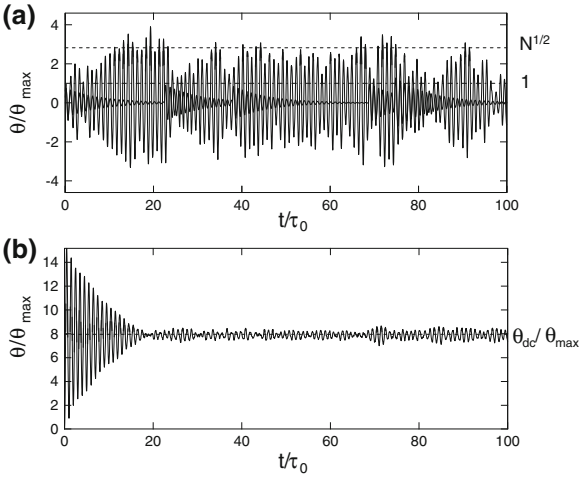

Fig. 4 Simulation of the θ oscillation described by Eq. (12). $Q = 50$ is chosen as a parameter, and $\theta(t)$ and t are normalized by $\theta_{\max}$ and τ_0, respectively. **a** For $\tau_t = 20\tau_0 (> \tau_{\text{decay}} = 7.96\tau_0)$, each oscillation is nearly independent and its maximum amplitude is close to $\theta_{\max}$ (*thick solid line*). In contrast, for $\tau_t = \tau_0 (< \tau_{\text{decay}} = 7.96\tau_0)$, the oscillation amplitude is enhanced by a factor of $N^{1/2} (= 2.82)$ due to the random-phase superposition (*thin solid line*). **b** $\tau_t = 0.02\tau_0$. After $t \sim \tau_{\text{decay}}$, $\theta(t)$ is nearly constant around $\theta_{\text{dc}} (= 7.96\theta_{\max})$

is small compared to $\pi/N_w (\sim 1)$, it may lead to a rotation if a multiple-electron process is involved. According to the above argument, if the above $\theta_{\max} \approx 0.01$ is to be intensified to 1, $N \sim 10^4$ is needed. If a high tunneling current of $I = 200$ nA (corresponding to $\tau_t \approx 1$ ps) is used, $N \sim 10^4$ leads to $\tau_{\text{decay}} \approx 10$ ns (which corresponds to $Q = \tau_{\text{decay}}/\omega_0 \sim 2.4 \times 10^5$). Although a much shorter decay time of $\tau_{\text{decay}} \approx 1$ ps is estimated for the O_2/Pt(111) system [24], $\tau_{\text{decay}} > 1$ ns is typical for an adsorbed molecule [28]. Thus, molecular rotation caused by the Einstein–de Haas effect may be experimentally observable, if we choose an appropriate molecular/substrate system. In contrast, assuming a "continuous" (not shot-noise like) current flow, Eq. (7) gives $\theta_{\text{dc}} = 5.7 \times 10^{-4} \ll 1$ for $I = 200$ nA. Therefore, the enhancement of oscillation amplitude is due to pulse-like torque originating from single-electron processes.

Here, we give two important remarks. First, although we have treated the problem classically, we should in reality describe it quantum mechanically. The energy in the potential well is quantized, and even classically inaccessible high-energy levels are generally occupied in nonequilibrium states. This means that the molecule can overcome the potential barrier and rotate below the classical threshold current, although with a small probability. Second, nevertheless, the rotational direction cannot be dictated in the above case, because the oscillation is nearly symmetric against $\theta = 0$ due to a long decay time (see Fig. 4a). In addition to the Einstein–de Haas effect, the molecular rotation can be induced by other mechanism;

a widely accepted example is electron injection on a resonance level and subsequent energy transfer to vibrational/rotational modes [27–29]. Therefore, distinction from irrelevant mechanisms is crucial to identify the Einstein–de Haas effect. The dependence of the rotational rate on the magnetic status of the tip should be studied for this purpose. For example, the rotational rate should be dependent on the angle θ between the magnetization direction of the STM tip and the rotational axis, i.e., the surface normal direction.

In the above argument, the superposition of multiple oscillations is not effective because the tunneling event is stochastic and the phase of each oscillation is random. Periodic tunneling events with its frequency matched to ω_0 would enable coherent superposition of the oscillations, resulting in amplitude amplification by a factor of N instead of $N^{1/2}$. This would lead to significant enhancement of the excitation efficiency. The situation corresponds to the MEMS oscillator driven by on-resonance ac current as described earlier. Its physical implementation is not straightforward, but we may be able to resort to the single-electron tunneling oscillations originating from the charging effect. The large charging energy associated with a single electron on a small tunnel junction capacitance regulates the timing of tunneling and makes it quasi-periodic [30]. A simple simulation can show that even a 20 % fluctuation within the phase 2π maintains an oscillation amplitude nearly equal to that for the complete in-phase oscillation.

In the following, we consider a molecular rotation with a preferential direction, which is crucial to realize a molecular motor. To have such a motion, the oscillation dynamics must be asymmetric about $\theta = 0$, requiring that the decay time τ_{decay} be comparable to the oscillation periodicity τ_0 (equivalently, $Q \sim 1$). This strongly suppresses the amplitude enhancement because only $N \sim 1$ is used for superposition of subsequent oscillations. Hence, we will first consider the single-electron process to estimate the required condition. Combination of Eq. (11) with $\omega_0 = (K/J)^{1/2}$ and $K = E_{\mathrm{b}} N_{\mathrm{w}}^2/2$ leads to $\theta_{\max} \propto E_{\mathrm{b}}^{-1/2}$; it is thus possible to increase $\theta_{\max}$ by reducing the potential barrier E_{b} while keeping J. This could be realized by introducing a smooth axle into the molecule, for example, by introducing a bearing atom ball or σ bonding in the surface normal direction [27, 28]. However, reduction of potential barrier also causes thermally activated random rotations. For example, $\theta_{\max}$ of the O_2/Pt(111) system can be enhanced to ~ 1 by reducing E_{b} down to 0.016 meV. This corresponds to a temperature of 0.19 K, requiring an experimental verification at much lower temperatures. Discussion based on energy transfer during the single-electron process gives another restriction concerning the energy scale. Energy quantum ΔE given to the molecular rotational mode by angular momentum change $\Delta L = \hbar/2$ is approximately

$$\Delta E = \frac{\Delta L^2}{2J}. \tag{13}$$

For $J = 2M\,r^2 = 2.0 \times 10^{-46}$ kg m^2 of O_2 molecule, one obtains $\Delta E = 0.082$ meV corresponding to 0.95 K. Therefore, a working temperature must be sufficiently lower than 1 K.

If the single-electron process cannot induce rotation, the only alternative way is to use a large current $I/e \gg \omega_0$ (equivalently, $\tau_t \ll \tau_0$); namely, a large number of multiple torque pulses should be accumulated before a single cycle of oscillation is completed. In this case, the electron flow can be seen quasi-continuous, and θ approaches the equilibrium value θ_{dc} given by Eq. (7). Figure 4b shows the result of a simulation of Eq. (12) for $\tau_t = 0.02\tau_0$ and $Q = 50$. After $t \sim \tau_{decay}$, $\theta(t)$ is nearly constant around $\theta_{dc} (= 7.96\theta_{max})$. For the molecule to overcome the potential barrier, this value must exceed $2\pi/N_w \sim 1$ (at least classically). For the O_2/Pt(111) system, it results in $I = 350$ μA, which is apparently a huge current for a single molecule to stand with. The situation seems hopeless, but the molecule may survive a huge current if it is only for a short time. The minimum required time for a pulse current to rotate the molecule is the oscillation periodicity τ_0, which is about 0.26 ps for the O_2/Pt(111) case. For example, a voltage pulse with a width of $\Delta t = 80$ ps was used for coherent electrical control of a superconducting quantum bit [31]. In an recent STM experiment, a time resolution of $\Delta t = 120$ ps was achieved in a pulse detection mode while obtaining atomically resolved images [32]. Such a pulse technology may also be used to induce the molecular rotation.

4 Conclusion

In this chapter, we have proposed to use the principle of the Einstein–de Haas effect to create spin-driven molecular motors. Its realization is a technical challenge, mainly because of very small torque produced by angular momentum transfer $\hbar/2$ and the finite potential barrier for rotation. The detection of the Einstein–de Haas effect in the molecular system will be feasible if the oscillation decay time τ_{decay} is much larger than the timescale of the oscillation τ_0. Nevertheless, rotation of molecule in a preferential direction, a prerequisite for realizing a molecular motor, is not straightforward. It requires either an extremely smooth molecular rotation and a low working temperature ($T \ll 1$ K) or a short (in the order of ps) but huge driving current (~ 100 μA) that the molecule can stand with. Theoretically, development of a fully quantum treatment of the spin-driven rotation is strongly desired. It should include various fundamental processes: angular momentum transfer from the spin to the lattice system, excitation of torsional oscillation mode, tunneling through the potential barrier of rotation, and finally rotational relaxation. We hope that cooperative and synergetic advancements of molecular architecture, measurement technology, and theoretical understanding will lead to realization of these fundamentally new molecular motors. We thank C. Joachim for fruitful discussions. The research has been financially supported by JSPS Grant-in-Aid No. 24651125/25247053 and by World Premier International Research Center (WPI) Initiative on Materials Nanoarchitectonics, MEXT, Japan.

References

1. Kottas, G.S., Clarke, L.I., Horinek, D., Michl, J.: Artificial molecular rotors. Chem. Rev. **105** (4), 1281–1376 (2005)
2. Schliwa, M., Woehlke, G.: Molecular motors. Nature **422**(6933), 759–765 (2003)
3. van den Heuvel, M.G.L., Dekker, C.: Motor proteins at work for nanotechnology. Science **317** (5836), 333–336 (2007)
4. Balzani, V., Credi, A., Raymo, F., Stoddart, J.F.: Artificial molecular machines. Angew. Chem. Int. **39**(19), 3348–3391 (2000)
5. Browne, W.R., Feringa, B.L.: Making molecular machines work. Nat. Nanotechnol. **1**, 25–35 (2006)
6. Kay, E., Leigh, D., Zerbetto, F.: Synthetic molecular motors and mechanical machines. Angew. Chem. Int. **46**(1–2), 72–191 (2007)
7. Gimzewski, J.K., Joachim, C.: Nanoscale science of single molecules using local probes. Science **283**(5408), 1683–1688 (1999)
8. Reimann, P., Hänggi, P.: Introduction to the physics of Brownian motors. Appl. Phys. A **75** (2), 169–178 (2002)
9. Ait-Haddou, R., Herzog, W.: Brownian ratchet models of molecular motors. Cell Biochem. Biophys. **38**(2), 191–213 (2003)
10. Astumian, R.D.: Thermodynamics and Kinetics of a Brownian motor. Science **276**(5314), 917–922 (1997)
11. Einstein, A., de Haas, W.J.: Experimenteller Nachweis der Ampereschen Molekularstrme. Verh. Dtsch. Phys. Ges. **17**, 152–170 (1915)
12. Richardson, O.W.: A mechanical effect accompanying magnetization. Phys. Rev. (Series I) **26** (3), 248–253 (1908)
13. Ono, T., Kohno, H.: Spin-transfer motor. J. Magn. Soc. Jpn. **31**, 305 (2007)
14. Kovalev, A.A., Bauer, G.E.W., Brataas, A.: Current-driven ferromagnetic resonance, mechanical torques, and rotary motion in magnetic nanostructures. Phys. Rev. B **75**, 014430 (2007)
15. Zolfagharkhani, G., Gaidarzhy, A., Degiovanni, P., Kettemann, S., Fulde, P., Mohanty, P.: Nanomechanical detection of itinerant electron spin flip. Nat. Nanotechnol. **3**(12), 720–723 (2008)
16. Mohanty, P., Zolfagharkhani, G., Kettemann, S., Fulde, P.: Spin-mechanical device for detection and control of spin current by nanomechanical torque. Phys. Rev. B **70**(19), 195301 (2004)
17. Tomonaga S: The Story of Spin. University of Chicago Press, Chicago (1997)
18. Ya, F.V.: On the history of the Einstein-de Haas effect. Sov. Phys. Usp. **22**(7), 580 (1979)
19. Berger, L.: Exchange interaction between ferromagnetic domain wall and electric current in very thin metallic films. J. Appl. Phys. **55**(6), 1954–1956 (1984)
20. Yamaguchi, A., Ono, T., Nasu, S., Miyake, K., Mibu, K., Shinjo, T.: Real-space observation of current-driven domain wall motion in submicron magnetic wires. Phys. Rev. Lett. **92**(7), 077205 (2004)
21. Ando, K., Fujita, S., Ito, J., Yuasa, S., Suzuki, Y., Nakatani, Y., Miyazaki, T., Yoda, H.: Spin-transfer torque magnetoresistive random-access memory technologies for normally off computing (invited). J. Appl. Phys. **115**(17), 172607 (2014)
22. Tatara, G., Kohno, H.: Theory of current-driven domain wall motion: spin transfer versus momentum transfer. Phys. Rev. Lett. **92**(8), 086601 (2004)
23. Koyama, T., Chiba, D., Ueda, K., Kondou, K., Tanigawa, H., Fukami, S., Suzuki, T., Ohshima, N., Ishiwata, N., Nakatani, Y., Kobayashi, K., Ono, T.: Observation of the intrinsic pinning of a magnetic domain wall in a ferromagnetic nanowire. Nat. Mater. **10**(3), 194–197 (2011)
24. Stipe, B.C., Rezaei, M.A., Ho, W.: Inducing and viewing the rotational motion of a single molecule. Science **279**(5358), 1907–1909 (1998)

25. Stipe, B.C., Rezaei, M.A., Ho, W.: Coupling of vibrational excitation to the rotational motion of a single adsorbed molecule. Phys. Rev. Lett. **81**(6), 1263–1266 (1998)
26. Kudernac, T., Ruangsupapichat, N., Parschau, M., Macia, B., Katsonis, N., Harutyunyan, S. R., Ernst, K.H., Feringa, B.L.: Electrically driven directional motion of a four-wheeled molecule on a metal surface. Nature **479**(7372), 208–211 (2011)
27. Tierney, H.L., Murphy, C.J., Jewell, A.D., Baber, A.E., Iski, E.V., Khodaverdian, H.Y., McGuire, A.F., Klebanov, N., Sykes, E.C.H.: Experimental demonstration of a single-molecule electric motor. Nat. Nanotechnol. **6**(10), 625–629 (2011)
28. Perera, U.G.E., Ample, F., Kersell, H., Zhang, J., Vives, G., Echeverria, J., Grisolia, M., Rapenne, G., Joachim, C., Hla, S.W.: Controlled clockwise and anticlockwise rotational switching of a molecular motor. Nat. Nanotechnol. **8**, 46–51 (2013)
29. Tamar, S.: Current-driven dynamics in molecular-scale devices. J. Phys.: Condens. Matter **15** (14), R521 (2003)
30. Delsing, P., Likharev, K.K., Kuzmin, L.S., Claeson, T.: Time-correlated single-electron tunneling in one-dimensional arrays of ultrasmall tunnel junctions. Phys. Rev. Lett. **63**(17), 1861–1864 (1989)
31. Nakamura, Y., Pashkin, Y.A., Tsai, J.S.: Coherent control of macroscopic quantum states in a single-Cooper-pair box. Nature **398**(6730), 786–788 (1999)
32. Saunus, C., Bindel, J.R., Pratzer, M., Morgenstern, M.: Versatile scanning tunneling microscopy with 120 ps time resolution. Appl. Phys. Lett. **102**(5), 051601 (2013)

Single-Molecular Motors and Gears Based on Star-shaped Ruthenium Complexes

Roman Stefak, Jorge Echeverria, Saw-Wai Hla, Christian Joachim and Gwénaël Rapenne

Abstract In the last fifteen years, a few molecular motors have been designed and synthesized. In the present review paper, we present and discuss our contribution to the field. The strategy followed to control the rotation in a molecular rotary motor is based on the manipulation of the motors as single molecules. This specificity implies the use of adapted architectures. The molecules have a piano-stool structure with a "stator" meant to be grafted on a surface and a "rotor" bearing peripheral ferrocenyl redox-active groups, so that addressing the molecule with nanoelectrodes in a planar configuration or with a STM tip in a vertical configuration would trigger rotation.

Keywords Single molecule · STM · Molecular gear · Molecular motor · Ruthenium complexes

1 Introduction

In the last decade, the continuous improvement of near-field microscopy techniques such as scanning tunneling microscopy (STM) and atomic force microscopy (AFM) has led to the imaging and the study of physico-chemical properties of various molecules [1]. These techniques allow the visualization and manipulation of only one

R. Stefak · J. Echeverria · C. Joachim · G. Rapenne (✉)
CEMES-CNRS, NanoSciences Group and MANA Satellite,
29 Rue Marvig, BP 94347, Toulouse Cedex 4 3105, France
e-mail: rapenne@cemes.fr

S.-W. Hla
Nanoscale and Quantum Phenomena Institute,
Physics and Astronomy Department, Ohio University,
Athens, OH 45701, USA

C. Joachim
IMRE, A*STAR, 3 Research Link, Singapore 117602, Singapore

G. Rapenne
Université de Toulouse, UPS, 118 Route de Narbonne, Toulouse Cedex 9 31062, France

C. Joachim and G. Rapenne (eds.), *Single Molecular Machines and Motors*,
Advances in Atom and Single Molecule Machines, DOI 10.1007/978-3-319-13872-5_7

molecule, and therefore, the mechanical properties of a single molecule deposited on a surface can be investigated. Since multistep chemical synthesis allows chemists to prepare tailor-made compounds with predetermined shape and programmed movement or function, sophisticated designed molecules are expected to play a major role in the development of the field. In the bottom-up strategy, a variety of artificial molecular machines and motors have recently emerged that resemble macroscopic machinery. These so-called technomimetic molecules [2] are daily life macroscopic objects such as nanowheels [3–6], nanocars [7–9], wheelbarrows [10–12], nanogears [13–16], molecular rotors [17–19] or motors [20–23] that have been miniaturized, down to the nanometer scale by molecular synthesis. There is no physical limitation to the miniaturization of a machine down to the scale of a single molecule or, conversely, to the monumentalization of a molecule until it becomes a machine.

A mono-molecular motor is a nanoscale machine which consumes energy to produce work via a unidirectional and controlled movement of one of its parts. Some very elegant examples of molecular rotary motors described so far have been studied collectively and have many degrees of freedom [18–21]. Their behaviour is the average behaviour of a weak assembly of molecules and not of a single molecule. On the contrary, the molecules described here have been designed with the intention to study and manipulate them individually with the tip of a STM. To recover and use the work produced by the rotation of the motor, its structure should be as rigid as possible and with a minimum number of degrees of freedom in order to be manipulated on a surface with a maximum control on its movement. In particular, the movement of a molecule can be efficiently restricted by attaching the molecule to a surface with a tripod [24, 25], which not only prevents the translation but also gives a very efficient control on the geometry of the whole architecture thanks to the three points of attachment. Therefore, a structurally rigid bifunctional molecule combining coordinating sites and anchoring groups is of special interest since it would allow the covalent attachment of coordination complexes on a surface, for instance giving rise to surface-mounted molecular gears or motors [26, 27].

In this article, we will develop in a first part the design of an electrically addressed molecular motor. In a second part, we will focus on the synthesis of the first prototype of a molecular motor, and then, we will exploit this strategy to make molecular gears based on star-shaped organometallic ruthenium complexes. Finally, we will present a dissymmetrized motor which undergoes controlled clockwise or counterclockwise unidirectional rotation.

2 Design of an Electron-triggered Molecular Motor

The ultimate miniaturization of electronic and mechanical devices is reached when addressing one single molecule and not a population of molecules in solution or on a surface. To reach this goal, operating at the single molecular level is more important than working at a molecular scale. Achieving molecular-scale rotational

motion faces three major difficulties/challenges: (1) the driving energy should be delivered with nanometric spatial resolution to the same single molecule; (2) the rotation should be unidirectional to avoid a pure loss of energy through random oscillations [28]; (3) the observer should have a means to know experimentally the exact motions, distorsions or conformational changes undergone by the molecule during the experiment.

In the absence of direct time-resolved microscopy to provide an image of the real intramolecular motion or movement of a mono-molecular machine, one has to record those changes via the variation of tunnelling current [29] with an STM or cantilever forces using a non-contact atomic force microscope (NC-AFM) [30]. In both cases, this puts constraints on the molecular design in order to simplify or amplify this recording and the way it is reported to the macroscopic scale.

2.1 Early Design

Looking at the requirements for an exploitable unidirectional rotation, including the constraints of a deposition on a surface in order to study the molecular motor as a single molecule between two nanoelectrodes, several difficulties can be identified. Among them, a major requirement concerns the architecture of the molecule, which must necessarily be made of essentially rigid parts. This condition is frequently absent in many proposals of molecular motors, which neglect the extreme flexibility of most molecules. In our technomimetic design of a molecular motor, the source of energy is a tunnel current. The target molecule is supposed to convert the flow of electrons tunnelling through the molecule into a directionally controlled rotary motion. The molecular motor has been designed to be individually interconnected after its deposition between two nanoelectrodes separated by a few nanometers (i.e. a nanojunction).

The molecule contains a mobile part bearing redox-active units, which can exchange electrons. During the rotation motion, the redox sites can approach the extremity of the electrodes and be oxidized or reduced.

Our early design principle [31] is shown in Fig. 1. The electroactive group (EG) closest to the anode would be oxidized to yield EG^+ (step 1) and pushed back by electrostatic repulsion (step 2). This phenomenon has already been described for a [60]-fullerene which has been shown to act as a shuttle transporting electrons one

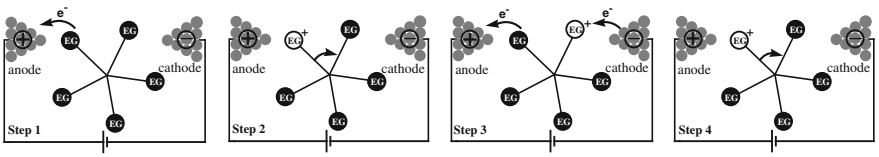

Fig. 1 Schematic representation of a molecule placed between the two electrodes of a nanojunction. The transfer of electrons from the cathode to the anode through successive oxidation and reduction processes is expected to result in the clockwise rotation of the rotating part of the molecule

by one from one electrode to the other [32]. As a result, the oxidized electroactive group would approach the cathode and subsequently be reduced (step 3). At the same time, a second electroactive group would come close to the anode and a second cycle would occur (step 4). A complete 360º turn would be achieved after five cycles, corresponding to the shuttling of five electrons from the cathode to the anode. This would represent the conversion of an electron flow into a movement of rotation, i.e. a redox-triggered molecular rotary motor powered by the irreversible transport of electrons from the negative to the positive electrode through a tunnel junction. Figure 1 is represented a fifth of a turn corresponding to the movement induced by the transfer of one electron.

2.2 The Horizontal Connection

In order for the rotation to be directional, the molecule should be placed in a dissymmetric environment. This could be achieved by its dissymmetric positioning in the nanojunction as shown in Fig. 1. The directionality would be obtained because the two directions of rotation are no longer equivalent, as a result of the dissymmetric positioning of the molecule with respect to the electrodes. This arrangement could be obtained either by chance or by building the electrodes around the deposited molecule. The construction of such a device necessitates to design a complex molecule which will be anchored on the surface and also to master the fabrication of nanoelectrodes and positioning of the molecule.

This connection is called “horizontal” and necessitates to use an insulating surface such as alumina which prevents the use of STM techniques.

2.3 The Vertical Connection

The vertical connection follows the same principle but instead of two nanoelectrodes, the STM tip will be used as one electrode and the second electrode being constituted by the surface. In this case, the surface must be metallic to allow the use of STM techniques.

With this kind of connection, only the STM tip is a localized, atomic scale electrode. The second electrode, i.e. the surface, constitutes an infinite electrode. As a consequence, only the STM tip can induce dissymmetry in the design.

3 First Prototype: The Pentaferrocenyl Motor

The gap from the design to the chemical structure has been bridged by using our knowledge in organic, organometallic and coordination chemistry. The constraint to dispose of both a fixed and a rotating part has been addressed by the use of a mixed sandwich complex of ruthenium.

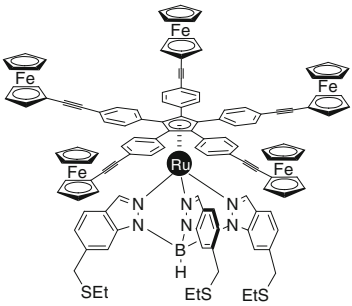

Fig. 2 Molecular motor functionalized for deposition on a metallic surface

The active core of our molecular motor is represented in Fig. 2. It comprises a stator, i.e. one part fixed between two electrodes, and on this stator is connected a rotor which should transform a current of electrons into a unidirectional rotation motion. The upper part should be free to turn while the basis should stay still, anchored on the surface between the two electrodes of the addressing system. The rotor is a cyclopentadienyl ligand (Cp) functionalized with five linear and rigid arms, each terminated by an electroactive group. The stator is a hydrotris(indazolyl) borate tripodal ligand of the family of scorpionates developed by Trofimenko [33]. The joint between the rotor and the stator is a ruthenium(II) ion chosen to obtain a kinetically stable molecule bearing zero net charge. Both criteria are essential for surface deposition and hence in view of performing single molecule experiments. There is indeed essentially one degree of freedom in our target molecule: the rotation of the upper part with respect to the lower one. The lower part has a locked conformation even if rotation about the single bonds of the arms is of course possible, but it does not alter significantly the geometry of the molecule.

A second requirement consists in the introduction of redox-active sites. Ferrocene units were chosen since they exhibit reversible oxidation in various solvents [34], and their chemistry is relatively versatile, with many well-known coupling reactions.

3.1 Synthesis and Coordination of the Rotor

Pentaphenylcyclopentadienide is an attractive ligand, as its precursors are readily synthesized in large quantities and are air-stable. The $C_5Ph_5^-$ ligand appears to be more electron-withdrawing than cyclopentadienyl and pentamethylcyclopentadienyl anions, and its large volume is reported to confer enhanced kinetic stability to its organometallic derivatives [35].

The synthesis of the pentaphenylcyclopentadienyl ligands used in this design is outlined in Scheme 1. The commercially available 1,2,3,4,5-pentaphenylcyclopentadiene was brominated in *para* positions and at the saturated carbon of the cyclopentadiene ring in neat bromine to give the hexabrominated derivative in almost quantitative yield [36]. Various palladium-catalysed coupling reactions gave

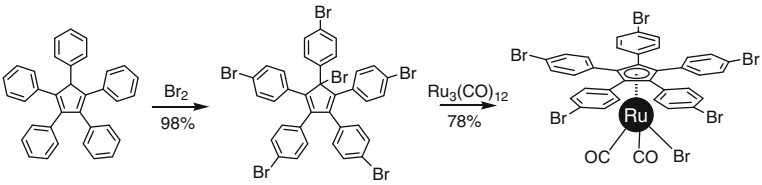

Scheme 1 Synthesis of the organometallic core of the molecular motor

us access to various functionalized ligands. These new ligands are versatile precursors to form the half-sandwich ruthenium complexes which make the core of our molecular motor by binding the Cp ring.

The pentaphenylcyclopentadienyl ligands are highly hindered, and this structural property confers them a peculiar reactivity for instance in their coordination to a ruthenium(II) centre [37]. Coordination via the formation of the pentaphenylcyclopentadienide anion did not give access to the target complexes. Only the methodology described by Manners [38], which uses the oxidative addition of a brominated Cp ring on the $Ru_3(CO)_{12}$ cluster, yielded the bromo η^5-1,2,3,4,5-penta (4-bromophenyl)cyclopentadienyl dicarbonyl ruthenium(II) as shown on Scheme 1.

3.2 Synthesis of the Stator with Anchoring Groups for Various Surface Deposition

The next step towards a molecular motor consisted in the design and synthesis of two new tripodal ligands in view of anchoring the ruthenium complexes onto surfaces. The functionalized borate ligands were designed to have three functional groups pointing on the opposite direction of the coordination site, in order not to interfere sterically with it. Each of the three legs of the tripodal unit bears a functional group connected at the 6-position of indazole, which should be, on the basis of the X-ray structures, obtained on the cyclopentadienyl model complexes [39], the optimal orientation for anchoring on a surface.

The two functionalized tripodal ligands are represented in Fig. 3. The first one incorporates ester-functionalized indazoles ($Tp^{4Bo,6\text{-}COOEt}$) to anchor complexes onto the oxide surface used as insulator in molecular scale NC-AFM experiments. The second synthesized tripode bears thioether-functionalized indazoles ($Tp^{4Bo,6\text{-}CH2SEt}$) to anchor complexes onto metal surfaces to be able to study the rotation of the rotor (including rotation barrier) and also STM tip-induced rotational motions.

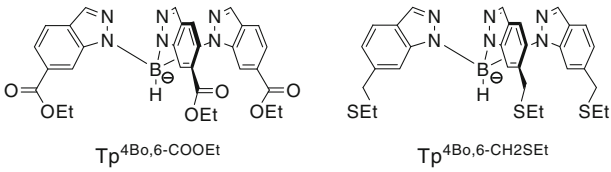

Fig. 3 Functionalized tripodal ligands equipped with ester functions (*left*) to deposit the molecular motors on an insulating oxide surface and with thioether groups (*right*) to anchor the corresponding ruthenium complexes on metallic surfaces

3.3 Coordination of the Tripodal Ligand and Coupling of the Electroactive Ferrocenyl Groups

Coordination of both tripodal ligands was achieved using microwave heating. The two functional tripodal ligands have coordination and redox properties similar to those of the unfunctionalized ones [39].

The presence of the five aryl bromide groups allows the direct connection of the ferrocene electroactive groups after a quintuple Pd-catalysed C–C coupling reaction with ethynylferrocene using the Negishi conditions [40]. The pentaferrocenyl molecular motor was isolated in 42 % yield (Scheme 2). ^{1}H-NMR spectroscopy clearly showed an AA'BB' pattern for the phenyl groups attached to the central Cp ring and the signals of the ferrocene units integrating for 45 protons. The presence of the five ethynylferrocene units was also confirmed by mass spectrometry. This ruthenium complex is the prototype of our family of molecular motors.

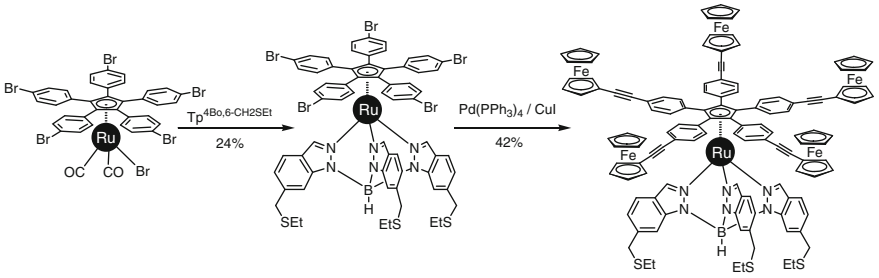

Scheme 2 Synthesis of the pentaferrocenyl molecular motor

3.4 Behaviour in Solution: Electrochemistry and NMR

Once the first prototype of molecular motor terminated with five ferrocenes was synthesized, all the requirements for such a molecule to operate as a molecular motor were analysed. First, the oxidation potential of the iron was lower by

300 meV than the oxidation potential of the Ru centre. This is compatible with our objective in the sense that the ruthenium centre would remain inert towards the redox cycles of the peripheral electroactive groups. In addition, electrochemical processes were reversible, showing the robustness of the molecule towards oxidation. No intervalence band was observed by spectroelectrochemistry, showing that the electronic communication between two iron centres is very weak. Electronic communication is here an unwanted phenomenon since it would allow a charge transport by intramolecular electron hopping between different ferrocene centres, without real motion of the rotor.

As shown by NMR and DFT calculations, the rotation barrier of the rotor fragment was found to be very low [36]. This is a random process in which the rotor part of the molecule explores rapidly many conformations, with back and forth irregular motions. This is very different from the rotation occurring in a macroscopic mechanical motor. At the molecular scale, the inertial forces play a negligible role and cannot sustain the directionality of the motion [28].

3.5 Incorporation of Insulating Spacers

A key requirement in our design was to have the electroactive groups connected through insulating arms, to avoid intramolecular electron transfer between redox sites. Such a process would act as a short-circuit by allowing charges to cross the molecule without the need for an actual motion. Even if electronic communication seems to be low due to the non-planarity of the phenyl rings connected to the central Cp, incorporation of insulating spacers between the ferrocenes and the cyclopentadiene would contribute to annihilate totally these undesired electron transfers. It must be noted that the absence of intervalence transition in the complex (from spectroelectrochemical measurements) does not guarantee that the rate of ferrocene–ferrocenium exchange will be sufficiently small. Since a conjugated skeleton can clearly not separate electronically the electroactive groups, we developed the synthesis of insulating spacers based on platinum acetylide complexes [41, 42] or bicyclo[2, 2, 2]octane fragments [43].

3.5.1 The Trans-platinum Fragment: A Rotor 3 nm in Diameter

Such spacers are presumed to insulate the ferrocene groups by disrupting the electronic communication between them, possibly due to the strong σ character of the Pt–C bonds which breaks the conjugation of the different submodules [44]. Therefore, the charge localization on one single oxidized ferrocenyl unit, which should be the place of the oxido-reduction cycles in the desired process, should be favoured.

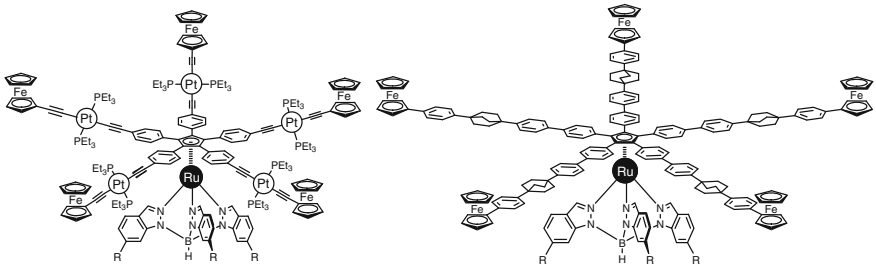

Fig. 4 Chemical structure of the two insulated motors obtained

The synthesis of the ruthenium complex with *trans*-platinum(II) spacers (Fig. 4, left) was achieved by introducing first the alkyne functions and subsequent coordination to a chloro ethynylferrocenyl platinum complex [41]. In this complex, the electronic communication between ferrocene units is again not measurable by spectroelectrochemistry. A theoretical approach combining geometry optimization by DFT and extended Hückel calculations on bis-ferrocenyl model compounds allowed to estimate the electronic communication parameter V_{ab} between ferrocene units. We obtained a fourfold attenuation of V_{ab} in the presence of a *trans*-platinum spacer [42] and an increase from 2 to 3 nm in diameter with the platinum insulating fragments.

3.5.2 The Bicyclo[2.2.2]Octane Spacer: A Rotor 4 nm in Diameter

In order to obtain a better insulation, we also synthesized a molecular motor where the electroactive groups are separated by bicyclo[2.2.2]octane spacers (Fig. 4, right) [43].

DFT and extended Hückel calculations showed in this case a 12-fold decrease of the electronic coupling between ferrocene units. Since there are by design two insulating groups between two ferrocenes, the total effect will be of a factor 144 (12 × 12) which is one order of magnitude more important than the effect from the platinum fragment with a global effect of a factor 16 (4 × 4). In addition, the diameter is now close to 4 nm (double the diameter without insulating groups) which also prevents efficiently through-space intramolecular electron transfers. Moreover, the absence of triple bonds in the backbone gives rise to a more rigid structure that should be more stable towards the deposition process. This alkyne-free architecture was obtained following another type of carbon–carbon bond formation: Suzuki coupling using Buchwald's recent universal catalyst [45], which is very active even for deactivated substrates as in our case.

3.6 Introducing Chirality to Promote Unidirectional Motion

To control the direction of the rotation, we have to consider how a molecule and a surface interact. This interaction establishes the coupling of the different conformations of the motor and allows to decrease its rotational energy. The latter is not controlled because the surface is a thermal energy source which can provide only a local thermal fluctuation. Applied to our design, as shown in Sect. 5.2, the potential energy curve is symmetric and the molecule turns in one or the other direction in a random manner since the activation barriers are equal in both directions.

To obtain a unidirectional rotation, a strong dissymmetrization of the two directions of rotation is required in order to obtain a highly dissymmetric potential energy curve for the system. The two corresponding rotational rates could be differentiated by coupling the molecule with an energy source such as the electric field created between the two electrodes of a nanojunction. In the case of our molecular motor, a unidirectional rotation should be obtained by placing it in a dissymmetric manner in the nanojunction as it is presented in Fig. 1. This dissymmetry should favour the rotation in one direction.

To achieve directionality in the rotation, one could also think of introducing chirality in the chemical backbone. In agreement with the second principle of thermodynamics [46], chirality alone is not sufficient to obtain a unidirectional rotation in a movement driven only by thermal energy. Nevertheless, chirality could be an additional way to enhance the difference of rotational rate corresponding to the two directions.

We tried to prepare enantiopure C_3-symmetrical hydrotris(pyrazolyl)borate ligands derived from (5*R*)-dihydrocarvone, commercially available as a (2*R,* 5*R*) and (2*S,* 5*R*) diastereomeric mixture from the chiral pool. Its olefin moiety was converted into an ester function for the future immobilization of the molecular motor onto insulating oxide surfaces. Molecular modelling was performed on the ruthenium complex with Cerius2 (Fig. 5, left) in order to check that the target tris (pyrazolyl)borate coordinated to the ruthenium centre (Fig. 5, right) would indeed induce the desired helicity once coordinated.

The chirality of the tripodal ligand, and particularly the methyl groups at the 4-position of the ring, strongly interact with the cyclopentadienyl ligand, which is the key to induce a strong dissymmetry in the system. Unfortunately, we were not able to resolve the pyrazole sub-unit [47] which prevented us to obtain the enantiopure tripodal ligand.

4 Molecular Gears Based on Star-shaped Complexes

After the seminal work of Mislow on molecular gears [13], a few groups designed and synthesized molecular gears studied in solution. Only one recent example has been studied at the single-molecular scale [16]: hexa(4-*tert*-butylphenyl)benzene.

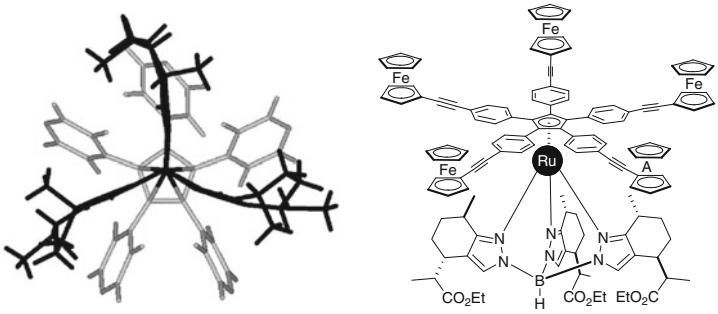

Fig. 5 Molecular modelling (*left*, *bottom view*) and chemical structure (*right*) of the ruthenium complex integrating a chiral hydrotris(pyrazolyl)borate ligand. The modelling has been performed on the full molecule, but to obtain a clear representation, the ester and the ethynylferrocenyl fragments have been omitted. The modelling clearly shows the induced helicity of the molecule in its minimum energy conformation (UFF, Cerius2 software)

However, its use as gear is prevented by the lateral diffusion of the molecule on the surface since there is no functional group to anchor the molecule.

The star-shaped geometry of the family of molecular motors based on organometallic ruthenium complexes inspired us to design notched circular molecules as potential gears. For that purpose, the presence of the peripheral ferrocene groups is not necessary and must be avoided since the lateral rotation around the axis of the spacers would prevent their use as gears.

Our aim is to manipulate molecules on a surface to build a train of gears and rotate the first gear mechanically with the STM tip to see if the rotation propagates through the train of gear. It must be noted that the tripodal ligand functionalized with three thioether functions is able to anchor the molecule on a Au(111) surface at very low temperature. Warming up to 77 K (liquid N_2) allows us to move the molecules in order to align them as we wish. Then, cooling the surface at 5 K (liquid He) allows us to study the propagation of the rotation through neighbouring molecules as shown in Fig. 6.

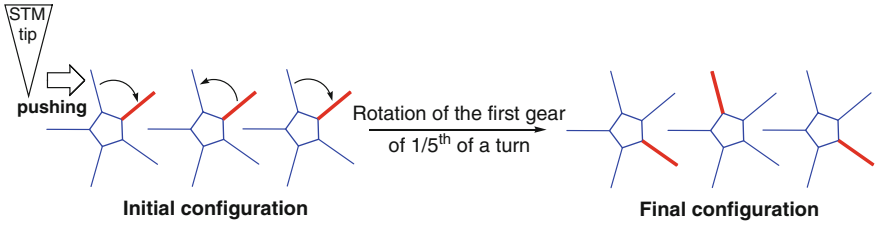

Fig. 6 Pushing the STM tip will start the rotation of the first gear (*left*). Rotation of 1/5th of a turn could be transferred to neighbours thanks to a gearing mechanism. Following the rotation transfer is enabled by the tagged arm (in *bold*)

4.1 Strategy Derived from the Pentaphenylcylopentadienyl Ruthenium Complexes

For that purpose, we designed and synthesized ruthenium complexes as notched elements with a tripodal ligand functionalized to be anchored on metallic surface and built around a Cp ligand equipped with four biphenyl paddles and one phenylpyridine as fifth paddle (Fig. 7, left). Replacement of a CH fragment by a nitrogen atom has proven its efficiency to induce a strong difference in the contrast on STM images [4]. This tag will allow us to discriminate one paddle and thus to follow its rotation.

Due to the tripodal ligand that alleviates the Cp ring, the gear is decoupled from the surface and at the same time maintained precisely at the same distance from its neighbouring gear.

4.2 Alternative Strategy

Preliminary, STM studies showed the ineffectiveness of such gears, since the rotation induced by the STM tip did not propagate to neighbours. Theoretical calculations showed it possible for two intricated gears to have the first gear rotating without inducing any rotation of the neighbour: this is due to the vertical deformation of the arms, which avoid contact with the next gear.

To bypass this obstacle, we designed a second generation of gears for which the synthesis is underway. Instead of 1D-arms, the idea is to have 2D-arms which are not arms anymore, but rather act as paddles (Fig. 7, right). In this design, steric hindrance forces the 2D-paddles to be perpendicular to the cyclopentadiene ring, and despite vertical deformation, it seems sterically impossible to rotate the first gear without rotating its neighbour.

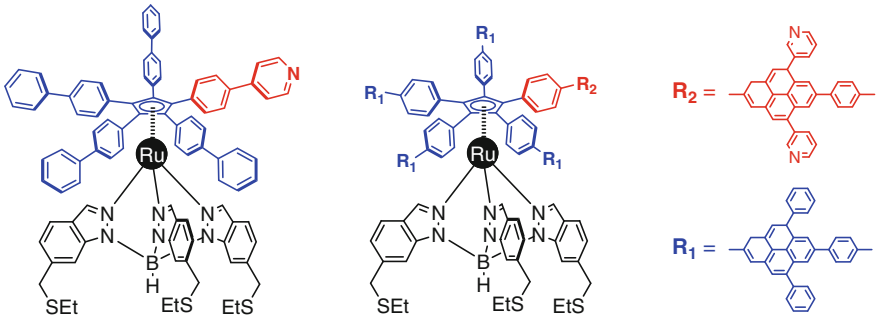

Fig. 7 A molecular gear free to rotate anchored on the surface by a ruthenium trisindazolylborate centre. *Left* the first generation equipped with 1D-arms; *right* the second generation with 2D-paddles. Nitrogens on the pyridine rings of the rotor will act as tags to follow the rotation

5 Dissymmetrization of the Motor: The Tetraferrocenyl Motor

5.1 Breaking the Symmetry to Help Visualize the Rotation

In order to monitor the rotation by near-field microscopy, a crucial problem lies in a practical way to evidence the rotation. Due to the high symmetry of the molecule, two images obtained after a fifth of a turn would be indistinguishable with a C_5-symmetric rotor. However, this issue can be partly addressed using compounds of lower symmetry. For that purpose, we designed and synthesized a dissymmetrized rotor in which one ferrocene electroactive group is missing [48]. Lowering the symmetry of the molecule should help to prove a movement and monitor the rotation, the missing ferrocene acting as a probe for the precise position of the rotor. Since the coupling of four equivalents of ethynylferrocene with 1-bromo-1,2,3,4,5-penta(*p*-bromophenyl) cyclopentadiene gives access to an unseparable mixture of penta-, tetra-, tri-, di- and mono-ferrocenyl compounds, a rational synthesis of a dissymmetrized pentaphenylcyclopentadienyl ligand, a tetra-ferrocenyl derivative, was needed.

The key feature of our strategy was to block one position of the Cp ring during the synthesis of the pentaphenylcyclopentadiene building block. The cyclopentadienone precursor was reacted with *p*-tolylmagnesium bromide to insert the fifth phenyl moiety on the cyclopentadiene ring with a methyl group, as a convenient probe, instead of a bromine atom in the *para* position (Scheme 3).

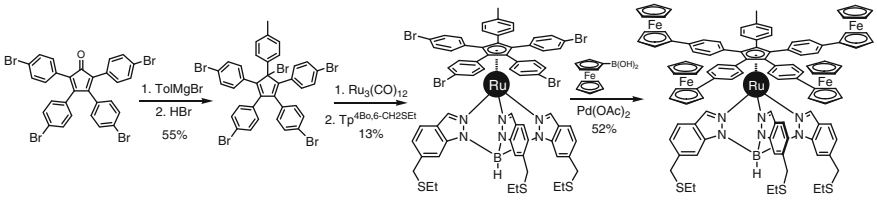

Scheme 3 Synthesis of the dissymmetrized tetraferrocenyl molecular motor

Following the same methodology developed to prepare the pentaferrocenyl derivative, the tetraferrocenyl molecular motor was obtained in three steps from the brominated Cp.

5.2 Calculation of the Potential Energy Curve

To understand the rotation process of the rotor relative to the stator and the role of the interaction between these two sub-units, theoretical calculations were performed for a free molecule and for a molecule chemisorbed by its thioether groups to a Au (111) surface. Despite the molecular complexity due to the large number of atoms

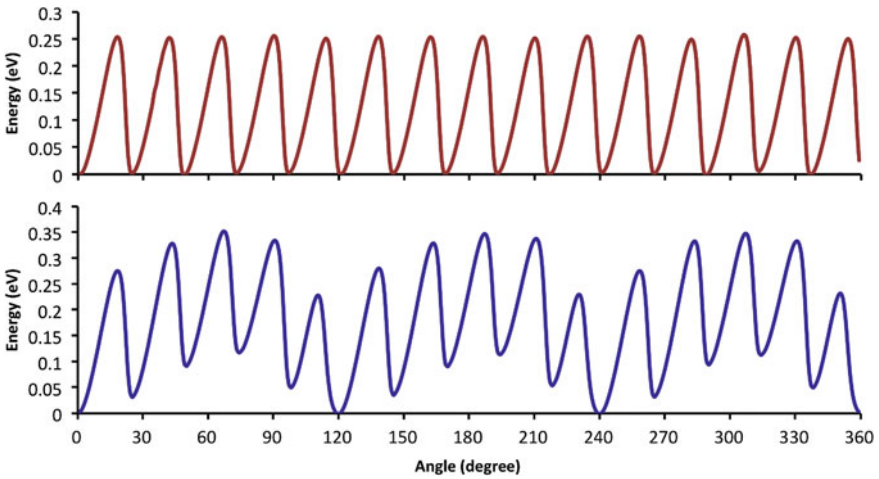

Fig. 8 *Top* fifteen uniform potential wells of the ground-state potential energy for a 360° rotation of the pentaferrocenyl rotor; *bottom* when one ferrocene is missing, the lower symmetry induces a dissymmetry in the ground-state potential

composing the molecule (215) including one ruthenium and four or five irons and while attached to the surface, the system mechanics can be described using a simplified reaction path determined by minimizing the full conformation of the molecule for each value of a collective rotation angle of the upper rotor around the central Ru axis. Of course, we are aware that the rotation angle is not the only possible motion. However, the presence of the stator and the relative rigidity of the rotor allow the five arms to remain practically in the same plane during the rotation process. The associated ground-state rotation energy profile was calculated by means of the ASED + semi-empirical technique by forcing the rotation in steps of one degree. Computational details can be found in Ref. [49]. The results are shown in Fig. 8.

The asymmetry of the peaks arises from the interaction of the phenyl rings of the arms with the legs of the stator, which are anchored to the surface. The combination of the upper pseudo-C_5 and the lower C_3 concurrent symmetries leads to 15 potential wells per turn and, thus, a period of 24° (a longer period of 120° is observed for the tetraferrocenyl molecular motor). The ASED+ calculated rotation barrier height is 0.25 eV for the pentaferrocenyl motor. In the case where one ferrocene is missing, due to the lower symmetry, this barrier varies between 0.22 and 0.35 eV (Fig. 8) depending on the position of the truncated arm with respect to the stator. It is worth noting that the asymmetry observed in Fig. 8 is the result of a forced rotation. Therefore, this asymmetry is artificial since it is associated to the pseudo-ratchet effect created by us when forcing the rotation, and thus, it is not an intrinsic characteristic of the molecular motor.

Due to the modulation of its rotation barriers, the motor with one ferrocene missing thus seems to be a particularly interesting candidate to obtain a unidirectional rotation.

5.3 Controlled Clockwise or Counterclockwise Unidirectional Rotation

In order to obtain a unidirectional rotation, electrons were transferred through the motor using the tip apex of an STM serving both as an observation instrument and an energy source. Stepwise rotation has been performed at 4.6 K on a Au(111) surface [49]. The direction of rotation depends on the blade of the rotor above which the STM tip apex is positioned. The lack of one ferrocene induces an asymmetry in the rotation, which leads to unidirectional motion into both clockwise and counterclockwise directions. This has been achieved experimentally by selectively exciting different sub-units of the motor: excitation of the truncated arm (the arm with one ferrocene missing) induces clockwise rotation, while excitation on one of the four ferrocene-terminated arms induces counterclockwise rotation (Fig. 9).

Contrary to our initial design (Sect. 2.1), unidirectional rotation is obtained without oxidation and reduction of the ferrocenyl electroactive groups. In this vertical configuration using the STM tip as a source of electron and a metallic surface as electron drain, the electron transfer processes are too fast to induce

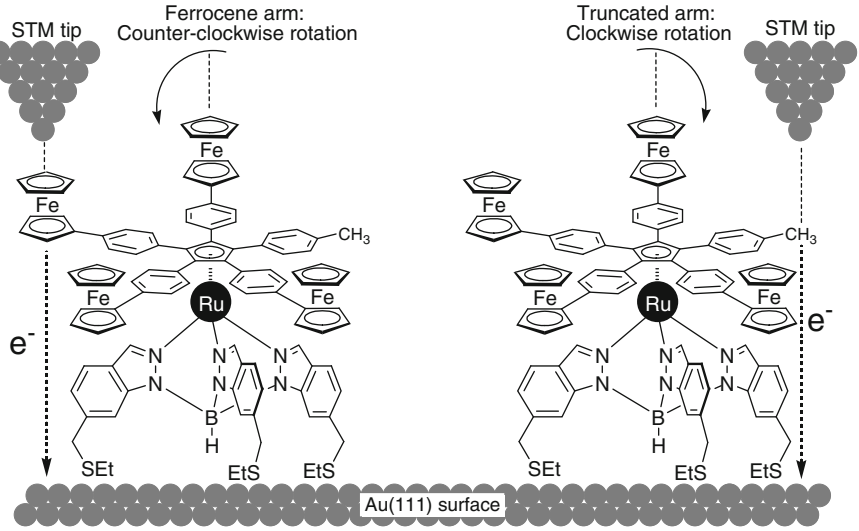

Fig. 9 Unidirectional rotation of the rotor obtained by positioning the STM tip on a ferrocene arm or on the truncated arm

oxidation or reduction processes. The electrons are tunnelling via different excited states when going through different sub-units of the molecule. This induces rotation in opposite directions, which can be reversed at will. For the first time, the directional rotation was solely determined by the internal molecular structure, independently of the surface adsorption site, and it is possible to reverse the direction of rotation at will.

6 Conclusion and Perspectives

Work is now underway to anchor these molecules on an insulating oxide surface in view of addressing them as single molecules with two metallic nanoelectrodes (horizontal connection) to see if rotation can occur via oxido-reduction processes. Moreover, the synthesis of the next generation of molecular motors is also in progress in order to estimate and explore strategies to use the work furnished by the unidirectional rotation of the rotor. Although some progress has been made, it is still a long way to practical applications.

Acknowledgements This work was supported by the CNRS, the Université Paul Sabatier (Toulouse), the Institut Universitaire de France, the European Union and the ANR P3N (AUTOMOL project no. ANR 09-NANO-040). We are also grateful to the researchers who participated in all the work discussed here and whose names appear in the references, in particular Prof. Saw-Wai Hla (Ohio University, USA) who performed the STM study on the molecular motor.

References

1. Moresco, F.: Manipulation of large molecules by low-temperature STM: model systems for molecular electronics. Physics Reports, vol. 399, p. 175 and references therein (2004)
2. Rapenne, G.: Synthesis of technomimetic molecules: towards rotation control in single molecular machines and motors. Org. Biomol. Chem. **3**, 1165 (2005)
3. Grill, L., Rieder, K.H., Moresco, F., Rapenne, G., Stojkovic, S., Bouju, X., Joachim, C.: Rolling a single molecular wheel at the atomic scale. Nature Nanotechnol. **2**, 95 (2007)
4. Jacquot de Rouville, H.-P., Garbage, R., Ample, F., Nickel, A., Meyer, J., Moresco, F., Joachim, C., Rapenne, G.: Synthesis and STM imaging of symmetric and dissymmetric ethynyl-bridged dimers of boron-subphthalocyanine bowl-shaped nano-wheels. Chem. Eur. J. **18**, 8925 (2012)
5. Nickel, A., Meyer, J., Ohmann, R., Jacquot de Rouville, H.-P., Rapenne, G., Joachim, C., Cuniberti, G., Moresco, F.: STM manipulation of boron-subphthalocyanine nano-wheel dimers on Au(111). J. Phys. Condens. Matter **24**, 404001 (2012)
6. Chu, P.L.E., Wang, L.Y., Khatua, S., Kolomeisky, A.B., Link, S., Tour, J.M.: Synthesis and single-molecule imaging of highly mobile adamantane-wheeled nanocars. ACS Nano **7**, 35 (2013)
7. Vives, G., Tour, J.M.: Synthesis of single-molecule nanocars. Acc. Chem. Res. **42**, 473 (2009)
8. Jacquot de Rouville, H.P., Garbage, R., Cook, R.E., Pujol, A.R., Sirven, A.M., Rapenne, G.: Synthesis of polycyclic aromatic hydrocarbon-based nanovehicles equipped with triptycene wheels. Chem. Eur. J. **18**, 3023 (2012)

9. Kudernac, T., Ruangsupapichat, N., Parschau, M., Maci, B., Katsonis, N., Harutyunyan, S.R., Ernst, K.-H., Feringa, B.L.: Electrically driven directional motion of a four-wheeled molecule on a metal surface. Nature **479**, 208 (2011)
10. Jimenez-Bueno, G., Rapenne, G.: Technomimetic molecules: synthesis of a molecular wheelbarrow. Tetrahedron Lett. **44**, 6261 (2003)
11. Grill, L., Rieder, K.H., Moresco, F., Jimenez-Bueno, G., Wang, C., Rapenne, G., Joachim, C.: Imaging of a molecular wheelbarrow by scanning tunneling microscopy. Surf. Sci. **584**, 153 (2005)
12. Rapenne, G., Jimenez-Bueno, G.: Molecular machines: synthesis and characterization of two prototypes of molecular wheelbarrows. Tetrahedron **63**, 7018 (2007)
13. Chance, J.M., Geiger, J.H., Mislow, K.: A parity restriction on dynamic gearing immobilizes the rotors in tris(9-triptycyl)germanium chloride and tris(9-triptycyl)cyclopropenium perchlorate. J. Am. Chem. Soc. **111**, 2326 (1989)
14. Clayden, J., Pink, J.H.: Concerted rotation in a tertiary aromatic amide: towards a simple molecular gear. Angew. Chem. Int. Ed. **37**, 1937 (1998)
15. Carella, A., Jaud, J., Rapenne, G., Launay, J.-P.: Technomimetic molecules: synthesis of an organometallic molecular turnstile. Chem. Commun. 2434 (2003)
16. Manzano, C., Soe, W.-H., Wong, H.S., Ample, F., Gourdon, A., Chandrasekhar, N., Joachim, C.: Step-by-step rotation of a molecule-gear mounted on an atomic-scale axis. Nature Mater. **8**, 576 (2009)
17. Gimzewski, J.K., Joachim, C., Schlitter, R., Langlais, V., Tang, H.: Rotation of a single molecule within a supramolecular bearing. Science **281**, 531 (1998)
18. Leigh, D.A., Wong, J.K.Y., Dehez, F., Zerbetto, F.: Unidirectional rotation in a mechanically interlocked molecular rotor. Nature **424**, 174 (2003)
19. Kottas, G.S., Clarke, L.I., Horinek, D., Michl, J.: Artificial molecular rotors. Chem. Rev. **105**, 1281 (2005)
20. Kay, E.R., Leigh, D.A., Zerbetto, F.: Synthetic molecular motors and mechanical machines. Angew. Chem. Int. Ed. **46**, 72 (2007)
21. Ruangsupapichat, N., Pollard, M.M., Harutyunyan, S.R., Feringa, B.L.: Reversing the direction in a light-driven rotary molecular motor. Nature Chem. **3**, 53 (2011)
22. Vives, G., Jacquot de Rouville, H.P., Carella, A., Launay, J.P., Rapenne, G.: Prototypes of molecular motors based on star-shaped organometallic ruthenium complexes. Chem. Soc. Rev. **38**, 1551 (2009)
23. Tierney, H.L., Murphy, C.J., Jewell, A.D., Baber, A.E., Iski, E.V., Khodaverdian, H.Y., McGuire, A.F., Klebanov, N., Sykes, E.C.H.: Experimental demonstration of a single-molecule electric motor. Nature Nanotechnol. **6**, 625 (2011)
24. Yao, Y., Tour, J.M.: Facile convergent route to molecular caltrops. J. Org. Chem. **64**, 1968 (1999)
25. Guo, W., Galoppini, E., Rydja, G., Pardi, G.: Synthesis of a molecular tripod to anchor molecular coordination compounds to semiconductor nanoparticles. Tetrahedron Lett. **41**, 7419 (2000)
26. Vacek, J., Michl, J.: A molecular "Tinkertoy" construction kit: Computer simulation of molecular propellers. New J. Chem. **21**, 1259 (1997)
27. Jian, H., Tour, J.M.: En route to surface-bound electric field-driven molecular motors. J. Org. Chem. **68**, 5091 (2003)
28. Joachim, C., Gimzewski, J.K.: Single molecular rotor at the nanoscale. Struct. Bond. **99**, 1 (2001)
29. Moresco, F., Meyer, G., Rieder, K.H., Tang, H., Gourdon, A., Joachim, C.: Recording intramolecular mechanics during the manipulation of a large molecule. Phys. Rev. Lett. **87**, 088302 (2001)
30. Loppacher, C., Guggisberg, M., Pfeiffer, O., Meyer, E., Bammerlin, M., Lüthi, R., Schlittler, R.R., Gimzewski, J.K., Tang, H., Joachim, C.: Direct determination of the energy required to operate a single molecule switch. Phys. Rev. Lett. **90**, 066107 (2003)

31. Carella, A., Rapenne, G., Launay, J.-P.: Design and synthesis of the active part of a potential molecular rotary motor. New J. Chem. **29**, 288 (2005)
32. Park, H., Park, J., Lim, A.K.L., Anderson, E.H., Alivisatos, A.P., McEuen, P.L.: Nanomechanical oscillations in a single-C_{60} transistor. Nature **407**, 57 (2000)
33. Trofimenko, S.: Scorpionates: The Coordination Chemistry of Polypyrazolylborate Ligands. Imperial College Press, London (1999)
34. Astruc, D.: Electron and proton reservoir complexes: thermodynamic basis for C–H activation and applications in redox and dendrimer chemistry. Acc. Chem. Res. **33**, 287 (2000)
35. Broadley, K., Lane, G.A., Connelly, N.G., Geiger, W.E.: Electrochemical routes to paramagnetic dinuclear and mononuclear palladium π complexes stabilized by the pentaphenylcyclopentadienyl ligand. J. Am. Chem. Soc. **105**, 2486 (1983)
36. Carella, A., Launay, J.-P., Poteau, R., Rapenne, G.: Synthesis and reactivity of penta(4-halogenophenyl)cyclopentadienyl hydrotris (indazolyl)borate ruthenium(II) complexes: rotation-induced Fosbury flop in an organometallic molecular turnstile. Chem. Eur. J. **14**, 8147 (2008)
37. Vives, G., Carella, A., Launay, J.-P., Rapenne, G.: The chemistry of 1,2,3,4,5-pentaphenylcyclopentadienyl hydrotris(indazolyl)borate ruthenium(II) complexes, building blocks for the construction of potential organometallic molecular motors. Coord. Chem. Rev. **252**, 1451 (2008)
38. Connelly, N.G., Manners, I.: Reduction–oxidation properties of organotransition-metal complexes. Part 29. Pentaphenylcyclopentadienyl complexes of ruthenium. J. Chem. Soc. Dalton Trans. 283 (1989)
39. Carella, A., Vives, G., Cox, T., Jaud, J., Rapenne, G., Launay, JP.: Synthesis of new tripodal tri-functionalized hydrotris(indazol-1-yl)borate ligands and X-ray structure of their ruthenium cyclopentadiene complexes. Eur. J. Inorg. Chem. 980 (2006)
40. King, A.O., Negishi, E., Villani, F.J., Silveira, A.: A general synthesis of terminal and internal arylalkynes by the palladium-catalyzed reaction of alkynylzinc reagents with aryl halides. J. Org. Chem. **43**, 358 (1978)
41. Vives, G., Carella, A., Launay, J.-P., Rapenne, G.: A star-shaped ruthenium complex with five ferrocenyl-terminated arms bridged by trans-platinum fragments. Chem. Commun. 2283 (2006)
42. Vives, G., Sistach, S., Carella, A., Launay, J.-P., Rapenne, G.: Synthesis of triester-functionalized molecular motors incorporating bis-acetylide trans-platinum insulating fragments. New J. Chem. **30**, 1429 (2006)
43. Vives, G., Gonzalez, A., Jaud, J., Launay, J.-P., Rapenne, G.: Synthesis of molecular motors incorporating bicyclo [2.2.2] insulating fragments. Chem. Eur. J. **13**, 5622 (2007)
44. Siemsen, P., Gubler, U., Bosshard, C., Gunter, P., Diederich, F.: Pt-tetraethynylethene molecular scaffolding: synthesis and characterization of a novel class of organometallic molecular rods. Chem. Eur. J. **7**, 1333 (2001)
45. Walker, S.D., Barder, T.E., Martinelli, J.R., Buchwald, S.L.: A rationally designed universal catalyst for Suzuki-Miyaura coupling processes. Angew. Chem. Int. Ed. **43**, 1871 (2004)
46. Mandl, C.P., König, B.: Chemistry in motion—unidirectional rotating molecular motors. Angew. Chem. Int. Ed. **43**, 1622 (2004)
47. Jacquot de Rouville, H.-P., Vives, G., Tur, E., Crassous, J., Rapenne, G.: Synthesis and analytical resolution of chiral pyrazoles derived from dihydrocarvone. New J. Chem. **33**, 293 (2009)
48. Vives, G., Rapenne, G.: Directed synthesis of symmetric and dissymmetric molecular motors built around a ruthenium cyclopentadienyl tris(indazolyl)borate complex. Tetrahedron **64**, 11462 (2008)
49. Perera, U.G.E., Ample, F., Echeverria, J., Kersell, H., Zhang, Y., Vives, G., Rapenne, G., Joachim, C., Hla, S.-W.: Clockwise or counterclockwise unidirectional step-by-step rotation of a single molecular motor. Nature Nanotechnol. **8**, 46 (2013)

Assembling Supramolecular Rotors on Surfaces Under Ambient Conditions

Josep Puigmartí-Luis, Wojciech J. Saletra, Asensio González, Lluïsa Pérez-García and David B. Amabilino

Abstract The formation of supramolecular rotor-type systems on surfaces under ambient conditions is discussed. We present in detail the assembly of a rotor on a gold surface from solution, where the surface acts as a stator, a pyridyl containing thiol acts as the axle, and a C_4 symmetrical porphyrin bearing "paddle-like" arms is the intended rotator. The effective non-covalent attachment of the rotator to the axle is achieved instantly in solution. However, when the axle forms part of a self-assembled monolayer (SAM), the complex formation is practically negated if the SAM's organization is not appropriate. Thus, the SAM formed on gold by the pyridyl thiol subject of this study does not bind the rotator part of the system—a zinc(II)porphyrin bearing four biphenyl moieties. This negative allosteric surface effect can be overturned by combining the pyridyl thiol with dodecanethiol: the resulting mixed SAM contains pyridyl groups which are oriented quasi-perpendicular to the surface and are therefore available for binding. The difference in the surface organization is achieved using only 1 part in 10 of the alkanethiol (which forms small ordered domains alone). This dramatic effect may find use in other areas where SAMs are used as template layers because the capacity for the surface-anchored ligand to bind solution-borne compounds is affected by its orientation. Exposure of this mixed monolayer to a solution of the zinc(II)porphyrin results in attachment of this rotator component to the surface, which was imaged by scanning tunnelling microscopy (STM). Alternatively, formation of the axle–rotator complex in solution followed by chemisorption of this supramolecular object to the metal surface leads (in places) to a dense layer of the rotators. The presence of the

J. Puigmartí-Luis · W.J. Saletra · D.B. Amabilino (✉)
Institut de Ciència de Materials de Barcelona (ICMAB-CSIC),
Campus Universitari de Bellaterra, 08193 Cerdanyola del Vallès,
Catalonia, Spain

A. González · L. Pérez-García (✉)
Departament de Farmacologia i Química Terapèutica, Universitat de Barcelona,
Av. Joan XXIII, s/n, 08028 Barcelona, Spain

L. Pérez-García
Institut de Nanociència i Nanotecnologia IN2UB, Universitat de Barcelona,
08028 Barcelona, Catalonia, Spain

C. Joachim and G. Rapenne (eds.), *Single Molecular Machines and Motors*,
Advances in Atom and Single Molecule Machines, DOI 10.1007/978-3-319-13872-5_8

porphyrin was confirmed by mass spectrometry. The results show how the bottom-up route employed can influence the arrangement of ligating moieties in a monolayer, provide a protocol for the preparation of sparse and dense layers of rotors on surfaces, and thereby help plot the road map to the bottom-up creation of surface-based molecular machines based on interconnected rotors.

1 Introduction

A current challenge in molecular nanoscience is the assembly of nanometre-scale functional systems using precise bottom-up surface modification [1–4]. Biological processes such as cellular transport or muscle contraction are based on molecular motion and function at interfaces on the micro- and even nanometre scale [5, 6] and provide an inspiration for the fabrication and employment of synthetic molecular machinery [7]. Control over the interfaces is essential in both systems for correct function. Progress in conceiving man-made systems that are supported on a more or less rigid material and that are able to perform some function is challenging for a number of reasons. To control function and performance of molecular-sized machines on surfaces has become a matter of great effort in recent years. Research into molecular motion at the (sub)molecular level on surfaces has demonstrated single artificial molecular machines [8–10], and yet very little is known about systems and approaches that lead to an accurate geometry of anchoring on a surface. A precise molecular orientation is important because minor differences could cause large modifications of motional dynamics. The gap between artificial and biological-based machinery remains considerably large at present because of the difficulty in anchoring efficiently and accurately machine components using purely bottom-up protocols from a substrate.

Considerable achievements have been made showing molecular motion on non-chemisorbed or weakly bound systems under relatively extreme environments, i.e. ultrahigh vacuum and low-temperature conditions [11–14]. For example, multilayer assemblies of multidecker porphyrin complexes constructed on surfaces through van der Waals interactions have currently led to the description of promising supramolecular assemblies with rotational and electrical function at the nanometre scale [15]. Surface spatial recognition and positioning and specific anchored configuration are needed for further molecular machine system development. Only with a specific surface structure in hand, can one tackle precisely a supramolecular organization above it. Therefore, unlike mono- and multilayer physisorbed assemblies [16], a key point for future development would be to design and construct optimized surface anchoring supramolecular components.

A very interesting particular case is the formation of layers which contain rotor systems in which the rigid axle is oriented perpendicularly to the surface with the mobile components parallel to it [17–19]. We target solution-based bottom-up methods for the preparation of supramolecular rotors (Fig. 1) [20]. Towards this

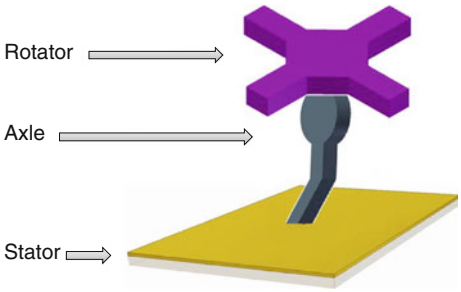

Fig. 1 A cartoon representing the kind of surface-based molecular rotor that is the objective of our work

goal, we will use the axial coordination of large π-functional molecules—which can be readily imaged using scanning probe microscopies and which act as rotators—bound to axles which link to a surface which is the stator component.

A zinc(II)porphyrin is used as the large π-functional molecule in our approach. These compounds complex pyridyl-type ligands in an axial way, either in solution [21, 22] or on a surface [23–26], so that the metal ion has square-based pyramidal pentacoordinate geometry. Metalloporphyrins are great components for primitive synthetic molecular machinery, especially double-decker systems where rotation of one ring with respect to another takes place [27, 28], and of rotors and turnstiles in solution [29, 30], systems where the porphyrin supplies energy from photoexcitation to another component [31]. Also, their large size allows imaging of their movement in some examples [32–34]. Therefore, the discovery of new mechanisms for anchoring of metalloporphyrins on surfaces is potentially useful. Thereby, novel functioning molecular machines could be effectively incorporated into surfaces and eventually into devices.

As the surface, a flat metal will be used. The conductivity of this substrate will allow imaging of the eventual system by scanning tunnelling microscopy (STM) (and therefore, the axle part of the system should not be too long to allow for efficient electron tunnelling). A flat, symmetrical surface will avoid any corrugation affecting rotor movement: A (111) metal surface is therefore ideal, the lower symmetry surfaces containing ruts and steps.

Here, we present results concerning the anchoring of the porphyrin rotator motifs on the highest symmetry surface of gold (which is the stator) and the foundation for the creation of these motifs whereby the axle that binds the rotator has its orientation controlled in a self-assembled monolayer (SAM). The presence of the monolayer is foreseen as being necessary to prevent the tipping of the axle and "crashing" of the rotator into the surface. It also turned out in our studies that the structure of the monolayer is essential to efficient binding, and the orientation of the groups involved in the rotor must be controlled. This has been proven here firstly using a mixed monolayer. We exploit a well-established and well-organized SAM —a dodecanethiol monolayer—on metallic gold to force the orientation of a

pyridine end group in a particular way. The aim is to orient the pyridine moiety perpendicularly from the gold surface plane so that the coordination of a zinc–porphyrin derivative can be achieved readily. If the ligating pyridyl group were tilted to the perpendicular, one would expect that binding of the porphyrin would be more difficult because the side groups on the porphyrin core could come into contact with the surface even before binding took place, making the system too dynamic in the best-case scenario. On the other hand, solution-based preassembly of the rotor is an efficient pathway to a monolayer with oriented axle components. The bottom-up assembly of this kind of multicomponent system—comprising surface, two-component monolayer, rotator and solvent—is a step towards novel surface-based functional molecular systems where "intelligent" components can self-assemble onto substrates to give complex arrangements that display novel behaviours at the molecular and supramolecular level.

2 Results and Discussion

The thiol **1** (Fig. 2) was used as the axle component. The conformation of this molecule on the gold surface should allow the perpendicular arrangement of the dipole of the pyridyl ring to the substrate when the thiol is attached to it by chemisorption as a result of thiolate formation. This hypothesis is based on the assumption that the gold–sulphur bond is perpendicular to the gold surface (Fig. 2). In between these axle components, molecules of **1** that are not complexed in the eventual rotor serve to fill the space underneath the porphyrin; dodecanethiol (**2**, Fig. 2) was also used for the space-filling purpose. Although longer than **1**, **2** forms well-defined layers that can be identified by STM [35, 36] and on the other hand could serve to restrict the motion of the rotator which could otherwise have rapid motion on the timescale of the STM experiment.

The SAMs (Fig. 2) of the thiols **1** and **2** chemisorbed onto Au(111) surfaces were visualized individually by STM in air. These studies were conducted on SAMs of the separate thiols in order to understand the organization of the two molecules in their own right under identical adsorption conditions and to explore whether molecules of **1** have observable pyridyl groups standing quasi-perpendicular to the surface plane in the monocomponent assembly, as we had envisaged. Figure 2a shows a representative STM image of **1** chemisorbed on Au(111) by deposition of a toluene solution of the molecule. The white areas present in the STM images correspond to higher tunnelling current when compared with the darker surround where tunnelling current is lower. The brighter areas logically correspond to the pyridyl rings [37]. A disordered layer of molecules of **1** is patent on the gold substrate when compared with that of a SAM of **2** on a similar Au(111) film and formed under identical conditions. Figure 2b shows a familiar highly organized SAM of **2** on gold. Details of the internal structure and packing arrangement are presented in a close-up image showing the unit cell packing structure of **2** on Au(111) (Fig. 2b inset). In fact, molecules of **2** organize forming a

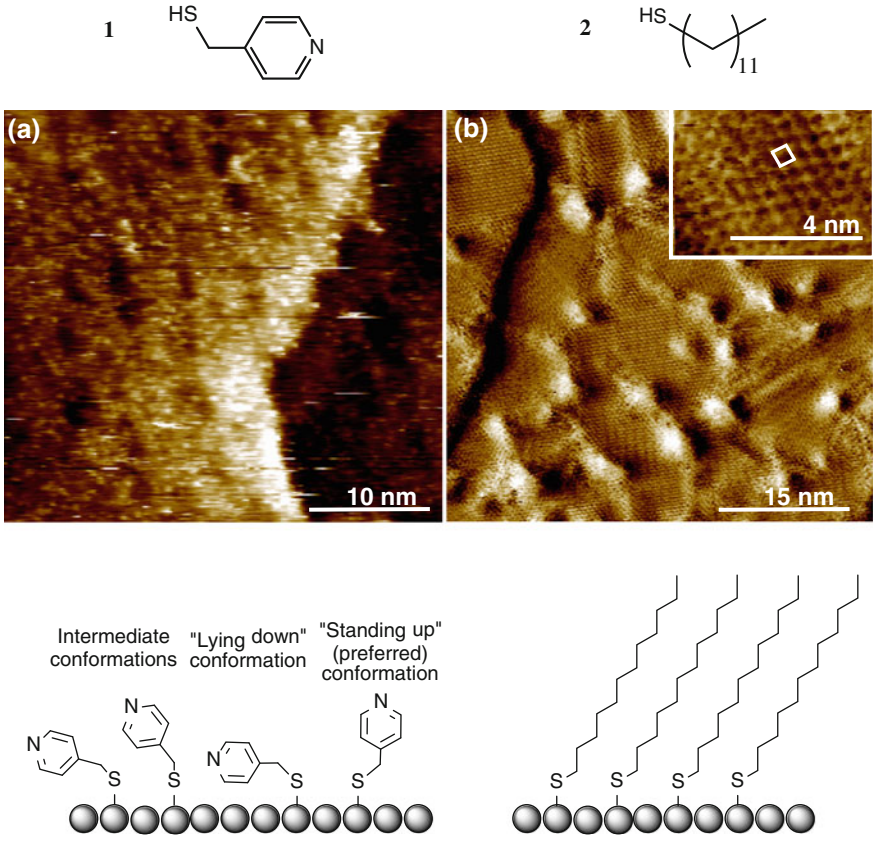

Fig. 2 The chemical structures of **1** and **2** and images recorded using scanning tunnelling microscopy in air of self-assembled monolayers on Au(111) of **a 1** (I_{set} = 0.05 nA, V_{bias} = −0.8 V) in topographical mode and **b** 2 (I_{set} = 0.6 nA, V_{bias} = 0.85 V) in current mode on Au(111). The closely packed arrangement and the unit cell present in SAMs of **2** are evident in the inset in **b**. Below are the representations of the possible conformations of the pyridyl thiol in the layer and the well-ordered structure of dodecanethiolate

dense and stable ($\sqrt{3} \times \sqrt{3}$)R30° hexagonal lattice, a superstructure that is commensurate with the metal substrate, with distances between each molecular unit of 0.5 nm, as seen previously [35, 36]. With respect to the self-assembly of **1** on Au (111), similar non-periodic structures have been observed for SAMs of other aromatic thiolates on gold [38], where data indicated a lying-down arrangement of molecules on the surface, that is in a co-parallel orientation with respect to the plane of the surface (Fig. 2), a conformation which in principle is not convenient for our proof of concept adlayer formation with a zinc(II)porphyrin derivative.

Hence, our results indicate that **1** does not organize forming densely packed SAMs on gold, possibly as a result of the interactions of the pyridyl ring with the gold surface and the lack of significant lateral packing forces, such as edge-to-face

π-interactions or van der Waals interactions, that could produce a periodic structure commensurate with the metal substrate, as in the SAM of **2**. Our suspicions concerning the poor orientation were confirmed when the monolayer of **1** was exposed to a solution of the porphyrin **3** in toluene, which forms a complex in the same solvent with the ligand (vide infra, Scheme 1). While the attachment of the rotator to the surface can be seen clearly by STM in other cases (vide infra, Figs. 4 and 5), for a monolayer of **1**, features that could correspond to **3** were hardly ever observed. As to be expected, because there are no molecular recognition sites in the SAM of **1**, it is even less capable of binding than the monolayer of **2** and no adsorption of the porphyrin to the surface was witnessed.

The preparation of mixed SAMs wherein a compound forming a well-defined periodic layer acts as a guide for organization of a co-adsorbent in a more precise position is appealing. In order to improve the orientation of **1** with respect to the gold surface, this thiol was co-deposited with **2** (at different proportions) to give mixed SAMs that were studied by STM at room temperature. The STM images of the mixed SAMs deposited at solution molar ratios of 1:1 and 10:1 of **1**:**2**, respectively, are shown in Fig. 3. It is important to note that unlike the SAM of pyridine derivative **1** (Fig. 2a), the 1:1 mixed SAM has regions of distinct repeat structure. One can observe striped domains in the STM image, which contain

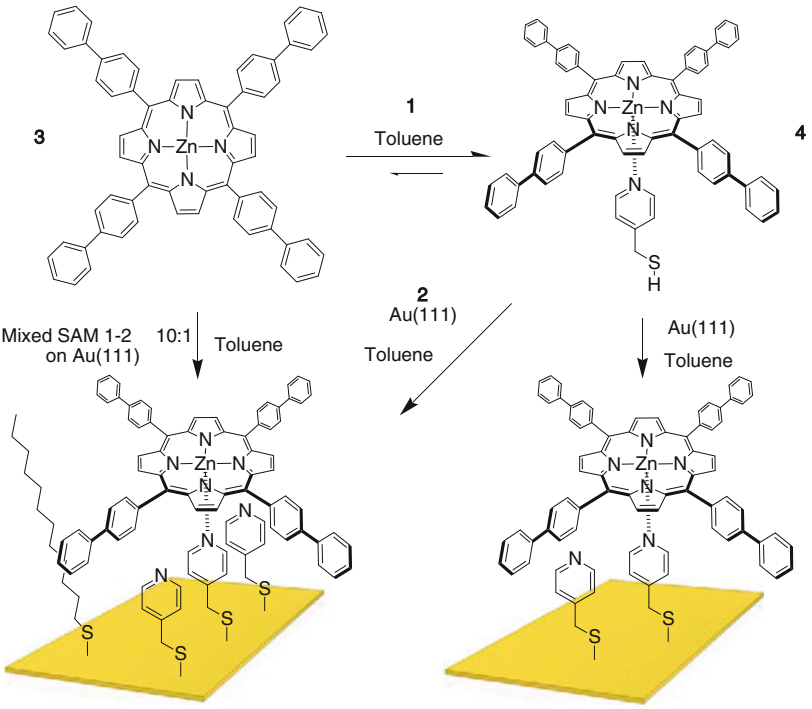

Scheme 1 Routes to surface-anchored supramolecular rotors described in this work

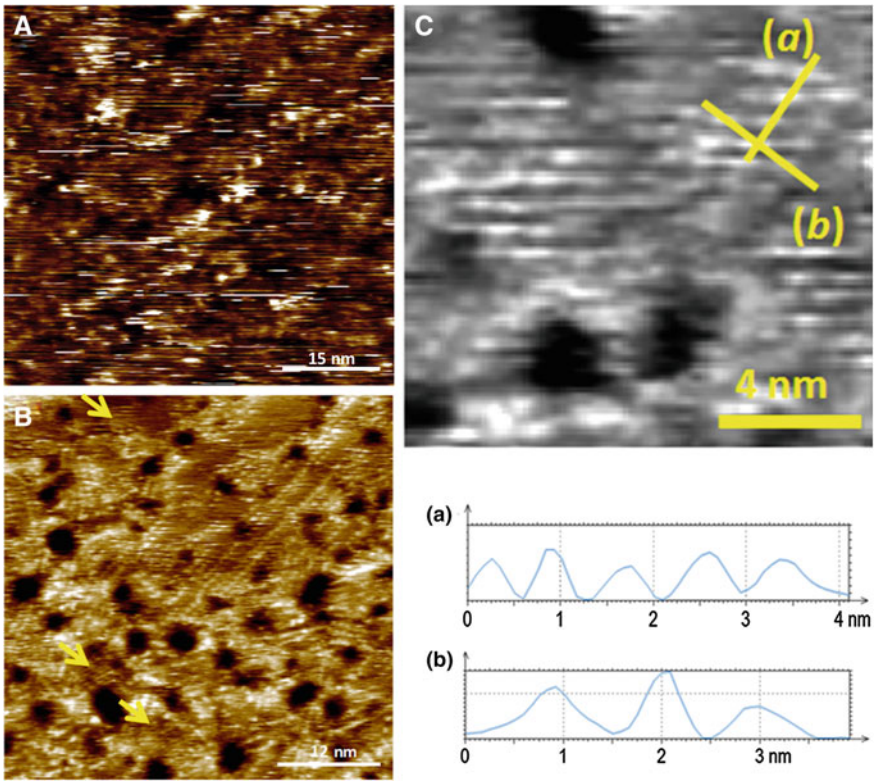

Fig. 3 STM images of mixed SAMs comprising **1** and **2** at solution deposition ratios of **A** 1:1 (I_{set} = 0.04 nA, V_{bias} = −0.8 V) and **B** 10:1 (I_{set} = 50 pA, V_{bias} = −0.8 V), respectively. *Yellow arrows* indicate areas of monolayers formed by **2**. **C** Shows an expanded region of the SAM incorporating **1** in image **b**. *Lines* (*a*) and (*b*) corresponding to the profiles shown below the image

brighter spots presumably associated with the pyridyl rings of **1** (Fig. 3a). The appearance of stripe features was never observed in homo-monolayers of the pyridyl compound **1** alone. We hypothesize that this better organization of **1** in the mixed SAM as compared with the pure SAM is induced by the surrounding ordered area of **2** present in the sample. In similar mixtures of totally different thiolated moieties with different functions on gold, a similar ordering effect has been observed previously [39]. The molecular resolution in the STM images of the layer of **1** and **2** at a deposition ratio of 1:1 was very limited, probably because molecules of **1** are partially overshadowed by the taller molecules of **2**. The difference in length between the component molecules complicates their clear imaging on gold and makes their simultaneous visualization by STM extremely difficult, as previously reported by others for mixed SAMs [40]. A feature that indicates the trouble encountered is the high amount of noise lines appearing in the STM images of these SAMs, despite the measuring of different samples and with different tips (Fig. 3a).

We were not even able to observe the highly ordered structure formed by **2**. Owing to the poor imaging conditions, and the need for good resolution in subsequent experiments, in an attempt to optimize the arrangement and orientation of **1** on the Au(111) surface, SAMs with a higher content of **1** were studied.

The STM images of the mixed SAM formed by **1** and **2** from a solution ratio of the thiols of 10:1, respectively, are surprisingly well resolved (Fig. 3b), particularly compared with the 1:1 mixture. Notably, in this case, the thiolates formed from **1** can be observed to line up neatly, side by side, with an ordered spatial environment of the pyridyl groups over the gold surface lattice. Neighbouring pyridyl moieties have a distance between their centres of approximately 0.9 nm [Fig. 3c (a)]. This distance is significantly larger than the expected separation between molecules of **2** in SAMs of the pure compound, which is 0.5 nm [35, 36].

These results are consistent with spacing distances determined for aromatic- and alkane-thiolated-based SAMs on gold [36]. The distance between the centres of the rows of molecules of **1** is about 1.1 nm [Fig. 3c (b)], parameters that are not consistent with a lying-down conformation of the thiolate, in which the inter-row distance is predicted to be 50 % bigger [41]. Rather, a tilted arrangement must be present because a completely perpendicular arrangement would give rise to a shorter distance between molecules. Therefore, apparently, a preferential arrangement arising from the co-deposition of molecules of **2** is observed. In addition to the pyridine striped-line structure present in the 10:1 mixed SAM, locally segregated $(\sqrt{3} \times \sqrt{3})R30°$ structures assigned to domains of **2** are present in the monolayer (Fig. 3b yellow arrows). The dramatic influence of a minority densely packed alkylthiol SAM (**2** in this case) can have on the ordering, and orientation of a ligand-based thiolated molecule, such as **1**, is unprecedented as far as we are aware. Even small proportions of alkylthiol can give rise to this effect, in the present system 10 %. This phenomenon could be useful because the surface-anchored ligand's ability to bind compounds in solution over the layer to give surface-attached complexes will be changed upon varying the direction in which it points with respect to the surface.

As a proof of concept in the use of oriented ligands for substrate binding and to approach our goal of creating surface-based rotors, with this nicely imaged mixed SAM available, the coordination studies were conducted using the pyridyl units for complexation of the zinc(II)porphyrin derivative **3** that has C_4 symmetry [42]. As shown in Scheme 1, the biphenyl units were incorporated into the porphyrin core to act as paddles. We reasoned that this feature would facilitate visualization of an eventual azimuthal molecular rotation on a surface by STM.

The 10:1 mixed SAM was placed in a toluene solution of **3** (1×10^{-4} M) for 12 h. The samples were then washed with toluene thoroughly to remove non-specifically physisorbed molecules of **3** before STM analysis was then conducted on the dry monolayer (Fig. 4). Interactions between **3** and the pyridyl coordination sites in the mixed SAM are expected in this particular case where pyridyl groups apparently emerge quasi-vertically from the surface and can coordinate the zinc(II) ion at the centre of the porphyrin ring (Scheme 1).

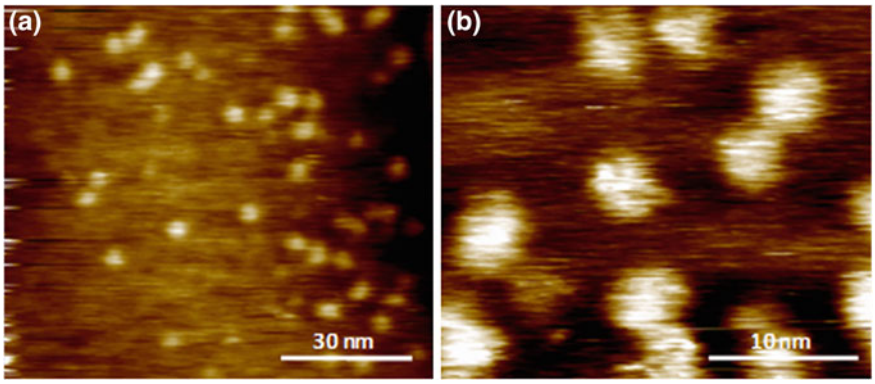

Fig. 4 Typical wide area STM images of adsorbed **3** on mixed SAM of **1** and **2** at a 10:1 ratio on Au(111)

Although the interaction between porphyrin and ligand is relatively weak (when compared with covalent bonds) and in principle reversible, it still facilitates the favourable coordination of one building block to the other on the surface, as demonstrated by both mass spectrometry and STM. Laser desorption ionization time-of-flight (LDI-TOF) mass spectrometry studies clearly support the presence of complexes **4** on 10:1 mixed SAM surfaces with a distinctive peak appearing at 980 m/z.

Figure 4 shows representative STM images of complexes formed from a 10:1 mixed SAM of **1** and **2** and deposition of **3** from solution. Bright areas of high tunnelling current and with uniform diameter (approximately 3 nm) and contrast were observed. We assigned the higher conductive areas in the STM images to the porphyrin cores coordinated with the pyridine groups in the monolayer. The porphyrin units in the complexes—that would correspond to the circular regions of high tunnelling current—cannot be imaged with sub-molecular resolution in these STM images, and furthermore, the images are noisy, possibly as a result of the interaction of the tip with the molecule. In this layer, vertically oriented molecules of **1** are assumed to coordinate the porphyrin molecules in an azimuthal rotor configuration, where rotation about the axis defined by the nitrogen–zinc bond could enhance the apparent image size of the porphyrin significantly. Unfortunately, the resolution of the STM imaging of the porphyrin complex in the layer could not be improved under the experimental conditions used; however, the porphyrin azimuthal rotation denoted in our STM images is consistent with literature data showing pivoting around a central pivot point of freely moving single molecule on Au(111) [43]. The rotation of **3** perpendicular to the axle units **1** would cause a blurry image during acquisition by STM, as shown in the close-up STM image in Fig. 4b. We attribute the blurring effect at the edges of **3** to the weak interaction of the biphenyl units with the 10:1 mixed SAM underneath. This effect might be surprising, because the surrounding molecules of **2** are actually longer

than the pyridyl derivatives and as such we expected them to act as a hindrance to rotor formation: empirically, the alkyl thiol does not seem to be sufficiently influential to stop motion.

Importantly, no bright areas were observed with SAMs of either **1** or **2** after 12-h immersion in a toluene solution of **3** (1×10^{-4} M), corroborating the poor coordination ability assigned to the lack of order in the monolayer of **1** on Au(111) and confirming that the dots of high tunnelling current arise from a specific binding to the SAM rather than to non-specific adsorption.

The adhered molecules of **3** are distributed randomly on the surface with low coverage and no order even very locally. The pyridine anchoring sites of **1** present in the 10:1 ratio mixed SAMs—despite being better organized than in the pure monolayer of **2**—do not provide optimum sites for binding of **3**, possibly because high steric energy barriers may exist during the complexation of the porphyrin from solution. This situation would lead to the randomly distributed porphyrin complexes in the SAM. The possibility that a negative allosteric effect could be impeding the coordination of molecules of **3** on the pyridyl groups in the 10:1 mixed SAM was supported by the results of functionalizing the Au(111) directly with a solution of the complex **4** from toluene.

Thus, prior to surface adsorption, the binding of **1**–**3** in solution to give complex **4** (Scheme 1) was determined by a titration using UV–visible absorption spectroscopy: the coordination complex forms in solution with great efficacy. In toluene —the solvent used for deposition of the material—the titration experiment showed an increase in the absorptivity of the solution as the pyridine derivative was added [20] because of the greater solubility of the complexed porphyrin when compared with its pure form. The result shows the benefits of axial coordination for the processing of this kind of material from solution.

Exposure of an Au(111) surface for 12 h to complex **4** in toluene led to an efficient adsorption of the nominal rotor. Much higher coverage was observed when compared to prior formation of monolayer, followed by rotator attachment. As is evident from inspection of the STM image in Fig. 5a, a high density of large objects is formed by direct adsorption of **4** on the gold. The feature size (the light dots of approximately 4 nm diameter) is very similar to that of the complexes observed from the adsorption of **3** to the 10:1 mixed SAMs (Fig. 4a, b). This experimental result emphasizes that the presence of anchoring groups on the gold substrate markedly limits the number of coordination events, probably as a result of the steric hindrance during the coordination process on a functionalized surface and/or by the high number of constraints induced by molecules of **2** present in the 10:1 mixed SAM. However, in the layer formed from complex **4**, some of the dots assigned to the porphyrin complex are wider and much brighter than others. The features are approximately 30 % larger than the duller objects (that have the expected dimensions of the porphyrin molecule). The profiles in Fig. 5 show the two types of feature next to one another.

As the duller objects are similar in size and shape to those seen in the adsorption of **3** to the mixed SAM of **1** and **2**, their environment is presumably similar in the two layers where non-complexed **1** could be located underneath the rotator in the

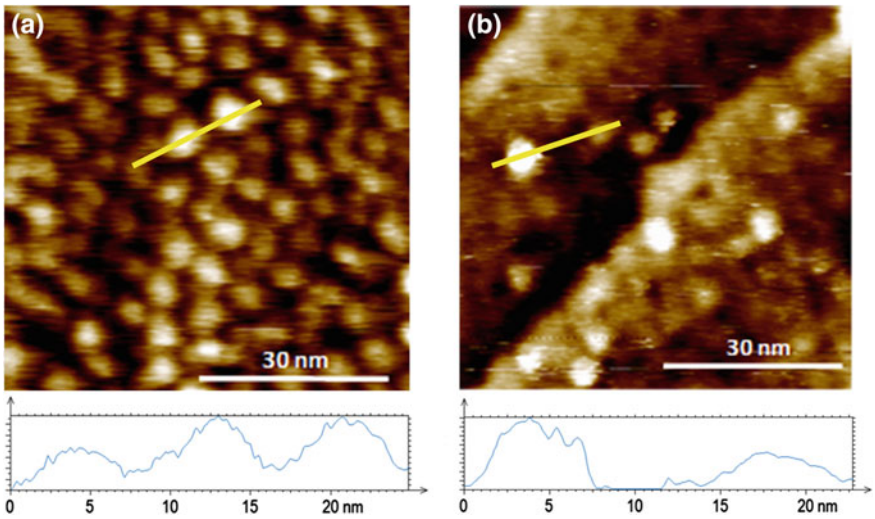

Fig. 5 STM images of complexes **4** adsorbed on Au(111) through **a** deposition of the complex **4** from toluene solution and **b** the complex **4** and **2** from toluene solution

SAM. This observation points to non-homogeneous binding sites for the rotator when the complex **4** is deposited and possibly to different dynamics in these positions. The observation of different environments corresponding to the same complex highlights the tremendous influence that the assembly approach used has on the dynamics, homogeneity and structural surrounding the adhered rotor.

When a mixture of **1** (1×10^{-5} M), **2** (1×10^{-6} M) and **3** (1×10^{-4} M) in toluene was used for direct functionalization of Au(111) to give a mixed monolayer with (in principle) similar composition to that formed by the attachment of **3** to the preformed mixed SAM of **1** and **2**, a significant number of bright areas were observed by STM, corresponding to anchored rotor **4** (Fig. 5b). When compared with the attachment of the complex **4** alone, the number of attached porphyrins is inferior. However, it is superior to that of adsorption of **3** to the preformed mixed SAM of **1** and **2**. It is not possible at this stage to give a precise reason for these experimental observations; however, a possible rationale would be the very different diffusion coefficients of the compounds in solution. The diffusion would be expected to be faster for **2** when compared with complex **4**. This situation would prompt preferential transport of **2** through the fluid and chemisorption to the metal surface before the larger complex arrived, so its adsorption on gold from the solution would be less probable. As in the case of the direct adsorption of **4** on the gold, the porphyrin exhibits different environments in the STM images. Some complexes exhibit high tunnelling current and large dimensions. This feature indicates that the gold surface is close to the porphyrin, again demonstrating the route-dependent outcome of complex environment in the SAM.

3 Conclusions

We have outlined here two feasible strategies for the preparation of supramolecular rotors on a solid surface from solution, each one giving rise to a distinct surface density of the nominal molecular machine component. In the first route, the rotator group is attached to a surface-anchored axle which requires prior defined orientation with respect to the surface so that it can bind the rotator. To achieve this goal, the orientation of pyridyl groups in a molecule that is not naturally tilted perpendicularly to a Au(111) surface can be modulated by employing mixed SAMs. A well-packed alkane thiol assembly suffices to force the pyridyl thiolate into a quasi-perpendicular direction to the substrate plane making the nitrogen atom available for complexation, a situation that is not present in homo-SAMs of the pure ligand. Surprisingly, only small amounts of the alkane thiol were necessary to induce order and a quasi-vertical orientation of the pyridyl moieties with respect to the gold substrate. This influence in the arrangement at the molecular level on surfaces enables recognition sites to be created for subsequent adlayer formation and hence opens up the way for the manufacture of complex hierarchical assemblies from the bottom-up. This route leads to a relatively low coverage of rotors on the surface when compared with a direct attachment of the non-covalent complex of axle and rotator components directly onto the surface (which acts as a stator). In this latter case, different surface environments are observed for the porphyrin. The homogeneity of the rotator environments is far higher when the porphyrin is adsorbed onto the preformed mixed monolayer. The reason for this heterogeneity upon formation of the layer from the complex is due to the conformational freedom of the supramolecular object upon chemisorption, and that once formed, thiols do not penetrate between the porphyrin and the gold surface.

The mixed SAMs allow the formation of specific anchoring/recognition surfaces, but the interaction between the pyridyl ligand and the metalloporphyrin is not sufficiently strong to lead to dense layers of rotors. If this limitation can be overcome, by modifying ligand and porphyrin characteristics, the combination of surface molecular design with surface-assisted recognition assembly could originally be employed to localize site-specifically a broad number of different molecular functional systems on a surface, which undoubtedly holds great promise for future bottom-up assembly of molecular machines and other functional supramolecular systems. Using this approach, we predict that it will be possible to reveal new physical phenomena at the nanoscale [17, 44, 45]. The case described here of the formation of rotor components on the gold surface could act as inspiration for a number of systems which could have novel nanoscale machine characters. In this sense, we are presently working on related rotator components [46].

Acknowledgments The research reported here was supported by the MINECO, Spain (projects CTQ2010-16339 and TEC2011-29140-C03-02), and the DGR, Catalonia (Project 2009 SGR 158). The authors acknowledge warmly Dr. Daniel Ruiz-Molina for the loan of the STM head. JPL thanks the MINECO for a Ramón y Cajal contract (RYC-2011-08071).

References

1. Koepf, M., Cherioux, F., Wytko, J.A., Weiss, J.: 1D and 3D surface-assisted self-organization. Coord. Chem. Rev. **256**, 2872–2892 (2012). doi:10.1016/j.ccr.2012.05.039
2. Slingenbergh, W., de Boer, S.K., Cordes, T., Browne, W.R., Feringa, B.L., Hoogenboom, J.P., De Hosson, J.T.M., van Dorp, W.F.: Selective functionalization of tailored nanostructures. ACS Nano **6**, 9214–9220 (2012). doi:10.1021/nn303571p
3. Biswas, A., Bayer, I.S., Biris, A.S., Wang, T., Dervishi, E., Faupel, F.: Advances in top-down and bottom-up surface nanofabrication: techniques, applications and future prospects. Adv. Colloid Interface Sci. **170**, 2–27 (2012). doi:10.1016/j.cis.2011.11.001
4. Fabiano, S., Pignataro, B.: Selecting speed-dependent pathways for a programmable nanoscale texture by wet interfaces. Chem. Soc. Rev. **41**, 6859–6873 (2012). doi:10.1039/c2cs35074b
5. Bakewell, D.J.G., Nicolau, D.V.: Protein linear molecular motor-powered nanodevices. Aust. J. Chem. **60**, 314–332 (2007). doi:10.1071/CH06456
6. Schaap, I.A.T., Carrasco, C., de Pablo, P.J., Schmidt, C.F.: Kinesin Walks the line: single motors observed by atomic force microscopy. Biophys. J. **100**, 2450–2456 (2011). doi:10.1016/j.bpj.2011.04.015
7. Boyle, M.M., Smaldone, R.A., Whalley, A.C., Ambrogio, M.W., Botros, Y.Y., Stoddart, J.F.: Mechanised materials. Chem. Sci. **2**, 204–210 (2011). doi:10.1039/c0sc00453g
8. Sauvage, J.-P.: Transition metal-containing rotaxanes and catenanes in motion: toward molecular machines and motors. Acc. Chem. Res. **31**, 611–619 (1998). doi:10.1021/ar960263r
9. Browne, W.R., Feringa, B.L.: Making molecular machines work. Nat. Nanotech. **1**, 25–35 (2006). doi:10.1038/nnano.2006.45
10. Balzani, V., Credi, A., Venturi, M.: Molecular machines working on surfaces and at interfaces. ChemPhysChem **9**, 202–220 (2008). doi:10.1002/cphc.200700528
11. Chiang, P.-T., Mielke, J., Godoy, J., Guerrero, J.M., Alemany, L.B., Villagómez, C.J., Saywell, A., Grill, L., Tour, J.M.: Toward a light-driven motorized nanocar: synthesis and initial imaging of single molecules. ACS Nano **6**, 592–597 (2012). doi:10.1021/nn203969b
12. Chiaravalotti, F., Gross, L., Rieder, K.-H., Stojkovic, S.M., Gourdon, A., Joachim, C., Moresco, F.: A rack-and-pinion device at the molecular scale. Nat. Mater. **6**, 30–33 (2007). doi:10.1038/nmat1802
13. Manzano, C., Soe, W.-H., Wong, H.S., Ample, F., Gourdon, A., Chandrasekhar, N., Joachim, C.: Step-by-step rotation of a molecule-gear mounted on an atomic-scale axis. Nat. Mater. **8**, 576–579 (2009). doi:10.1038/NMAT2467
14. Gimzewski, J.K., Joachim, C., Schlittler, R.R., Langlais, V., Tang, H., Johannsen, I.: Rotation of a single molecule within a supramolecular bearing. Science **281**, 531–533 (1998). doi:10.1126/science.281.5376.531
15. Tanaka, H., Ikeda, T., Takeuchi, M., Sada, K., Shinkai, S., Kawai, T.: Molecular rotation in self-assembled multidecker porphyrin complexes. ACS Nano **5**, 9575–9582 (2011). doi:10.1021/nn203773p
16. Yoshimoto, S., Honda, Y., Ito, O., Itaya, K.: Supramolecular pattern of fullerene on 2D bimolecular "chessboard" consisting of bottom-up assembly of porphyrin and phthalocyanine molecules. J. Am. Chem. Soc. **130**, 1085–1092 (2008). doi:10.1021/ja077407p
17. Kottas, G.S., Clarke, L.I., Horinek, D., Michl, J.: Artificial molecular rotors. Chem. Rev. **105**, 1281–1376 (2005). doi:10.1021/cr0300993
18. Tierney, H.L., Murphy, C.J., Jewell, A.D., Baber, A.E., Iski, E.V., Khodaverdian, H.Y., McGuire, A.F., Klebanov, N., Sykes, E.C.H.: Experimental demonstration of a single-molecule electric motor. Nat. Nanotech. **6**, 625–629 (2011). doi:10.1038/NNANO.2011.142
19. Perera, U.G.E., Ample, F., Kersell, H., Zhang, Y., Vives, G., Echeverria, J., Grisolia, M., Rapenne, G., Joachim, C., Hla, S.W.: Controlled clockwise and anticlockwise rotational switching of a molecular motor. Nat. Nanotech. **8**, 46–51 (2013). doi:10.1038/NNANO.2012.218

20. Puigmartí-Luis, J., Saletra, W.J., González, A., Amabilino, D.B., Pérez-García, L.: Bottom-up assembly of a surface-anchored supramolecular rotor enabled using a mixed self-assembled monolayer and pre-complexed components. Chem. Commun. **50**, 82–84 (2014). doi:10.1039/C3CC44794D
21. Vogel, G.C., Beckmann, B.A.: Binding of pyridine to the phenyl-substituted derivatives of zinc tetraphenylporphine. Inorg. Chem. **15**, 483–484 (1976). doi:10.1021/ic50156a054
22. Mamardashvili, G.M., Kulikova, O.M.: The effect of a solvent on complexation of Zn porphyrinates with pyridine. Russ. J. Coord. Chem. **32**, 756–760 (2006). doi:10.1134/S1070328406100101
23. Da Cruz, F., Driaf, K., Berthier, C., Lameille, J.-M., Armand, F.: Study of a self-assembled porphyrin monomolecular layer obtained by metal complexation. Thin Solid Films **349**, 155–161 (1999). doi:10.1016/S0040-6090(99)00169-8
24. Ferreira, Q., Alcácer, L., Morgado, J.: Stepwise preparation and characterization of molecular wires made of zinc octaethylporphyrin complexes bridged by 4,4′-bipyridine on HOPG. Nanotechnology **22**, 435604 (7p) (2011). doi:10.1088/0957-4484/22/43/435604
25. Dreas-Wlodarczak, A., Müllneritsch, M., Juffmann, T., Cioffi, C., Arndt, M., Mayor, M.: Immobilization of zinc porphyrin complexes on pyridine-functionalized glass surfaces. Langmuir **26**, 10822–10826 (2010). doi:10.1021/la100638u
26. Salassa, G., Coenen, M.J.J., Wezenberg, S.J., Hendriksen, B.L.M., Speller, S., Elemans, J.A.A.W., Kleij, A.W.: Extremely strong self-assembly of a bimetallic salen complex visualized at the single-molecule level. J. Am. Chem. Soc. **134**, 7186–7192 (2012). doi:10.1021/ja3030802
27. Ikeda, M., Takeuchi, M., Shinkai, S., Tani, F., Naruta, Y.: Synthesis of new diaryl-substituted triple-decker and tetraaryl-substituted double-decker lanthanum(III) porphyrins and their porphyrin ring rotational speed as compared with that of double-decker cerium(IV) porphyrins. Bull. Chem. Soc. Jpn **74**, 739–746 (2001). doi:10.1246/bcsj.74.739
28. Otsuki, J., Kawaguchi, S., Yamakawa, T., Asakawa, M., Miyake, K.: Arrays of double-decker porphyrins on highly oriented pyrolytic graphite. Langmuir **22**, 5708–5715 (2006). doi:10.1021/la0608617
29. Ghiggino, K.P., Hutchison, J.A., Langford, S.J., Latter, M.J., Lee, M.A.P., Lowenstern, P.R., Scholes, C., Takezaki, M., Wilman, B.E.: Porphyrin-based molecular rotors as fluorescent probes of nanoscale environments. Adv. Func. Mater. **17**, 805–813 (2007). doi:10.1002/adfm.200600948
30. Guenet, A., Graf, E., Kyritsakas, N., Hosseini, M.W.: Porphyrin-based switchable molecular turnstiles. Chem. Eur. J. **17**, 6443–6452 (2011). doi:10.1002/chem.201100057
31. Cnossen, A., Hou, L., Pollard, M.M., Wesenhagen, P.V., Browne, W.R., Feringa, B.L.: Driving unidirectional molecular rotary motors with visible light by intra- and intermolecular energy transfer from palladium porphyrin. J. Am. Chem. Soc. **134**, 17613–17619 (2012). doi:10.1021/ja306986g
32. Otsuki, J., Komatsu, Y., Kobayashi, D., Asakawa, M., Miyake, K.: Rotational libration of a double-decker porphyrin visualized. J. Am. Chem. Soc. **132**, 6870–6871 (2010). doi:10.1021/ja907077e
33. Yan, S.C., Ding, Z.J., Xie, N., Gong, H.Q., Sun, Q., Guo, Y., Shan, X.Y., Meng, S., Lu, X.H.: Turning on and off the rotational oscillation of a single porphine molecule by molecular charge state. ACS Nano **6**, 4132–4136 (2012). doi:10.1021/nn301099m
34. Lensen, D., Elemans, J.A.A.W.: Artificial molecular rotors and motors on surfaces: STM reveals and triggers. Soft Matter **8**, 9053–9063 (2012). doi:10.1039/c2sm26235e
35. Widrig, C.A., Alves, C.A., Porter, M.D.: Scanning tunnelling microscopy of ethanethiolate and normal-octadecanethiolate monolayers spontaneously adsorbed on gold surfaces. J. Am. Chem. Soc. **113**, 2805–2810 (1991). doi:10.1021/ja00008a001
36. Vericat, C., Vela, M.E., Salvarezza, R.C.: Self-assembled monolayers of alkanethiols on Au (111): surface structures, defects and dynamics. Phys. Chem. Chem. Phys. **7**, 3258–3268 (2005). doi:10.1039/b505903h

37. Silien, C., Buck, M., Goretzki, G., Lahaye, D., Champness, N.R., Weidner, T., Zharnikov, M.: Self-assembly of a pyridine-terminated thiol monolayer on Au(111). Langmuir **25**, 959–967 (2009). doi:10.1021/la802966s
38. Tao, Y.-T., Wu, Ch-Ch., Eu, J.-Y., Lin, W.-L.: Structure evolution of aromatic-derivatized thiol monolayers on evaporated gold. Langmuir **13**, 4018–4023 (1997). doi:10.1021/la9700984
39. Pace, G., Petitjean, A., Lalloz-Vogel, M.-N., Harrowfield, J., Lehn, J.-M., Samorì, P.: Subnanometer-resolved patterning of bicomponent self-assembled monolayers on Au(111). Angew. Chem. Int. Ed. **47**, 2484–2488 (2008). doi:10.1002/anie.200704731
40. Chen, S., Li, L., Boozer, C.L., Jiang, S.: Controlled chemical and structural properties of mixed self-assembled monolayers of alkanethiols on Au(111). Langmuir **16**, 9287–9293 (2000). doi:10.1021/la000417i
41. Wan, L.-J., Hara, Y., Noda, H., Osawa, M.: Dimerization of sulfur headgroups in 4-mercaptopyridine self-assembled monolayers on Au(111) studied by scanning tunneling microscopy. J. Phys. Chem. B **102**, 5943–5946 (1998). doi:10.1021/jp981218z
42. Penon, O., Marsico, F., Santucci, D., Rodríguez, L., Amabilino, D.B., Pérez-García, L.: Multiply biphenyl substituted zinc(II)porphyrin and phthalocyanine as components for molecular materials. J. Porphyrins Phthalocyanines **16**, 1293–1302 (2012). doi:10.1142/S1088424612501453
43. Baber, A.E., Tierney, H.L., Sykes, E.C.H.: A quantitative single-molecule study of thioether molecular rotors. ACS Nano **2**, 2385–2391 (2008). doi:10.1021/nn800497y
44. Coskun, A., Banaszak, M., Astumian, R.D., Stoddart, J.F., Grzybowski, B.A.: Great expectations: can artificial molecular machines deliver on their promise? Chem. Soc. Rev. **41**, 19–30 (2012). doi:10.1039/c1cs15262a
45. von Delius, M., Leigh, D.A.: Walking molecules. Chem. Soc. Rev. **40**, 3656–3676 (2011). doi:10.1039/c1cs15005g
46. Penon, O., Moro, A.J., Santucci, D., Amabilino, D.B., Lima, J.C., Pérez-García, L., Rodríguez, L.: Molecular recognition of aliphatic amines by luminescent Zn-porphyrins. Inorg. Chim. Acta **417**, 222–229 (2014). doi:10.1016/j.ica.2013.12.028

Single Molecular Machines on Semiconductor Surfaces

Younes Makoudi, Frank Palmino and Frédéric Chérioux

Abstract The development of nanomachines is a key challenge for the future electronics, energy conversion, biology, and medicine. Semiconductor surfaces have been one of the basic elements of many technologies for 40 years. However, despite their promising interest, semiconductor-based nanomachines are almost unstudied. In this work, a panel of single nanomachines-based semiconductor surfaces is described. The role of molecule–surface interaction for the development of nanomachines is highlighted.

Keywords Molecular machines · STM · Semiconductors · Activation · Molecular interaction · Switch

1 Introduction

The formation and control of artificial molecular nanomachines adsorbed onto a surface are two of the most promising challenges in nanotechnology [1–6]. Most of the studies on surface-mounted nanomachines by STM have been achieved on noble metal substrates. Nevertheless, from the viewpoint of future hybrid organic/inorganic molecular devices, while molecular interaction with metallic substrates is better understood, semiconducting interfaces are natural choices due to their wide-range acceptability by the industry. In this chapter, we propose to review some proofs of concept of single molecular machines on semiconductor surfaces. The development and fabrication as well as the activation of nanomachines are described. The role of molecule–surface interaction is described in detail due to its important role for the achievement of molecular machines on semiconductors.

Y. Makoudi · F. Palmino · F. Chérioux (✉)
Institut FEMTO-ST, Université de Franche-Comté, CNRS, ENSMM, 15B Avenue des Montboucons, F-25030 Besancon Cedex, France

C. Joachim and G. Rapenne (eds.), *Single Molecular Machines and Motors*,
Advances in Atom and Single Molecule Machines, DOI 10.1007/978-3-319-13872-5_9

2 Molecular Motions

2.1 1D Molecular Rotation

Semiconductor surfaces in ultra-high vacuum are well known to interact strongly with organic molecules. For example, on Si surfaces, several dangling bonds can lock the molecules adsorbed onto the surface. To circumvent this problem, we need to use less reactive surfaces. In the case of molecular rotation, one of the possibilities is to anchor the molecule to only one dangling bond acting as a rotation axis. This idea has been developed on Si(100)-2 × 1 surface with metal phthalocyanine molecules (MPc) [7, 8]. The authors have shown by STM that on the Si(100)-2 × 1 reconstruction, CoPc and CuPc are bound to the surface via their central metal atom. In these conditions, the molecules, parallel to the surface, are in a stationary position (Fig. 1a). To induce a rotation via a single dangling bond, the surface must be, in a first step, passivated. The Si(100)-2 × 1 H-passivated surface is achieved by the exposure of the initial substrate to 1×10^{-6} Torr of hydrogen for 10 min with a hot tungsten filament. Subsequently, isolated dangling bonds are created by feedback control lithography (FCL) using the STM tip to induce the desorption of one hydrogen atom (Fig. 1b).

After evaporation of MPc onto this surface, the 4-lobe structures previously observed were not detected but circular depression with a double diameter of CoPc is observed. This is assigned to one MPc molecule bound to the surface through its outer benzene ring which rotates as depicted in Fig. 1c. A molecular modeling study confirmed that bonding between the benzene ring and the surface induces the lowest adsorption energy. Due to the hydrogen-passivated surface, the adsorption energy difference for different angles around the rotation axis is negligible compared to kT energy. In these conditions, the CoPc molecule rotates easily around the benzene ring.

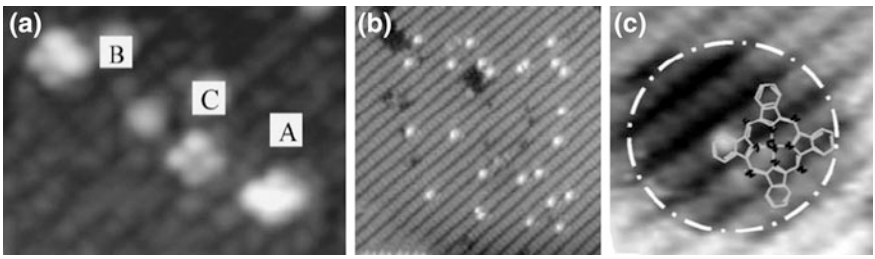

Fig. 1 **a** STM CoPc image on Si(100)-2 × 1 surface (*Vs* = −2.5 V, *It* = 0.2 nA) showing three different configurations. No rotation is observed. **b** Si(100)-2 × 1:H surface where the *bright* protrusions correspond to dangling bonds made by FCL (*Vs* = −3 V, *It* = 0.2 nA). **c** Schematic view of CoPc anchored to a dangling bond via one of its benzene rings and rotated around this benzene ring (*Vs* = −2 V, *It* = 0.2 nA). Reprinted with permission from [8]

2.2 1D Molecular Sliding on InSb

Thermally activated motion often leads to a molecular Brownian motion [4]. To control the direction of the motion, the use of 1D periodic surfaces or step edges is a good choice to induce a linear movement. Contrary to metallic surfaces, which offer few possibilities to obtain 1D periodic surfaces (Cu–O/Cu [9] or Au(111) [10]), semiconductor or metal–semiconductor interfaces possess a high number of 1D surface reconstructions [11–14]. Few of them have been tested for molecular motion; nevertheless, the results obtained on InSb or SmSi are very convincing. In each case, we can note that the adsorption site as well as the matching between the surface unit-cell dimension and the molecular dimensions is a crucial factors to obtain good conditions for the achievement of matter transport.

The InSb(001)-(8 × 2) reconstructed surface is strongly anisotropic and constituted by In chains in the top adlayer. Molecular diffusion along the chains has been observed with PbPc [15, 16], a non-planar phthalocyanine, as well as CuPc [17], a planar molecule. On the CuPc/InSb(001) interface, CuPc molecules are adsorbed along the step edges and on the terraces (Fig. 2).

Along the step edges, in the [1-10] direction, the molecules are very weakly bound to the surface and appear like two protrusions, while in the [110] direction, the molecules are strongly bound to the surface and no change is observed after several scans. On terraces, some noisy horizontal lines indicate mobile molecules while CuPc molecules appear as eight separated protrusions centered over the bright substrate rows, which correspond to the topmost In atoms. CuPc molecules form chains constituted by a few molecules, which diffuse between two frames. These room temperature STM observations show the high mobility of the molecules along the [110] direction. Based on symmetry considerations, an adsorption model is proposed in Fig. 3.

Two interactions are suggested between molecules and the surface: one between the Cu atom and the In adlayer atom, and the second one between the nitrogen atoms and the In adlayer atom.

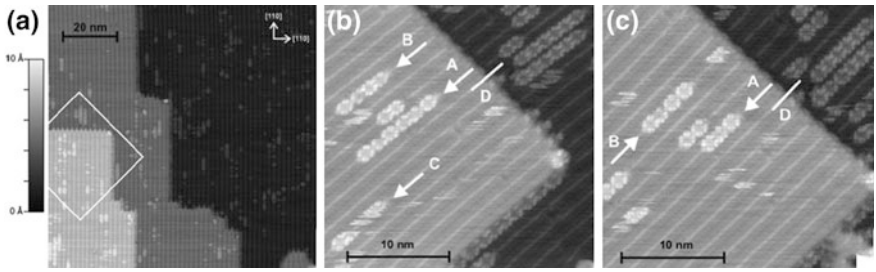

Fig. 2 **a** Large-scale STM image of CuPc/InSb(001)-(8 × 2) interface (100 × 100 nm^2, *Vs* = −1 V, *It* = 0.3 nA). The *white frame* indicates the area scanned and shown in **b** and **c**. **b** and **c** show CuPc molecular diffusion between two STM frames (30 × 30 nm^2, *Vs* = −1 V, *It* = 0.15 nA). Reprinted with permission from [17]

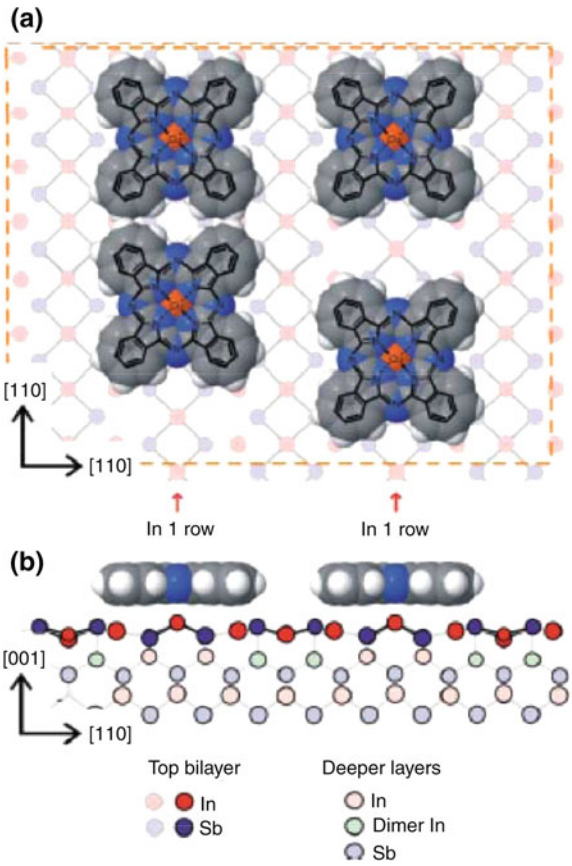

Fig. 3 Adsorption model **a** *top view* and **b** *side view* of CuPc on InSb(001)-(8 × 2) reconstruction. The copper atom is always positioned over the In adlayer atom. A major interaction is possible between In and nitrogen atoms. Reprinted with permission from [17]

2.3 1D Molecular Sliding on Rare Earth Silicides

Due to their low lattice mismatch and their valence changes, rare earth silicides on Si(111) induce a high number of reconstructions depending on rare earth coverage and annealing temperature. In particular, the SmSi(111) interface possesses a complex surface phase diagram with four different 1D reconstructions in the sub-monolayer range (Fig. 4) [18]. These reconstructions are based on a combination of Si honeycomb chain channels (HCCs), Si Seiwatz chains, and Sm rows. They appear like large stripes on the STM images (Fig. 5 b, c). The main interest of these reconstructions with similar electronic properties is the possibility to adapt the periodicity of the unit cell (×3, ×5, ×7, or ×8) to the molecular dimensions.

The 1,4-di(9-ethynyltriptycene)benzene molecule (DETB) (Fig. 5a) has been used to study the directional molecular sliding on the (8 × 2), the (5 × 1), and the (7 × 1) reconstructions described in Fig. 5 b–e [13, 19]. This molecule has been chosen because the distance of 1.64 nm between two Sm rows of SmSi interface corresponds to the length of the molecule.

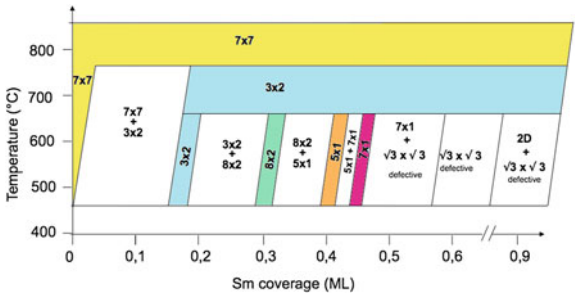

Fig. 4 Surface phase diagram of SmSi(111) interfaces. The (3 × 2), (8 × 2), (5 × 1), and (7 × 1) are 1D reconstructions in the submonolayer Sm coverage

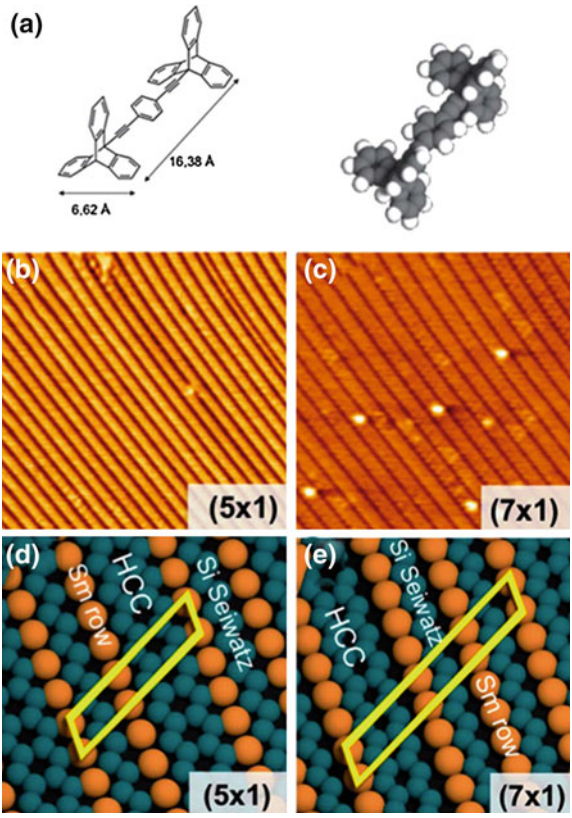

Fig. 5 **a** The 1,4-di (9-ethynyltriptycene)benzene molecule (DETB). **b–e** STM images (32 × 32 nm^2, Vs = 2 V, It = 0.18 nA) and structural models of both (5 × 1) and (7 × 1) reconstructions. Reprinted with permission from [19]

On the SmSi(111)-5 × 1 reconstruction at room temperature, the DETB appears on STM images like two paired protrusions attributed to the two triptycene wheels. All the DETB molecules are adsorbed onto the large stripes and are self-aligned along the [1-10] direction with the triptycene wheels above two Sm chains as described in Fig. 6b. Some noisy lines, corresponding to molecular diffusion, are

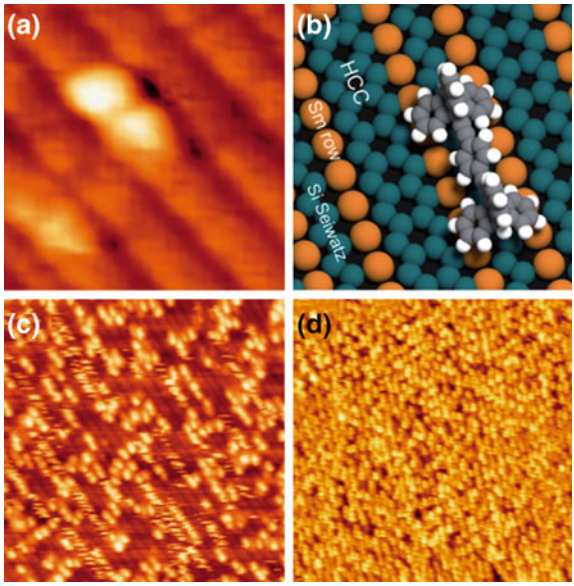

Fig. 6 **a** Isolated DETB molecule on SmSi-(5 × 1) (7 × 7 nm^2, *Vs* = 1.8 V, *It* = 0.7 nA). **b** DETB adsorption model on (5 × 1) reconstruction. **c** Interface for 0.3 monolayer molecule coverage. Noisy stripes correspond to DETB diffusion along Sm rows. **d** Interface for 0.9 monolayer molecule coverage showing the self-alignment after the surface diffusion. Reprinted with permission from [19]

observed along the stripes and prove that the movement is guided by a strong template effect of the surface.

The study of the template effect of the surface on the adsorption and the diffusion of DETB molecules has been done by Bouju et al. [19]. By using a larger unit cell, the SmSi-(7 × 1) instead of a the SmSi-(5 × 1), they shown that the DETB molecules can be adsorbed with a new orientation where their main axis is now perpendicular to the Sm rows (Fig. 7a, b). In these conditions, the molecular motions induce dual frizzled bands on the STM images (black arrows in Fig. 7) corresponding to the two-triptycene wheels. A semiempirical calculation (ASED-MO) confirms that in this orientation, the energy barrier is the most favorable to a sliding onto the surface and that the DETB molecules are confined between two HCC channels.

3 Tools to Induce Molecular Motion at a Semiconductor Surfaces

Self-assembly is an important tool in nanotechnology [20, 21]. In order to achieve self-assembly growth, molecules must be free to move across a surface. However, because of the dangling bonds, this movement is not often possible without an

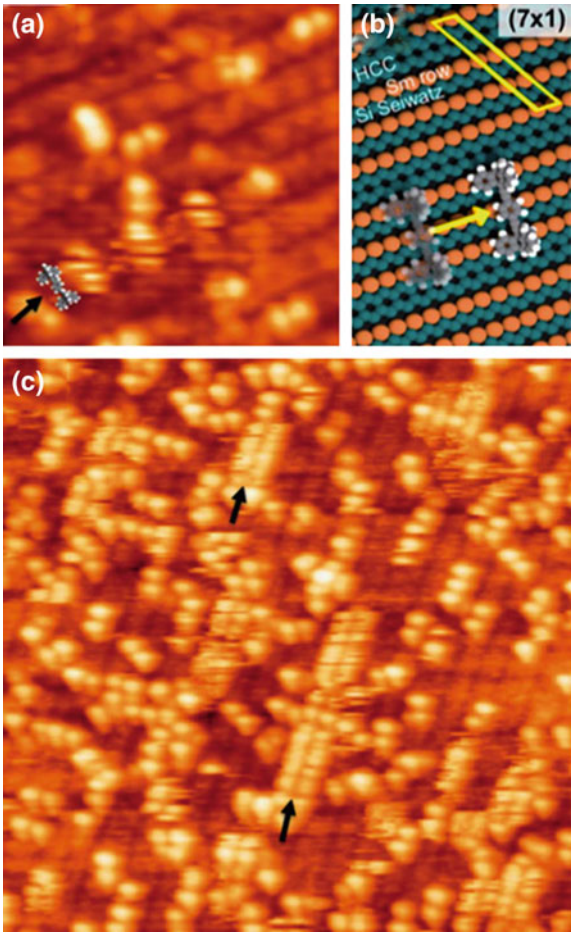

Fig. 7 **a** STM image of DETB molecules on SmSi-(7 × 1) (15 × 15 nm^2, *Vs* = 1.8 V, *It* = 0.02 nA). **b** DETB adsorption model which induces the sliding perpendicular to the Sm rows. **c** STM image showing the DETB sliding and the formation of dual bands (*black arrows*). Reprinted with permission from [19]

external intervention. The idea is to provide some energy to the system (molecule/surface) in order to overcome molecule–surface interactions and diffusion barriers. Three sources of energy (heat, light, or electrons) can be available in a STM chamber and can be used to induce molecular motions on semiconductor surfaces.

Despite the importance of this step for the development of molecular electronics, only very few examples dealing with the subject are available in the literature.

3.1 Heat

The usual and easiest method to provide energy in a STM is based on the heating of the investigated system. Our work in this domain illustrates well the effect of temperature in self-assembly formation [22–24]. Although molecular deposition

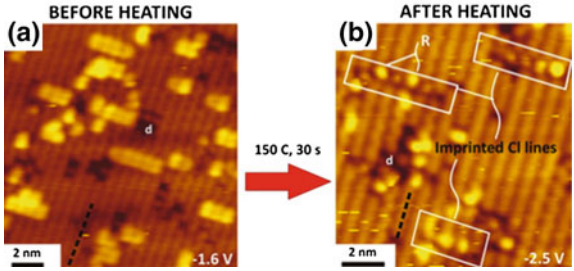

Fig. 8 STM images recorded at room temperature of a Si(100)-(2 X 1) surface exposed to 0.04 L dose of chloropentane. **a** *Before heating* the surface at 150 °C during 30 s (*Vs* = −1.6 V, *It* = 0.2 nA, 15 x 15 nm^2). **b** *After heating* (*Vs* = −2.5 V, *It* = 0.2 nA, 11 x 11 nm^2). Physisorbed lines of CP are imprinted as chemisorbed lines of Cl pairs. Reprinted with permission from [25]

was performed at room temperature, this thermal energy was sufficient for molecules to overcome diffusion barriers and then form different self-assemblies.

Heat can also be used to activate a local atomic reaction (LAR) as reported by Harikumar et al. Indeed, LAR of the physisorbed lines of 1-chloropentane (CP) pairs was induced by heat [25]. Figure 8 shows representative images of physisorbed lines of CP pairs after dosing at room temperature and after heating to 150 °C for 30 s. Some lines have completely reacted after heating and producing new lines of pairs of Si–Cl covalent bonds.

This result shows that we can transform a weakly attached physisorbed pattern, by using heat as source of energy, in order to induce chemical reaction with semiconductor surface and so rendering the pattern permanent.

3.2 Electrons

Excitation of molecules at a surface can be achieved by the STM tip and can induce molecular motions in four possible directions: (1) toward the surface (transition from a physisorbed interaction to chemisorbed one) [26]; (2) away from the surface (desorption) [27]; (3) parallel to the surface (migration, diffusion) [28]; or (4) rotating around a point of the surface (molecular switch) [29]. The third case is the direction favoring the self-assembly.

Harikumar et al. [30], for example, showed that electron excitation of chemisorbed benzene at Si(100) causes long-range (around 48–35 Å in Fig. 9) molecular recoil in the plane of the surface as illustrated in Fig. 9. This movement is induced by an electron pulse (−2 V, 0.2 nA, 1 s) with the STM tip and is followed by a chemisorptive reattachment of the molecule. The migration is due to molecular cartwheeling rotation. It is directed along the dimer rows and over a missing dimer defect, carrying the molecules over raised surface obstacles.

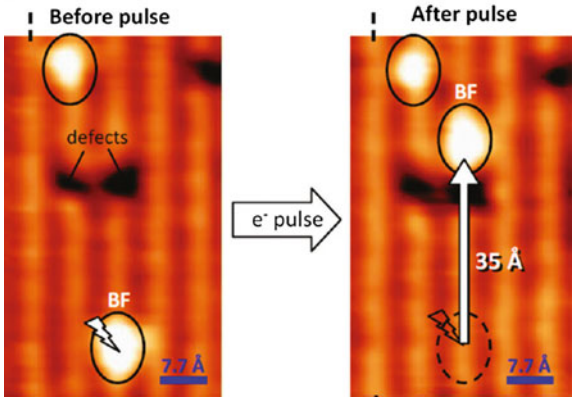

Fig. 9 Benzene migration over Si(100)-(2 x 1) surface at room temperature. STM images (*Vs* = −1.5 V, *It* = 0.2 nA) of the same area *before* and *after* an electron pulse (*Vs* = −2 V, *It* = 0.2 nA, 1 s). Reprinted with permission from [30]

3.3 Light

Although this excitation source is widely used in air and in liquid environments [31], to our knowledge, only one example has been reported for its use in UHV and on semiconductor surfaces. This example concerns, once again, the Harikumar et al. [25] work concerning 1-chloropentane on Si(100) surface. Like in the case of heat as energy source of excitation, LAR of the physisorbed lines of CP pairs can also be induced by light. Indeed, Fig. 10 shows photo-imprinted Cl lines after 2 h of laser irradiation of physisorbed CP on Si(100)-(2 x 1) surface. The photo-induced reaction is due to electrons ejected from the substrate rather than direct excitation of the molecule.

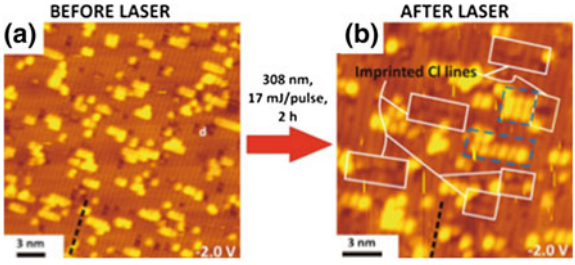

Fig. 10 STM images recorded at room temperature of a Si(100)-(2 x 1) surface exposed to 0.04 L dose of chloropentane. **a** *Before laser* irradiation (*Vs* = −2 V, *It* = 0.2 nA, 25 x 25 nm^2). **b** *After* 2 h of laser irradiation (*Vs* = −2 V, *It* = 0.2 nA, 18 x 18 nm^2). Physisorbed lines of CP are photo-imprinted as chemisorbed lines of Cl pairs (*white rectangles*). Non-reacted physisorbed CP lines are highlighted by *blue broken rectangles*. Reprinted with permission from [25]

4 Bistable Molecules as Model Systems of Molecular Machines

4.1 Adsorption of Bistable Azobenzene Molecules on Semiconductors

The most basic approach to study molecular bistability on a surface consists in the deposition of a molecule that is intrinsically bistable. Then, in a second step, one checks whether the molecular bistability is maintained or altered by the presence of the surface. Azobenzene derivatives have been deeply investigated as model system of bistable molecules in gas phase or in solution [32–37]. The presence of a N=N double bond located between two phenyl groups allows a reversible isomerization between *trans* and *cis* structural isomers (i.e., diastereoisomers). The adsorption of azobenzene derivatives has also been investigated on noble metal surfaces at low temperature (<100 K) [38–48]. The switching processes are based on the isomerization of molecules induced by an external stimulus, such as light or temperature (which are also used in gas phase or in solution experiments), inelastic tunneling electrons (IET), tip-induced molecular deformation, and electric field due to the presence of the STM junction. Semiconductor surfaces are fascinating for surface photo- or tip-induced switching due to their tunable optical and electronic properties.

The adsorption of *trans*-azobenzene (TAB) and *cis*-azobenzene (CAB) was investigated on Ag/Ge(111)-($\sqrt{3}$ x $\sqrt{3}$)-R30° by Wu et al. [49] at 100 K. Single TAB molecules were observed as two paired lobes on the surface. The formation of large, well-organized, and closely packed domains was achieved by increasing the coverage rate. From in situ observation of the substrate lattice, the TAB adsorption site was determined. TAB monolayer is commensurable with the substrate and forms a (2 × 1) structure (Fig. 11). The driving forces of TAB monolayer growth are hydrogen bonds between TAB molecules and molecule–substrate interactions. CAB molecules have been deposited on the same surface. However, it is quite difficult to obtain pure CAB molecules because of their unstability (spontaneous isomerization). Therefore, a mixture of TAB and CAB, containing 10 % of CAB, was adsorbed on the surface. CAB molecules are adsorbed on TAB domain boundaries. CAB molecules appear as two paired lobes, one spot being brighter than the other due to one out-of-plane phenyl group. Despite many attempts, TAB photoisomerization is unsuccessful on Ag/Ge(111)-($\sqrt{3}$ × $\sqrt{3}$)-R30°. The absence of TAB photo-isomerization is explained by the strong TAB–surface interaction that leads to a surface energy relaxation instead of the desired isomerization process.

Decreasing the molecule–surface interactions seems to be a key point for the successful achievement of azobenzene isomerization on semiconductors. Molecule–surface interaction can be tuned by using:

- Passivated semiconductors
- Tailored molecules

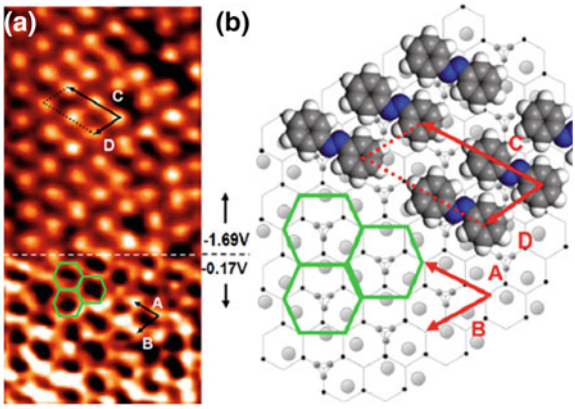

Fig. 11 **a** STM image (5×10 nm^2) of a TAB monolayer on Ag/Ge(111)-($\sqrt{3} \times \sqrt{3}$)-R30°. The tip bias is altered during the scan to image simultaneously the TAB molecules (*upper part* with $Vs = -1.69$ V, $It = 80$ pA) and the hexagonal pattern of the substrate atoms (*lower part* with $Vs = -1.69$ V, $It = 80$ pA). **b** Structural model of image shown in **a**. Reprinted with permission from [49]

When π-conjugated molecules, such as azobenzene derivatives, are deposited on a semiconductor, the main contribution to the molecule–surface interactions is the interaction of the molecule's π-electrons and electrons of surface dangling bonds. Recently, we have demonstrated that the molecule–surface interactions can be controlled by using the Si(111)-B-($\sqrt{3} \times \sqrt{3}$)-R30° surface, noted Si(111)-B. The silicon adatoms dangling bonds are depopulated because of the presence of a boron atom underneath each silicon adatom, leading to a weak π-conjugated molecule–surface interaction [22, 24, 50–52]. In all these cases, molecule–surface interaction is weak enough to achieve the formation of large-scale supramolecular networks. In order to check the feasibility of azobenzene isomerization on a Si(111)-B surface, we tried to deposit TAB molecules on this surface. However, the observation of single or self-assembled TAB molecules was impossible in the 100–300 K temperature range. Another azobenzene derivative, 4-pyridylazobenzene (PAB) molecule, has been synthetized (Fig. 12). Due to the presence of a pyridyl group, PAB-Si(111)-B interactions should be stronger than TAB-Si(111)-B. A single PAB molecule has indeed been observed on a Si(111)-B surface at room temperature. PAB molecules appear as two paired lobes, one being longer than the other. In empty states STM images, the interaction between the nitrogen atom lone pair and the silicon adatom is highlighted by a bright protrusion (Fig. 12b, c) [53].

PAB manipulation at room temperature was successfully achieved by applying a STM tip pulse bias voltage of 3 V during 300 ms after positioning the STM tip above a PAB molecule (Fig. 13a).

In these conditions, PAB molecules switch reversibly from one state to the other, which are mirror images of each other by a plane mirror; therefore, they are enantiomers. No *cis–trans* PAB isomerization occurs on a Si(111)-B surface, and it

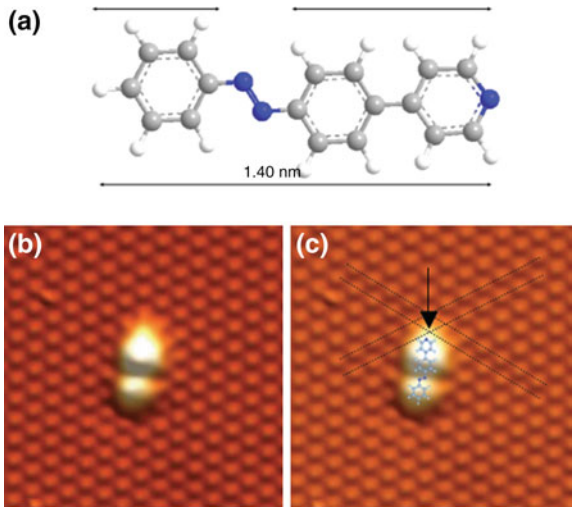

Fig. 12 **a** Molecular structure of 4-pyridylazobenzene (*PAB*). **b** Room temperature STM image (7×6 nm^2, *Vs* = 1.5 V, *It* = 76 pA) of a single PAB molecule deposited on Si(111)-B. **c** Superimposed structural model of PAB/Si(111)-B. PAB-Si(111)-B interaction is highlighted by a *black arrow*. Reprinted with permission from [53]

is a chiral switching between two enantiomers. PAB is not a chiral molecule but a prochiral molecule. The presence of the surface induces the formation of chiral adsorbates. From a mechanistic point of view, the PAB chiral switching is based on the tunneling electron transfer to PAB LUMO, located around 3 V (Fig. 13b), leading to a negatively charged transient state. Then, energy transfer to molecular vibrations leads to chiral switching by molecular rotation of the azophenyl group around the C–N bond (Fig. 13c) instead of *cis–trans* isomerization. This chiral switching is of interest in order to store information at the molecular level on a semiconductor surface because this switching occurs reversibly at room temperature and in a controlled manner.

In order to observe the *cis–trans* isomerization of azobenzene derivatives, Crommie et al. [54] proposed to use GaAs(110) as semiconductor surface and 3,3′,5,5′-tetra-*tert*-butylazobenzene (TTB-AB) as molecules at low temperature (<20 K). The (110) surface of GaAs was chosen due to the absence of surface states within its direct band gap (1.43 eV) [55], and TTB-AB was chosen because the TTB-AB aromatic molecular plane is held away from the surface by *tert*-butyl groups. Formation of TTB-AB large-scale monolayer islands on GaAs(110) was achieved in (Fig. 14a). The supramolecular network is commensurable with the surface, and TTB-AB shows the same shape (four-lobed structure) as the one observed on noble metals, corresponding to the *trans*-isomer [47]. TTB-AB photoswitching on GaAs(110) was investigated by STM with UV light illumination (375 nm) during 18 h. UV light exposure leads to morphological modifications of the TTB-AB monolayer islands. Several bright protrusions, forming some stripes,

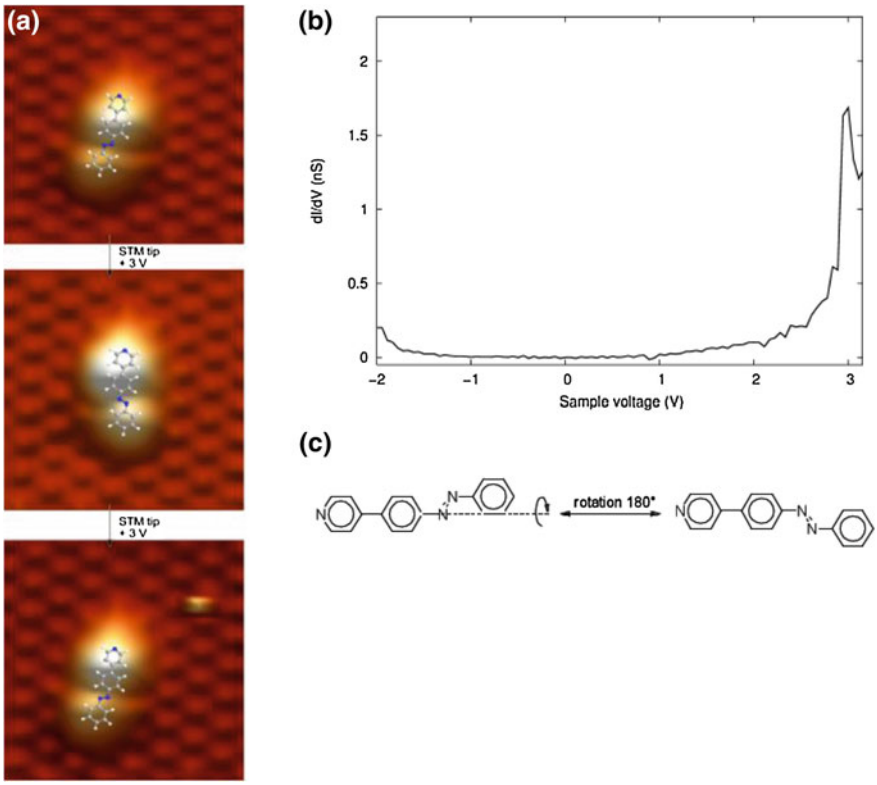

Fig. 13 **a** Sequence of PAB manipulation by STM tip bias voltage pulse on a Si(111)-B surface with superimposed structural model on STM images. **b** Spectrum of the differential conductance, dI/dV, recorded on a PAB molecule adsorbed on a Si(111)-B surface. **c** Two PAB conformers rotated by 180° of an azophenyl group around a C–N bond. Reprinted with permission from [53]

have appeared along preferential directions of the GaAs(110) surface (Fig. 14b). Bright protrusions have been assigned to TTB-AB *cis*-isomers, as previously observed on noble metal surface, due to the out-of-plane configuration of the *cis*-isomer [46].

On Au(111) surface, TTB-AB photoswitching is a random process because the bright protrusions are randomly distributed on the surface [46]. In the case of GaAs (110), formation of *cis*-isomer stripes is in favor of a cascade-like process. This very interesting process can be explained by the reduced steric hindrance after TTB-AB photo-isomerization. When a first *trans*-TTB-AB molecule is photo-isomerized, the *cis*-isomer occupies a smaller area than the *trans*-isomer because *cis*-TTB-AB is out of plane. But, as molecule surface is stronger on GaAs(110) than on Au(111), TTB-AB cannot diffuse on the surface and the network can no longer be re-organized to become once again compact. Therefore, after a first TTB-AB photo-isomerization, TTB-AB neighboring molecules can be more easily isomerized because local steric hindrance has decreased.

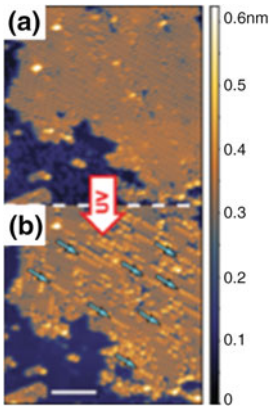

Fig. 14 TTB-AB photo-isomerization on GaAs(110) surface. The same TTB-AB molecular island is shown **a** *before* and **b** *after* an 18 h exposure to UV irradiation at 375 nm and 92 mW/cm^2 (*Vs* = −2.0 V, *It* = 25 pA). Molecules in the *cis* configuration appear to have one brighter lobe and occur in 1D stripes, as indicated by *blue arrows*. *White scale bar*, 10 nm. Reprinted with permission from [54]

To conclude, azobenzene derivatives switching on semiconductors are strongly dependent on the molecule–substrate interactions. The switching can be quenched, like on Ag/Ge(111)-($\sqrt{3} \times \sqrt{3}$)-R30° or used to form stripes, like on GaAs(110) or to form enantiomers, and like on Si(111)-B.

4.2 Molecular Bistability Induced by Adsorption on Semiconductors

In the previous paragraph, we described changes in the photomechanical properties of intrinsic bistable molecules after their adsorption on a semiconductor. Here, we propose to discuss the design of molecular bistability induced by the presence of the surface.

Dujardin et al. [56, 57] have investigated the induced bistability of biphenyl molecules on a Si(100) surface. Biphenyl is based on two phenyl groups linked by a single C–C bond. This molecule has no intrinsic bistability in solution, in solid state, or in gas phase. However, when biphenyl molecules are deposited at room temperature on a Si(100)-(2 × 1) surface and observed by STM at 5 K, they can be adsorbed with one of the two phenyl ring covalently linked with a silicon adatom of the surface, the second phenyl ring being covalently linked with two silicon adatoms (i.e., a butterfly configuration, Fig. 15a, d for the corresponding structural model). This strongly chemisorbed configuration is stable because no motion is observed from 5 to 300 K.

In the case of p-type boron-doped silicon surface, biphenyl molecules can be switched with tunneling electrons by applying a negative surface pulse voltage of

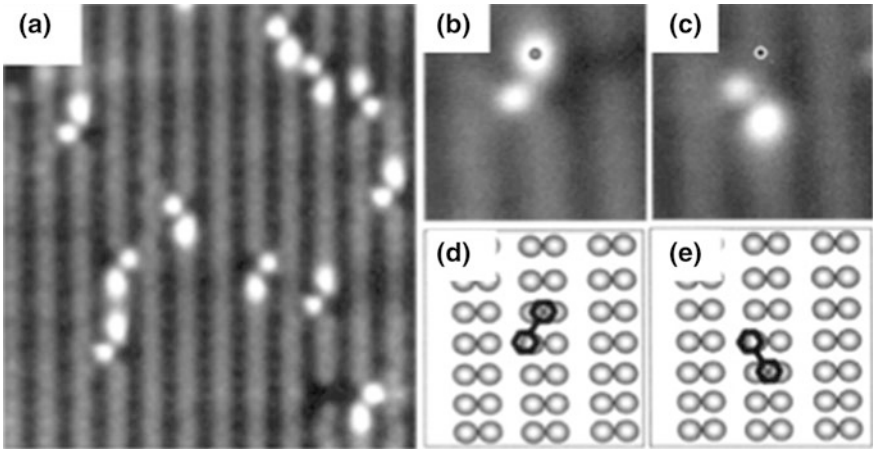

Fig. 15 **a** STM image of biphenyl molecules on a Si(100)-(2 × 1) surface at 5 K (9 × 9 nm^2, *Vs* = −2.0 V, *It* = 200 pA). **b** Zoom (2.1 × 2.1 nm^2) of STM image shown in **a** showing a single biphenyl molecule in a stable configuration. The STM position for surface voltage pulse is indicated by a *dot*. **c** STM image of the same zone showing in **b** recorded after the surface voltage pulse. **d** and **e** Superimposed structural model of, respectively, **b** and **c**. Reprinted with permission from [56]

−3 V on adsorbed molecules (Fig. 15b–e). The mechanism of this switching has been deeply investigated [56]. For the first time, an electronic excitation process, based on the resonant transfer of one electron from the biphenyl HOMO to the STM tip, has been fully demonstrated [56]. As the process implies a charged transient oxidative state of biphenyl molecule (i.e., due to the loss of one electron), the nature of the doped, p or n, silicon substrate is relevant. The electronic excitation and relaxation processes are not modified by changing p-doping to n-doping. Nevertheless, the dynamics of switching is strongly altered. Indeed, the transient state is negatively charged (due to charge delocalization on molecule), leading to a strong repulsive interaction with n-doped silicon surface instead of attractive interaction with p-doped silicon surface [57]. This example proves the role of the molecule–surface interaction for the development of nanomachines on semiconductor surfaces. Biphenyl molecules adsorption on Si(100)-(2 × 1) leads to other exotic bistable configurations which can be thermally activated [58].

Adsorption of 1,5-cyclooctadiene (COD) on a Si(001)-(2 × 1) surface at 7 K was investigated by STM experiments [59–61]. Free COD molecules are prochiral; therefore, COD adsorption on a Si(001) surface leads prevalently to the formation of two degenerate configurations, corresponding to a bridge structure, where the two C=C bonds are involved in a [2 + 2] cycloaddition reaction with two silicon dimers of the surface, as supported by DFT calculations [62] (Fig. 16a).

Time spectroscopy of the tunnel current under standard experimental setup (feedback loop turned off and STM tip at a fixed distance over adsorbed COD molecule) shows a random telegraph signal with an on–off ratio of 1.2:1 in (Fig. 17). Additional experiments were performed to determine the switching process.

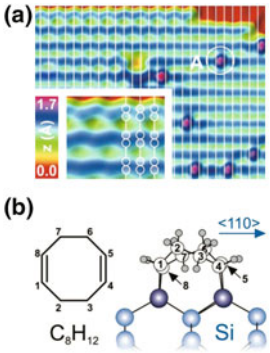

Fig. 16 **a** STM image of a COD molecule on a Si(001) surface at 7 K (10 × 8 nm^2, *Vs* = −2.0 V, *It* = 600 pA). The *inset* (3 × 2 nm^2) shows the Si dimer buckling at the upper step edge serving as a marker for the dimer position within a row. **b** COD molecule and structural model of the bridge structure. Reprinted with permission from [58]

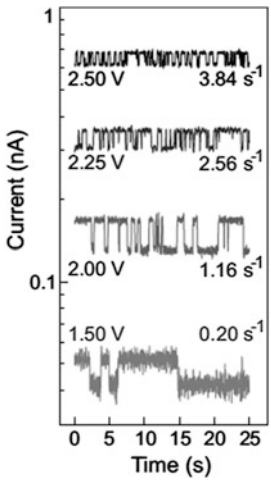

Fig. 17 Binary current fluctuations detected when tunneling through a COD molecule adsorbed in the bridge structure at a constant tip height (set point *It* = 150 pA, *Vs* = +2 V). The switching rate obtained for each current trace is indicated. Reprinted with permission from [59]

On the basis of experimental results, Nacci et al. proposed that COD switching between two degenerate configurations is triggered by an inelastic single electron process. This process is fully reversible and is achieved without any bond breaking or reforming, a case that remains rare in the literature.

4.3 Adatom Bistability Induced by Adsorption of a Molecule

Adsorption of a molecule on a semiconductor surface can induce the modification of molecular properties leading to molecular bistability, as described in the previous

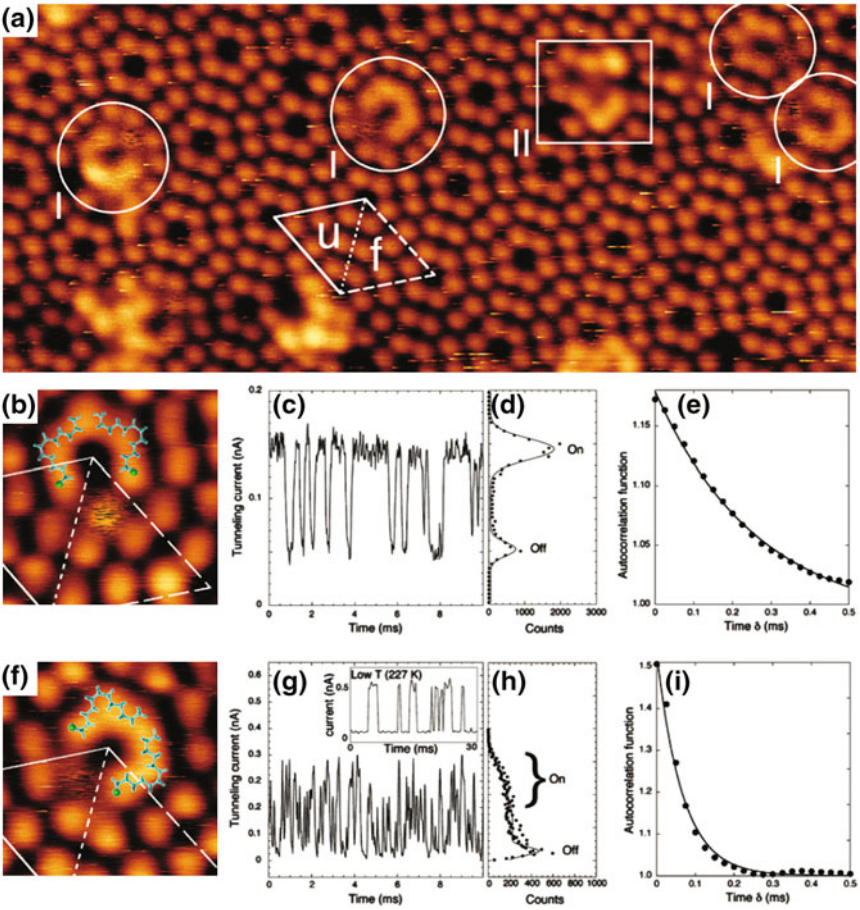

Fig. 18 **a** STM image (room temperature, 23 × 10 nm^2, *Vs* = 2.0 V, *It* = 100 pA) of chlorododecane molecules adsorbed on a Si(111)-(7 × 7) surface with two types of dimers surrounding a corner hole (*type I*) or corner adatom (*type II*). Faulted (*f*) and unfaulted (*u*) half-cells of Si(111)-(7 × 7) are marked. **b** High resolution STM image (3 × 3 nm^2, *Vs* = 2.5 V, *It* = 400 pA) of *type I* corral with superimposed structural model. **c** Tunneling current versus time measurements over a faulted corralled adatom (shown in **b**) at *Vs* = +2.5 V. **d** The corresponding tunneling current distribution with a pair of Gaussian functions fitted. High-current (on) and low-current (off) states are labeled. **e** The autocorrelation of the tunneling current time trace of **c**. Reprinted with permission from [64]

section. In this last part, we propose to describe the switching of an adatom (of the surface) induced by molecular adsorption. Polanyi et al. [63, 64] have investigated the adsorption of chlorododecane on the Si(111)-(7 × 7) surface. These molecules are non-covalently adsorbed on the surface. Pairs of chlorododecane molecules are self-assembled into two types of dimers, forming a corral surrounding a silicon corner hole or a corner adatom (respectively, I and II in Fig. 18).

When a pair of chlorododecane molecules surrounds a corner hole, a corner adatom, located between jaws of the corral, remains uncovered (Fig. 18b). This adatom exhibits a streaky appearance, corresponding to a switching between conductance states. This can be demonstrated by recording the tunneling current versus time (Fig. 18c–e). This switching has been interpreted as a single-atom electronic switch due to molecularly induced field effect. Small changes in the configuration of self-assembled pairs of chlorododecane molecules, which are dipoles, have a large electronic effect leading to high and low conductance. This interpretation is supported by DFT calculations. This is a new route toward molecular nanoelectronics induced by the adsorption of molecules on a silicon surface.

5 Conclusion and Perspectives

The development of single molecular machines on semiconductors is still a challenge. Some proofs of concepts have been successfully achieved. Molecule–surface interactions play a key role in this field because molecular motion is strongly conditioned by the molecule–surface interactions. In terms of perspective, semiconductors could be used as templates to guide molecular motions and to develop devices operating at room temperature.

References

1. Lensen, D., Elemans, J.A.A.W.: Artificial molecular rotors and motors on surfaces: STM reveals and triggers. Soft. Matter. **8**, 9053 (2012)
2. Perera, U.G.E., Ample, F., Kersell, H., Zhang, Y., Vives, G., Echeverria, J., Grisolia, M., Rapenne, G., Joachim, C., Hla, S.W.: Controlled clockwise and anticlockwise rotational switching of a molecular motor. Nat. Nanotech. **8**, 46 (2013)
3. Kottas, G.S., Clarke, L.I., Horinek, D., Michl, J.: Artificial molecular rotors. Chem. Rev. **105**, 1281 (2005)
4. Feringa, B.L.: In control of motion: from molecular switches to molecular motors. Acc. Chem. Res. **34**, 504 (2001)
5. Stroscio, J.A., Eigler, D.M.: Atomic and molecular manipulation with the scanning tunneling microscope. Science **254**, 1319 (1991)
6. Jung, T.A., Schlittler, R.R., Gimzewski, J.K., Tang, H., Joachim, C.: Controlled room-temperature positioning of individual molecules: molecular flexure and motion. Science **271**, 181 (1996)
7. Hersam, M.C., Guisinger, N.P., Lyding, J.W.: Isolating, imaging, and electrically characterizing individual organic molecules on the Si(100) surface with the scanning tunneling microscope. J. Vac. Sci. Technol., A **18**, 1349 (2000)
8. Liu, L., Yu, J., Viernes, N.O.L., Moore, J.S., Lyding, J.W.: Adsorption of cobalt phthalocyanine on Si(100)2 × 1 and Si(100)2 × 1:H surfaces studied by scanning tunneling microscopy and spectroscopy. Surf. Sci. **516**, 126–188 (2002)
9. Otero, R., Naitoh, Y., Rosei, F., Jiang, P., Thostrup, P., Gourdon, A., Lægsgaard, E., Stensgaard, I., Joachim, C., Bensenbacher, F.: One-dimensional assembly and selective

orientation of lander molecules on an O–Cu template. Angew. Chem. Int. Ed. **43**, 2092–2095 (2004)
10. Bellisario, D.O., Jewell, A.D., Tierney, H.L., Baber, A.E., Sykes, E.C.H.: Adsorption, assembly, and dynamics of dibutyl sulfide on Au{111}. J. Phys. Chem. C **114**, 14583 (2010)
11. Hong, I.H., Tsai, Y., Chen, T.M., Tuilier, M.H.: Self-organization of mesoscopically ordered parallel Gd-silicide nanowire arrays on a Si(110)-16 × 2 surface: a massively parallel active architecture. Appl. Phys. Lett. **98**, 193118 (2011)
12. Roge, T., Palmino, F., Savall, C., Labrune, J.C., Pirri, C.: Er-induced 2V3 × 2V3 R30 reconstruction on Si(111): influence on the very low Er coverage silicide growth. Surf. Sci. **383**, 350 (1997)
13. Makoudi, Y., Duverger, E., Arab, M., Chérioux, F., Ample, F., Rapenne, G., Bouju, X., Palmino, F.: Room-temperature electronic template effect of the SmSi(111)-8 × 2 interface for self alignment of organic molecules. ChemPhysChem **9**, 1437 (2008)
14. Netzer, F.P.: Rare earth overlayers on silicon. J. Phys.: Condens. Matter **7**, 991 (1995)
15. Papgeorgiou, N., Ferro, Y., Layet, J.M., Giovanelli, L., Mayne, A.J., Dujardin, G., Oughaddou, H., Le Lay, G.: Self-assembled molecular chains formed by selective adsorption of lead–phthalocyanine on InSb(100)-(4 × 2)/c(8 × 2). Appl. Phys. Lett. **82**, 2518 (2003)
16. Angot, T., Salomon, E., Papageorgiou, N., Layet, J.M.: Long range one-dimensional ordering of lead phthalocyanine monolayer on InSb(100)-4 × 2/c(8 × 2). Surf. Sci. **572**, 59 (2004)
17. Tekiel, A., Goryl, M., Szymonski, M.: Copper phthalocyanine molecules on an InSb(001) c (8 × 2) surface studied by ultra-high-vacuum STM and non-contact AFM. Nanotechnology **18**, 475707 (2007)
18. Ehret, E., Palmino, F., Mansour, L., Duverger, E., Labrune, J.C.: Sm-induced reconstructions on Si(111) surface. Surf. Sci. **569**, 23 (2004)
19. Bouju, X., Chérioux, F., Coget, S., Rapenne, G., Palmino, F.: Directional molecular sliding at room temperature on a silicon runway. Nanoscale **5**, 7005 (2013)
20. Bernstein, J., Davis, R.E., Shimoni, L., Chang, N.L.: Patterns in hydrogen bonding: functionality and graph set analysis in crystals. Angew. Chem. Int. Ed. **34**, 1555–1573 (1995)
21. Philp, D., Stoddart, J.F.: Self-assembly in natural and unnatural systems. Angew. Chem. Int. Ed. **35**, 1154–1196 (1996)
22. Makoudi, Y., Palmino, F., Arab, M., Duverger, E., Cherioux, F.: Complete supramolecular self-assembled adlayer on a silicon surface at room temperature. J. Am. Chem. Soc. **130**, 6670 (2008)
23. Makoudi, Y., Arab, M., Palmino, F., Duverger, E., Ramseyer, C., Picaud, F., Cherioux, F.: A stable room-temperature molecular assembly of zwitterionic organic dipoles guided by Si (111)-7 × 7 template effect. Angew. Chem. Int. Ed. **46**, 9287–9290 (2007)
24. Makoudi, Y., Baris, B., Jeannoutot, J., Palmino, F., Grandidier, B., Cherioux, F.: Tailored molecular design for supramolecular network engineering on a silicon surface. ChemPhysChem **14**, 900 (2013)
25. Harikumar, K.R., Lim, T., McNab, I.R., Polanyi, J.C., Zotti, L., Ayissi, S., Hofer, W.A.: Dipole-directed assembly of lines of 1,5-dichloropentane on silicon substrates by displacement of surface charge. Nature Nano. **3**, 222 (2008)
26. McNab, I.R., Polanyi, J.C.: Patterned atomic reaction at surfaces. Chem. Rev. **106**, 4321 (2006)
27. Avouris, P., Walkup, R.E.: Fundamental mechanisms of desorption and fragmentation induced by electronic transitions at surfaces. Annu. Rev. Phys. Chem. **40**, 173 (1989)
28. Backus, E.H.G., Eichler, A., Kleyn, A.W., Bonn, M.: Real-time observation of molecular motion on surface. Science **310**, 1790 (2005)
29. Nacci, C., Kanisawa, K., Fölsch, S.: Reversible switching of single tin phthalocyanine molecules on the InAs(111)A surface. J. Phys.: Condens. Matter **24**, 394004 (2012)
30. Harikumar, K.R., Polanyi, J.C., Zabet-Khosousi, A.: Directed long-range migration reaction of benzene on Si(100). J. Phys. Chem. C **115**, 22409 (2011)

31. El Garah, M., Palmino, F., Cherioux, F.: Reversible photoswitching of azobenzene-based monolayers physisorbed on a mica surface. Langmuir **26**, 943 (2010)
32. Tamaï, N., Miyasaka, H.: Ultrafast dynamics of photochromic systems. Chem. Rev. **100**, 1875 (2000)
33. Elbing, M., Blaszcyyk, A., von Hänish, C., Mayor, M., Ferri, V., Grave, C., Rampi, M.A., Pace, G., Samori, P., Shaporenko, A., Zharnikov, M.: Single component self-assembled monolayers of aromatic azo-biphenyl: influence of the packing tightness on the SAM structure and light induced molecular movements. Adv. Funct. Mater. **18**, 2972 (2008)
34. Liu, Z.F., Hashimoto, K., Fujishima, A.: Photoelectrochemical information storage using an azobenzene derivative. Nature **347**, 658 (1990)
35. Ikeda, T., Tsutsumi, O.: Optical switching and image storage by means of azobenzene liquid-crystal films. Science **268**, 1873 (1995)
36. Natansohn, A., Rochon, P.: Photoinduced motions in azo-containing polymers. Chem. Rev. **102**, 4139 (2002)
37. Yu, Y., Nakano, M., Ikeda, T.: Directed bending of a polymer film by light. Nature **425**, 145 (2003)
38. Schäfer, L.V., Müller, E.M., Gaub, H.E., Grubmüller, H.: Elastic properties of photoswitchable azobenzene polymers from molecular dynamics simulations. Angew. Chem. Int. Ed. **47**, 2232 (2007)
39. Zhu, Y., Fujiwara, M.: Installing dynamic molecular photomechanics in mesopores: a multifunctional controlled-release nanosystem. Angew. Chem. Int. Ed. **47**, 2241 (2007)
40. Koshima, H., Ojima, N., Uchimoto, H.: Mechanical motion of azobenzene crystals upon photoirradiation. J. Am. Chem. Soc. **131**, 6890 (2009)
41. Simic-Milosevic, V., Meyer, J., Morgenstern, K.: Chirality change of chloronitrobenzene on Au(111) induced by inelastic electron tunneling. Angew. Chem. Int. Ed. **48**, 4061 (2009)
42. Parschau, M., Passerone, D., Rieder, K.H., Hug, H.J., Ernst, K.H.: Switching the chirality of single adsorbate complexes. Angew. Chem. Int. Ed. **48**, 4065–4068 (2009)
43. Dri, C., Peters, M.V., Scharwz, J., Hetcht, S., Grill, L.: Spatial periodicity in molecular switching. Nat. Nanotech. **3**, 649 (2008)
44. Alemani, M., Peters, M.V., Hecht, S., Rieder, K.H., Moresco, F., Grill, L.: Electric field-induced isomerization of azobenzene by STM. J. Am. Chem. Soc. **128**, 14446 (2006)
45. Henzl, J., Mehlhorn, M., Gawronski, H., Rieder, K.H., Morgenstern, K.: Reversible cis-trans isomerization of a single azobenzene molecule. Angew. Chem. Int. Ed. **45**, 603 (2006)
46. Comstock, M.J., Levy, N., Kirakosian, A., Cho, J.W., Lauterwasser, F., Harvey, J.H., Strubbe, D.A., Frechet, J.M.J., Trauner, D., Louie, S.G., Crommie, M.F.: Reversible photomechanical switching of individual engineered molecules at a metallic surface. Phys. Rev. Lett. **99**, 038301 (2007)
47. Choi, B.Y., Kahng, S.J., Kim, S., Kim, H., Kim, H.W., Song, Y.J., Ihm, J., Kuk, Y.: Conformational molecular switch of the azobenzene molecule: a scanning tunneling microscopy study. Phys. Rev. Lett. **96**, 156106 (2006)
48. Wang, Y., Ge, X., Schull, G., Brendt, R., Tang, H., Bornholdt, C., Koehler, F., Herges, R.: Switching single azopyridine supramolecules in ordered arrays on Au(111). J. Am. Chem. Soc. **132**, 1196 (2010)
49. Wu, H.C., Chou, L.W., Lee, Y.R., Su, C., Lin, J.C.: STM study of azobenzene self-assembly on Ag/Ge(111)-($\sqrt{3} \times \sqrt{3}$)-R30. Surf. Sci. **603**, 2935–2944 (2009)
50. Makoudi, Y., Palmino, F., Duverger, E., Arab, M., Cherioux, F., Ramseyer, C., Therrien, B., Tschan, M.J.L., Suss-Fink, G.: Nondestructive room-temperature adsorption of 2,4,6-tri(2′-thienyl)-1,3,5-triazine on a Si–B interface: high-resolution STM imaging and molecular modeling. Phys. Rev. Lett. **100**, 076405 (2008)
51. Baris, B., Luzet, V., Duverger, E., Sonnet, P., Palmino, F., Cherioux, F.: Robust and open tailored supramolecular networks controlled by the template effect of a silicon surface. Angew. Chem. Int. Ed. **50**, 4094 (2011)
52. Baris, B., Jeannoutot, J., Palmino, F., Luzet, V., Rochefort, A., Cherioux, F.: Noncovalent bicomponent self-assemblies on a silicon surface. ACS Nano **6**, 6905 (2012)

53. El Garah, M., Baris, B., Luzet, V., Palmino, F., Cherioux, F.: Reversible single molecular switch operating at 300 K on a surface. ChemPhysChem **11**, 2568–2572 (2010)
54. Pechenezhskiy, I.V., Cho, J., Nguyen, G.D., Berbil-Bautista, L., Giles, B.L., Poulsen, D.A., Fréchet, J.M.J., Crommie, M.F.: Self-assembly and photomechanical switching of an azobenzene derivative on GaAs(110): scanning tunneling microscopy study. J. Phys. Chem. C **116**, 1052 (2012)
55. Feenstra, R.M., Stroscio, J.A., Tersoff, J., Fein, A.P.: Atom-selective imaging of the GaAs (110) surface. Phys. Rev. Lett. **58**, 1192 (1987)
56. Lastapis, M., Martin, M., Riedel, D., Hellner, L., Comtet, G., Dujardin, G.: Picometer-scale electronic control of molecular dynamics inside a single molecule. Science **308**, 1000 (2005)
57. Lastapis, M., Martin, M., Riedel, D., Dujardin, G.: Role of the dopant in silicon on the dynamics of a single adsorbed molecule. Phys. Rev. B **77**, 125316 (2008)
58. Mayne, A.J., Lastapis, M., Baffou, G., Soukiassian, L., Comtet, G., Hellner, L., Dujardin, G.: Chemisorbed bistable molecule: biphenyl on Si(100)-2 × 1. Phys. Rev. B **69**, 045409 (2004)
59. Nacci, C., Lagoute, J., Liu, X., Flösch, S.: Conformational switching of single 1,5-cyclooctadiene molecules on Si(001) induced by inelastic electron tunneling. Phys. Rev. B **77**, 121405 (2008)
60. Nacci, C., Lagoute, J., Liu, X., Flösch, S.: Bistability of single 1,5 cyclooctadiene molecules on Si(001). Appl. Phys. A **93**, 313 (2008)
61. Nacci, C., Flösch, S., Zenichowski, K., Dokic, J., Klamroth, T., Saalfrank, P.: Current versus temperature-induced switching in a single-molecule tunnel junction: 1,5 cyclooctadiene on Si (001). Nano Lett. **9**, 2996 (2009)
62. Cho, J.H., Oh, D.H., Kleinman, L.: Theoretical study of the structure of 1,5-cyclooctadiene on Si(001). Phys. Rev. B **64**, 241306 (2001)
63. Dobrin, S., Harikumar, K.R., Jones, R.V., Li, N., McNab, I.R., Polanyi, J.C., Sloan, P.A., Waqar, Z., Yang, J., Ayissi, S., Hofer, W.: Self-assembled molecular corrals on a semiconductor surface. Surf. Sci. **600**, L43 (2006)
64. Harikumar, K.R., Polanyi, J.C., Sloan, P.A., Ayissi, S., Hofer, W.A.: Electronic switching of single silicon atoms by molecular field effects. J. Am. Chem. Soc. **128**, 16791 (2006)

Driving Molecular Machines Using the Tip of a Scanning Tunneling Microscope

Francesca Moresco

Abstract Several methods were developed in the last decades to manipulate molecules using the tip of a scanning tunneling microscope (STM). In this chapter, experiments will be reviewed where the movement of model molecular machines is driven by the tip of a STM. By varying one of three main parameters, the chemical forces between tip and surface, the electric field, or the tunneling current, molecules can be exactly positioned on a metal surface and conformational changes in single molecules can be induced. For the development of larger and more complex machines, it is, however, important to move not only adsorbates one by one, but also structures composed by several molecules. Therefore, a purely electronic excitation method was recently developed for the controlled movement of weakly interacting assemblies of few molecules.

1 Introduction

Examples of molecular machines and molecular motors have been reported recently [1–6]. Most of these experiments were performed in solution without the possibility of controlling molecules one by one. However, the future of machines based on single molecules relies in the possibility of controlling them with an atomic-scale precision. To develop molecular machines based on single molecules, low-temperature scanning tunneling microscopy (LT-STM), with its high resolution and stability, is a very convenient technique. Prototypes of atomic-scale-controlled molecular machines can be tested by adsorbing specially designed molecules on a surface in ultra-clean conditions, imaging and manipulating them using the tip of an STM [7–9].

F. Moresco (✉)
Institute for Materials Science, Max Bergmann Center of Biomaterials,
and Center for Advancing Electronics Dresden, Technische Universität Dresden,
01062 Dresden, Germany
e-mail: francesca.moresco@nano.tu-dresden.de

C. Joachim and G. Rapenne (eds.), *Single Molecular Machines and Motors*,
Advances in Atom and Single Molecule Machines, DOI 10.1007/978-3-319-13872-5_10

The first step toward the development of reliable atomic-scale-controlled molecular machines is to understand the motion and the intramolecular mechanics of a single molecule on a surface. In the last few years, mechanically driven molecular machines have been demonstrated including molecular gears [10–12], motors [13–16], wheels [17–19], and different kinds of nanovehicles [20–24]. Moreover, the manipulation of a molecule with the tip apex of a scanning tunneling microscope (STM) has become a well-established technique to study the mechanics of a single molecule on a surface [8, 9].

In Fig. 1, a molecular machine driven by the tip of a STM is schematically represented. The controlled positioning of the tip allows to image and move a nanoscale machine on a surface. Both the geometry of the system and the molecular conformation are precisely controlled, while the tip is able to induce movements and conformational changes in the molecule.

Low-temperature scanning tunneling microscopy (LT-STM) is at present the only experimental method, which allows both precise sub-molecular imaging of a single molecule and the possibility of manipulation and measurement of the electronic properties in clean and controlled conditions. Such properties can be usefully applied to test molecular machines. In this case, the STM tip supplies the driving forces necessary to power the nanomachine, which can be driven electrically, by means of tunneling electrons or electric fields, or mechanically, by taking advantage of chemical and van der Waals forces between tip and molecule.

In this chapter, some recent experiments are presented, where single molecules and molecular nanostructures are moved on a metal surface by using the tip of a STM at low temperature and in UHV conditions. The presented examples include the rotation of a molecular rack along a pinion molecular structure, the trapping and moving of metal atoms during the manipulation of a molecule, conformational changes and rolling of complex molecules, as well as the electric field-induced isomerization of azobenzene derivatives, and the pulse-induced manipulation of hydrogen-bonded nanostructures.

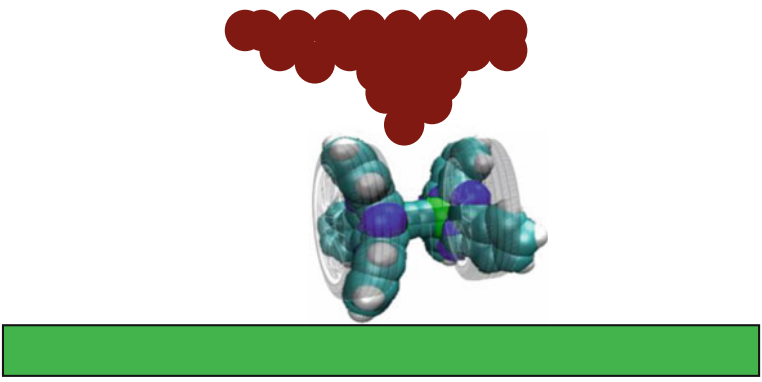

Fig. 1 Schematic drawing of a molecular machine driven by the tip of a STM

The experiments that are reported in this chapter have been performed at low temperature (5 K) in ultra-high vacuum (UHV) conditions on copper and gold substrates. Low Miller-index surfaces have been chosen because of their symmetry properties. The relatively strong interaction of the copper surfaces with the adsorbed molecules can facilitate conformational changes in the adsorbed molecules. On gold substrates, on the other hand, molecules weakly interact with the substrate, facilitating the controlled movement of molecules and molecular structures.

2 Mechanisms of Manipulation

The controlled manipulation of single atoms and molecules on surfaces by scanning tunneling microscopy is a well-established technique, which was developed during the last two decades [25–27]. In particular, STM has proven to be a versatile tool for the atomic-scale manipulation and the construction of nanostructures [8, 9, 25, 28–32]. Single atoms and molecules can be precisely positioned by lateral [30] or vertical manipulation [33]. Different mechanisms of manipulation were developed on metal [30], ultra-thin insulator [34, 35], or semiconductor [36] surfaces. Other manipulation techniques employ electric fields [37], inelastic tunneling electrons [38, 39], or, as was shown recently, induce conformational changes [40] in a molecule such that it walks across the surface [41]. Voltage pulses were used to desorb [42] or dissociate [43] molecules, to induce conformational changes [44] or chemical reactions [43].

The three main manipulation mechanisms are schematically shown in Fig. 2.

After having precisely positioned the tip on the molecule, one of the following parameters can be varied: the height of the tip on the surface, the tunneling current, or the applied bias voltage. In this way, the driving mechanism of the manipulation can be selected. By varying the height of the tip on the molecule [30], van der Waals and chemical forces can be activated. This procedure allows the control positioning of small molecules and single atoms, as well as repositioning and conformational changes in complex molecules (lateral manipulation, Fig. 2a). By selecting tip height and bias voltage in a combined way, the electric field applied on

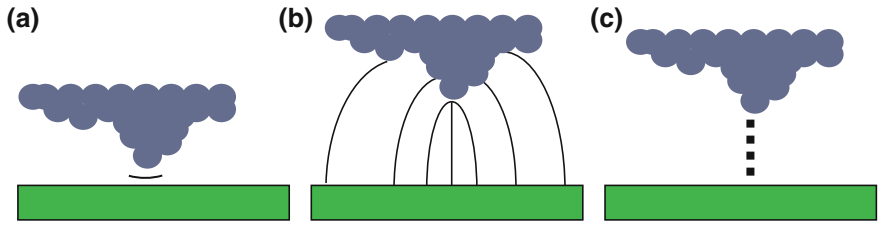

Fig. 2 Schematic drawing of the different mechanisms of manipulation described in this chapter. **a** Lateral manipulation induced by chemical and Van der Waals interaction. **b** Manipulation induced by electric fields. **c** Tunneling electron-induced manipulation

a single molecule can be controlled, making possible manipulation and conformational changes [37] (Fig. 2b). Due to the close distance between tip and surface, electric fields in the range of 10^7 V/cm are normally applied. Finally, as shown in Fig. 2c, the tunneling current can be varied, determining in this way the number of electrons tunneling through the molecule and inducing manipulation and conformational changes [38, 39].

In the following sections, a few examples of these three manipulation mechanisms will be described.

3 Lateral Manipulation

On metal surfaces, the standard method for lateral manipulation of single atoms [30], single molecules [8], or small groups of molecules [45] is to bring the tip of the STM close to the adsorbate, thereby increasing the tip adsorbate interaction, and then move the tip to the desired final location on the surface [29, 30], as schematically shown in Fig. 3.

In the first example of a single-atom STM lateral manipulation, Xe atoms were moved one at a time on metal surfaces [46]. To perform a lateral manipulation, the tip was first positioned above a Xe atom and its distance to the surface reduced, thereby reducing the interaction between the tip apex end atom and the Xe. The manipulation process was performed in constant-current mode and the Xe displaced by the lateral movement of the tip to the chosen final position. By reducing the tunneling current intensity, the tip finally retracts to a height characteristic for the normal STM imaging mode. With lateral manipulation experiments on single atoms

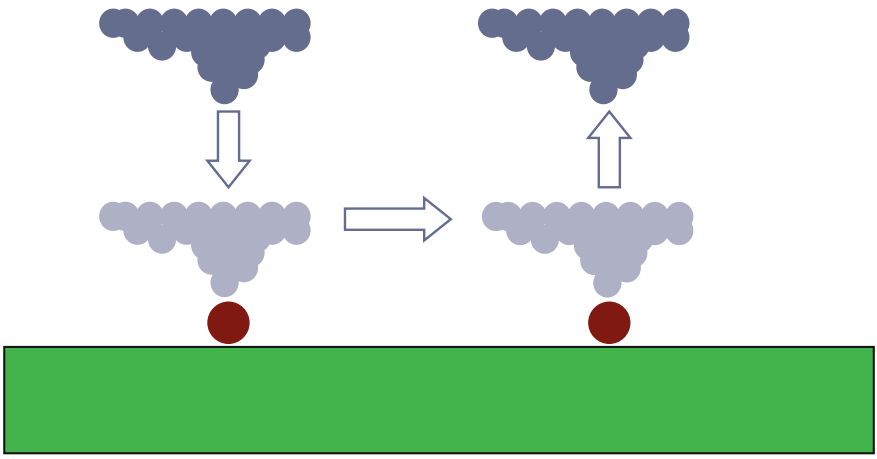

Fig. 3 Schematic representation of lateral manipulation. The STM tip is approached to the molecule and then moved laterally to the final position

or small molecules, different modes of manipulation such as pushing, pulling, and sliding can be distinguished by measuring the feedback signal during manipulation [30]. In particular, by manipulation in constant-current mode, detailed information on the process is obtained from the tip height signal, which reflects the interaction between the tip apex and the adsorbate [47].

A similar procedure can be used to manipulate complex molecules, inducing conformational changes [8]. For such molecules, the manipulation signal recorded through the STM feedback loop is normally more complex than for single atoms or small molecules like CO, especially when the mechanical internal degrees of freedom of the manipulated molecule play a role. For example, intramolecular conformation changes can be induced during the manipulation [48]. This type of movement is added to a rigid-like lateral-type motion on the surface, as one can observe from the manipulation signal. Manipulation signals for complex molecules therefore normally do not show the regular periodic modes over long periods observed for single atoms and small molecules. Changes from one mode to another during manipulation are often observed. In some cases, manipulation signals do not present any periodicity and the peaks are irregular in intensity, length, and shape [49]. Molecular flexure and reorientation of the internal conformations play a major role, as well as the reorientation of the molecule relative to the surface [8].

3.1 Inducing Conformational Changes

To succeed in the controlled positioning of a complex molecule and make easier the interpretation of a manipulation curve, it can be useful to manipulate it in constant height mode [50]. In this way, detailed information can be extracted concerning the role of the different degrees of freedom of the molecule during its movement on the surface.

In the constant height mode of manipulation, the tip is kept at a fixed distance from the surface when it is moved laterally across it. Such a technique makes the interaction between tip and molecule stronger and provides the molecule enough energy to overcome the diffusion barrier. To keep the tip height constant, the feedback loop is switched off. The current signal can then be recorded and contains the information about the mechanism of the manipulation process.

The technique of lateral manipulation at constant height was applied to investigate the internal mechanics of a TBPP molecule on Cu(100), with the aim of inducing motion and deformation of a part of the molecule, monitoring it in real time [48]. TBPP was specially designed to study the effects of LT-STM manipulation on the internal conformation of the molecule.

TBPP (*Cu-tetra-3,5 di-ter-butyl-phenyl porphyrin*) is a porphyrin-based molecule [8] with four phenyl-based lateral groups. The four lateral groups form legs, which electronically decouple the porphyrin central ring from the metallic surface. In the gas phase, the legs are oriented perpendicular to the central ring, but are able

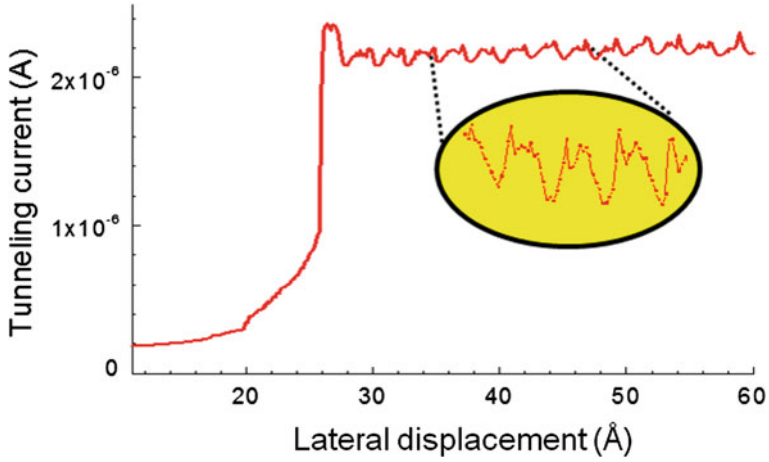

Fig. 4 Manipulation in constant height mode. Typical current signal for a TBPP molecule on Cu (100). The inset shows the details over four periods

to rotate around the σ-bond connecting each of them to the porphyrin, adapting themselves to the substrate corrugation.

Single TBPP molecules were pushed by the tip on a single leg, as shown in Fig. 4. The current curve recorded during the manipulation reflects first of all the Cu (100) lattice periodicity. However, details in each period do not resemble the regular sawtooth signals recorded during STM manipulations of atoms and diatomic molecules and show a specific intraperiod signature, peculiar of this specific type of manipulation. The contribution of each leg to the manipulation curve could be extracted by theoretical calculations.

3.2 Rolling of Single Molecules

Further studies on the manipulation of complex molecules have been devoted in the last years to the controlled rolling of molecules on a surface [17–19]. The rolling of a wheel at the nanoscale was demonstrated recently for a few systems. However, a reliable rotation of wheels was not observed so far. In the few cases where rotation of wheel was observed, this is limited to very small paths of sub-nanometer length, corresponding to a rotation over few single adsorption positions. A reliable rolling of a molecule on a metal surface is difficult to achieve for several reasons. On the one hand, a relatively strong interaction between molecule and surface is necessary to allow the rotation, avoiding the molecule to simply slide on the surface. On the other hand, the strong interaction with the surface makes difficult to observe at least the complete rotation of a wheel on his axis.

In the first example of controlled rotation [17], wheel-dimer molecules ($C_{44}H_{24}$), composed by two triptycene wheels connected by a C axle, were manipulated on the slightly corrugated Cu(110) surface. By applying lateral manipulation in constant height mode, it was possible to precisely tune the tip height, finding the conditions for rolling. The rotation of a single wheel by 120° was observed. Such result was confirmed by the unambiguous signatures in the manipulation curves recorded during the rolling motion.

However, the interpretation of the manipulation curves during the rolling remains very challenging and only few information can be extracted by manipulation curves in the case of rolling. Therefore, double-wheel molecules were designed, where the rolling could be detected directly from STM images or spectroscopy [18, 19].

The double-wheel molecule consists of two subphthalocyanine wheels connected by a central rotation carbon axis [18]. Each of the subphthalocyanine wheels has a nitrogen tag to monitor its intramolecular rolling during an STM manipulation sequence. The position of the tag can be followed by STM, allowing following the orientation of the wheels on the surface during manipulation. This new class of double-wheel molecules was investigated on the Au(111) surface. The idea of the experiment is schematically shown in Fig. 5.

Each wheel integrates an electronic tag (a nitrogen atom) which was designed to monitor the intramolecular rolling of the molecule. In the topographic STM images, the position of the tag can be determined by measuring the apparent height of the corresponding wheel. By lateral manipulations, the double-wheel molecule can be moved along the surface, mostly showing manipulation curves, which are similar to the curves, observed for rigid molecules and single atoms. In a few cases, however [19], a different STM feedback loop manipulation signature is observed and the rolling of a wheel confirmed by a change in the position of the tag.

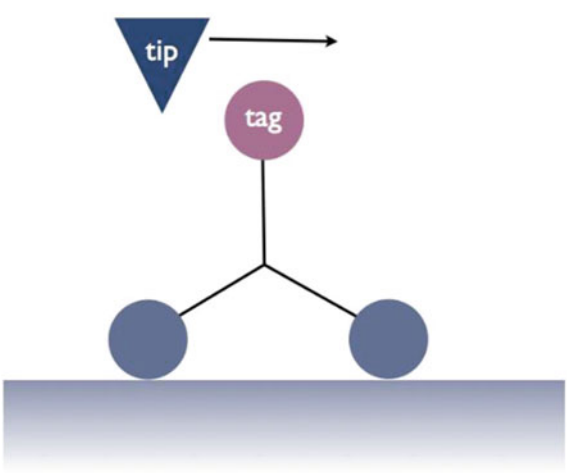

Fig. 5 Scheme of the rolling of a molecular wheel equipped with tag

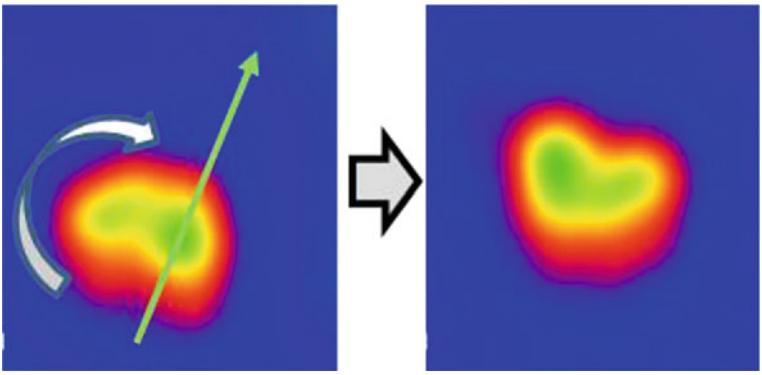

Fig. 6 Rolling of a double-wheel molecule on Au(111). The change in the apparent height of the wheels can be observed by STM topography

An example of rolling is shown in Fig. 6. The successful rolling was proven by measuring the apparent height of the corresponding wheel in the STM images.

Rolling experiments on more corrugated surfaces are presently performed to make intramolecular rotation easier, without, however, preventing the movement of the molecule on the surface. Moreover, new nanovehicles are designed, equipped with this new generation of subphthalocyanine molecular wheels.

3.3 Molecular Hoover

The possibility of using a molecule to collect and move single atoms and small clusters can open new possibilities of restructuring surfaces with atomic control [51]. Atomic structures were fabricated atom by atom in a controlled way combining lateral manipulation with the ability of a molecule to assemble atomic nanostructures.

The hexa-*t*-butyl-hexaphenylbenzene (HB–HPB) molecule was designed as a six-leg molecule [52]. Its structure is shown in the inset of Fig. 7. Such molecule was used to collect and carry up to six copper adatoms on a Cu(111) surface when manipulated with a STM tip.

The molecule consists of a central benzene ring connected to six phenyl groups by σ-bonds, and of six *t*-butyl lateral groups, each attached to a phenyl ring. The lateral phenyls can rotate, whereas steric hindrance between the phenyl groups forbids a full planar conformation of the molecule. The *t*-butyl end groups have the function of elevating the central HPB, avoiding the chemiadsorption of the molecule on a metal surface and facilitating its manipulation.

Because of their weak interaction with a metal surface, the molecules form on the Au(111) terraces ordered islands. No single molecules were observed by STM on the copper terraces.

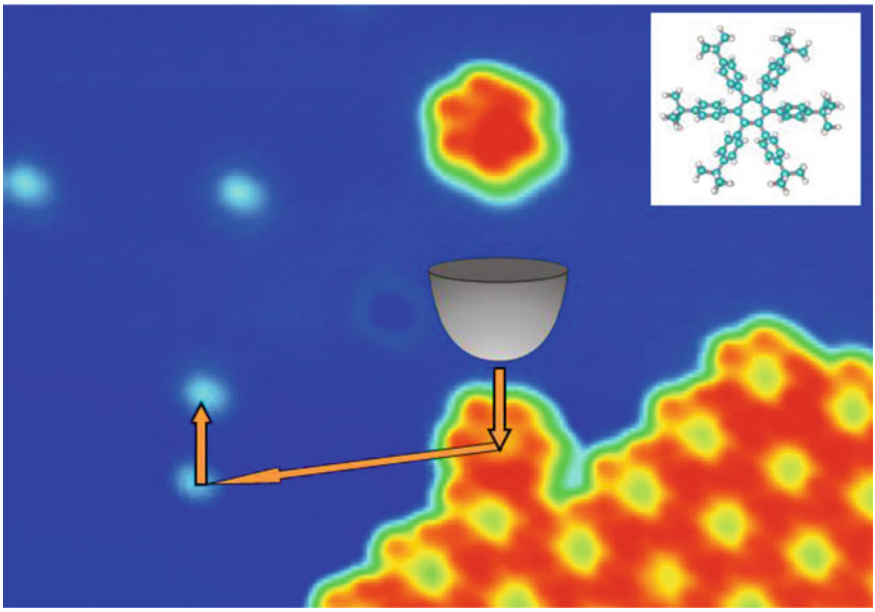

Fig. 7 Lateral manipulation of a HB–HPB molecule on a Cu(111) surface. The molecule can be moved from a molecular island edge to a Cu adatom. A single molecule can trap and move up to five copper adatoms. In the inset, the structural model of HB–HPB is shown

By means of lateral manipulation in constant-current mode, a molecule can be brought from the edge of a molecular island to the position of a copper adatom, as shown in Fig. 7. Analyzing the STM images recorded before and after the manipulation, it is clear that the molecule collects the atom and, when further manipulated, the whole complex of the molecule and atom moves simultaneously. This whole process of trapping and moving can be repeated until the molecule has collected six atoms.

However, the distance between tip and molecule during manipulation has to be decreased with increasing number n of captured atoms. This means that an increasing force should be applied by the tip by increasing the number of captured atoms. A molecule with six collected atoms cannot be moved at all.

The Cu atoms can be finally released by removing the molecule by vertical manipulation. By picking up the molecule with the STM tip after a collecting operation, it is possible to find all the previously accumulated Cu adatoms in the state of a coplanar packed cluster.

The number of Cu atoms remaining on the surface after the picking up of the molecule could be determined by comparison with Cu clusters that have been assembled by atom-by-atom manipulation without the use of an HB–HPB molecule.

The described experiment demonstrates that a specifically designed molecule is able to collect and carry a few metal atoms on a metal surface. This is possible

because adatoms are attracted by the phenyl groups of the front legs of the molecule. Moreover, the six legs create a propter cage for the collected atoms. The design of the central aromatic molecular group therefore influences the shape of the assembled cluster, whereas the molecular surface diffusion is governed by the chemical composition of the legs.

It would be extremely interesting to apply the described method to insulating or semiconducting surfaces, where the lateral manipulation of metal atoms was not successful so far. In this case, the molecular design has to be modified. This would make possible, for example, the interconnection of a molecular device to atomic-scale metallic electrodes on the surface of an insulator.

3.4 Molecular Rack and Pinion

Gears, wheels, and mechanically rotating systems are intensively studied by STM at the molecular scale. Lateral manipulation with the STM tip is a convenient technique to drive this kind of movements with atomic precision.

A self-assembled rack and pinion, where the STM tip apex is the rotation axis of the pinion, was recently demonstrated [10]. In this case, self-assembled molecular islands play the role of the rack, while a single molecule, driven by the STM tip, works as a pinion.

To assemble this kind of molecular rack-and-pinion device, a specific molecule comprising five phenyl groups and a pyrimidine group was designed. The molecule is called hexa-*t*-butyl–pyrimidopentaphenylbenzene (HB–NPB, $C_{64}N_2H_{76}$) and, like the HB–HPB molecule [52] described in the previous section, has the shape of a toothed gear with a cavity in its center. As for HB–HPB, the lateral rings of HB–NPB are tilted along the σ-bond axes because of the steric hindrance, giving the molecule a propeller shape. The *t*-butyl groups have the function of lifting the molecule to reduce the interaction of the aromatic parts with the substrate. However, in the case of HB–NPB, one of the six phenyl substituents is replaced by a pyrimidine group [53]. The aim of such substitution is to mark one of the lateral groups of the molecule, providing an orientation axis to the molecule. The pyrimidine ring acts therefore as a chemical tag that can be detected by STM, proving the rotation of the pinion molecule on the molecular rack. The idea of the experiment is shown in Fig. 8a.

As one can see in Fig. 8b, the substituted pyrimidine ring can be observed in STM images as a bright spot at particular bias voltages. It corresponds to a resonant-tunneling state localized on the pyrimidine ring, as observed by tunneling spectroscopy and confirmed by model calculations.

Similarly to the non-marked HB–HPB, the marked HB–NPB molecules physisorb on Cu(111), forming large ordered islands, and no single molecules are found on the free terraces. The same molecule was later used as molecular gear pinned on a defect of the Au(111) surface, demonstrating a controlled step by step rotation of the gear [12].

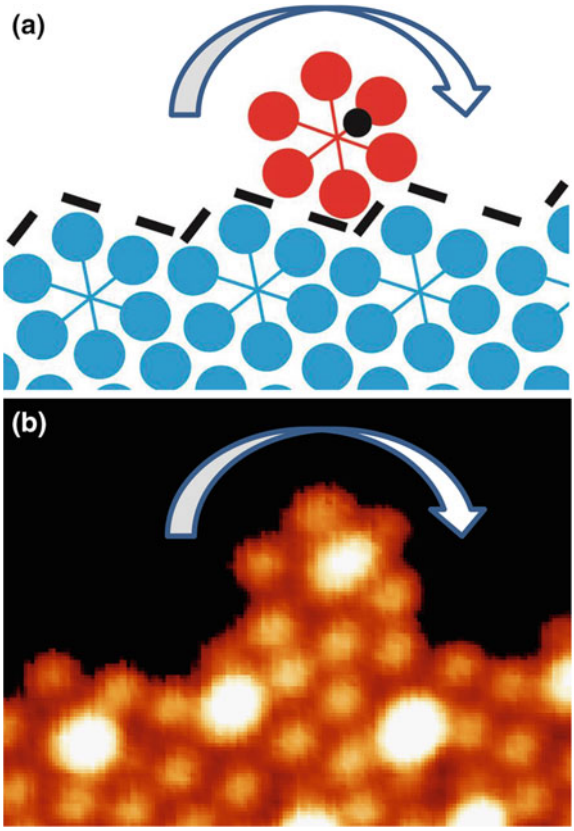

Fig. 8 **a** Model of a HB–NPB molecule adsorbed on a molecular island edge. **b** STM image of the border of an HB–NPB island (rack) with a single molecule (pinion) adsorbed on the island edge. The substituted pyrimidine group is visible as a bright spot on each molecule

To perform the rotation experiment, a single HB–NPB molecule was positioned along the rack by lateral manipulation in constant-current mode. Because of the intermolecular interaction, the pinion molecule adjusts spontaneously in one of the adsorption sites along the molecular island border, following its lattice structure. Then, the tip is moved at constant current parallel to the island edge, from the center of an adsorption site to the neighboring one. The tip is finally retracted back to the imaging conditions.

As a result, the pinion molecule has moved from one adsorption site to its neighbor, rotating. By performing series of manipulations, it is possible to prove that at each step of the manipulation, the orientation of the molecule in the surface plane changes by 60° clockwise. Because the STM tip approaches the molecule on its center, the rotational movement is uniquely determined by the shape of the molecular island border. The teeth of the pinion and of the rack are the *t*-butyl groups of the molecules. The rolling motion is made possible by the interlocking of the rack and of the pinion *t*-butyl groups, which prevents a sliding motion of the molecule and forces it to roll.

The described experiment is an interesting example of molecular machine, where a molecular rack-and-pinion device works with atomic-scale precision. It is important to note that such result was obtained after a long sequence of steps, comprising design and synthesis of the molecule, surface preparation, assembly of the molecular pinion on its molecular rack, and lateral manipulation experiments. The assembly of such a device opened a new way of exploring the functioning of a molecular machine.

4 Electric Field-Induced Manipulation

If a bias voltage is applied between the STM tip and the surface, a static electric field is created, which can be used to manipulate atoms or molecules [54–56]. The strength of such an electric field is very large, due to the close proximity of the tip to the surface, as schematically shown in Fig. 9.

The electric field between tip and surface in a common STM experiment has a typical value of 10^8 V/cm and is therefore comparable with the fields experienced by electrons in atoms or molecules. Depending on the tip shape, the electric field is concentrated in an inhomogeneous way near the tip apex, but its extension can reach hundred nanometers [28].

The interaction of an adsorbate with such a strong electric field in the STM junction has been first used to position Cs atoms on a semiconductor surface [57]. In this case, the interaction between the dipole moment of a Cs atom and the electric field induces a potential energy gradient along the surface, which allows the lateral positioning of single atoms.

Atoms and molecules can be manipulated by electric field even in the limit of zero tunneling current, as schematically shown in Fig. 10. In such a case, no tunneling current can be measured between tip and sample, but an electric field is present, able to manipulate molecules showing a dipole moment.

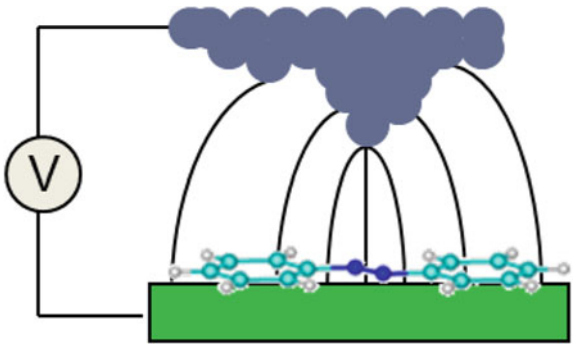

Fig. 9 Schematic representation of the electric field applied under the tip of an STM. Due to the vicinity of tip and surface, a relatively strong electric field is applied to an adsorbate, inducing its manipulation if a dipole moment is present

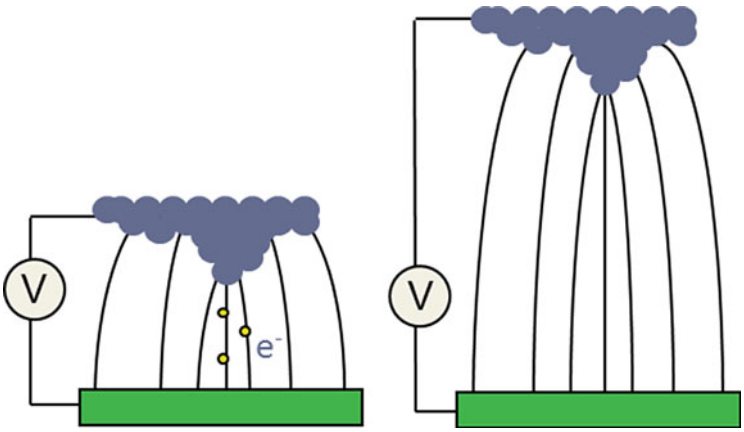

Fig. 10 Schematic representation of electric field applied in tunneling (*left*) zero current (*right*) conditions

Another kind of electric field-induced manipulation is possible when the applied voltage overcomes the value of the work function of the tip or the surface and electrons are therefore field-emitted [58].

4.1 Electric Field-Induced Isomerization of Azobenzene

Molecular switches are important building block for applications in molecular electronics and are since several years in the focus of research interest. In particular, azobenzene represents a very interesting example of molecular switch, being its operating mechanism based on the trans-cis isomerization of a double bond [59]. In the electronic ground state, azobenzene adopts two configurations: a nearly planar trans and a non-planar, three-dimensional cis form. The reversible switching of azobenzene is well studied in solution and in the gas phase, where the ground-state barrier for isomerization is typically overcome by photo-excitation.

The reversible isomerization of specifically designed azobenzene molecules was recently induced on Au(111) by the electric field in the STM junction, without tunneling of electrons [27, 59].

The 3,3′,5,5′-tetra-*tert*-butyl-azobenzene (TBA) is an azobenzene molecule carrying four lateral *tert*-butyl groups (Fig. 11a). The molecule was specially designed to increase the separation between surface and the azobenzene σ-system, leading to increased surface mobility and potentially lower electronic coupling. Its structure does not significantly alter the electronics of the azobenzene chromophore and does not impart steric hindrance upon the isomerization process.

Upon adsorption onto a clean Au(111) surface at room temperature, the molecules are mobile and form ordered islands consisting of parallel rows. Each molecule appears as four lobes with a rhombic shape where the lobes correspond to the

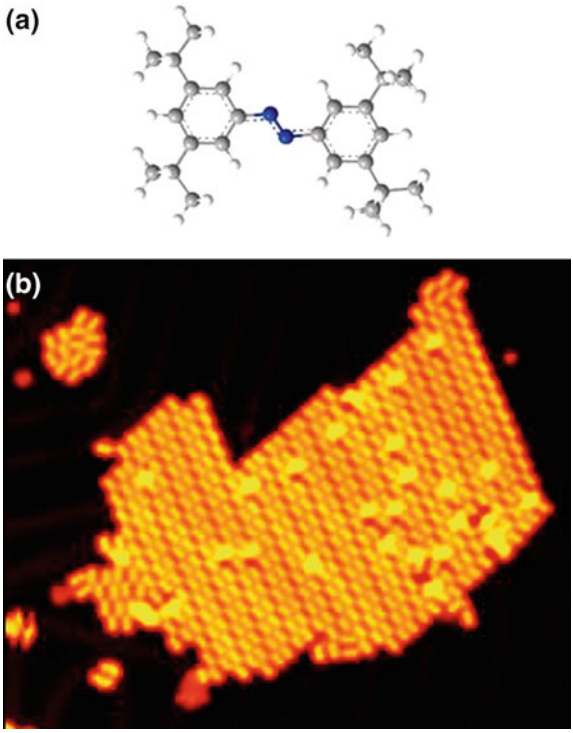

Fig. 11 **a** Structural model of the TBA molecule used in the electric field-induced isomerization experiment. **b** STM image recorded on a TBA island on Au(111) after the application of a voltage pulse. The *bright spots* indicate the switched trans molecules

tert-butyl groups, while the central azobenzene part is not visible. All observed molecules show the same planar configuration and were assigned to the thermodynamically favored trans-isomer.

The isomerization experiments were performed by positioning the STM tip at a fixed height above a molecular island with the feedback loop switched off. After applying voltage pulses, with the STM tip always at the same position above the island, STM images was recorded. As one can see in the example of Fig. 11b, after the pulses many molecules have changed their appearance, showing a brighter spot with a larger apparent height. Typically, the application of a single voltage pulse causes the switching of several molecules in a radius up to 50 nm around the position of the tip. The bright molecules are stable, and their initial appearance can be precisely restored by applying another pulse. Such switching experiments can be reproduced several hundred times and show the isomerization of single molecules from the trans to the cis form, and back to the trans form.

The isomerization process occurs also at very large tip distances where no tunneling current is flowing. Moreover, it is also possible to isomerize molecules when the tip is positioned above the bare surface nearby the island. All these observations, together with the large lateral extension over which switched molecules are observed, let to the conclusion that the isomerization of TBA molecules on Au(111) is driven by the electric field in the STM junction and does not involve tunneling of electrons.

5 Electron Tunneling-Induced Manipulation

Inelastic electron tunneling-induced manipulation is a process where tunneling electrons are injected from the tip positioned above the adsorbed molecule, thus moving it. The electron energy is normally transferred through an excited state, leading to excitation (rotational, vibrational, or electronic), the rate of which is controlled by the applied bias and the tunneling current [27]. A schematic representation of the process is shown in Fig. 12.

In an STM experiment, when an electron tunnels through an adsorbate, inelastic electron scattering may induce elementary electronic or vibrational excitations of the adsorbate [9]. The inelastic electrons, which represent a small fraction of the tunneling current, transfer energy from the electrons to the adsorbate. Such energy, stored in the electronic or vibrational excitation of the molecule, can trigger movement or chemical transformation at the atomic scale [9]. Electron tunneling-induced manipulation might be based on two different excitations depending on the applied bias voltage. At high voltages, an electron may transiently occupy an electronic excited level of the adsorbate; at low voltages, vibrational modes may be excited.

Experimentally, electron tunneling-induced manipulation is realized by positioning the STM tip above the location of the molecule at a fixed height. There the feedback loop is switched off, and tunneling current and/or voltage is increased from imaging to manipulation parameters. The electrons can be injected either from the tip or from the substrate depending on bias polarity. The moment of reaction is determined by monitoring the tunneling current in time. A sudden change in current is indicative of the success of the manipulation. These sudden changes are caused by changes in the apparent height of the molecule either through a motion of the molecule or through modification of the electronic structure [6].

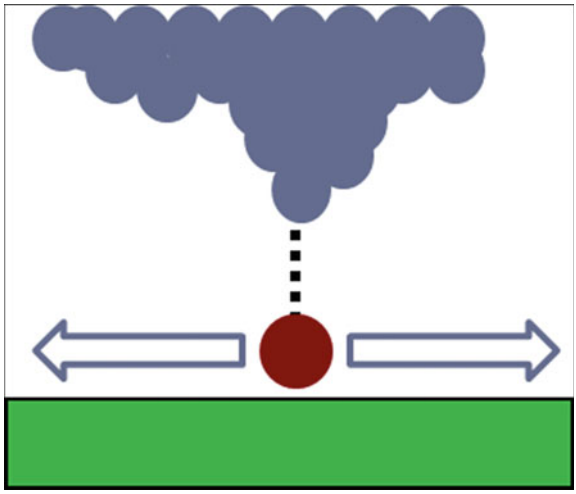

Fig. 12 Schematic representation of electron tunneling-induced manipulation. Tunneling electrons injected from the tip can induce movement or conformational changes in molecular adsorbates

Recently [60], electron tunneling was used to induce the controlled rotational switching of a molecular motor. A molecular motor adsorbed on a gold surface could be rotated in a clockwise or anticlockwise direction by selective inelastic electron tunneling through different sub-units of the motor.

5.1 Pulse-Induced Positioning of Supramolecular Structures

Electron tunneling-induced manipulation has the advantage to be triggered just by electronic excitations and to avoid any direct mechanical interactions of the STM tip apex with the adsorbate. Moreover, being mechanically less destructive than common lateral manipulation can be successfully applied to the controlled manipulation of weakly bonded supramolecular assemblies [61].

Recently, it was demonstrated that it is possible to manipulate in a controlled way supramolecular structure by electron tunneling-induced manipulation [61]. By applying voltage pulses just on one selected molecule of the structure, it is possible to move the complete supramolecular assembly to a chosen position on the surface without destroying it.

A small molecule, 4-acetylbiphenyl (ABP) molecule was used in the reported study. It is composed of two phenyl rings and an acetyl group. On Au(111), the ABP molecules self-assemble into small weakly bonded supramolecular structures. In most cases, the ABP molecules are organized in a windmill nanostructure. A STM image of a windmill is shown in Fig. 13, superposed to its chemical

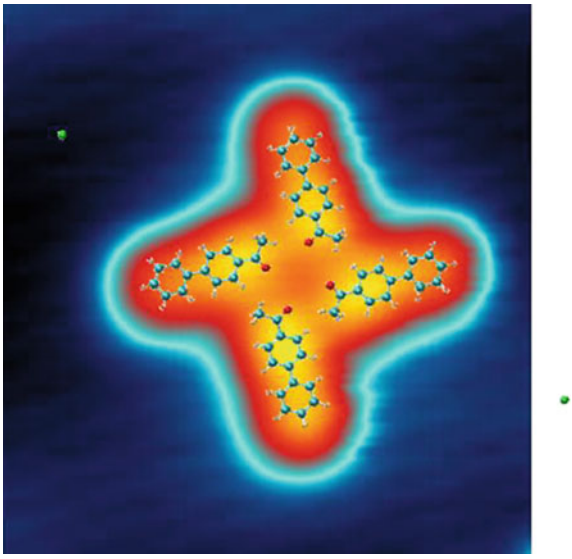

Fig. 13 STM topography image of a self-assembled tetramer (windmill) of ABP on Au(111) with superimposed molecular structure

structure. The structure is stabilized by hydrogen bond, as confirmed by calculations, and shows a bond length of 3.1 Å. These windmills are present on the surface in two mirror symmetric forms as a consequence of the prochiral nature of the single molecules.

Attempts to move the windmills using the conventional lateral manipulation technique described in Sect. 3 resulted in a destruction of the supramolecular nanostructure and the separation of its ABP components. In order to move the individual windmills, voltage pulses on top of or close to one of the ABP molecules of the nanostructure were applied. These resulted in a controlled collective movement of all ABP molecules of the chosen windmill at the same time. In Fig. 13, topography images taken before (left) and after (right) the voltage pulse are shown.

By changing the applied voltage, different types of motions can be selected. For negative voltages, the windmill moves in the direction away from the position of the tip. For positive voltages, two possible movement types could be observed. Most frequently, translational movements are induced. In this case, the direction of the translation is opposite to that for negative voltages; that is, the center of the supramolecular structure moves toward the position of the tip. In a few cases, however, the windmill rotates when positive voltages are applied. For translational movements, typical lateral jumps of 3 Å, corresponding to the surface lattice constant of Au(111), are observed. To move the windmill over larger paths, series of voltage pulses are applied (Fig. 14).

In order to understand the described manipulation events, the tip height traces taken during the time interval of the voltage pulses were systematically analyzed and the results compared with the STM tunnel junction dI/dV spectrum recorded over a windmill at the same position where the voltage pulse has been applied for manipulation. The energy onset position of the observed resonances corresponds to

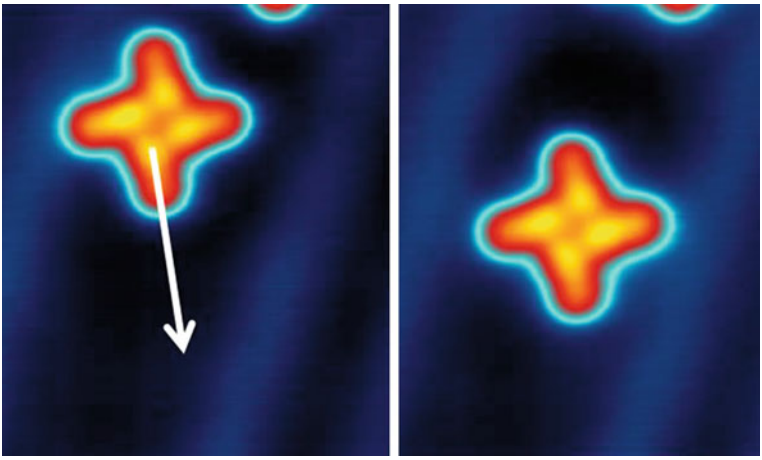

Fig. 14 STM topography images of self-assembled ABP on Au(111) taken before (*left panel*) and after (*right panel*) applying a series of voltage pulses

the measured quantum yield, indicating the presence of an inelastic input channel on the windmill. Such localized inelastic excitations on just one ABP molecule of the windmill are enough for the complete supramolecular windmill nanostructure to translate or to rotate without any internal apparent structural change. Once a threshold voltage has been reached, where tunneling in molecular resonances is possible, the supramolecular structure can be moved.

This experiment demonstrates a method to controllably move supramolecular structures on a metal surface by STM and can help in understanding the movements of weakly bound molecules on metal surfaces. It provides a novel procedure to manipulate individual nanostructures gently and purely electronically. The structures can be moved to the chosen positions on the surface without the need for complex intramolecular mechanical mechanisms, opening a new route for the construction of artificial molecular devices.

6 Conclusions and Outlook

In this chapter, some recent experiments were presented, where single molecules and molecular nanostructures are moved on a metal surface by using the STM tip. The possible manipulation modes were described in terms of the parameters that can be varied during a manipulation experiment and therefore considering the driving mechanism of the manipulation. The three fundamental parameters are in this respect the height of the tip on the surface, the tunneling current, and the applied bias voltage. A few recent examples of these three manipulation mechanisms were described in detail.

STM was developed in the last years from an analytical technique capable of imaging topography and electronic properties of structures at surfaces, into a tool, which can be used to drive nanomachines with atomic precision, restructuring metallic and non-metallic surfaces. Moreover, manipulation is useful to investigate basic physics and chemistry on the single atom or molecular scale, including quantum phenomena or magnetic properties.

Manipulation with the STM tip has reached a mature stage and can be used now in a reliable way to drive molecular machines with atomic control. Several different manipulation methods were developed for different applications. The understanding of mechanics at the atomic scale and the transport of movement and information from the atomic to the macroscale and back are new challenges, where STM manipulation will play a major role.

Acknowledgments The author acknowledges all scientists that collaborated to the described works, especially at the physics department of the FU Berlin, the CEMES-CNRS Toulouse, and the Institute for Materials Science of the TU Dresden.

Support from the ICT-FET Integrated Project AtMol, the European Union (ERDF) and the Free State of Saxony via the ESF project 100087859 ENano and ECEMP A2, the German Research Foundation (DFG) within the Cluster of Excellence "Center for Advancing Electronics Dresden," the DFG-NSF project 11-568 is gratefully acknowledged.

References

1. Fletcher, S.P., Dumur, F., Pollard, M.M., Feringa, B.L.: A reversible, unidirectional molecular rotary motor driven by chemical energy. Science **310**, 80–82 (2006). doi:10.1126/science.1117090
2. Pijper, D., van Delden, R.A., Meetsma, A., Feringa, B.L.: Acceleration of a nanomotor: electronic control of the rotary speed of a light-driven molecular rotor. J. Am. Chem. Soc. **127**, 17612–17613 (2005). doi:10.1021/ja054499e
3. Chatterjee, M.N., Kay, E.R., Leigh, D.A.: Beyond switches: ratcheting a particle energetically uphill with a compartmentalized molecular machine. J. Am. Chem. Soc. **128**, 4058–4073 (2006). doi:10.1021/ja057664z
4. Van Delden, R.A., Koumura, N., Schoevaars, A., Meetsma, A., Feringa, B.L.: A donor–acceptor substituted molecular motor: unidirectional rotation driven by visible light. Org. Biomol. Chem. **1**, 33–35 (2003). doi:10.1039/b209378b
5. Hernandez, J.V., Kay, E.R., Leigh, D.A.: A reversible synthetic rotary molecular motor. Science **306**, 1532–1537 (2004). doi:10.1126/science.1103949
6. Van Delden, R.A., ter Wiel, M.K.J., Pollard, M.M., Vicario, J., Koumura, N., Feringa, B.L.: Unidirectional molecular motor on a gold surface. Nature **437**, 1337–1340 (2005). doi:10.1038/nature04127
7. Jung, T.A., Schlittler, R.R., Gimzewski, J.K., Tang, H., Joachim, C.: Controlled room-temperature positioning of individual molecules: molecular flexure and motion. Science **271**, 181–184 (1996). doi:10.1126/science.271.5246.181
8. Moresco, F.: Manipulation of large molecules by low-temperature STM: model systems for molecular electronics. Phys. Rep. **399**, 175–225 (2004). doi:10.1016/j.physrep.2004.08.001
9. Morgenstern, K., Lorente, N., Rieder K.-H.: Controlled manipulation of single atoms and small molecules using the scanning tunnelling microscope. Phys. Status Solidi B, pp. 1–81 (2013). doi:10.1002/pssb.201248392
10. Chiaravalloti, F., Gross, L., Rieder, K.-H., Stojkovic, S.M., Gourdon, A., Joachim, C., Moresco, F.: A rack-and-pinion device at the molecular scale. Nat. Mater. **6**, 30–33 (2007). doi:10.1038/nmat1802
11. Carella, A., Launay, J.-P., Poteau, R., Rapenne, G.: Synthesis and reactivity of [penta (4-halogenophenyl) cyclopentadienyl hydrotris (indazolyl) borate] ruthenium(II) complexes: rotation-induced fosbury flop in an organometallic molecular turnstile. Chem. Eur. J. **14**, 8147 (2008). doi:10.1002/chem.200800689
12. Manzano, C., Soe, W.H., Wong, H.S.J., Ample, F., Gourdon, A., Chandrasekhar, N., Joachim, C.: Step-by-step rotation of a molecule-gear mounted on an atomic-scale axis. Nat. Mater. **8**, 576–579 (2009). doi:10.1038/NMAT2467
13. Koumura, N., Zijlstra, R.W.J., van Delden, R.A., Harada, N., Feringa, B.L.: Light-driven monodirectional molecular rotor. Nature **401**, 152–155 (1999). doi:10.1038/43646
14. Kottas, G.S., Clarke, L.I., Horinek, D., Michl, J.: Artificial molecular rotors. Chem. Rev. **105**, 1281–1376 (2005). doi:10.1021/cr0300993
15. Kay, E.R., Leigh, D.A., Zerbetto, F.: Synthetic molecular motors and mechanical machines. Angew. Chem. Int. Ed. **46**, 72–191 (2007). doi:10.1002/anie.200504313
16. Vives, G., de Rouville, J.H.-P., Carella, A., Launay, A., Rapenne, G.: Prototypes of molecular motors based on star-shaped organometallic ruthenium complexes. Chem. Soc. Rev. **38**, 1551–1561 (2009). doi:10.1039/B804684K
17. Grill, L., Rieder, K.-H., Moresco, F., Rapenne, G., Stojkovic, S., Bouju, X., Joachim, C.: Rolling a single molecular wheel at the atomic scale. Nat. Nanotech. **2**, 95–98 (2007). doi:10.1038/nnano.2006.210
18. de Rouville, J.H.-P., Garbage, R., Ample, F., Nickel, A., Meyer, J., Moresco, F., Joachim, C., Rapenne, G.: Synthesis and STM imaging of symmetric and dissymmetric ethynyl-bridged dimers of boron-subphthalocyanine bowl-shaped nanowheels. Chem. Eur. J. **18**, 8925–8928 (2012). doi:10.1002/chem.201201123

19. Nickel, A., Meyer, J., Ohmann, R., Jacquot de Rouville, J.-P., Rapenne, G., Ample, F., Joachim, C., Cuniberti, G., Moresco, F.: STM manipulation of a subphthalocyanine double-wheel molecule on Au(111) J. Phys. Condens. Matter **24** 404001–4040016 (2012). doi:10.1088/0953-8984/24/40/404001
20. Kudernac, T., Ruangsupapichat, N., Parschau, M., Maciam, B., Katsonis, N., Harutyunyan, S. R., Ernst, K.-H., Feringa, B.L.: Electrically driven directional motion of a four-wheeled molecule on a metal surface. Nature **479**, 208–211 (2011). doi:10.1038/nature10587
21. Grill, L., Rieder, K.- H., Moresco, F., Jimenez-Bueno, G., Wang, C., Rapenne, G., Joachim, C.: Imaging of a molecular wheelbarrow by scanning tunneling microscopy. Surf. Science **584**, L153–L158 (2005). doi: 10.1016/j.susc.2005.03.062
22. Rapenne, G., Jimenez-Bueno, G.: Molecular machines: synthesis and characterization of two prototypes of molecular wheelbarrows. Tetrahedron **63**, 7018–7026 (2007). doi:10.1016/j.tet.2007.05.019
23. Vives, G., Kang, J.H., Kelly, K.F., Tour, J.M.: Molecular machinery: synthesis of a "nanodragster". Org. Lett. **11**, 5602–5605 (2009). doi:10.1021/ol902312m
24. Shirai, Y., Osgood, A.J., Zhao, Y.M., Kelly, K.F., Tour, J.M.: Directional control in thermally driven single-molecule nanocars. Nano Lett. **5**, 2330–2334 (2005). doi:10.1021/nl051915k
25. Eigler, D.M., Schweizer, E.K.: Positioning single atoms with a scanning tunneling microscope. Nature **344**, 524–526 (1990). doi:10.1038/344524a0
26. Custance, O., Perez, R., Morita, S.: Atomic force microscopy as a tool for atom manipulation. Nat. Nanotechnol. **4**, 803–810 (2009). doi:10.1038/nnano.2009.347
27. Moore, A.M., Weiss, P.S.: Functional and spectroscopic measurements with scanning tunneling microscopy. Annu. Rev. Anal. Chem. **1**, 857–882 (2008). doi:10.1146/annurev.anchem.1.031207.112932
28. Stroscio, J.A., Eigler, D.M.: Atomic and molecular manipulation with the scanning tunneling microscope. Science **254**, 1319–1326 (1991). doi:10.1126/science.254.5036.1319
29. Jung, T.A., Schlittler, R.R., Gimzewski, J.K., Tang, H., Joachim, C.: Controlled room-temperature positioning of individual molecules: molecular flexure and motion. Science **271**, 181–184 (1996). doi:10.1126/science.271.5246.181
30. Bartels, L., Meyer, G., Rieder, K.-H.: Basic steps of lateral manipulation of single atoms and diatomic clusters with a scanning tunneling microscope tip. Phys. Rev. Lett. **79**, 697–701 (1997). doi:10.1103/PhysRevLett.79.697
31. Hla, S.-W.: J. Scanning tunneling microscopy single atom/molecule manipulation and its application to nanoscience and technology. Vac. Sci. Technol. B **23**, 1351–1360 (2005). doi:10.1116/1.1990161
32. Stroscio, J.A., Tavazza, F., Crain, J.N., Celotta, R.J., Chaka, A.M.: Electronically induced atom motion in engineered $CoCu_n$ nanostructures. Science **313**, 948–951 (2006). doi:10.1126/science.1129788
33. Eigler, D.M., Lutz, C.P., Rudge, W.E.: An atomic switch realized with the scanning tunneling microscope. Nature **352**, 600–603 (1991). doi:10.1038/352600a0
34. Repp, J., Meyer, G., Paavilainen, S., Olsson, F.E., Persson, M.: Imaging bond formation between a gold atom and pentacene on an insulating surface. Science **312**, 1196–1199 (2006). doi:10.1126/science.1126073
35. Swart, I., Sonnleitner, T., Niedenführ, J., Repp, J.: Controlled lateral manipulation of molecules on insulating films by STM. Nano Lett. **12**, 1070–1074 (2012). doi:10.1021/nl204322r
36. Lastapis, M., Martin, M., Riedel, D., Hellner, L., Comtet, G., Dujardin, G.: Picometer-scale electronic control of molecular dynamics inside a single molecule. Science **308**, 1000–1003 (2005). doi:10.1126/science.1108048
37. Xu, Y.-Q., Zhang, J., Yuan, B.-K., Deng, K., Yang, R., Qiu, X.-H.: Electric field assisted hopping of tert-butylamine on Cu(111) Surface. Acta Phys. Chim. Sin. **26**, 2686–2690 (2010). doi:10.3866/PKU.WHXB20101012
38. Stipe, B.C., Rezaei, M.A., Ho, W.: Inducing and viewing the rotational motion of a single molecule. Science **279**, 1907–1909 (1998). doi:10.1126/science.279.5358.1907

39. Ohmann, R., Vitali, L., Kern, K.: Actuated transitory metal-ligand bond as tunable electromechanical switch. Nano Lett. **10**, 2995–3000 (2010). doi:10.1021/nl1014348
40. Moresco, F., Meyer, G., Rieder, K.-H., Tang, H., Gourdon, A., Joachim, C.: Conformational changes of single molecules induced by scanning tunneling microscopy manipulation: a route to molecular switching. Phys. Rev. Lett. **86**, 672–675 (2001). doi:10.1103/PhysRevLett.86.672
41. Kudernac, T., Ruangsupapichat, N., Parschau, M., Maciá, B., Katsonis, N., Harutyunyan, S. R., Ernst, K.-H., Feringa, B.L.: Electrically driven directional motion of a four-wheeled molecule on a metal surface. Nature **479**, 208–211 (2011). doi:10.1038/nature10587
42. Sloan, A. P., Sakulsermsuk, S., Palmer, R. E.: Nonlocal desorption of chlorobenzene molecules from the Si(111)-(7 × 7) surface by charge injection from the tip of a scanning tunneling microscope: remote control of atomic manipulation. Phys. Rev. Lett. **105**(4), 048301 (2010). doi:10.1103/PhysRevLett.105.048301
43. Hla, S.W., Bartels, L., Meyer, G., Rieder, K.-H.: Inducing all steps of a chemical reaction with the scanning tunneling microscope tip: towards single molecule engineering. Phys. Rev. Lett. **85**, 2777–2780 (2000). doi:10.1103/PhysRevLett.85.2777
44. Henzl, J., Mehlhorn, M., Gawronski, H., Rieder, K.-H., Morgenstern, K.: Reversible cis/trans isomerization of a single azobenzene molecule. Angew. Chem. Int. Ed. **45**, 603–606 (2006). doi:10.1002/anie.200502229
45. Böhringer, M., Morgenstern, K., Schneider, W.-D., Berndt, R.: Separation of a Racemic Mixture of Two Dimensional Molecular Clusters by Scanning Tunneling Microscopy. Angew. Chem. Int. Ed. **38**, 821-8(2010), 23 (1999). doi:10.1002/(SICI)1521-3773(19990315)38:6<821::AID-ANIE821>3.0.CO;2-A
46. Eigler, D.M., Schweizer, E.K.: Positioning single atoms with a scanning tunnelling microscope. Nature **344**, 524–526 (1990). doi:10.1038/344524a0
47. Bouju, X., Joachim, C., Girard, C.: Single-atom motion during a lateral STM manipulation. Phys. Rev. B **59**, 7845–7848 (1999). doi:10.1103/PhysRevB.59.R7845
48. Moresco, F., Meyer, G., Rieder, K.-H., Tang, H., Gourdon, A., Joachim, C.: Recording intramolecular mechanics during the manipulation of a large molecule. Phys. Rev. Lett. **87**, 088302 (2001). doi:10.1103/PhysRevLett.87.088302
49. Alemani, M., Gross, L., Moresco, F., Rieder, K.-H., Wang, C., Bouju, X., Gourdon, A., Joachim, C.: Recording the intramolecular deformation of a 4-legs molecule during its STM manipulation on a Cu(211) surface. Chem. Phys. Lett. **402**, 180–185 (2005). doi:10.1016/j.cplett.2004.12.026
50. Moresco, F., Meyer, G., Rieder, K.-H.: Low temperature manipulation of big molecules in constant height mode. Appl. Phys. Lett. **78**, 306–308 (2001). doi:10.1063/1.1339251
51. Gross, L., Rieder, K.-H., Moresco, F., Stojkovic, S.M., Gourdon, A., Joachim, C.: Trapping and moving metal atoms with a six-leg molecule. Nat. Mater. **4**, 892–895 (2005). doi:10.1038/nmat1529
52. Sadhukhan, S.K., Viala, C., Gourdon, A.: Syntheses of hexabenzocoronene derivatives. Synthesis **10**, 1521–1525 (2003). doi:10.1055/s-2003-40526
53. Gross, L., Rieder, K.-H., Gourdon, A., Joachim, C., Moresco, F.: Molecular aggregation within self-ordered monolayers. Chem. Phys. Chem. **8**, 245–249 (2007). doi:10.1002/cphc.200600587
54. Rezaei, M.A., Stipe, B.C., Ho, W.: Atomically resolved adsorption and scanning tunneling microscope induced desorption on a semiconductor: NO on Si(111)-(7 × 7). J. Chem. Phys. **110**, 4891–4896 (1999). doi:10.1063/1.478390
55. Saalfrank, P.: Manipulation of adsorbates with electric fields. J. Chem. Phys. **113**, 3780–3791 (2000). doi:10.1063/1.1287656
56. Lyo, I.W., Avouris, P.: Field-induced nanometer- to atomic scale manipulation of silicon surfaces with the STM. Science **253**, 173–176 (1991). doi:10.1126/science.253.5016.173
57. Whitman, L.J., Stroscio, J.A., Dragoset, R.A., Celotta, R.J.: Manipulation of adsorbed atoms and creation of new structures on room-temperature surfaces with a scanning tunneling microscope. Science **251**, 1206–1210 (1991). doi:10.1126/science.251.4998.1206

58. Martel, R., Avouris, P., Lyo, I.W.: Molecularly adsorbed oxygen species on Si(111)-(7 × 7): STM-induced dissociative attachment studies. Science **272**, 385–388 (1996). doi:10.1126/science.272.5260.385
59. Alemani M.: Low temperature STM investigation of molecular manipulation, decoupling, and switching. Dissertation, FU, Berlin (2006)
60. Perera, U.G.E., Ample, F., Kersell, H., Zhang, Y., Vives, G., Echeverria, J., Grisolia, M., Rapenne, G., Joachim, C., Hla, S.-W.: Controlled clockwise and anticlockwise rotational switching of a molecular motor. Nature Nanotech. **8**, 46–51 (2013). doi:10.1038/NNANO.2012.218
61. Nickel, A., Ohmann, R., Meyer, J., Grisolia, M., Joachim, C., Moresco, F., Cuniberti, G.: Moving nanostructures: pulse-induced positioning of supramolecular assemblies. ACS Nano **7**, 191–197 (2013). doi:10.1021/nn303708h

Nanogears Mechanics: From a Single Molecule to Solid-State Nanogears on a Surface

We-Hyo Soe, Cedric Troadec, Carlos Manzano, Jie Deng, Francisco Ample, Yang Jianshu and Christian Joachim

Abstract The first experimental demonstration of a controllable rotating molecule gear is presented. A scanning tunneling microscope (STM) is used to construct, manipulate, and observe the rotation of the molecule gear. The appropriate combination of molecule design, molecule manipulation protocol, and surface atomic structure selection leads to the functioning of the molecule gear. Rotation of the molecule gear is done step-by-step and totally under control. The fabrication of solid-state SiO_2 nanogears with diameters ranging from 30 nm up to 1 μm and their manipulation using an atomic force microscope tip on a graphite surface is also presented. Ranging in sizes from few tens of nanometers up to submicron diameters, they are going to enable the transmission of mechanical motion from functional mechanical molecule machineries to larger submicron or micron-sized devices through series of solid-state gears and mechanical components compatible with the semiconductor and electronics industry technology.

Keywords Molecule gears · STM manipulation · Nanolithography · Solid-state nanogears · AFM manipulation

1 Introduction

Miniaturizing mechanical components is important not only to enable the creation of mechanical nanomachines, but also for data input on an atomic-scale circuit, information encoding, energy harvesting, and also possibly production of energy from the background. In this regard, as of 2007, solid-state gears (one of the basic components of any mechanical machinery) have been downsized to diameters of

W.-H. Soe · C. Troadec · C. Manzano · J. Deng · F. Ample · C. Joachim (✉)
IMRE, A*STAR (Agency for Science, Technology and Research), 3 Research Link, Singapore 117602, Singapore
e-mail: joachim@cemes.fr

Y. Jianshu · C. Joachim
CEMES/CNRS, PicoLab, 29 Rue Marvig, BP 94347, Toulouse Cedex 31055, France

C. Joachim and G. Rapenne (eds.), *Single Molecular Machines and Motors*,
Advances in Atom and Single Molecule Machines, DOI 10.1007/978-3-319-13872-5_11

about 500 nm making use of a top-down approach [1]. In 2009, a gear-shaped molecule, hexa-t-butyl-pyrimidopentaphenylbenzene (HB-NBP), i.e., $C_{64}N_2H_{76}$, was used to construct a molecule gear by pinning it on an atom size axle and rotated successfully using a scanning tunneling microscope (STM) [2].

This molecule gear having 1.2 nm diameter equipped with six teeth is the smallest known working gear.

The construction of a rotating molecule gear device evidenced that gears with intermediate sizes in between 500 and 1 nm in diameter are lacking. Then, we engaged the exploration of fabricating intermediate nanogear size between a molecule gear and the 500 nm solid-state nanogear limit set in 2007. In this chapter, we develop this story into two parts. First, we present the intentionally constructed molecule gear where an HB-NBP molecule is mounted and centered on an atom axis uprising at a herringbone elbow on an Au(111) reconstructed surface. Thereafter, we describe the nanofabrication process of solid-state nanogears down to 40 nm in outer diameter using electron beam nanolithography techniques, where a hydrogen silsesquioxane (HSQ) layer was selected as an ultrathin starting material for this nanolithography, leading to the fabrication of SiO_2 solid-state gears with a minimum thickness of 15 nm.

2 A Single Molecule Gear

The HB-NBP molecule reported here has a gear-like structure and is chemically structured with six t-butyl outer legs uplifting a central aromatic core which is composed of five phenyl rings and one pyrimidine ring, all connected to a central planar phenyl. The pyrimidine group works as an electronic tag for STM imaging facilitating its identification and enabling to discriminate this gear tooth from the other ones, since it appears as a bright protrusion during STM imaging (see Fig. 1) [3]. Sub-monolayer amounts of this molecule were thermally sublimed on a cleaned Au(111) single crystal substrate kept at room temperature. After this molecular sublimation, the sample was cooled down to cryogenic temperatures before transferring it to the LT-UHV-STM chamber.

In general, the lateral manipulation of single atom and molecule using the STM tip can be carried out in both constant-current and constant-height modes. In the constant-current manipulation mode, the feedback loop enabling to keep the tunneling current constant is switched on during the whole manipulation process. Once a manipulation path is defined, the tip is moved horizontally along the input pathway set while concurrently adjusting vertically the tip-substrate height to keep the tunneling current constant. In a successful STM atom/molecule manipulation, the most important parameter is the tunneling resistance, which can be adjusted by changing the tip-molecule distance or by directly increasing or decreasing the tunneling current or the bias voltage [4]. The tunneling resistance is reduced to bring the tip very close to the atom or molecule to be manipulated, so close that the tunneling junction is forming a potential energy trap strong enough for an atom or

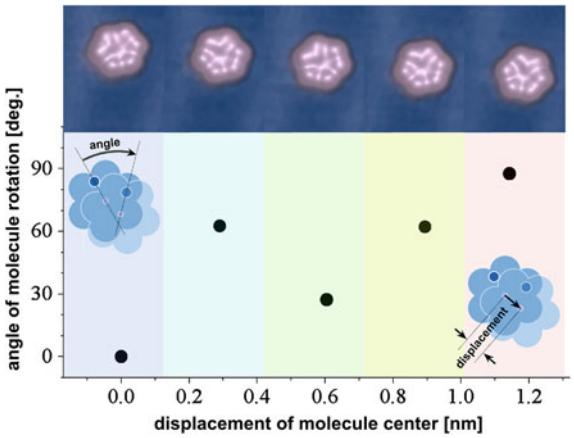

Fig. 1 Orientation and position changes of a HB-NBP molecule manipulated by the shortest possible distance between two surface ridges. *Leftmost* STM image shows the initial conformation of the molecule before manipulation, i.e., angle and displacement are equal to zero, the following images in order from *left* to *right* were taken after each manipulation step; $I = 5$ pA, $V = 100$ mV. After each manipulation, the molecule was displaced around 0.3 nm and turned in multiples of 30°

molecule to stay moving along the tip tracking its lateral displacement. Therefore, this mode is ideal for manipulating over a long distance. On the other hand, with the feedback turned off, during the manipulation process, the tip is moved parallel to the substrate surface keeping the tip height constant. Initial experiments show that when the gear molecule is manipulated, its movement involves translation and random rotation because it moves from adsorption site to adsorption site on Au (111) looking for stable positions for its six tertbutyl legs at the same time in registry with the underlying Au surface atoms and adapting its conformation accordingly on the surface at every step through its travel along the manipulation path. Because of the molecule conformation changes resulting in its rotation, during manipulation using the constant-height mode, the molecule might move off the given tip trajectory, then it would stop moving and follow the tip during manipulation. Therefore, this mode is suitable for a short-range manipulation; accordingly, it was used in the gear experiments described here since our purpose is solely to rotate the gear molecule through very short manipulation steps.

Before constructing the molecule gear, it was investigated how a freestanding HB-NBP molecule behaves during STM manipulations. When the molecule was manipulated to move the shortest distance possible which is equal to the distance between nearest neighboring surface atoms in an Au(111) plane, i.e., 0.288 nm, the molecule rotates randomly by approximately 30°, as presented in Fig. 1. Here, a series of STM images show the orientation and position changes of a gear molecule after each manipulation in between two herringbone ridges which is clearly seen in the STM image background. While moving along that path, the molecule turns

randomly in clockwise and anticlockwise directions while simultaneously being displaced by about 0.3 nm, intuitively indicating that the molecule needs a gear axis to be able to rotate without lateral displacement.

To explore whether it is possible to control the rotation of a HB-NBP molecule, three types of atomic-scale pinning centers have been tested as well as an atom quantum corral as presented in Fig. 2. The explored pinning centers are: one gold ad-atom, a pure herringbone elbow, an impurity natively bound to a herringbone elbow, and a circular potential moat created by superimposed surface states standing waves scattering at surrounding gold atoms.

Neither the bare elbow nor the Au ad-atom is suitable for a centered rotation. Because the interaction between the aromatic core of HB-NBP molecule and the herringbone elbow is not strong enough, small lateral displacements of the molecule during its rotation happen easily. When the molecule is moved on the Au ad-atom, it is never able to be concentric to the atom, and it always stabilizes with the atom in the middle of two tertbutyl legs [5]. As an inevitable consequence, the molecules are rotated pinned on an off-centered axis. The potential corral is not able to confine the molecule but because it does not have a solid pinning center like an ad-atom the molecule rotates while swaying inside the corral. Besides, this confining structure is unsuitable for the construction of a gear train, even if it is made by just two gears, because the surrounding ad-atoms will perturb the interactions between the molecules. Finally, the HB-NBP molecule gear was constructed on an atomic-scale impurity bound to one herringbone elbow as shown in Fig. 3. Here, the constant-current manipulation mode was used to mount the molecule on top of the impurity.

The concentrically mounted molecule gear on its atomic pinning center as presented in Fig. 3b is able to rotate by pushing one of the molecule legs with the

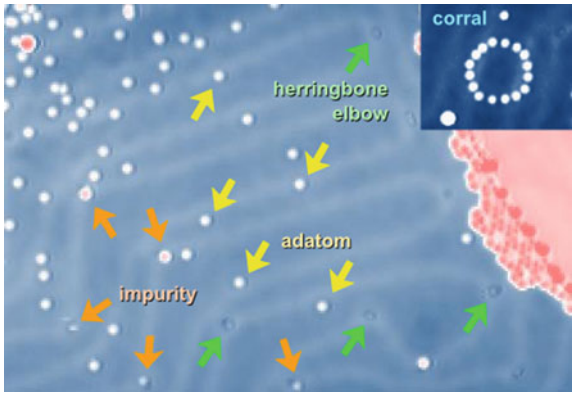

Fig. 2 Three candidates of atomic-scale pinning center used to mount the molecule gear: gold ad-atom (indicated by *yellow colored arrows*), clean herringbone elbow (*green arrows*), and atomic sized impurity natively bound to the elbow (*orange arrows*). Gold ad-atoms were created by gently crashing the STM tip into the gold surface outside the *top left* corner of the scanning area. *Inset* shows a corral structure built with gold ad-atoms using the STM atom manipulation technique

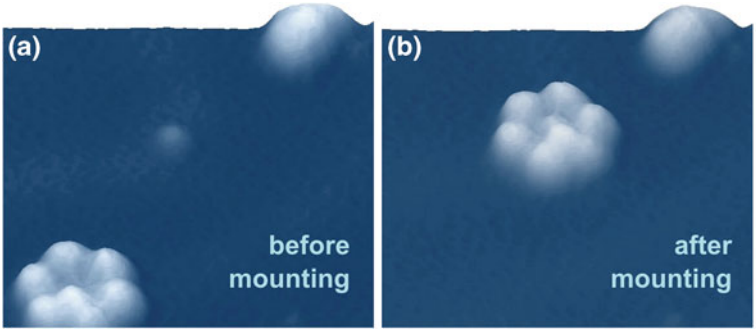

Fig. 3 STM images showing a single HB-NBP molecule **a** *before* and **b** *after* manipulation. **a** An atomic sized impurity bound to an elbow appears as a small protrusion. **b** The molecule and the impurity are concentric after the molecule is mounted on the impurity. I = 10 pA, V = 100 mV

STM tip, generally the one with the pyrimidine group. The reproducible step-by-step rotations of the molecule gear were carried out in both clockwise and anti-clockwise directions by gently pushing the molecule's leg using the constant-height manipulation mode. In Fig. 4, a sequence of STM images showing a full rotation of the molecule gear is presented. These images were taken after each manipulation

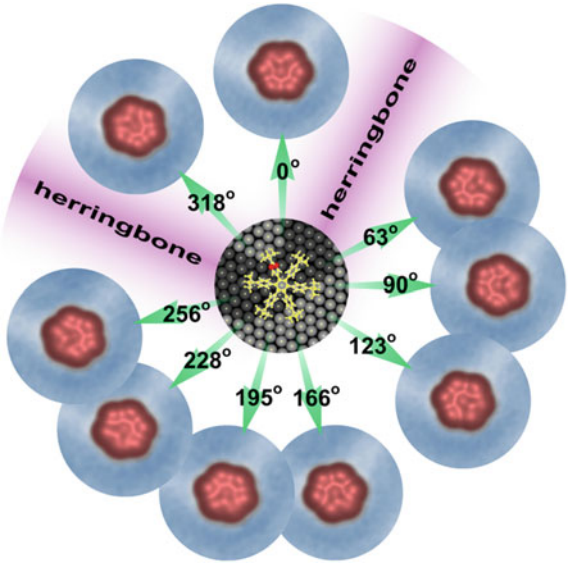

Fig. 4 Full step-by-step molecule gear rotation. The image at 0° shows the initial configuration imaged before starting the manipulations sequence. The following images taken after each manipulation in clockwise direction show the molecule gear rotated and stabilized at different molecule angles. Repulsive barriers between the gear legs and the ridges forming the herringbone elbow are located between 0°–63° and 256°–318°, respectively. There is also a rotation barrier between 123° and 166°

step to capture the new in-plane configuration of the molecule with respect to the surface substrate, and the pyrimidine tag was used as a reference to follow the molecule step-by-step rotation and to calculate the molecule's rotation angle. The rotation angle between each neighboring stable conformation is in average 30°–40°, except for two 63° jumps (0º–63º and 256º–318º). These two larger angular separations in between stable rotational positions are due to the influence of the two ridges forming the underlying herringbone extending from the elbow. The ridge's potential energy barrier bounces back the HB-NBP molecule by interacting with its t-butyl-end groups.

An analysis of the rotation sequence shows that there are nine stable positions for the molecule gear pinned on that herringbone elbow. These stable conformations were identified using ASED+ molecular mechanics calculations performed by taking into account the atomic-scale surface structure under and around the molecule gear and by calculating the STM image using the ESQC technique. The detailed atomic-scale model of the surface including the elbow defined an effective Au(111) surface where the molecule gear conformation was optimized, the constant-current STM image was calculated and compared to the experimental one [2].

3 Solid-State Gears Nanofabrication and Manipulation

Although the diameter of a molecule gear can be increased by synthesizing a molecule with a larger diameter and by adding more tertbutyl legs at the periphery, ultimately, there is a need for a nanosize scale solid-state gear to mechanically link a molecule gear to the existing micron size gears [6]. Furthermore, larger in diameter molecule gears will be too flexible to ensure a good transmission of motion. Part of the energy required for rotating a larger molecule would be distributed among the multiple degrees of freedom of such large molecule and just a little portion of it would reach the collective rotation degrees of freedom. An alternative to the synthesis of large molecule gears is the fabrication of solid-state gears robust and small enough, with diameters in the range of nanometers, to be able to rotate all the atoms in a cohesive manner through the transmission of rotational motion started from a macroscopic gear all the way down to the molecule gear.

In our previous work, six teeth solid-state nanogears made of HSQ were fabricated down to sizes of about 60 nm outer diameter and 30 nm in thickness. A sacrificial layer of gold deposited on top of the native oxide of the silicon substrate was used to release the gears. This process works fine, but for molecule gears to be added on the same substrate, an inexpensive, abundant, atomically smooth, and easily processed substrate has to be used. Highly oriented pyrolytic graphite (HOPG) fulfills all these requirements, and the following results will be based solely on this substrate. Furthermore, a 30 nm thickness is not very compatible with the 1 nm van der Waals height of a molecule gear as presented above together with the fact that 60 nm is still a gigantic diameter as compared to the 1.2 nm of the molecule gear Fig. 4.

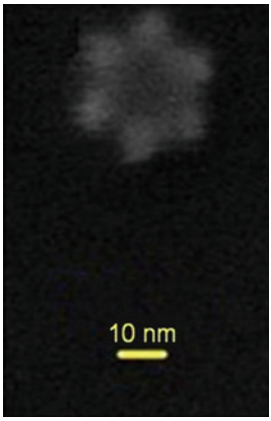

Fig. 5 The SEM image of the smallest solid-state gear ever nanofabricated on a graphite surface with a diameter below 30 nm in diameter for a thickness of 15 nm

Using an HOPG substrate, the fabrication process is greatly simplified: a minimum 15 nm HSQ layer (XR1541 from Dow Corning) was spun on a freshly cleaved HOPG substrate and then baked at 90 °C for 5 mn. E-beam lithography defines the nanogears, which are revealed after removing the surplus HSQ (the detailed process will be reported elsewhere). The resulting sample can be directly used for scanning electron microscopy (SEM) and atomic force microscopy (AFM) characterization and manipulations. Figure 5 shows the smallest solid-state gear fabricated to date, about 30 nm in diameter. The teeth are clearly defined, but are at the limit of the fabrication process.

Figure 6 shows an example of manipulation of such nanogear on the graphite substrate. This was obtained in an AFM tapping mode by mounting the graphite substrate on a movable piezo table. The AFM tip apex was fixed in x and y during the manipulation sequence, and the piezo table was moved step-by-step towards the targeted position on the graphite surface. A train of gears of different sizes can be assembled this way and AFM imaged afterwards (see Fig. 6a). An SEM image can be also recorded at the same location to appreciate the exact entanglement of the teeth between the nanogears of the train since this cannot be determined using the AFM images even in a taping mode (See Fig. 6b). The step edges on the graphite substrate can be clearly resolved by the AFM in taping mode of operation.

Solid-state gears of bigger size have also been achieved with the same process up to a diameter of 10 μm. This is large enough to offer a possibility to link with the existing micron size gears [6]. However, manipulation of such gears was only realized for diameter up to 1 μm, as demonstrated in Fig. 7. Two AFM images of the same location show a 1-μm-diameter solid-state HSQ gear before (a) and after (b) the AFM tip located on the red cross was moved along the drawn path resulting in a slight rotation and translation of the gear. This interplay between rotation and translation has been discussed earlier [7] and depends on the friction exerted on the gear by the substrate.

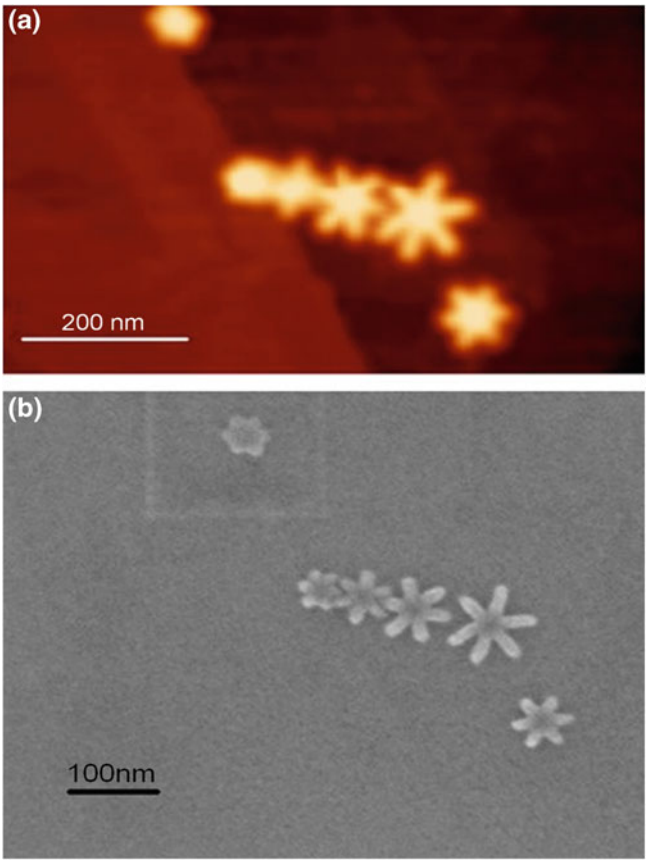

Fig. 6 **a** AFM imaging of manipulated nanogears in an AFM tapping mode forming a train of gears in interaction with a step edge. **b** SEM image of the same graphite surface area as in **a**

The new process using graphite as a substrate is very promising as it will enable to integrate the solid-state gears with the molecule gears, but two challenges remain in order to fulfill the gap between molecular scale and nanoscale gears.

The first challenge is the coupling between a molecule gear and a solid-state gear. The teeth defined by e-beam lithography are still too rough, uneven, and big to directly couple with a molecule. Van der Walls coupling could be achieved, but might be too small to pass a torque along. A mechanical coupling would still be a better choice, and decorating a solid-state disk with the same chemical group which terminates the molecule legs/teeth would be a valid option. Another option would be to use the emerging 2-dimensional materials available (graphene, h-BN, MoS_2, etc.…) to nanofabricate an intermediary nanogear, but that would require cutting the outlay of the gear with atomic precision, which is not yet achieved.

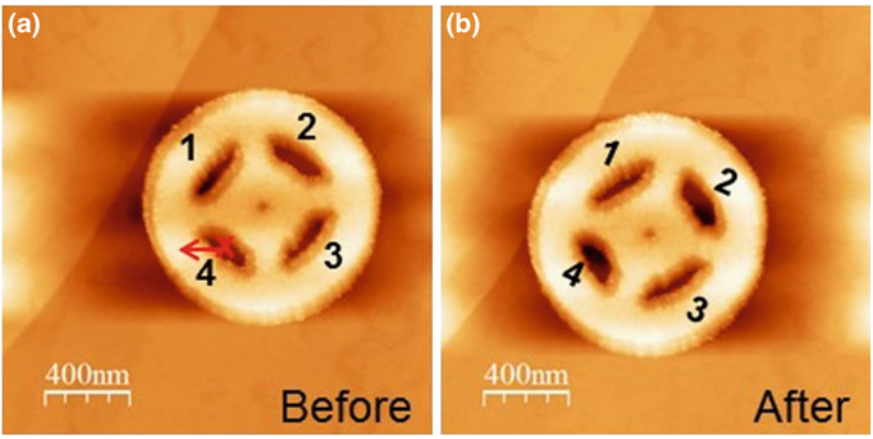

Fig. 7 AFM images of a 1-μm-HSQ solid-state gear nanofabricated on a graphite surface. **a** *Before* manipulation by the AFM tip following the path depicted by the *red arrow*. **b** *After* manipulation, the nanogear clearly rotated and translated toward the interaction with the AFM tip

The second challenge that linger concerns the axle. It is of prime importance to tackle this issue for practical nanomechanical mechanisms to be created. Using the tips of a multiprobe system [8] in place of axle is very useful to study and understand the mechanics in such nanogears. But it is not a long-term and scalable option. Focused ion beam-assisted chemical vapor deposition offers an alternative which is scalable. A small nanometer dot deposited using this technique could potentially be used as an axle. The deposition could be done at different stages, with each its own challenge: The dot can be patterned prior to the deposition of the HSQ layer, so the e-beam lithography step to define the gear will have to be done in a very precise manner, but the gear will be pinned from the start. If high resolution in the post-patterned gear cannot be achieved, the FIB assisted dot could be made after the gear making process. Thus, the gear will have to be either mounted on the axle using AFM or multiprobe manipulation or the gear will be put in the desired position before the dot is deposited. This method would be advantageous as it would be more flexible in making complex machinery.

4 Conclusion

The precise manipulation of a molecule gear by a STM tip has been achieved on an atomically flat gold surface. This itself is an achievement, but in order to harness the possibilities opened by these tiny gears, we also presented the smallest solid-state gears we could achieve by nanopatterning a 15-nm-thick HSQ layer by e-beam lithography to fabricate gears from micrometer size down to 30 nm outer diameter. These gears can be manipulated by an atomic force microscope tip to construct

various assemblies which could potentially be used to be interconnected with planar single molecule mechanical machines. However, we are still facing a few important challenges such as the lack of solution to easily create an axle and the problem of coupling molecule and solid-state gears.

Acknowledgments This work was supported by A*STAR (the Agency for Science, Technology and Research) funding under project no 1021100072.

References

1. Yun, Y.J., Ah, C.S., Kim, S., Yun, W.S., Park, B.C., Ha, D.H.: Manipulation of freestanding Au nanogears using an atomic force microscope. Nanotechnology **18**, 505304 (2007)
2. Manzano, C., Soe, W.-H., Wong, H.S., Ample, F., Chandrasekhar, N., Joachim, C.: Step-by-step rotation of a molecule-gear mounted on an atomic-scale axis. Nat. Mater. **8**, 576 (2009)
3. De Sarkar, A., Manzano, C., Soe, W.-H., Chandrasekhar, N., Joachim, C.: Conformation dependence of tag induced intramolecular STM contrast in hexaphenylbenzen molecules. Surf. Sci. **603**, L57 (2009)
4. Hla, S.W., Braun, K.F., Rieder, K.H.: Single-atom manipulation mechanisms during a quantum corral construction. Phys. Rev. **B67**, 201402(R) (2003)
5. Gross, L., Rieder, K.H., Moresco, F., Stojkovic, S.M., Gourdon, A., Joachim, C.: Trapping and moving metal atoms with a six-leg molecule. Nat. Mater. **4**, 892 (2005)
6. Rogers, M.S., Sniegowski, S.S., Miller, S., LaVigne, G.F.: Designing and operating electrostatically driven microengines. In: Proceedings of the 44th International Instrumentation Symposium, Reno, NV, pp. 56–65, 3–7 May 1998
7. Deng, J., Troadec, C., Ample, F., Joachim, C.: Fabrication and manipulation of solid-state SiO_2 nano-gears on a gold surface. Nanotechnology **22**, 275307 (2011)
8. Joachim, C., Martrou, D., Rezeq, M., Troadec, C., Deng, J., Chandrasekhar, N., Gauthier, S.: J. Phys. Condens. Matter **22**, 084025 (2010)